Records of volcanism and controls on volcanic processes in southern Chile

Sebastian F. L. Watt

Worcester College and the Department of Earth Sciences,
University of Oxford

Thesis submitted for the degree of Doctor of Philosophy

26th February 2010

Supervisors: Prof. David M. Pyle and Dr Tamsin A. Mather

Abstract

Records of volcanism and controls on volcanic processes in southern Chile

Sebastian F. L. Watt

This thesis describes volcanic records from the Andean southern volcanic zone, based on the collection of field data between Calbuco and Puyuhuapi volcanic centres, with a particular focus on the Hualaihue peninsula, combined with existing records from the region as a whole. These data, extending the understanding of the volcanic history of southern Chile, are examined for evidence of spatial or temporal variability, which may be used to explore underlying controls on volcanic processes.

All three volcanoes on the Hualaihue peninsula have been active in the Holocene. A large mafic scoria unit from Apagado is unusually primitive, providing a potential window into primary magma generation in the arc. Dynamically similar eruptions occurred at Hornopirén and widely along the regional scale Liquiñe-Ofqui fault zone (LOFZ). Although the Hualaihue centres are closely related, petrological evidence indicates a complex magmatic storage system. Effusive activity is predominant at Yate and Hornopirén, and the tephrostratigraphy of the Hualaihue area is dominated by units from Calbuco volcano, to the north. The 2008 eruption of Chaitén provided an analogue for past large explosive eruptions in the region, with tephra deposition reflecting variable eruption intensity in a changing wind field.

The regional tectonic setting and the LOFZ influence dyke ascent, volcano morphology and, as demonstrated at Yate, edifice stability, determining the orientation of collapse. Explosive eruption records over the post-glacial period also indicate a limited response of volcanism to deglaciation, suggesting a control on magma storage arising from changing crustal stress regimes, both at the arc front and along the LOFZ. On short timescales, large earthquakes are shown to influence eruption rate across the arc, implying a triggering role for dynamic seismic stresses. This work demonstrates the existence of a range of external forcings affecting Chilean arc volcanism, but the degree to which these are quantifiable is strongly constrained by the quality of the available data.

Extended Abstract

Records of volcanism and controls on volcanic processes in southern Chile

Sebastian F. L. Watt

The southern section of the Andean southern volcanic zone, located in Chile from 41.5°-44° S, has been little studied in the past. The eruptive history of several volcanoes in this region is poorly understood. By constructing an explosive eruption stratigraphy and investigating petrological and geochemical characteristics in the region between Calbuco and Puyuhuapi volcanoes, with a focus on the Hualaihue area, the data presented in this thesis render more complete the record of volcanism in this arc segment. The records produced link with results from previously studied volcanoes both to the north and south of Hualaihue.

The southern Chilean volcanic arc presents an ideal location in which to investigate spatial and temporal variability in volcanism. The compiled records provide an opportunity to test hypotheses relating to the influence of external controls on volcanic processes. Crustal and subduction parameters are relatively constant across much of the region, but a range of large-scale tectonic structures characterise the crust beneath the arc, and particularly large thrust earthquakes occur along the adjacent destructive plate margin. This part of Chile has also been widely affected by late Cenozoic glaciations. Thus, an array of potential interactions between volcanism and external systems may be examined in order to assess evidence for underlying controls on eruption behaviour.

The Hualaihue region comprises three related volcanoes: Apagado, Hornopirén and Yate. The focus of Holocene activity has been in the Yate-Hornopirén area. These volcanoes lie on the transpressional system of the Liquiñe-Ofqui fault zone (LOFZ). Holocene activity at Apagado is limited to a single scoria cone eruption, nested within deeply eroded older volcanics. The early stages of the Apagado eruption produced unusually primitive volatile-rich magmas, approaching picritic compositions. There is petrological evidence for similarly primitive compositions being parental to magmas erupted at Yate. While rock compositions at Apagado and Hornopirén are limited to basalts and basaltic andesites, more silicic compositions occur at Yate, which forms a large, prominent stratovolcano and was the main focus of Pleistocene volcanism on the Hualaihue peninsula. Distinctive groups of products are recognised on the basis of petrological characteristics, with rocks on the south flank of Yate distinct from those on the north. Although the Hualaihue rocks as a whole indicate a complex array of stored magma compositions, widely affected by

mixing processes, the Apagado scoria unit provides an insight into magmatic compositions largely unaffected by later modification processes. Explosive eruptions of a similar style to the Apagado unit, but erupting less primitive compositions, occurred in the Holocene at Hornopirén as well as at several centres along the LOFZ. In these cases, they commonly formed clusters associated with fractures parallel to the fault strike. While most of these scoria units show arc-type chemical signatures, the rocks at Puyuhuapi are unique in a regional context, with an alkaline composition enriched in incompatible elements.

In general, Holocene explosive activity in Hualaihue was limited, particularly at Yate, in comparison with volcanoes to the north and south. The tephrostratigraphy of the area is dominated by multiple pumice units from Calbuco, to the north of Yate, and also overlaps with an early Holocene tephra from Chaitén, to the south. These records have been compiled with those from elsewhere in the region to examine arc-scale variability in eruption rates. Their analysis is, however, limited by spatially variable rates of sampling across the region. Explosive eruption fluxes and eruption parameters, quantified on the basis of sparse data, are in many cases poorly constrained. The potential reduction in precision resulting from the extrapolation of limited data is well illustrated by the complexity of the tephra deposit from the 2008 Chaitén eruption. This large explosive eruption (magnitude >4), although producing a regionally-unusual rhyolitic composition, provides an analogue to older eruptions investigated in the region. Detailed mapping of the tephra unit showed a complex ash dispersal pattern, resulting from eruption over a week-long period during which wind directions and eruption column heights varied.

The regional stress regime, transpressional beneath the arc in Hualaihue, has influenced dyke ascent, with alignment of volcanic structures corresponding to the maximum principal stress direction. Furthermore, evidence at Yate suggests that the volcano's location on the LOFZ has imposed a structural grain, leading to edifice weakness and resultant collapse, through landslide generation, in an orientation oblique to the fault zone in the Riedel shear direction. Multiple landslides at Yate have dissected the edifice, in conjunction with glacial erosion, giving rise to mass flows with potentially devastating impacts. Such hazards may increase in frequency upon continued retreat of summit ice caps at several of the region's volcanoes.

The arc-scale explosive eruption record, spanning the post-glacial period, and analysed only for eruptions of magnitude ≥ 4 in order to reduce the effects of temporal sampling bias, shows a limited amount of temporally variable structure. The total length of the record decreases southwards, reflecting better preservation associated with the earlier retreat of ice in the north of the region. Limited evidence for both unusually large eruptions and a slightly higher eruption frequency in the early post-glacial period tracks the pattern of southward ice sheet retreat, but the small size of the data-set limits rigorous analysis. It is clear, however, that the overall impact of deglaciation on rates of arc volcanism is small in comparison with the large increases observed in other tectonic settings. The post-glacial records in southern Chile also suggest that the presence of a thicker and broader ice sheet in the south of the region may have promoted monogenetic basaltic volcanism along the LOFZ, in response to rapidly changing crustal strain rates and decompression associated with ice removal. Along the arc front, the available evidence of a relatively small increase in activity does not require a model of increased melt generation to be invoked (as in different settings, such as Iceland, where a large pulse in post-glacial volcanism has been documented), and may simply reflect relatively impeded magma ascent during glaciation, coupled with enhanced release upon retreat due to changes in upper crustal stress regimes resulting from removal of the vertical ice load.

On shorter timescales, statistical outliers in arc-scale eruption rate, compiled using historical eruption records for the whole of the Andean southern volcanic zone (33°-46° S), indicate a correlation with the occurrence of large earthquakes ($M_W > 8$) in the adjacent subduction zone. The duration of the increase is several months, and the distance of potentially triggered volcanic systems from earthquake rupture zones suggests that dynamic triggering effects, associated with the passage of seismic waves, as well as static stress changes, result in eruption triggering on this time scale. The precise mechanisms by which such interactions operate remain poorly understood.

Overall, the data gathered in this thesis have led to the recognition of several new explosive eruption units in southern Chile, enabling magnitudes of activity and rates of volcanism to be constrained at the parental volcanoes, and these records are augmented by petrological and geochemical data. Exploration of structure within records of volcanic activity in this region indicates the existence of a range of controls, modulating volcano location, construction, eruption style and rate, and edifice destruction, across a broad range of temporal and spatial scales. Interactions of this type may be used to better understand crustal magma dynamics and eruption mechanisms, but precise and quantitative exploration of these linked systems relies on the existence of comprehensive data-sets relating to past volcanic activity.

Acknowledgements

For their invaluable advice, ideas, suggestions and guidance, in all aspects of this project, my principal thanks must go to my supervisors, David Pyle and Tamsin Mather; without their input this thesis could not have attained its present form. I gratefully acknowledge funding from NERC for the project as a whole, for the Chaitén fieldwork, and for analytical time at the radiocarbon and ion microprobe facilities, as well as Worcester College and the Abbey-Santander and Burdett-Coutts funds, for travel grants. I thank Conall Mac Niocaill and Jennie Gilbert for examining this thesis.

José Antonio Naranjo shared his expertise in Chilean volcanism through many helpful discussions. In Chile, for assisting during fieldwork I am grateful to Carolina Guzmán and to José Luis Urrutia and CONAF staff at Parque Nacional Hornopirén; for the sharing of data to Daniel Sellés and Mauricio Mella; and for a range of reasons to, among others, Juan Freddy Antiñirre, Ercilia Mancilla, Antonio Paillén, Gastón and Marcos Gallardo, Klaus Hopperdietzel, and Hardy and Nery Garcia. In Argentina the assistance of Alfredo Fierro, the municipal administration of Esquel and Gustavo Villarrosa in facilitating fieldwork was greatly appreciated.

This project involved a wide range of laboratory work in Oxford, and for all their advice and assistance over the past three years I am particularly grateful to Steve Wyatt, Owen Green and Norman Charnley. Others who provided analytical expertise across a range of techniques include Vicki Smith, Conall Mac Niocaill, Cees-Jan de Hoog, Chris Jackson and Andrew Mason in Oxford, Steve Moreton at the radiocarbon laboratory in East Kilbride, Richard Hinton at the ion probe facility in Edinburgh and John Watson at the Open University, as well as laboratory staff in all these places.

My thanks also go to Richard Herd, for the sharing of software, to Chuck and Laura Connor and Alain Volentik for their hospitality and help with tephra dispersion modelling, to Si Flanagan for proof reading, to Naomi Matthews and Rob Martin for inputs to the Chaitén work, to John Elliott for wide-ranging assistance in Oxford, and finally, to Helen, for always being on hand to provide a welcome distraction.

Contents

List of Figures

List of Tables

Chapter 1

Introduction

Dynamic geological processes operating within and upon the Earth's crust control the planet's climate, topography and capacity for life. Such processes, manifested as diverse phenomena ranging from earthquakes to glaciation, may be explored individually to understand the fundamental behaviour of the Earth. However, this reductionist approach does not imply complete independence between different Earth processes, and there are mutiple possible controls and feedbacks within a complex and inter-connected Earth surface system. In this thesis I explore such ideas through the investigation of records of arc volcanism in southern Chile, initially examining the volcanic history of the region, on a range of timescales, before considering how spatial and temporal variability in volcanism may reflect interactions with external processes.

Southern Chile (Figure 1.1) represents an ideal area in which to study variation in volcano-magmatic behaviour. The volcanoes of the region span a wide latitudinal range, along which both subduction and crustal parameters vary systematically and are relatively well-characterised. The same area encompasses a range of climatic zones, and the southern part of the region has been affected by Pleistocene glaciations. The subduction system along the Chilean margin is characterised by extremely large earthquakes, and large-scale tectonic structures related to plate convergence directly underlie part of the volcanic arc. Thus, there is the potential in this region to explore a range of controls and interactions between volcanism and other crustal processes. In addition, several of southern Chile's volcanoes are little known and poorly studied, and valuable new information regarding regional volcanic activity may be obtained through detailed field investigation in these locations.

This thesis is divided into three sections. The first describes volcanism in the field areas investigated for this work, principally in the Hualaihue region. The Hualaihue volcanoes are introduced in Chapter 2, which includes a discussion of their petrology and geochemistry, while Chapter 3 documents in more detail the eruption style and magmagenesis of the Holocene mafic explosive eruptions in Hualaihue, comparing them to similar eruptions elsewhere in the Andean Southern Volcanic Zone (SVZ), many of which show a close spatial association to the regional-scale Liquiñe-Ofqui fault zone (LOFZ). The second section comprises two case studies of recent volcanic events in the region: Chapter 4 investigates landslide generation and edifice collapse at Yate volcano, in Hualaihue and also situated upon the LOFZ, while Chapter 5 describes the tephra fallout from the 2008 explosive eruption of Chaitén volcano, 120 km further south. This large eruption provides an analogue for the events producing older tephra units, investigated in Chapter 6. This chapter, a tephrochronological reconstruction of the post-glacial explosive volcanism in the vicinity of Hualaihue, based on new field observations, introduces the third section of this thesis, which explores temporal eruption patterns. The Hualaihue tephrochronology is expanded in Chapter 7 to examine evidence for variability in the regional post-glacial volcanic record relating to deglaciation. Chapter 8 analyses eruption records in the SVZ on the historical timescale, and discusses the relationship between large earthquakes and volcanic eruptions.

The following sections of this chapter provide a background to volcanism in the SVZ, describe the geological history and tectonics of southern Chile, including the LOFZ, and introduce the specific field areas studied in this thesis.

1.1 Southern Andean volcanism

Resulting from plate convergence along the western edge of South America, the Andean mountain chain runs the length of the continent. Coincident with the Andes are the volcanoes of the Andean arc, which form four distinct groups [Thorpe and Francis, 1979, Thorpe, 1984] separated by gaps in which volcanism is currently absent (Figure 1.1) due to shallowly dipping subduction [e.g., Barazangi and Isacks, 1976, Ramos, 1999, Parada et al., 2007]. The southernmost group of volcanoes forms the Austral volcanic zone, relating to subduction of the Antarctic plate beneath southernmost Chile [e.g., Stern, 2008]. North of here, subduction of the Nazca plate, along the remainder of the South American margin, gives rise to the northern, central and southern volcanic zones [e.g., Stern, 2004]. The northern part of Chile contains volcanoes of the central volcanic zone, which extends into neighbouring Peru, Bolivia and Argentina. South of a 680 km volcanic gap the SVZ begins, at the approximate latitude of Santiago (33.4° S).

1.1.1 The southern volcanic zone (SVZ)

The Andean southern volcanic zone (SVZ; Figure 1.1) is the focus of this thesis. It is the largest of the South American volcanic groups, with approximately as many historically recorded eruptions as all the other segments combined. Over sixty volcanoes in the SVZ are considered to have erupted in the Holocene [Siebert and Simkin, 2002-]. González-Ferrán [1995] identified 1334 individual eruptive centres, including numerous monogenetic cones and maars. The SVZ extends from Tupungatito (33.4° S) in the north to Hudson (45.9° S) in the south, forming a continuous arc segment over 1400 km in length [Stern et al., 2007]. Its northern margin coincides with an abrupt shallowing of the seismic zone [Bevis and Isacks, 1984], corresponding approximately with the locus of the subducting Juan Fernández ridge [Stern, 2004], and defining the southern edge of the Pampean flat-slab segment [Barazangi and Isacks, 1976, Cahill and Isacks, 1992]. To the south, the SVZ ends with the subduction of the spreading Chile Rise, defining the Nazca-Antarctic-South America triple junction (Figure 1.1). The active volcanic front of the SVZ lies at the eastern edge of the Andean mountain chain, which spans the Chilean border with Argentina. As such, the majority of the SVZ volcanoes, and all those with historically recorded eruptions, lie wholly or partly in Chile.

Over 70% of the population of Chile live at latitudes spanning the SVZ, and the Central Valley region south of Santiago is one of the most heavily populated South American regions lying within <100 km of active volcanic centres [Stern, 2004]. Villarrica and Llaima, the most active SVZ volcanoes, have each had over 50 reported historical eruptions. Centres in the northern and central parts of the SVZ are relatively better known than those to the south, due to greater accessibility, a longer historical record of activity, and a larger local human population. No specific pre-Columbian eruption records exist, and in the southern half of the SVZ there are few records before the start of the 19$^{\text{th}}$ century. However, the two largest eruptions of recent decades have occurred in this region: Hudson in 1991 and Chaitén in 2008 (Chapter 5). In spite of the large number of potentially active centres, few SVZ volcanoes are monitored. Field evidence exists from several centres of Holocene eruptions much larger than those recorded in historical times [e.g., Naranjo and Stern, 1998, Clavero and Moreno, 2004].

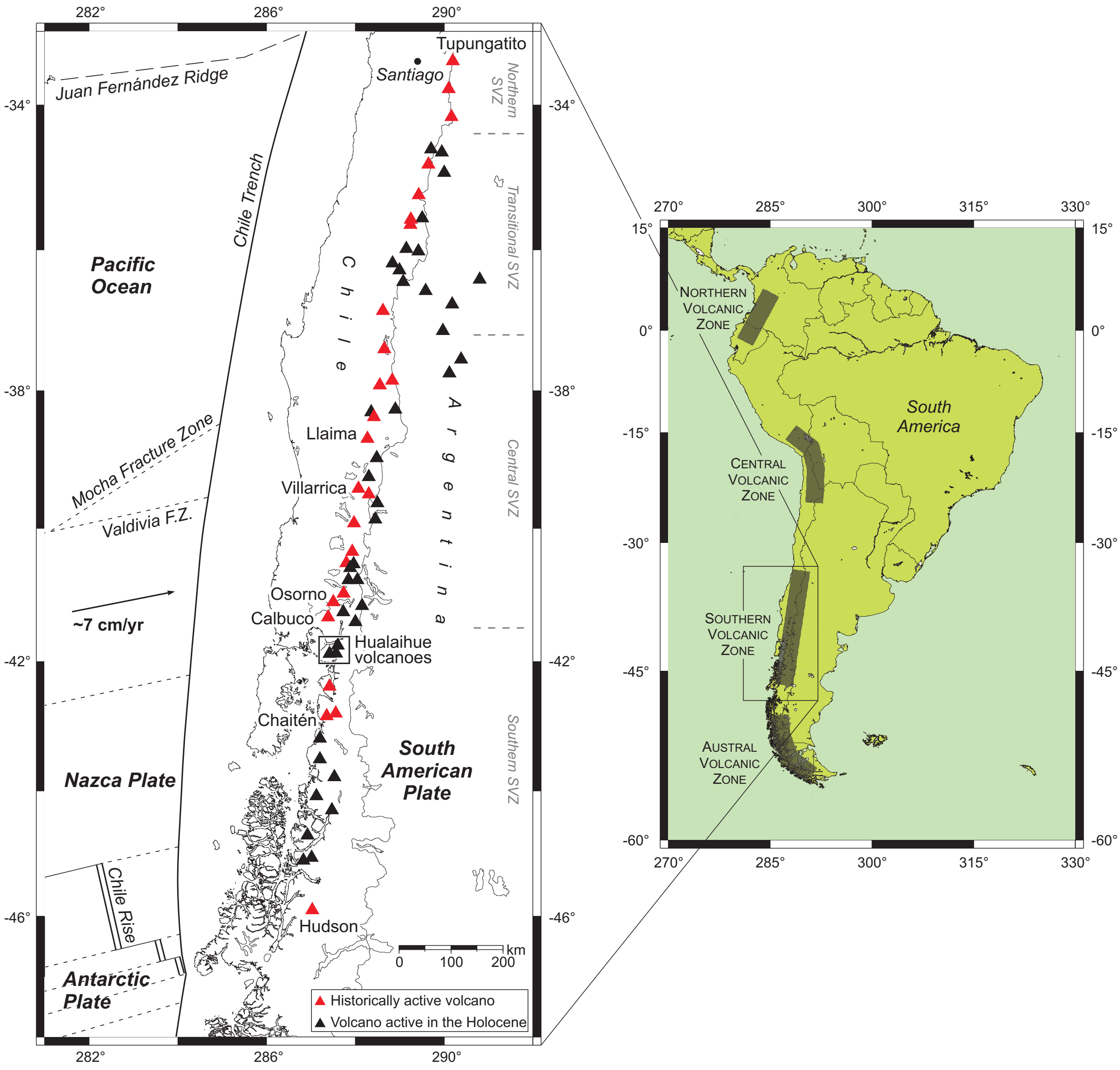

Figure 1.1: Maps of South America and the Andean southern volcanic zone. Volcanically active regions of South America are shaded in grey on the continental map, and define four discrete regions. The three northern regions result from subduction of the Nazca plate beneath South America, while the southermost zone results from Antarctic plate subduction. The main map shows volcanic centres of the SVZ, running from Tupungatito to Hudson, that are considered to have been active in the Holocene, while those shown in red have historically recorded eruptions. Selected volcanoes are named. Major features of the downgoing oceanic plate, including the active spreading boundary and inactive fracture zones (short dashed lines) are also marked [DeMets et al., 1994, Naranjo and Stern, 2004, Stern, 2004, Siebert and Simkin, 2002-].

1.1.2 Structure of the SVZ

The centres of the present volcanic arc comprise numerous Pleistocene-Holocene stratovolcanoes as well as several Holocene monogenetic centres. Additionally, the remains of older Cenozoic volcanoes occur along the line of the arc. South of 38° S the SVZ is characterised by the presence of the LOFZ (see Section 1.2.3), along which, in its broad sense, the volcanic front is situated. Here, the magmatic front has been stable since the mid-Miocene [Lara and Folguera, 2006]. North of here Cenozoic activity has been more variable, with repeated episodes of elevated magmatic production and eastward relocation of arc segments related to periods of crustal thickening and subduction erosion, resulting in a substantial loss of crustal width over time [Kay et al., 2005].

Further subdivision of the arc (see Figure 1.1) may be made based on upper crustal structures and the distribution and chemistry of Pleistocene-Holocene volcanism [Stern, 2004, Stern et al., 2007]. In this formulation, the northern half of the arc is divided into the northern SVZ (33°-34.5° S) and the transitional SVZ (34.5°-37° S). The northern SVZ comprises just the three northernmost volcanic complexes of the SVZ, lying on the continental divide. The transitional SVZ represents a broader belt of stratovolcanoes and monogenetic cones on uplifted basement blocks separated by intra-arc basins, the southern boundary of which may relate to the locus of the subducting Mocha fracture zone (Figure 1.1), which separates older oceanic crust to the north from younger crust subducting to the south [López-Escobar et al., 1995a, Stern, 2004]. The central SVZ is broad in its northern parts, narrowing south of 39° S, at the locus of the subducting Valdivia fracture zone [Herron, 1981], which is roughly coincident with the historically most active portion of the arc. In the central SVZ the volcanic front lies west of the continental divide, in Chile, and intra-arc extensional basins are absent [Stern, 2004]. The volcanoes of the southern SVZ all lie in Chilean northern Patagonia, overlying deeply eroded basement rocks and the Patagonian batholith, forming a narrow arc of stratovolcanoes with occasional monogenetic centres.

1.2 Geology and tectonics of the southern Andes

The pre-Andean basement at the latitudes of the SVZ (33°-46° S) records a complex history of multiple collisional episodes characterised by both extensional and contractional periods and associated with a variable rate of plate convergence. Accretion of metamorphic complexes at the continental edge began in the Cambrian [530 Ma; Rapela et al., 1998], in progressively younger collisional stages, although such processes are best recorded in rocks of late Devonian and younger ages, accreted onto the south-western margin of Gondwana and accompanied by arc development and magmatism [cf. Charrier et al., 2007].

The proto-Pacific Gondwanan margin comprised Palaeoproterozoic cratonic basement in central Chile, with Neoproterozoic orogenic belts at the western margin, and the Neoproterozoic massifs of Patagonia to the south, extending as far as the Antarctic Peninsula. These Patagonian terranes are considered to have been approximately in their present relative position and autochthonous to the margin of Gondwana throughout the Palaeozoic [Pankhurst et al., 2003]. Metamorphic complexes originating in these episodes crop out today west of the Andes in central Chile, accompanied by the coastal batholith, forming the Chilean Coastal Cordillera. These mountains are separated from the main Andean range by the Central Depression, defining three morphological units across Chile at these latitudes [Charrier et al., 2007]. Further south, the batholith rocks constitute a major component of the Andean cordillera. These rocks, known as the Patagonian batholith, were formed in numerous plutonic episodes from Jurassic to Miocene times [Munizaga et al., 1988, Pankhurst et al., 1999, Parada et al., 2000], associated in its early parts with metamorphic complexes cropping out both to the east and west [Hervé et al., 2007]. Through the Permian and Triassic, subduction slowed and then ceased, in association with the assembly of Gondwana. This period was accompanied by the development of widespread, predominantly silicic magmatism in Argentina and northern Chile, and extensional basin development across Chile and Argentina [e.g., Suárez and Bell, 1992, Charrier et al., 2007], possibly associated with suture zones of the previously accreted Palaeozoic terranes [Ramos, 1994].

1.2.1 Onset of the Andean orogeny

Construction of the Andes began in the early Jurassic (190 Ma) in association with Gondwanan break-up and opening of the Atlantic ocean [Stern, 2004, Charrier et al., 2007], accompanied by renewed subduction and arc magmatism. Evolution north of 39° S comprised several stages, beginning with arc and back-arc basin development (e.g., the Mendoza-Neuquén basin, Argentina) in extensional conditions, accompanied by plutonism to the west. During the late Cretaceous changes in convergence conditions resulted in contractional deformation and intense uplift, with an eastward shift of the arc and the development of foreland basins. This was accompanied by the onset of major trench-parallel shear zones resulting from oblique subduction of the Farallon plate [Charrier et al., 2007], including formation of the Liquiñe-Ofqui fault zone (LOFZ; see Section 1.2.3), which extends far to the south. This period is associated with development of the Coastal Cordillera, Central Depression and Andean Cordillera, accompanied by continued plutonic activity along the Coastal Cordillera through to the early Cenozoic [Parada et al., 2007]. The region south of 42° latitude, forming the Chilean part of northern Patagonia, may be considered separately. Here, initial continental break-up resulted in Jurassic back-arc extension accompanied by major silicic volcanism and plutonism affecting the entire Patagonian region [e.g., Pankhurst et al., 1998, 2000], and followed by thermal subsidence into the Cretaceous. Continued arc plutonism generated the Patagonian batholith along the main Andean axis and predominantly east of the LOFZ [Charrier et al., 2007, Parada et al., 2007]. This was followed by inversion, foreland basin (distinct from the Neuquén system to the north) and thrust-fold belt development from the late Cretaceous onwards.

1.2.2 Cenozoic Andean development

Most of the Andean uplift at the latitudes of the SVZ has occurred since the late Cretaceous [Ramos, 1999], while the present configuration of the Andes is a result of the final stages of collision and uplift from the late Neogene to the present [Charrier et al., 2007], with many features acquired during the Miocene [Stern, 2004]. For much of the Cenozoic, subduction conditions and crustal stress partitioning were similar to the present situation, with relatively shallow slab dip, oblique subduction, and a high degree of interplate coupling. Magmatic activity fluctuated through this period due to changes in the dip of the subducting slab and the convergence angle [e.g., Dewey and Lamb, 1992, Ramos, 1999, Jordan et al., 2001, Kay et al., 2005, Charrier et al., 2007]. The volcanic arc reached its approximate present position during the early Cenozoic.

While uplift and deformation were high during the mid-Eocene, this subsequently decreased in a period of oblique convergence and associated motion on the LOFZ, which bounded basins forming to the west, resulting in inhibited magmatism [Charrier et al., 2007]. A significant departure from the predominant situation occurred in the late-Oligocene (26-28 Ma) due to the onset of near orthogonal convergence until 12 Ma, associated with the breakup of the Farallon plate into the Nazca and Cocos plates [Pilger, 1984, Pardo-Casas and Molnar, 1987, Somoza, 1998]. This period saw the onset of subduction of the Juan Fernández ridge, related to slab shallowing and subsequent formation of the current flat-slab configuration and the volcanic gap north of the SVZ, from around 11 Ma [Barazangi and Isacks, 1976, Pilger, 1984, Yáñez et al., 2001, 2002]. The increased convergence rate widened the magmatic arc both westwards [e.g., Parada et al., 2007] and east into Argentina [Stern, 2004], with extension and basin development occurring regionally into the early-Miocene [Jordan et al., 2001], altering fore-arc deformation patterns [Hervé et al., 1995], before developing into tectonic shortening. Accelerated rates of uplift occurred during this period, when the locus of maximum uplift migrated eastwards to the present topographic divide [Thomson et al., 2001, Charrier et al., 2007]. The onset of Andean glaciations has been linked to a shift from erosion to accretion at the margin [Melnick and Echtler, 2006], thought to have occurred episodically in the later Cenozoic [Bangs and Cande, 1997]. The same period was associated with renewed plutonism, which in the north decreased in intensity in association with a shallowing slab dip, ending at 5 Ma [Kay and Mpodozis, 2002, Parada et al., 2007].

The magmatic arc narrowed by the mid-Miocene [Stern, 2004, Lara and Folguera, 2006]. Shortening and uplift have continued to present [e.g., Khazaradze and Klotz, 2003], although subduction returned to a more oblique situation after the mid-Miocene, and convergence rate has gradually slowed since this time [Norabuena et al., 1999]. The variable effects of collisional history from north to south across the region has resulted in a southward diminishing gradient in crustal thickness and shortening along the SVZ, and a corresponding lowering of the mean Andean elevation [e.g., Ramos, 1999]. Plutonism continued through the later Cenozoic along the main cordillera in the south of the region, through continued episodic growth of the North Patagonian batholith in the early Miocene and again in the late Miocene to Pliocene, primarily along and west of the LOFZ [Munizaga et al., 1988, Pankhurst et al., 1999, Parada et al., 2007]. Subduction of the Chile Rise spreading centre beneath southernmost South America occurred at 14 Ma, forming a plate triple junction, the position of which has migrated northward to its present position [Charrier et al., 2007]. This was associated with a further phase of rapid exhumation of the North Patagonian batholith along the LOFZ in the late Miocene to Pliocene [Adriasola et al., 2006]. Subduction of this ridge and the Juan Fernández ridge, to the north of the SVZ, has exerted strong controls on the pattern of Neogene magmatism at each end of the SVZ [Stern and Skewes, 1995, Parada et al., 2007]. Between the Pliocene and Pleistocene a westward narrowing of the volcanic arc occurred, possibly due to the ongoing reduction in subduction velocity [Lara et al., 2001], but potentially also related to the onset of renewed dextral transpression along marginal scale fault systems (the LOFZ) at the volcanic front from the late Miocene onwards [Lara and Folguera, 2006].

1.2.3 The Liquiñe-Ofqui fault zone (LOFZ)

The Nazca plate subducts at an angle 22-30° N of the orthogonal [Cembrano et al., 1996, Lavenu and Cembrano, 1999]. This convergence is absorbed along the Andean margin in a variety of ways, allowing distinct neotectonic zones to be recognised [Dewey and Lamb, 1992, Somoza, 1998, Kendrick et al., 2003, Iaffaldano and Bunge, 2008]. The southernmost of these zones [cf. Dewey and Lamb, 1992] is associated with the Liquiñe-Ofqui fault zone (LOFZ), and is coincident with the central and southern SVZ. Here, the slip vector is partitioned into approximately orthogonal Wadati-Benioff zone slip and distributed dextral deformation in the over-riding slab. This margin-scale dextral transpressional deformation is accommodated along an array of curved and north-trending lineaments occurring in the western part of the main Andean cordillera, collectively forming the LOFZ [Cembrano and Hervé, 1993, López-Escobar et al., 1995a, Cembrano et al., 1996, 2000, 2002, Lavenu and Cembrano, 1999], with a total length of over 1000 km (Figure 1.2). The subduction related strain taken up along this system explains the comparatively low deformation in the orogen to the east when compared to the Andes north of the LOFZ [Hervé, 1994].

The main arm of the LOFZ, forming its eastern edge, is topographically clear as a series of arc-parallel fjords and valleys. The LOFZ has a general NNE orientation, but comprises straight segments, splayed structures, and en-echelon features, particularly at its southern end, where lineaments bend to the SW, forming a duplex structure [Cembrano and Hervé, 1993, Arancibia et al., 1999]. At its southern termination the LOFZ joins a pull apart basin south of the Taitao peninsula and the plate boundary triple junction [Forsythe and Nelson, 1985]. To the north of the LOFZ a region of complex fault dynamics and rotational shear occurs in the transition to a zone without slip partitioning [cf. Dewey and Lamb, 1992, Cembrano et al., 1992, 2000, Folguera et al., 2004].

Structural analyses of the LOFZ in the northern SSVZ indicate ductile deformation in the late Miocene to Pliocene, with fault slip analyses throughout the SSVZ showing that the Pliocene was characterised by a general E-W compressive tectonic regime, with a dextral strike-slip component in places [Lavenu and Cembrano, 1999, Cembrano et al., 2000, 2007]. This situation developed in the later Pliocene to brittle deformation and a general NE-SW compressive regime, which has continued to the present. For example, data consistent with Pleistocene intra-arc dextral transpression and dextral displacement along the LOFZ has been recognised in the Hualaihue region [e.g., Lavenu and Cembrano, 1999, Rosenau et al., 2006]. Ridge subduction of the Chile Rise at the triple

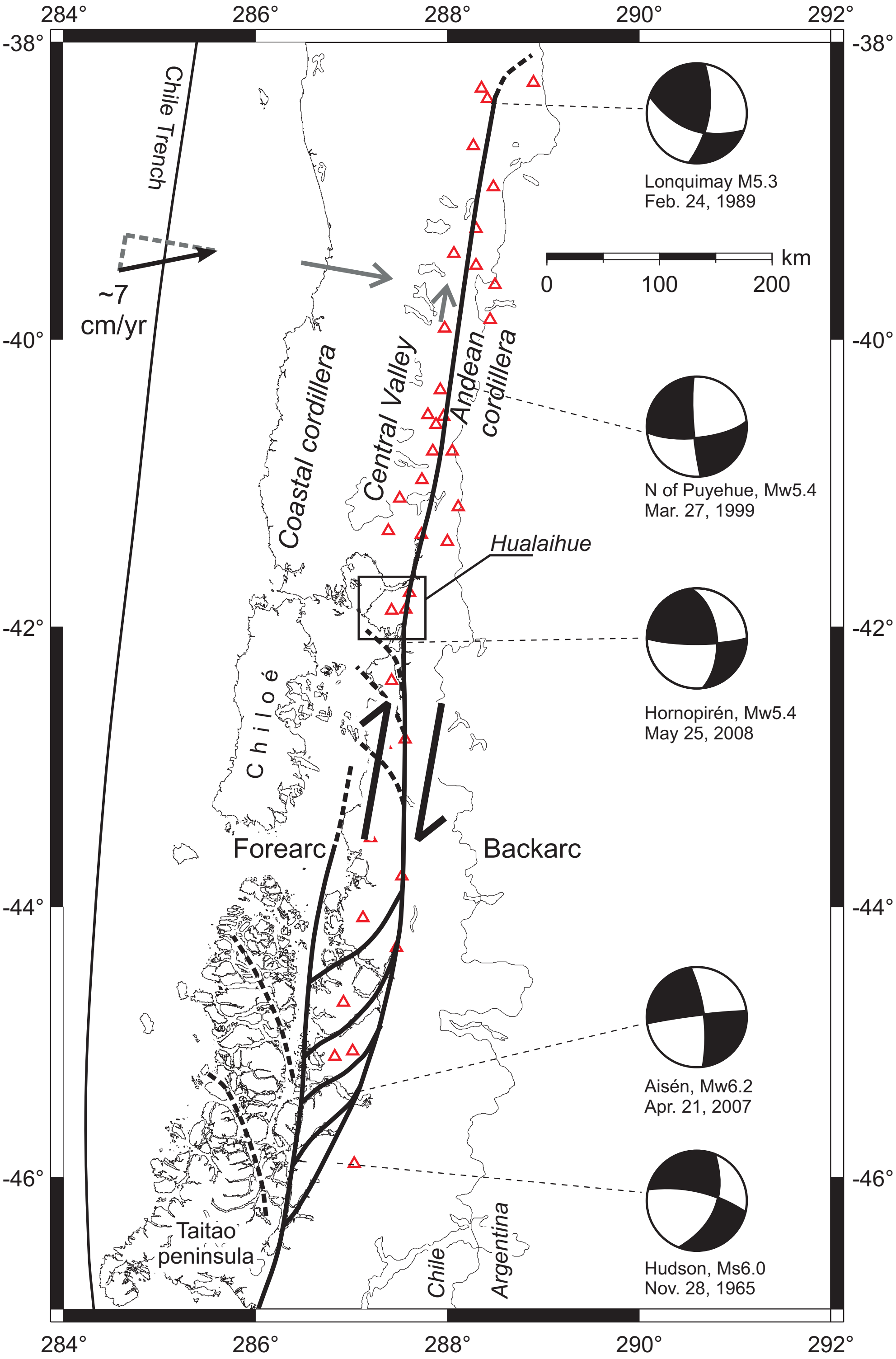

Figure 1.2: The Liquiñe-Ofqui fault zone. The map shows the various lineaments associated with the LOFZ in bold black lines [Cembrano et al., 1996]. Focal mechanisms and moment magnitudes (M_W) of historical earthquakes associated with the fault zone are also shown [Chinn and Isacks, 1983, Barrientos and Acevedo, 1992, Global CMT Project, 2010-].

junction may have enhanced the dextral strike-slip regime along the LOFZ, particularly in its southern half and since the Pliocene [Nelson et al., 1994, Cembrano et al., 2000, 2002]. Clockwise rotation associated with dextral shear has taken place within the LOFZ [Cembrano et al., 1992, Rosenau et al., 2006], while a small amount of rigid-block anticlockwise rotation has occurred in the fore-arc [Garcia et al., 1988, Dewey and Lamb, 1992, Rojas et al., 1994, Cembrano et al., 2007]. The overall situation, arising from slip partitioning in the forearc, has generated the Chiloé fore-arc continental sliver (or slivers) [Fitch, 1972, Nelson et al., 1994, Rojas et al., 1994, Forsythe and Diemer, 2006] with the LOFZ forming the boundary between this and the back-arc region of the South American plate. E-W extension occurs in the outer fore-arc, N-S contraction in the inner fore-arc, and transpression along the volcanic arc (and LOFZ) [Cembrano et al., 2007].

Lineaments associated with the LOFZ have provided a focus for the region's Pleistocene-Holocene volcanism [e.g., Lara et al., 2006a]. Volcanic cone elongation, apparent at Hornopirén, and alignments of monogenetic cones [cf. Wacaster et al., 2007], such as those at Puyuhuapi, are consistent with dextral transpression [Dewey and Lamb, 1992, López-Escobar et al., 1995a, Cembrano et al., 2007]. Minor centres usually occur on alignments striking NNE or NE, while stratovolcanoes commonly develop along NE alignments; less commonly NW. This may be related to a transpressional combination of dextral strike slip and across-arc shortening [López-Escobar et al., 1995a]. In Miocene-Pliocene times high-strain domains along the fault zone may have controlled the ascent of young plutons of the Patagonian batholith [Munizaga et al., 1988, Hervé et al., 1993], through which the LOFZ runs. Rapid denudation and uplift of the Patagonian batholith has occurred along the LOFZ from the mid-Miocene, increasing from east to west across the zone, and coupled with glacial erosion [Cembrano et al., 2002, Adriasola et al., 2006, Adriasola and Stöckhert, 2008]. Onset of rapid uplift may be related to collision and subduction of the Chile Rise [Thomson et al., 2001]. Prior to this, deformation may have been transtensional and associated with pull-apart basin generation to the west in the Eocene to early Miocene [Pankhurst et al., 1992, Hervé et al., 1995, Thomson et al., 2001].

The LOFZ is considered to be seismically active [e.g., Forsythe and Diemer, 2006, Naranjo et al., 2009], although amounts of movement are highly uncertain, with estimates varying by up to two orders of magnitude [cf. Rosenau et al., 2006, Adriasola and Stöckhert, 2008]. Rates of dextral shear are thought to decrease northwards, suggesting complete partitioning of oblique subduction south of Hualaihue and partial partitioning to the north [Rosenau et al., 2006]. The Pleistocene to recent regime of dextral transpression [Lavenu and Cembrano, 1999] is consistent with focal mechanisms from the few recorded earthquakes (Figure 1.2) associated with the fault zone [e.g., Chinn and Isacks, 1983, Barrientos and Acevedo, 1992, Global CMT Project, 2010-], as well as local seismicity measured along the LOFZ [Lange et al., 2008].

1.3 Study regions

This thesis describes volcanism in the Andean SVZ. The earlier sections focus on specific regions where field samples were collected, while Chapters 7 and 8 expand on these data to explore arc-scale eruption patterns, first in the central and southern SVZ, and then across the SVZ as a whole.

The main body of this work, derived from field investigations, is based on a few volcanoes in the southernmost portion of the SVZ (Figure 1.3), particularly in the Hualaihue region. Here, the volcanoes of Yate, Hornopirén and Apagado are little-studied, and the fieldwork described in this thesis focusses predominantly on the post-glacial eruption history of these centres and of those nearby, including Calbuco volcano. This aims to characterise volcanism in this little known segment of the arc, which will link with previously established records to the north and south [e.g., López-Escobar et al., 1995b, Naranjo and Stern, 2004]. Mafic explosive eruptions in Hualaihue are compared to similar events along the LOFZ, particularly at Palena and Puyuhuapi. Separate fieldwork was undertaken to investigate tephra fallout following the 2008 explosive eruption of Chaitén volcano.

1.3.1 The southern SVZ (SSVZ)

The southern SVZ (SSVZ; Figure 1.3) runs from Yate volcano in the north to Hudson in the south [Stern, 2004]. At the northern end of the arc-segment the Central Valley meets the sea, and this part of Chile is characterised by a deeply dissected topography of fjords and islands, with many of the volcanic centres lying on or near the coast of the mainland, on the western edge of the Patagonian Andes. The SSVZ contains at least 13 stratovolcanic centres thought to have been active in the Holocene [Siebert and Simkin, 2002-], in addition to several minor eruptive centres associated with the LOFZ [Stern et al., 2007]. Many of these volcanoes are poorly known and remote; access to the region is difficult, and the wet, cool climate ensures a dense, rapidly regenerating cover of vegetation. Several of the SSVZ stratovolcanoes have extensively eroded glaciated summits and the potential for both lahar and landslide generation is high (Chapter 4;

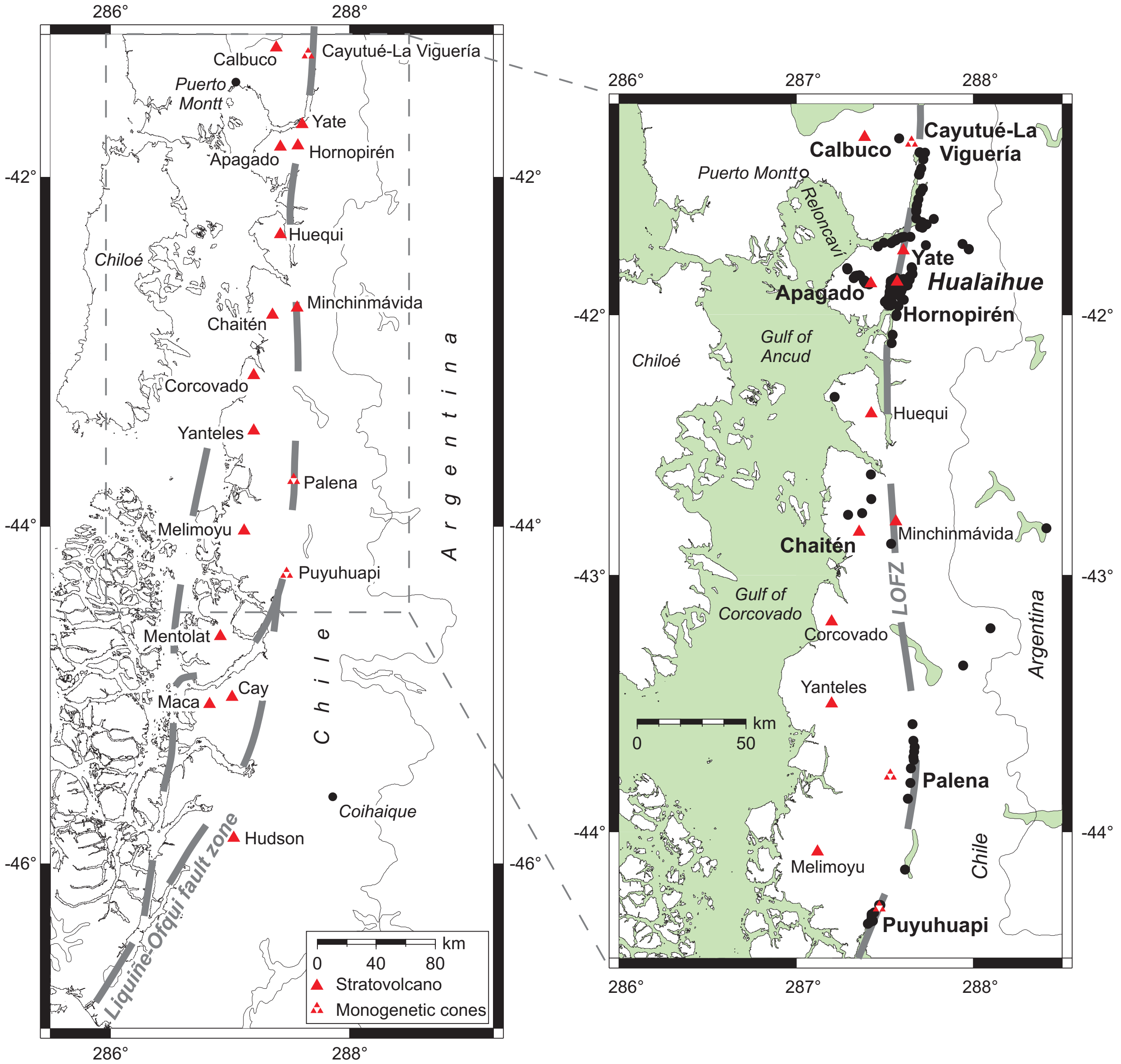

Figure 1.3: Maps of main field sites and the southern SVZ. The map on the left shows the volcanoes of the southern SVZ [Stern, 2004], which runs from Yate to Hudson. The trace of major lineaments of the Liquiñe-Ofqui fault zone (LOFZ) is also shown, along which several stratovolcanoes and monogenetic cones are situated. The grey dashed rectangle shows the area covered by the right-hand map, which indicates the main field sites of this thesis. The volcanic areas forming the principal centres of study in this thesis are shown in bold. All field sites are marked as black dots except for field sites associated with the tephra deposit of the May 2008 eruption of Chaitén (Chapter 5), which are not marked.

Stern et al., 2007). Given the size of many of these edifices and their eroded nature, it is likely that their volcanic history stretches back into the Pleistocene. The human population in this part of Chile is sparsely distributed, although several small towns lie within tens of kilometres of the region's volcanoes, and the impact of tephra fallout from explosive eruptions may reach far into Argentina (e.g., Chapter 5). The region was glaciated during the last ice-age, and good records exist of the extent and evolution of regional ice sheets [e.g., Denton et al., 1999b]. A direct tectonic control over volcano location is evident, since many regional volcanoes are situated along lineaments of the LOFZ [e.g., Cembrano et al., 2007].

The volcanic rocks of the SSVZ may be grouped, compositionally, with those in the central SVZ. Volcanics of the central SVZ form a chemical spectrum along the arc, correlating with crustal thickness, which decreases southwards, as well as crustal age, composition [e.g., Hildreth and Moorbath, 1988, Tormey et al., 1991a] and possibly subduction inputs [Hildreth and Moorbath, 1991, Stern, 1991]. Degrees of continental crustal assimilation are variable but generally low, with some rocks from the volcanic front showing similarities to oceanic island arc basalts [e.g., Hickey et al., 1986, Stern et al., 2007]. Dominant rocks in the arc segment are tholeiitic and high-Al basalts and basaltic andesites [e.g., López-Escobar et al., 1995a], with olivine and plagioclase almost ubiquitous as a phenocryst phase [Stern et al., 2007]. The degree of magmatic evolution has been related to crustal stress conditions and residence time [e.g., Tormey et al., 1991b].

1.3.2 Subduction and crustal parameters

The Andes at the latitudes of the SSVZ are topographically relatively subdued, with a mean elevation of ~1500 m along the continental divide. All the SSVZ volcanoes lie west of this divide, along a line coincident with the various lineaments of the LOFZ, and all are at distances of less than 280 km east of the trench [Naranjo and Stern, 1998, Stern, 2004], with some closer than 250 km. The most distant centres are the monogenetic cones along the easternmost, and main, lineament of the LOFZ, such as those at Puyuhuapi. Throughout this region the volcanoes are among the highest peaks; several have elevations of >2000 m. Crustal thickness is relatively constant along the SSVZ, at 30-35 km [Stern, 2004, Tašárová, 2007].

The age of the subducting slab at the trench varies from 0 Ma at the triple junction to 15 Ma at the locus corresponding to Yate [Tassara and Yáñez, 2003]. Subduction proceeds at ~7 cm yr^{-1} [DeMets et al., 1994, Somoza, 1998, Norabuena et al., 1999, Kendrick et al., 2003, Iaffaldano and Bunge, 2008] at 080°, or approximately 25° towards the north relative to trench-orthogonal convergence (Figure 1.3). The slab dip of 30° is relatively constant [Barazangi and Isacks, 1976, Lange et al., 2007], while slab depth at the volcanic front is 90-100 km [Stern, 2004, Tašárová, 2007]. Subduction zone seismicity in this region is much less than further north in the Andes, with the Wadati-Benioff zone only reaching a depth of 200 km [Yuan et al., 2006]. The region's high levels of precipitation, in excess of 3 m yr^{-1} [e.g., Ziegler et al., 1981, Lamy et al., 2001], result in high sediment supply to the trench, enhanced by glacial erosion [Stern, 2004]. Terrigenous sediment fill at the trench is high [Melnick and Echtler, 2006], with significant input from the plutonic rocks of the Patagonian batholith. The trench axis is as shallow as 4 km at 42° S [Schweller et al., 1981, Thornburg and Kulm, 1987], and the sediment fill thickness is 2-2.2 km along most of the arc, decreasing rapidly near the tiple junction [Bangs and Cande, 1997].

1.3.3 Holocene eruption history

There are thirteen stratovolcanoes within the SSVZ listed by Siebert and Simkin [2002-] as having been active in Holocene times, although very few of these have been studied in detail [cf. López-Escobar et al., 1995a, and references therein]. The heavily eroded nature of some volcanoes, such as Corcovado, suggest only minor amounts of post-glacial activity.

Historical eruptions have occurred at Hudson, where the largest eruption globally since that of Pinatubo, the Philippines (April, 1991), occurred shortly after the latter event, in August 1991. Activity is also reported from Minchinmávida (most recently in 1835), Huequi (several times between 1890 and ~1920), and Mentolat (in 1710) [Siebert and Simkin, 2002-]. While there is no reason to doubt the veracity of reported activity at Huequi and Mentolat, particularly the multiple eruptions at Huequi, neither volcano is mentioned in the summaries of historically active centres in some accounts of the region [e.g., Stern, 2004, 2008]. Further eruption reports from Yanteles and Corcovado, stemming from information received and summarised by Darwin [1835], should be considered doubtful. The only other historical activity from the arc segment is the recent explosive eruption of Chaitén, which began in May 2008 (see Chapter 5).

As well as the larger stratovolcanoes, several monogenetic cones occur in the SSVZ, mainly associated with the LOFZ, and most notably at Palena and Puyuhuapi. Their youthful morphology indicates a Holocene origin. Additionally, some stratovolcanoes, such as Melimoyu and Minchinmávida, are associated with young parasitic cones situated away from the main edifice.

The low number of historically reported SSVZ eruptions may, in part, be attributed to the remoteness of the region, but it has also been suggested that the SSVZ is characterised by a relatively low rate of volcanic production when compared to the central SVZ [Naranjo and Stern, 2004]. The exception to this is Hudson, which has produced at least twelve Holocene explosive eruptions and several widespread tephra layers. This high level of activity has been related to Hudson's proximity to the subducting Chile Rise [e.g., Haberle and Lumley, 1998, Naranjo and Stern, 1998, 2004, Stern, 2008]. The Holocene eruption history of SSVZ volcanoes (except for Hudson) has only been specifically investigated by Naranjo and Stern [2004], who mapped the extent of regional tephra and identified a record of explosive eruptions for the arc between Chaitén and Maca. This comprised eleven tephra-producing eruptions, and Cay was the only volcano in the sector without identified activity. Beyond this work, tephra have been noted from sediment cores in regional climatic studies [e.g., Heusser et al., 1992, 1999], without data on the composition or source. The SSVZ centres from Yate to Huequi, as well the segment's monogenetic cones, are particularly little known. A few studies have been undertaken on Calbuco, the stratovolcano at the southern end of the central SVZ, north of Yate [López-Escobar et al., 1992, 1995b], but the eruption chronology here is not well understood.

This thesis seeks to contribute to further understanding volcanism in this little studied arc segment, and to use the new data obtained, in combination with other records of volcanism from southern Chile, to answer broader geological questions concerning arc volcanic processes.

Part I

Volcanism in the SSVZ

Chapters 2 and 3 of this thesis are currently not available in ORA.

Part II

Recent Events and Volcanic Hazards

This chapter is an updated version of: Watt, SFL, DM Pyle, JA Naranjo, TA Mather, 2009. Landslide and tsunami hazard at Yate volcano, Chile as an example of edifice destruction on strike-slip fault zones. Bulletin of Volcanology 71(5), 559-574, doi: 10.1007/s00445-008-0242-x, which was published by Springer, and which is available at http://www.springerlink.com/content/j71x0h575770g280/.

Chapter 4

Edifice destruction on the LOFZ at Yate[1]

4.1 Introduction

A major hazard posed by many volcanoes is that of edifice collapse, generating landslides and associated phenomena on a range of magnitudes and timescales. Such events have been documented at several Pleistocene-Holocene Chilean volcanoes [Sepúlveda et al., 2006], the dominant cause usually being massive slope failure unrelated to volcanic activity, rather than explosive edifice destruction accompanying eruption [e.g., Siebert, 1984]. External triggers implicated in non-volcanogenic collapses include earthquakes [Davis and Karzulovíc, 1963] and extreme rainfall [Iverson, 2000], but such triggers are immediate causes, operating on rocks previously weakened and destabilised through processes including mechanical weathering, deglaciation and hydrothermal alteration. Here, I provide recent examples of partial edifice collapse at Yate volcano, including an examination of a catastrophic landslide and tsunami in 1965. The situation is of interest not only because of the potential for similar occurrences at other Chilean volcanoes, but specifically because the tectonic situation at Yate, a volcano constructed on the strike-slip Liquiñe-Ofqui fault zone (LOFZ), appears to have exerted a control on edifice destruction behaviour.

---

[1] Much of the material in this chapter is published in Watt et al. [2009c], *Bulletin of Volcanology*.

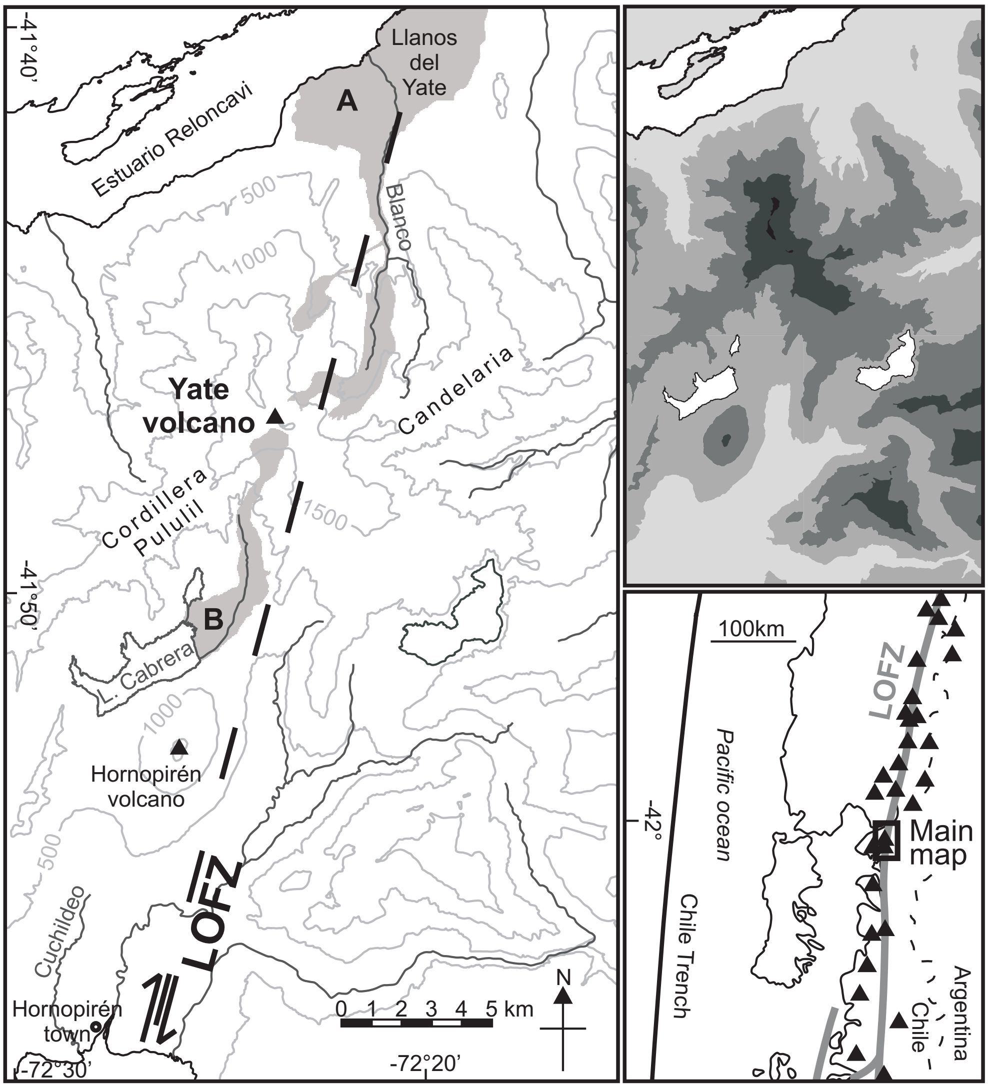

Figure 4.1: Location and topography of Yate volcano. *Main panel*: Yate and the surrounding area, showing the approximate line of the Liquiñe-Ofqui fault zone (LOFZ), on which the volcanoes Yate and Hornopirén lie. The extent of damage and deposition caused by debris flows from the NNE and SSW summit areas is shown shaded grey for **A** 1870 and 1896 [Hauser, 1985] and **B** 1965 and 2001. *Upper right*: Shaded relief map of the area in the main panel, from sea level (white) to $>$ 2000 m (black) at 500 m intervals. *Lower right*: Regional map showing the central portion of the Andean southern volcanic zone, marking the LOFZ and volcano locations.

4.1.1 Yate volcano

Yate is a compound volcano situated at 41.8° S in the Andean Southern Volcanic Zone (SVZ). It is one of three Holocene volcanoes situated on the Hualaihué peninsula, and while it is probably intermediate in age in terms of the full history of the three centres it comprises by far the largest volcanic edifice, rising to over 2000 m (Figure 4.1). The edifice is cruciform in structure, with a main ridge.trending at 155°, here referred to as the Yate complex, consisting of bedded Pleistocene lavas and pyroclastics rocks overlying a Plio-Pleistocene volcanic basement. Aligned volcanic ridges cross-cut this, at approximately 060° (parallel to the late-Pliocene to present direction of maximum horizontal stress [cf. Lavenu and Cembrano, 1999]), referred to as the Cordillera Pululil and Candelaria ridges. The total basal diameter approaches 20 km. The structure is glacially eroded, but has grown through Holocene effusive activity for which evidence exists on the flanks. Although there are no records of historical volcanic activity at Yate, tephrochronological evidence for minor post-glacial explosive eruptions is summarised in Chapter 6. The edifice lies on the regional dextral strike-slip Liquiñe-Ofqui fault zone (LOFZ), which extends for over 1000 km along the volcanic arc of southern Chile [Cembrano et al., 1996] (Figure 4.1). The fault zone is manifested topographically as a heavily eroded series of glacial valleys and fjords, with several branching curved limbs, particularly in its southern half. Along this line several of the region's volcanoes, both stratocones and monogenetic groups, are situated.

South of Yate, the course of the LOFZ is marked by a glacially-sculpted valley. Within this valley the Holocene volcano Hornopirén forms a youthful elliptical cone, blocking drainage southwest of Yate to form the Lago Cabrera basin. The shape and location of Hornopirén appear to have been controlled by a pull-apart structure in the LOFZ in this area [Dewey and Lamb, 1992]. A lake is likely to have formed in the Lago Cabrera basin following early Holocene eruptions of Hornopirén, with subsequent eruptions producing a narrower and deeper basin. The present-day lake has an area of approximately 5 km^2.

Deglaciation proceeded rapidly at these latitudes at the end of the last glaciation, and was nearly complete by 12,300 ^{14}C yr BP [Heusser, 2002]. The summit ridge of Yate still supports glaciers, with a snowline at approximately 1500 m. Aerial photographs indicate significant snowline retreat in recent decades, a feature that has been widely recognised in the southern Chilean Andes [Carrasco et al., 2005].

4.1.2 Past landslides at Yate

Destruction of the summit of Yate through successive collapses probably began soon after the end of the last glaciation. Debris flows, originating from rockfalls high on the flanks of Yate, have formed fan deposits at the east end of Lago Cabrera, SSW of the summit, and at Llanos del Yate to the NNE (Figure 4.1), modifying local topography extensively. Landslides originate from horseshoe-shaped collapse scars NE and SW of Yate's summit area. The resultant mass movements are modified and controlled by local topography and consist of volcanic rock and ice; they are best classified as volcanic debris flows. Historical records suggest that most of the fan material was emplaced during large individual events, four of which have occurred since 1870.

Two major collapses NNE of Yate occurred in 1870 and 1896 and have been documented by Hauser [1985]. From these, debris flows followed the Rio Blanco to the coast at Llanos del Yate (Figure 4.1). Here, deposits from the two events cover an area of approximately 25 km^2 and blanket a region of gentle topography. The extent of the fan at Llanos del Yate, and the scale of the collapse scars at Yate's summit, suggest that such landslides have been frequent throughout post-glacial time. Debris flows occurred SSW of Yate in 1965 and 2001, but are only documented in contemporaneous newpaper reports [Flash, 1965, Mercurio, 2001], though events are recalled by local people. The deposits are confined to the Lago Cabrera area (Figure 4.2), and form the hummocky outflow of the El Derrumbe valley. This name, meaning landslide, was given to the valley prior to 1965, and suggests local awareness of the instability of Yate's summit. The El Derrumbe debris fan has built westward and upward over time, modifying and raising the lake shoreline. Here, I examine in detail the largest historical landslide from Yate's SW sector, that of 1965. The immediate and long-term factors that give rise to repetitive mass-wasting events at Yate are investigated, in an effort to estimate the frequency and characterize the scale of this type of event. This work goes on to examine the role of glacial erosion and deglaciation in collapse, and shows how the pattern of edifice destruction is consistent with a model of volcano deformation by the underlying strike-slip LOFZ.

4.2 The 1965 landslide and tsunami

The most catastrophic historical landslide at Yate occurred in 1965, when a mass of rock and ice detached from the SW region of Yate. The failed material was transported south down the

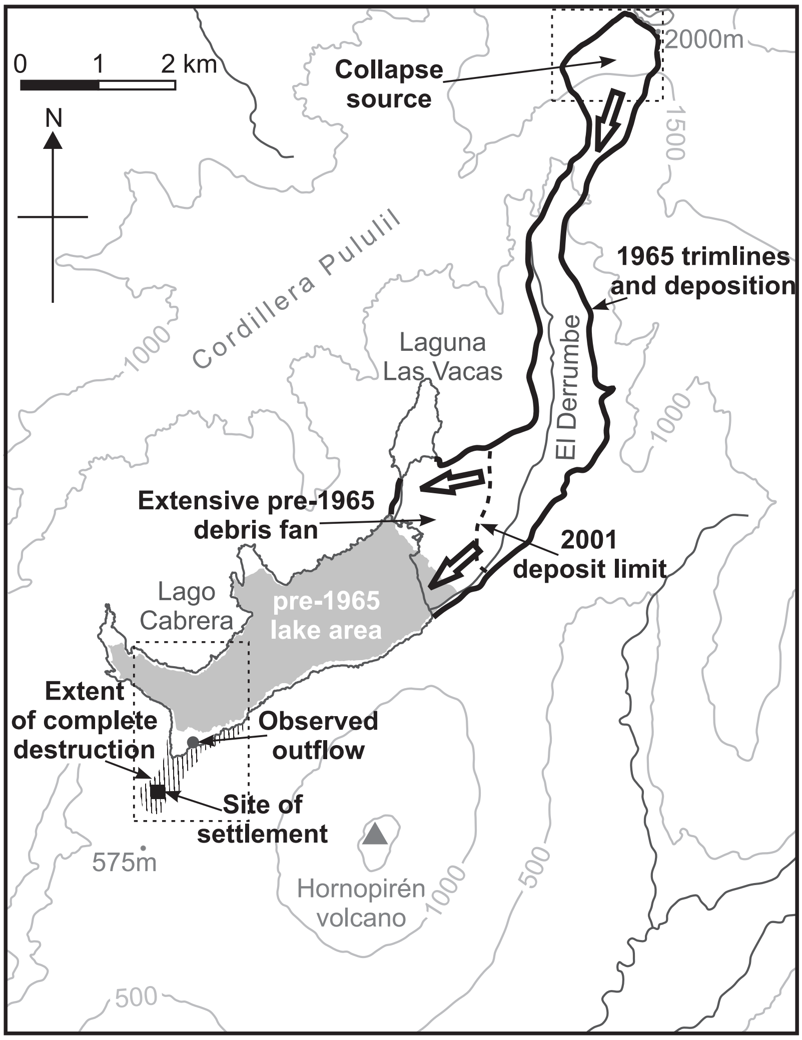

Figure 4.2: Map of SW Yate and Lago Cabrera, showing the extent of major historical debris flows, the change in shoreline of Lago Cabrera following the 1965 landslide, debris flow and tsunami, and the principal area of destruction due to the tsunami. Dashed boxes show the position of the aerial photo detail in Figures 4.4 and 4.7.

confined El Derrumbe valley, and its run-out and super-elevation behaviour is consistent with rapid transformation into a saturated debris flow, which incorporated debris from below the collapse scar and entrained vegetation along its path. Unfortunately, its remoteness and inaccessibility due to dense forest cover meant that close examination of the deposit was not possible, limiting the interpretations of the failed rock body deposited material. While the flow regime cannot be directly ascertained, comparison may be made with debris flow deposits NE of Yate. Here, the two historical events formed saturated debris flows with long run-outs, altering the course of the Rio Blanco on the Llanos del Yate debris fan [Hauser, 1985]. The deposits are poorly-sorted mixtures of rock, ash, sand, soil and vegetation, but lack fine material and mud. They contain clasts of up to 7 m diameter. Deposits SW of Yate contain boulders of up to 2 m diameter, and form mounds and hollows on length scales of 10–30 m, although some of this relief may be inherited from older debris fan deposits. The scale of these features is similar to the deposits NE of Yate. Hollows within the deposit suggest that large ice blocks were present, analogous to the ‘kettles’ observed by Hauser [1985] at the Llanos del Yate and described from many rock and ice collapse deposits [e.g., Branney and Gilbert, 1995, Clavero et al., 2002]. Thus, morphological evidence, from photographs, aerial photographs, and from field examination using binoculars suggests deposits SW of Yate are comparable to those produced by the saturated debris flows NE of the summit, which originated from landslides in the same lithologies and travelled similar courses.

Part of the debris flow entered Lago Cabrera, generating an impulse wave, the effects of which are still clearly visible around the lakeshore (Figure 4.2). Here, I use field observations, eyewitness interviews and aerial images from 1960 and 1982, to analyse this event. The smaller 2001 debris flow followed a similar course, partially covering the 1965 deposits. There is no evidence to suggest that it reached Lago Cabrera, though it killed 50 cattle in the lower El Derrumbe valley [Mercurio, 2001]. The unvegetated 2001 deposit covers about one third of the 1965 subaerial deposit, primarily on the south side of the lower El Derrumbe valley. The 2001 flow left fresh vegetation trimlines in the upper El Derrumbe but, due to the lack of aerial photography following this event, it is not possible to locate the source or quantify the scale of this event. Ground-based observations and 1982 aerial photographs suggest the 2001 debris flow did not originate from the same part of the summit region as the 1965 landslide.

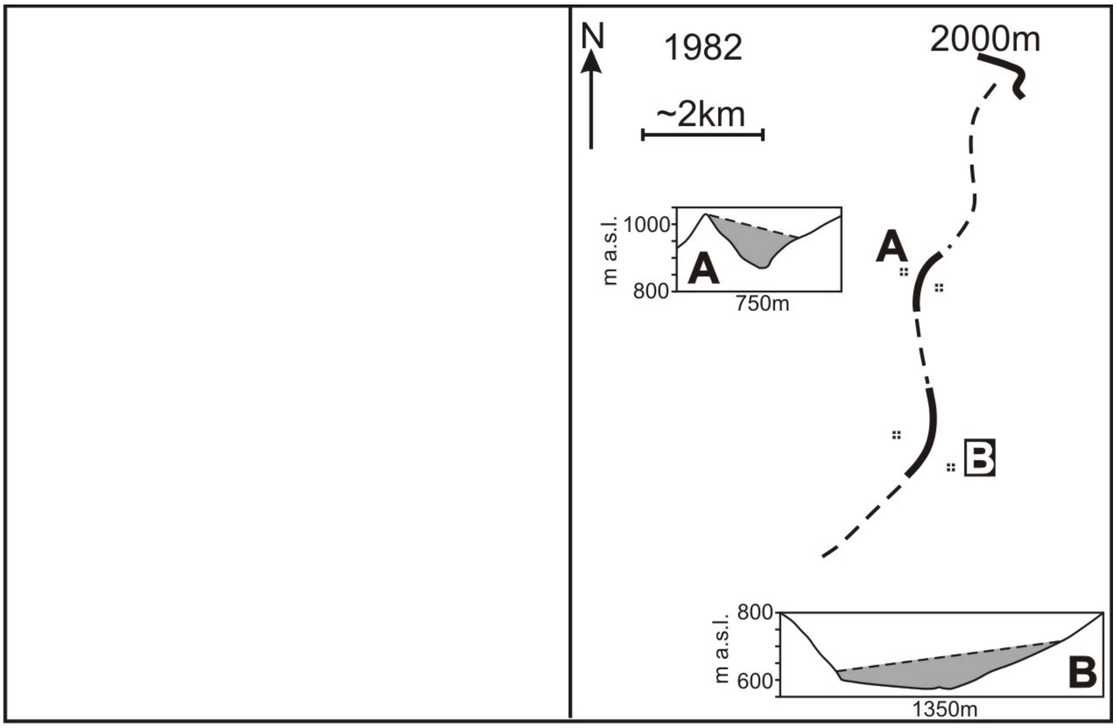

Figure 4.3: Aerial photographs of the 1965 debris flow, with super-elevation velocity estimates. Photographs were taken in 1961 and 1982. Locations of the bends in the path used for flow velocity calculations and the centreline of the flow are shown on the 1982 photograph. Inset topographic cross-sections (vertical scale exaggerated) show the height of vegetation trimlines used to estimate super-elevation.

4.2.1 Accounts and observations

In the early morning of 19th February, 1965, a landslide resulting from a collapse in the SW region of Yate's summit produced a debris flow that travelled down the El Derrumbe valley and entered the northeast end of Lago Cabrera (Figure 4.2). Farm buildings, sited on the fan at this end of the lake, were buried without trace. The debris flow overran older vegetated deposits and entered the lake, extending the pre-event shoreline westward by up to 250 m. The surface of the 1965 flow deposit is uneven and variably vegetated, and its upper part is now buried under the 2001 deposit.

An impulse wave, generated as the debris flow entered the water, travelled the length of Lago Cabrera, running up over gently sloping land bordering the southwest corner of Lago Cabrera (Figures 4.2 and 4.3). Here, three farmhouses were destroyed, and 27 inhabitants were killed [Flash, 1965]. Eyewitness accounts[2] record just one wave, synchronous with the first noise, possibly

---

[2] The following is a précis of interviews with eyewitnesses of the 1965 landslide. *Juan Freddy Antiñirre* and *Ercilia Mancilla* (who lost her father, a brother and a sister in the tsunami), Chaihuaco, 15th January 2007: The wave arrived in the early hours of the morning on 19th February 1965, completely destroying three houses (at SW lake corner). One house containing two people survived, situated 30 m beyond today's shrine (situated near site of houses). This land was forested, with mature living coigüe. Twenty-seven lives were lost, and extensive searching, including by boat, yielded only the partial remains of one person. Water, not debris, did the damage, but ankle-deep

followed by a second loud sound. Land along the lake shorelines, and particularly in the populated southwest corner, was scoured of vegetation, including mature coigüe forest, up to 35–40 m above the present shoreline (Figure 4.4). The debris entering the lake included rock, snow and ice, but the damage around the lake was caused entirely by the water wave, which deposited only 20–30 cm of fine mud at the west end, where it ran inland. This deposit is preserved below felled tree trunks, and contains intraclasts (Figure 4.5), with rare angular lithic fragments that increase in frequency and size (up to a few cm diameter) towards the shoreline.

The Lago Cabrera shoreline was altered by the 1965 landslide (Figures 4.2 and 4.3). An eyewitness estimated an increase in water level of 6 m immediately following the event, but aerial photograph analysis suggests a change of 10–15 m, although this may not have been instantaneous. The deposit blocked drainage at the northeast end of the lake, forming Laguna Las Vacas, with surface area 0.45 km^2 [CONAF, 2007]. A drowned forest is still evident at the shallow north end of this lake.

4.3 Analysis of the 1965 debris flow and tsunami

The scale of the 1965 events has been investigated using aerial photographs, maps and field measurements. I have also attempted to quantify the scale of the subsequent tsunami in Lago Cabrera, primarily to assess the approximate wavemaker volume (i.e., the volume of the submerged deposit). Estimates of lake bathymetry and the extent of the submerged deposit are poorly constrained, and the sensitivity of results to these uncertainties are discussed in the following sections. Results should be regarded as semi-quantitative, but are made in an effort to constrain the parameters relevant to the 1965 landslide.

Four regions relating to the landslide and tsunami are defined for the following section (Figure 4.6): the collapse source; the upper El Derrumbe valley; the lower El Derrumbe valley and

---

soft mud was deposited. The water travelled well beyond the region where the vegetation was removed (into the forest). There were no signs of previous debris flows at the east lake end; the land there was a flat forested valley, farmed, with one farmhouse, empty that night. This area was completely buried by rock, snow and ice, leaving hummocks 6-8 m high, and rocks. Following the event the lake was turbid and contained icebergs, and was different in terms of shape and size. The SW shoreline moved by about 100 m and the water level rose by about 6 m. Bubbles appeared occasionally in the shallow water here after the event. Before the event the Yate summit had a smooth conical profile, resembling a volcano, where the cliff is today. Unusually bad summer weather, of heavy rainfall, had occurred for 15 days before the landslide. *Antonio Paillén*, Hornopirén, 16th January 2007: Corroborated the above account. He was in the house that survived at the SW end of the lake, playing cards at 2.00 am local time, when he heard a noise, that he attributes to the rockfall. Water arrived against the walls of his house concurrent with the noise. He lived about 100 m beyond the main zone of damage, and noted a second noise after the wave, but only one wave.

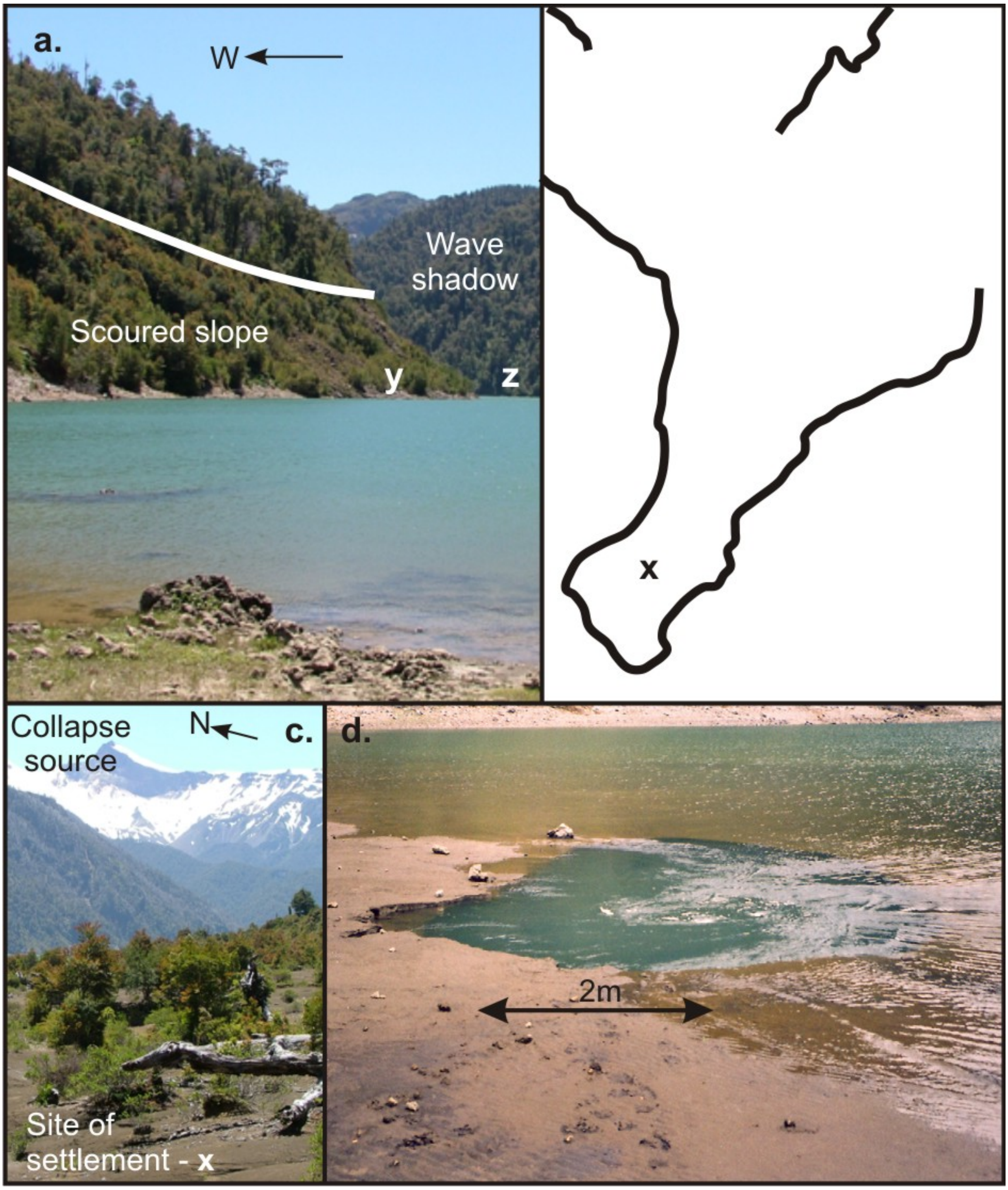

Figure 4.4: Photographs of Lago Cabrera and tsunami impacts following the 1965 landslide. **a** A view across the SW corner of the lake, showing vegetation scour up to 30 m above present water level at the W end of the lake (y). On the far bank (z), which is SW-facing and was in the shadow of the westward travelling wave, mature trees extend down to the lake shore. **b** Aerial photograph of SW corner of Lago Cabrera following the 1965 tsunami, showing directions of wave motion. Points x y z refer to locations shown in images **a** and **c**. **c** SW lake corner, showing bare ground and young vegetation in zone of complete stripping of cover, and the approximate site of the settlement, several hundred metres from the lake shore. The summit area of Yate is in the background. **d** Lago Cabrera outflow at the edge of muds at the SW lakeshore, carrying water beneath Hornopirén lavas.

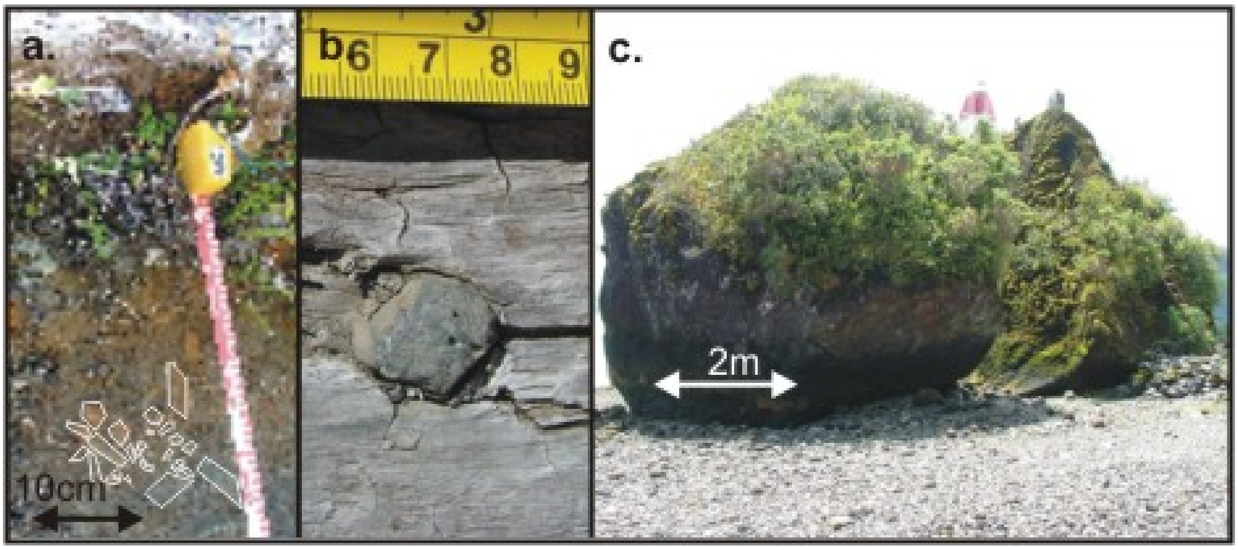

Figure 4.5: Photographs of clasts relating to landslide and tsunami deposits at Yate. **a** Intraclasts of rip-up soil fragments in the mud deposit left at the SW corner of Lago Cabrera following the tsunami, preserved under a felled tree. Selected clasts have been outlined for clarity. **b** Embedded clast in wood of felled trunk at SW corner of lake, scale in centimetres. **c** Individual fractured clast of volcanic rock from the NE area of the Yate summit, carried in the debris flow of 1870 or 1896, and transported approximately 12 km from source. The rock now lies on the coastline, and the objects on top are navigational beacons.

debris fan; and the submerged deposit and Lago Cabrera.

4.3.1 The collapse source

Aerial photographs from 1961 show debris trails on the upper slopes of the SW region of Yate, as well as lines of rocky crags, indicating active erosion of steep slopes and also marking probable lines of past failure (Figure 4.7). On the 1982 images similar features show active erosion and unstable cliffs, and at the present day the snow below the higher rock faces is littered with fallen material.

Detailed examination of aerial photographs bracketing the 1965 landslide indicates a collapse source near the summit ridge of Yate (Figure 4.7), in a southward-opening amphitheatre-shaped depression. This feature is likely to be the result of previous collapses, coupled to some degree with subsequent glacial erosion. Collapse occurred in two main areas, one on each side of this depression, across a maximum E-W width of 1.3 km. All of the material removed in the collapse entered the El Derrumbe valley, through a narrow (400 m wide) opening at the head of the valley.

The images show a large cliff formed on the east side of the summit depression, interpreted as the source of a deep-seated landslide. This subvertical cliff, with a headscarp breadth of 700 m,

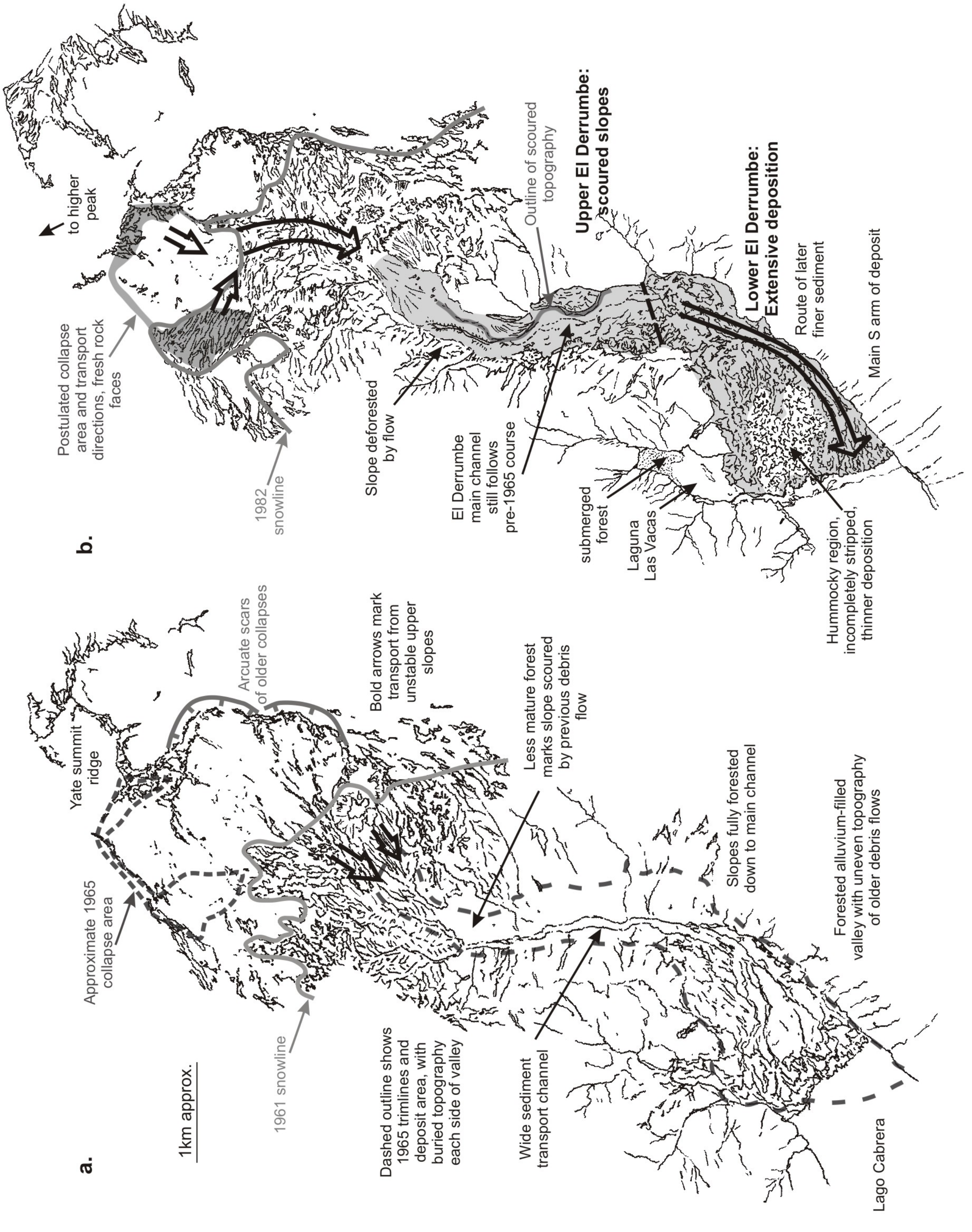

Figure 4.6: Aerial photograph interpretations of the El Derrumbe valley. The area covered is between the summit ridge of Yate and the east end of Lago Cabrera, and shows features relating to the landslide and debris flow. **a** From photographs taken on 28/12/1961. **b** From photographs taken in 1982 at unknown date. Scale is approximate.

has been reconstructed using ground-based photogrammetry, in order to examine its shape and scale. The method used in this reconstruction involved using two images taken from the shore of Lago Cabrera, approximately 10 km from the summit area, with a difference in the horizontal lines of sight forming an angle of 10°. Five well-separated points were selected, common to each image, whose co-ordinates could be found using the area map. Using these as control points, over 700 matched points were marked on each image. The program used (`PicWorks`, supplied by R. Herd, personal communication) then calculated xyz co-ordinates for each of these 700 points by translating matched pixel positions into vector locations, calibrated using the control points. By plotting these locations a 3-dimensional surface model of the cliff morphology is thus produced, as shown in Figure 4.8. The scale, based on the calibrated control points, should be considered approximate. The modelled surface and photographs reveal a subvertical upper cliff face, formed of subhorizontal lavas, up to 80 m thick. The lavas overlie a lower cliff of heavily weathered rocks, judged from their appearance to be pyroclastic material, up to 100 m thick, with more uneven topography. The pyroclastic rocks erode recessively as a series of gullies with a concave profile, becoming snow-covered and ending in a small plateau at the base. The collapsing mass of rock and ice travelled around the west side of a rocky slope below the plateau, which was exposed after the event and may have been a source of additional debris. According to eyewitness reports, prior to the 1965 landslide the failure region formed a craggy slope with a rounded profile, in contrast to the present-day cliff. It is possible that differential erosion of the pyroclastic rocks underlying the lava cap in the failure region contributed to rockface instability. The result is likely to have been a slump-like valley-head landslide, and similar landslides are likely to recur from the newly exposed cliff.

After the 1965 landslide, 0.1 km^2 of steep stony ground was exposed on the west side of the amphitheatre, in an area that previously had thick ice cover. This shallow slab failure may have occurred simultaneously with the failure on the east side, or in response to it, following entrainment of material at the base of the slope, potentially reducing relative glacier strength here [cf. Huggel et al., 2007]. This region contributed a high proportion of ice as well as rock to the landslide.

To estimate the volume of failed material the collapse source is treated as two main regions. In the east (**X** in Figure 4.7), along a headscarp of 700 m, the mean vertical cliff height is approximately 150 m. From maps, aerial photographs and eyewitness accounts the pre-failure slope angle is estimated at 40–50°, implying a rock failure volume of approximately 6–9 × 10^6 m^3. To

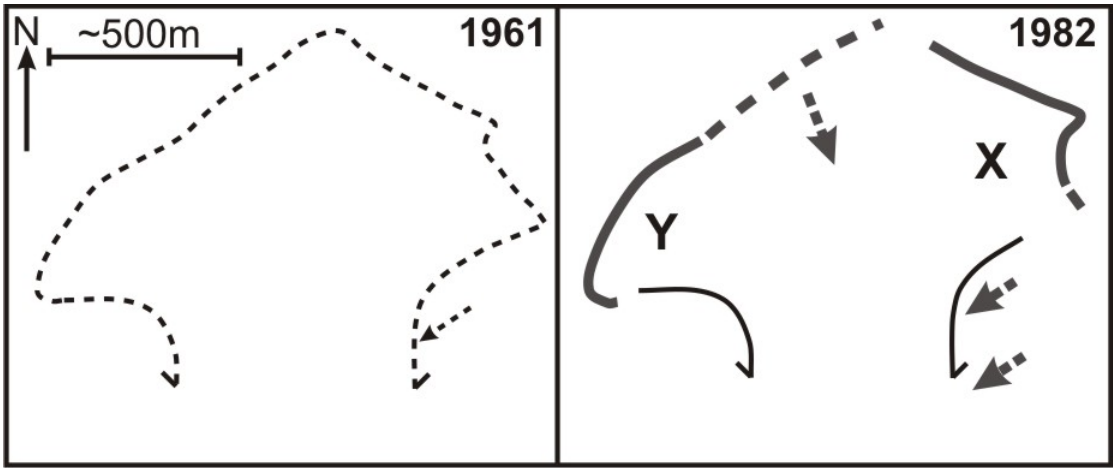

Figure 4.7: Aerial photographs of the Yate summit collapse area in 1961 and 1982, showing the main east (**X**) and west (**Y**) source regions of the 1965 landslide. Failure region is shown as a dashed outline in the pre-failure 1961 image.

the west (**Y** in Figure 4.7) it is estimated that 1–10 m of ice and rock cover was removed from an area of 0.1 km^3; a volume of 10^5 –10^6 m^3. The total source region failure volume was therefore approximately 6×10^6 – 1×10^7 m^3, the bulk of which originated from the east cliff. Entrainment of unconsolidated material from the slopes below the failure area is unconstrained, but may have increased this volume substantially (see Section 4.3.2.1).

4.3.2 El Derrumbe valley and debris deposit

A topographic profile of the debris path from the top of the failure scarp at 2000 m shows a horizontal length of 7500 m to the pre-event shoreline of Lago Cabrera, with a 1490 m vertical drop (Figure 4.9). Below the collapse amphitheatre the slope steepens, marking the top of the El Derrumbe valley.

The most prominent difference between the aerial photographs of 1961 and 1982 is the unvegetated deposit along the El Derrumbe valley (Figure 4.3). Prior to the 1965 landslide the slopes of the upper El Derrumbe were heavily forested. The debris flow cleared vegetation across an 1100 m width in the north-south trending upper El Derrumbe valley, overriding topography to approximately 100 m above the valley floor. The river course in the upper El Derrumbe was unaltered by the landslide and local topographic shapes are still discernible, albeit stripped of vegetation, suggesting only minor deposition in this region.

The lower El Derrumbe valley trends southwest, and prior to 1965 had a gently sloping but uneven topography covered by mature forest. The 1965 debris flow overran this area, forming a

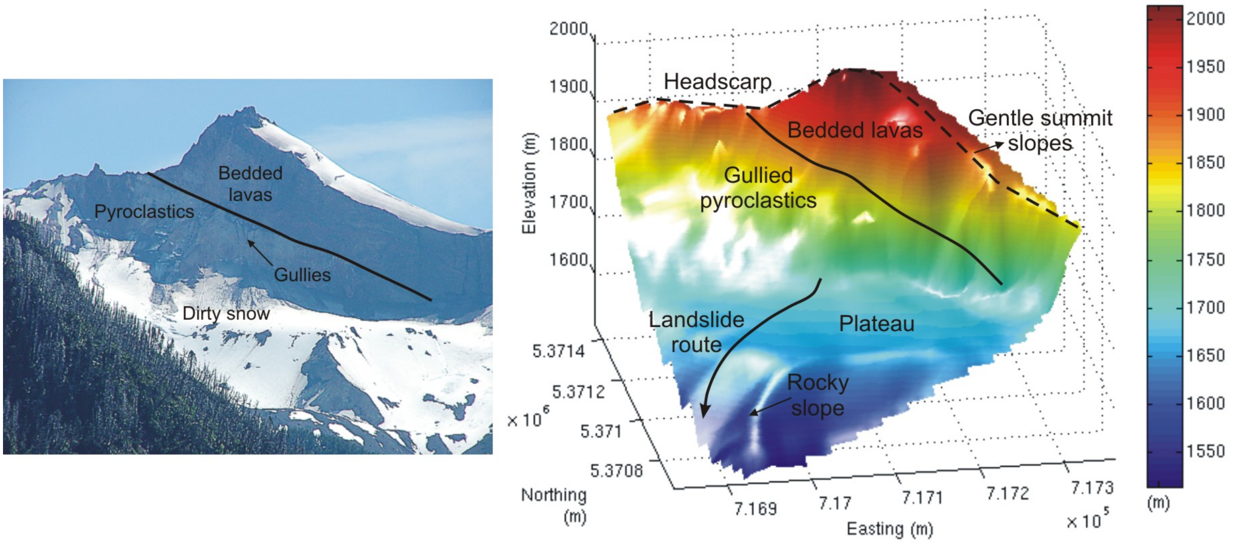

Figure 4.8: Photograph and photogrammetric image of the eastern failure region of the 1965 landslide. This region contributed the bulk of rocky material to the debris flow and left a cliff of bedded lavas overlying recessively eroding pyroclastic rocks.

fan with a maximum width of 1.5 km towards the east lake shore. Although all of the mature forest in this region was cleared by the 1965 debris, the main flow split into two arms, carrying the bulk of material around hummocky topography in the centre of the pre-1965 fan, suggesting deceleration of the flow. In this central area, scrub rapidly re-established, today forming patches of low woodland close to the lakeshore. In contrast, the clastic material in the main channels has only a sparse vegetative cover today (Figure 4.10). The north arm of debris followed the pre-1965 main river course, damming drainage from the north and forming Laguna Las Vacas (Figure 4.2). The south arm transported the greater volume of debris, forming a fan at the east end of Lago Cabrera, and generating an impulse wave. The modern river follows the south edge of this fan, directly below steep valley slopes. It may have modified the fan morphology, through deposition and transport of fine sediment from higher in the valley, in the years following the landslide.

4.3.2.1 Deposit volume

Debris flow deposition in the upper El Derrumbe valley (area of 2.0 km^2; Figure 4.6) is considered to be negligible. The debris flow deposited subaerially in the lower El Derrumbe valley (area of 3.0 km^2), where topography suggests an irregular deposit thickness. This reaches thicknesses estimated at 10 m in some areas, such as the area of blocked drainage that subsequently formed Laguna Las Vacas. From this the mean deposit thickness in the lower El Derrumbe valley is estimated to be between 3–5 m (a volume of 9×10^6 – 1.5×10^7 m^3), and after accounting

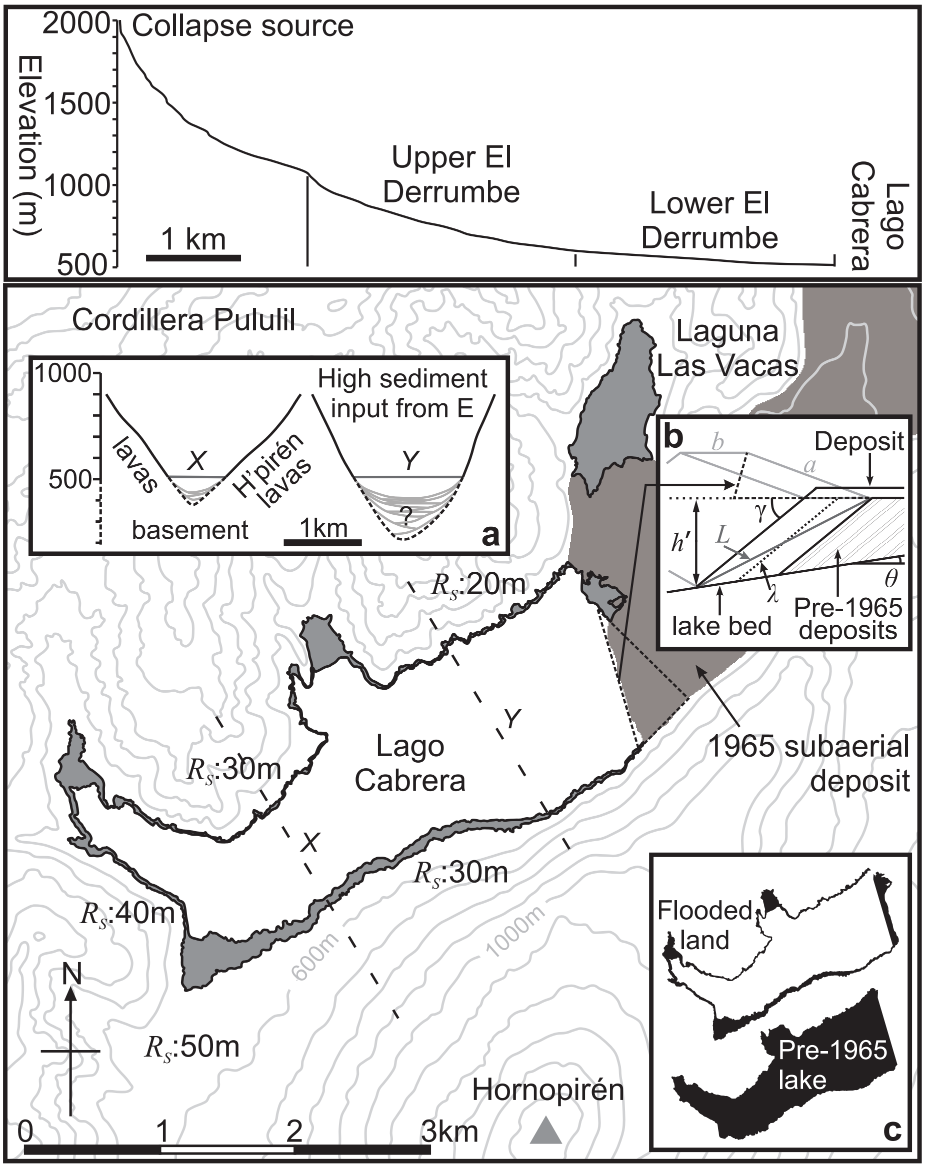

Figure 4.9: Lago Cabrera map and calculation parameters. *Upper panel*: longitudinal profile of the debris flow route, from the source to the shore of Lago Cabrera, with divisions into the regions mentioned in the text. *Lower panel*: map detail of Lago Cabrera after the 1965 landslide, with the debris flow deposit outlined. Flooded land around the original lake shore is shaded. R_S values show estimates of wave run-up (above pre-event water level) based on vegetation trimlines. Insets define the parameters used in calculations in the text: **a** Topographic profiles for two sections across the lake used for bathymetric approximation (see Section 4.3.3). **b** Wavemaker dimensions. The dashed triangle on the main map indicates the debris fan extent at the pre-event lake water level and is used to estimate wavemaker volume (see Section 4.3.3.2). a and b are the approximated dimensions of the wavemaker at pre-event water level, h' is the water depth at the foot of the wavemaker, θ is the lake floor slope angle, γ is the wavemaker angle of rest, L is the submerged deposit length and λ is the deposit centreline length. **c** Original and flooded lake areas used to estimate water displacement and lake volume change (see Section 4.3.3.3).

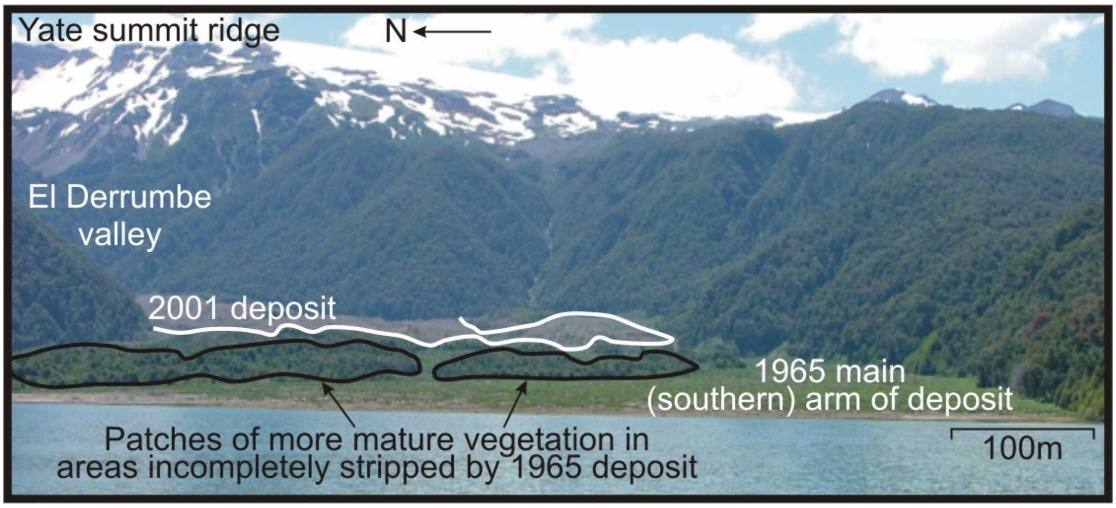

Figure 4.10: Photograph of the debris flow deposits. View looking east up the lower El Derrumbe valley, showing features left by the 1965 and 2001 debris flows.

for the submerged deposit (Section 4.3.3), a total deposit volume of ~1.5–2.7 × 10^7 m^3. The collapsed source material would have expanded during disintegration and transformation into a debris flow. Without field constraints, a bulking factor of 0.25 is assumed, following Hungr and Evans [2004] use of the median porosity of loosely-crushed rock, to infer a pre-bulking source volume of 1.2–2.2 × 10^7 m^3.

This volume is approximately twice as large as the estimated volume of the failure region (Section 4.3.1), implying substantial entrainment of colluvium and vegetation along the flow path. The deposit volume is an order of magnitude smaller than some non-eruptive volcanic collapses such as that at Iriga, Philippines [cf. Lagmay et al., 2000] or the 1970 rock and ice avalanche of Nevados Huascarán, Peru. In the debris flow classification scheme (range 1–10) of Jakob [2005] the 1965 event at Yate has a magnitude of 7. However, the scale and inferred recurrence rate (see Section 4.5) of the 1965 and similar-sized events at Yate is high compared to catastrophic flank failures at many volcanoes, such as those at Casita in 1998 (1.6 × 10^6 m^3 [Kerle, 2002]) and earlier in the Holocene [Scott et al., 2005].

4.3.2.2 Velocity estimates

The entire landslide volume was funnelled through a notch 400 m wide at the head of the El Derrumbe valley, and the flow remained confined for 5 km before fanning out and decelerating in the lower El Derrumbe valley. Following Evans et al. [1989], the longitudinal horizontal path of 7500 m and vertical change of 1490 m give a *fahrböschung* (the ratio of vertical change to horizontal

Table 4.1: Debris flow velocity estimates

Location[a]	**A**	**B**
y (m)	65	90
r (m)	450	1750
j (m)	400	1000
v (super-elevation[b]) (m s^{-1})	26.8	39.3
v (velocity head[b]) (m s^{-1})	35.7	42.0

[a] See Figure 4.3

[b] Pierson [1985]

path) of 0.2 (11.3°). This value would be lower if the debris had not entered Lago Cabrera, but continued to run out on land, and it is similar to that of other volcanic debris avalanche deposits [Ui et al., 2000], indicating relatively high mobility. Rapid transformation into a debris flow would have been enhanced by entrainment of saturated colluvium [Hungr and Evans, 2004]. Comparison with similar channelised landslides that developed into debris flows [Evans et al., 1989, Boultbee et al., 2006] suggests the flow was of high mobility given its volume.

Indirect estimates of debris flow velocity, v, may be derived from evidence of debris flow super-elevation using the vegetation trimline at bends in the flow path [Pierson, 1985]. From the tilting of the free surface in a bend

$$v = \sqrt{\frac{gyr}{j}} \tag{4.1}$$

where g is acceleration due to gravity, y is the difference in trimline elevation, r is the radius of curvature at the centre of the flow path, and j is the channel width. Calculations at two points in the flow path (**A** and **B** in Figure 4.3) are given in Table 4.1. Using estimates from aerial photographs and topographic maps these give velocities of 27 and 39 m s^{-1}. The application of equation 4.1 has not been rigorously tested for debris flows of this type, and it may underestimate the true velocity [Pierson, 1985, Evans et al., 2001]. Using a velocity-head calculation [Pierson, 1985] at the same points (Table 4.1), based on the conversion of kinetic to gravitational potential energy, gives comparable but slightly higher velocities:

$$v = \sqrt{2gy} \tag{4.2}$$

where y, the vertical run-up, is approximated by the trimline elevation difference. Since frictional energy losses are not accounted for in this calculation, and also given that impact was not perpendicular to flow direction, it provides an estimate of minimum velocity. The lower velocities at point **A** may reflect underestimation of run-up, as part of the flow appears to have overridden the crest of the valley side here. These estimates indicate a maximum velocity of approximately 40 m s^{-1} in the upper El Derrumbe valley, a value comparable to similar flows elsewhere [e.g., Evans et al., 2001, 2007, Boultbee et al., 2006]. Having lost energy in the corner at **B**, the flow decelerated on the gentler topography of the lower El Derrumbe valley, with extensive deposition of debris, before entering Lago Cabrera.

4.3.3 Lago Cabrera and the 1965 tsunami

Impulse waves in lakes or reservoirs resulting from mass movements have been documented in alpine environments [e.g., Evans, 1989, Panizzo et al., 2005] and as a result of volcanogenic collapses [Freundt et al., 2007]. The resulting waves are a class of tsunami, and have the capacity to cause significant damage on a local scale, being commonly associated with very large wave run-up on surrounding lake shores, and with very short travel times relative to tsunamis in more open settings.

Field and aerial photograph measurements of wave destruction at Lago Cabrera (Figure 4.9) provide a good proxy for tsunami parameters. On steep lakeshore slopes slightly oblique to the direction of wave travel vegetation was completely removed at heights of up to 30 m above pre-event water level. From this observation, allowing for a small amount of run-up, the wave amplitude, η, is approximated at 25 m above ambient water level. The following calculations rely on lake water depth as an input. Water depth, h, is estimated in the centre of the lake by extrapolating topographic slopes (Figure 4.9). These suggest that Hornopirén lavas abut early post-glacial topography at the base of the Pululil lava ridge, forming a basin that deepens to the east. Active slope sedimentation and debris flow input from the east is likely to have infilled much of this basin in post-glacial time, but by an unknown amount. This suggests the lake depth does not exceed 200 m, but may be as little as 50 m, and this range is used in the following calculations.

4.3.3.1 Wave run-up

The wave run-up in the gently sloping southwest corner of Lago Cabrera provides an additional constraint on wave amplitude, and can be used to test whether the estimate of wave-height given above is realistic. In the SW lake corner all buildings and vegetation, except for the largest tree trunks (> 1 m in diameter), were removed for up to 1000 m inland; a ca. 50 m vertical climb from the pre-event shoreline. Water travelled beyond this point, but without sufficient energy to remove vegetation, and thus wave run-up (total vertical height climb of water), R, exceeded 50 m. The minimum ground slope in this region is 1:20, but the ground steepens towards the shore to approximately 1:10, and this slope is taken to estimate the submerged slope angle, β. The estimated wave amplitude η, of 25 m can be taken as a proxy wave source input.

A solitary wave on a planar slope will break when $\frac{\eta}{h} > 0.818 (\cot \beta)^{-\frac{10}{9}}$, where $\frac{\eta}{h}$ is the ratio of wave height to water depth [Synolakis, 1987]. The lake depth estimates used (Section 4.3.3) give a $\frac{\eta}{h}$ range of 0.125–0.5. This exceeds the wave-breaking criterion (0.063 in this case), suggesting that the wave broke early during run-up. Using the numerical results of Li and Raichlen [2002] quoted for plane beach slopes of 1:19.85 and 1:15, $\frac{R}{h}$ is 0.35–0.9, giving an inferred run-up range of 37.5–80 m. This estimate of run-up, which is based on the field-estimated wave height of 25 m, corresponds well with field observations of total run-up ($R > 50$ m), and suggests that these estimates are self-consistent, and that the lake depth range used is plausible.

4.3.3.2 Wavemaker volume

To estimate the volume of submerged solid material (the wavemaker) that generated the tsunami, I use a model of wave behaviour produced by Walder et al. [2003], constrained by the field estimate of wave amplitude ($\eta = 25$ m) and using h of 100 m (50–200 m range). In the following section I work back from this model to find the wavemaker volume, and its dimensions, necessary to produce an impulse wave of the observed magnitude. Other parameters remain unknown and consequently, although care is taken to select the most realistic possible assumptions, the volume derived is only approximate.

Following Walder et al. [2003], Lago Cabrera may be divided into three regions: the *splash zone*, extending to the foot of the submerged debris flow and characterised by complex dynamics; the *near-field*, where kinetic energy is imparted to a coherent wave; and the *far-field*, where wave propagation effects become significant. The properties of the leading wave hump in the near-field are, to the first order, independent of mass-flow type, with a ratio of amplitude to water depth that is a function of the wavemaker volume and underwater travel time. Walder et al. [2003] provide a scaling analysis where wave properties may be estimated without the need to characterize the complexities of the splash zone. From this, wave amplitude η may be expressed as

$$\eta^\star = c\left(\frac{t_s^\star}{V_W^\star}\right)^{-d} \tag{4.3}$$

where * indicates a dimensionless variable, t_s is time of submerged debris flow motion, V_W is debris flow volume per unit width (the near-field lake width is 1000 m) and c and d are regression coefficients of 1.32 and 0.68 respectively. This equation holds true for $2 < t_s^\star/V_W^\star < 100$. The dimensionless variables are defined:

$$V_W^\star = \frac{V_W}{h^2} \tag{4.4}$$

$$t_s^\star = \frac{[x]}{h'} \tag{4.5}$$

$$\eta^\star = \frac{\eta}{h} \tag{4.6}$$

where $[x]$ is a distance measure of long-wave water displacement during landslide motion. To estimate $V_W^\star$ and $\eta^\star$ a near field depth, h, in the range of 50–200 m is used, as discussed above, but to estimate $t_s^\star$ it is necessary to use the depth at the foot of the submerged debris, or wavemaker, which is here called h'. A first order approximation for $t_s^\star$ is made from [Walder et al., 2003]:

$$t_s^\star \approx C_s\sqrt{\frac{L}{h'}} \tag{4.7}$$

where C_s is equal to 4.5, appropriate for a Coulomb frictional grain flow [Savage and Hutter, 1989], and L is the submerged deposit length, comparable to the extent of the splash zone.

The wavemaker entered the east end of Lago Cabrera in a direction approximately parallel to the lake length and decelerated to rest. The wavemaker is treated as a poorly sorted sedimentary deposit, with an angle of rest [e.g., Carrigy, 1970], γ, of 35°. The submerged slope on which the deposit settled is assumed to be formed from previous debris deposits, also with an angle of rest of 35°. The basal lake slope, on which the debris deposits rest, has an unknown angle, θ. The horizontal extent of the submerged fan at the pre-event lake level has been found using the area of the fan at present water level (Figure 4.9), assuming a 35° lakeshore slope with a 10 m height change. This area is equivalent to a rectangle with dimensions a (900 m) × b (250 m), and using this the wavemaker can be modelled as a quadrilateral prism, with centreline length λ (Figure 4.9b), such that

Table 4.2: Tests of the sensitivity of wavemaker and tsunami parameter estimates to input lake parameters.

Variables						
γ °	35	20	35	35	35	35
θ °	10	10	5	15	10	10
h (m)	100	100	100	100	50	200
Results						
h' (m)	68.7	84.4	55.1	90.2	58.4	82.8
L (m)	355	482	329	379	333	368
$[x]$ (m)	703	915	610	843	632	796
V ($\times$ 10^6 m^3)	8.8	9.4	9.6	8.1	6.5	12

$$V = \lambda ab \sin\gamma \tag{4.8}$$

where V is the wavemaker volume. From Figure 4.9b the values of h' and L are defined as:

$$h' = \sin\gamma \left(\lambda + \frac{\frac{b}{2}\sin\theta}{\sin(\gamma - \theta)} \right) \tag{4.9}$$

$$L = \sqrt{h\prime^2 + (b + h'\cot\gamma)^2} \tag{4.10}$$

Equations 4.3, 4.4 and 4.6-4.10 can now be solved to find λ such that η is equal to 25 m, thus producing an estimate of wavemaker volume, V. To achieve this solution, the above method relies on estimates of the poorly-constrained parameters γ, θ and h. The potential errors involved in these estimates produces uncertainty in the derived volumes, and the sensitivity of the final results to these input values should be tested. By varying these parameters within a range of plausible values the uncertainties involved and the ability of the method to constrain wavemaker volume can be indicated. Results from this process are shown in Table 4.2.

The assumed submerged deposit angle of rest, γ, of 35° may overestimate the value of a deposit entering the lake with an initial lateral velocity. From the sensitivity analysis if is seen that reducing this value to 20° increases estimated V by 6% (Table 4.2). Similar sensitivity is shown by changing lake-floor slope, θ, within the estimated range of 5–15°. Results are most sensitive to changes in lake depth, h. Within the estimated possible range of 50–200 m the wavemaker volume varies from 6.5×10^6 – 1.2×10^7 m^3 . Using what are considered the most likely parameters (Table 4.2), an estimate for wavemaker volume, V, of $9 \pm 3 \times 10^6$ m^3 is produced, acknowledging the multiple uncertainties in the above calculations, the most significant of which is lake depth. In spite of these uncertainties, the ranges of all output parameters fall within a single order of magnitude. Other final estimates produced include the submerged deposit depth, h', of 55–90 m, and the wavemaker block length, L, of 330–490 m. From these, using equation 4.5, a range for $[x]$ is found of 610–910 m. These results suggest that most of the lake lay within the near-field, which extends to approximately $3\,[x]$ beyond the splash zone, and that wave propagation effects can therefore be neglected from the calculations.

These estimates of wavemaker volume suggest that no more than 50% of the debris flow entered Lago Cabrera. The scale of the tsunami generated is similar to those documented in comparable settings elsewhere, such as the 1946 tsunami at Mount Colonel Foster and Landslide Lake, Canada (η est. 29 m; R est. 51 m), which was formed by a smaller wavemaker with volume 7×10^5 m^3 [Evans, 1989].

4.3.3.3 Hydrological effects

Prior to the 1965 landslide the outflow of Lago Cabrera was subterranean, travelling beneath Hornopirén lavas before emerging as the headwaters of the Cuchildeo River, 5 km to the south (Figure 4.1). A rapid and sustained increase in water level, estimated at 6 m by eyewitnesses, occurred after the event, indicating disruption of the outflow coupled with water displacement by the submerged deposit. However, the lake level stabilised at an increase of approximately 10 m. The present-day outflow is observable at the current shoreline in muds adjacent to Hornopirén lavas (Figures 4.2 and 4.4), at an elevation far above the pre-event shoreline, and can therefore only have formed here following re-establishment of the lake outflow after the 1965 events.

If the change in lake level was simply due to displacement by the submerged deposit, the wavemaker volume could be directly estimated. For a 10 m change in water level following the event, an original lake area (excluding the 1965 deposit) of 4438000 m^2, and a newly flooded area of 918000 m^2 (Figure 4.9c), assuming a linear topographic slope implies a wavemaker volume of $\sim$4.9 $\times$ 10^7 m^3. This volume is considerably larger than that estimated from tsunami modelling (Section 4.3.3.2), and greatly exceeds the estimated source area volume, in spite of substantial subaerial deposition. Moreover, if used as a starting point in the scaling analysis of Walder et al. [2003], this volume suggests a wave amplitude of approximately 50 m and a resultant run-up [Li and Raichlen, 2002] at the SW lake shore of 90 m, neither of which agree with field observations.

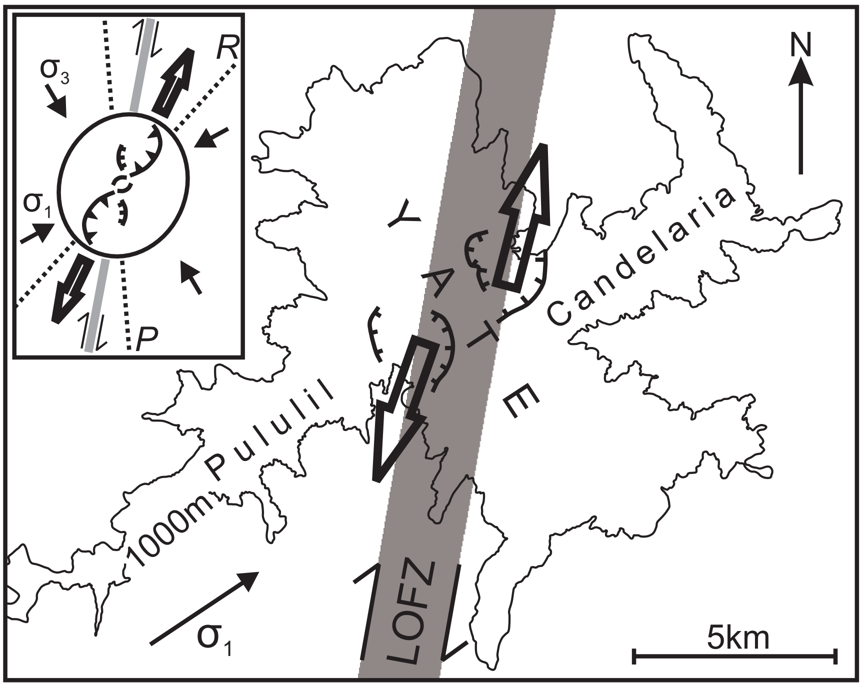

Figure 4.11: Edifice morphology and the LOFZ stress regime. The map of Yate in the main figure shows the 1000 m contour and scars of summit collapses. Directions of failure motion, the line of the LOFZ, and the maximum horizontal stress direction for a strike-slip system, σ_1, are shown. The inset shows the model results of Lagmay et al. [2000] for edifice failure on a strike-slip fault zone. *P* and *R* show synthetic faults generated in the Lagmay et al. [2000] analogue models, which approximately parallel the **P** and Riedel shear directions, respectively.

Thus, it is apparent that hydrological changes in lake outflow took place following the tsunami, with an increase in lake volume of approximately 4×10^7 m^3, presumably due to riverine input, after equilibration of the lake at a new level. There may also be some seasonal fluctuation in lake volume affecting this estimate, which is seen in lake level differences between aerial photographs from 1944 and 1961.

4.4 Strike-slip tectonics and edifice stability

Yate lies on the major dextral strike-slip Liquiñe-Ofqui fault zone [Cembrano et al., 1996]. Lagmay et al. [2000] showed how strike-slip fault systems underlying volcanoes may induce edifice instability, and produced a structural model of failure for such volcanoes (Figure 4.11). Their experiments show that fault shear results in two sigmoids of normal and reverse faults with an internal edifice flower structure, creating two oversteepened and destabilized flank regions where avalanching occurs at angles of 10–20° to the trend of the underlying fault, towards the direction of the Riedel shear.

4.4.1 The influence of regional stress on edifice structure

The continental margin at the latitudes of Yate is best classified as lying within a transpressional regime, as a result of oblique subduction. Deformation along the LOFZ results from this, with variable partition of transpression into regions of contractional and strike-slip kinematics along the regions of the coincident LOFZ and SVZ [Cembrano et al., 2002]. Along the LOFZ deformation is taken up along a broad zone of ductile distributed shear in the basement rocks, with marked differences in the precise nature of deformation along strike [Cembrano et al., 2000, 2002]. Fault populations in the region indicate a dextral strike-slip regime, accompanied by a compressive regime just north of Yate [Cembrano et al., 2000]. Dextral strike-slip behaviour is also consistent with recent seismicity observed along the fault zone [Lange et al., 2008].

Regional stress regimes have been found to influence many volcanic processes, including crater opening direction, vent distribution and dike orientation [e.g., Lagmay and Valdivia, 2006, Tibaldi and Lagmay, 2006]. Such interaction may result in cone elongation parallel to the regional maximum compressive stress direction [Nakamura, 1977]. Dike orientation, influenced by the local stress regime on the LOFZ, appears to have exerted a control over entire edifice morphology in the case of the elliptical cone of Hornopirén [Dewey and Lamb, 1992]. The model of Nakamura [1977] has been used to suggest that crater opening, and similarly flank failure, may occur perpendicular to the maximum regional compressive stress [Moriya, 1980], but further investigations suggest these models may be too simplistic, and a variety of responses is seen in different locations, varying with the kinematic setting and influenced by the precise relationship between the fault system and the volcanic edifice [cf. Wooller et al., 2003, Lagmay et al., 2000]. Tibaldi [1995] found that fault-perpendicular cone breaching was most common in extensional settings, whereas strike-slip settings were characterised by fault-parallel failure. The analogue modelling of Lagmay et al. [2000] concurs with this and provides a mechanism by which this process may occur.

4.4.2 Yate and the LOFZ

Edifice morphology and historical events at Yate suggest that major landslides initiate north and south of the volcano summit at an angle of 5–10° to the local trace of the LOFZ towards the Riedel shear direction (Figure 4.11). Thus, the model of [Lagmay et al., 2000] provides a good analogue for the situation at Yate, with the scarps around the north and south failure zones forming sigmoids, exaggerated by subsequent erosion. This implies that the regional tectonic system is an important factor in determining failure orientation at Yate.

There is little historical record of seismic activity on this portion of the LOFZ, although local seismicity indicates dextral strike-slip motion [Lange et al., 2008]. The influence of regional tectonics does not imply that large-magnitude fault movement is concurrent with failure, but that instabilities resulting in failure are inherited from movement on the fault during the lifetime of the volcano, concurrent with at least part of the main period of edifice construction. Lagmay et al. [2000] predict that 100 m of motion is sufficient to produce critical instabilities for a cone of 1500 m in elevation (Yate's summit is over 2000 m). Although the times and amounts of movement on the LOFZ are not well understood it has been active throughout the Cenozoic [Cembrano et al., 2000, Forsythe and Diemer, 2006], and the total Pleistocene-Holocene displacement may fulfil the above failure criterion. However, given the lack of evidence for this order of Holocene movement along this portion of the LOFZ, it may be that in the case of a glaciated edifice such as Yate this amount of fault displacement is not necessary to induce orientated edifice failure. In this situation, the first-order role of strike-slip tectonics may be to impose linear zones of weakness within the edifice, forming easily erodible belts that are then exploited by glaciers to initiate orientated glacial valleys. Mechanical weakening, both on the edifice scale through strike-slip faulting, and at the surface through glacial action and subsequent debuttressing during deglaciation, may produce a situation with predictable failure directions. The interaction of glaciation with strike-slip tectonics may explain the repetitive but relatively small-scale collapses at Yate, gradually removing masses of mechanically-weathered rock, and distinct from the single catastrophic failures at volcanoes such as Iriga, Philippines [Lagmay et al., 2000], where fault movement is greater and is the only major factor influencing long-term instability. It should also be noted from Figure 4.11 that the Candelaria and Pululil ridges radiate away from the main edifice in the direction of maximum horizontal stress (σ_1), suggesting an influence of the regional stress field on the orientation of upper-crustal magma transport [cf. Nakamura, 1977], and a further control on volcanism by the regional tectonic regime.

Several other southern Chilean volcanoes lie along the LOFZ, including stratocones (e.g., Hornopirén), and older complexes, similar to Yate, such as Minchinmávida (Figure 4.12). The tectonic systems that control the structure of these edifices on a local scale have important implications for hazard assessment in terms of the orientation of mass-wasting events. At Minchinmávida, a large Pleistocene-Holocene composite volcano 115 km south of Yate, a 3 km wide

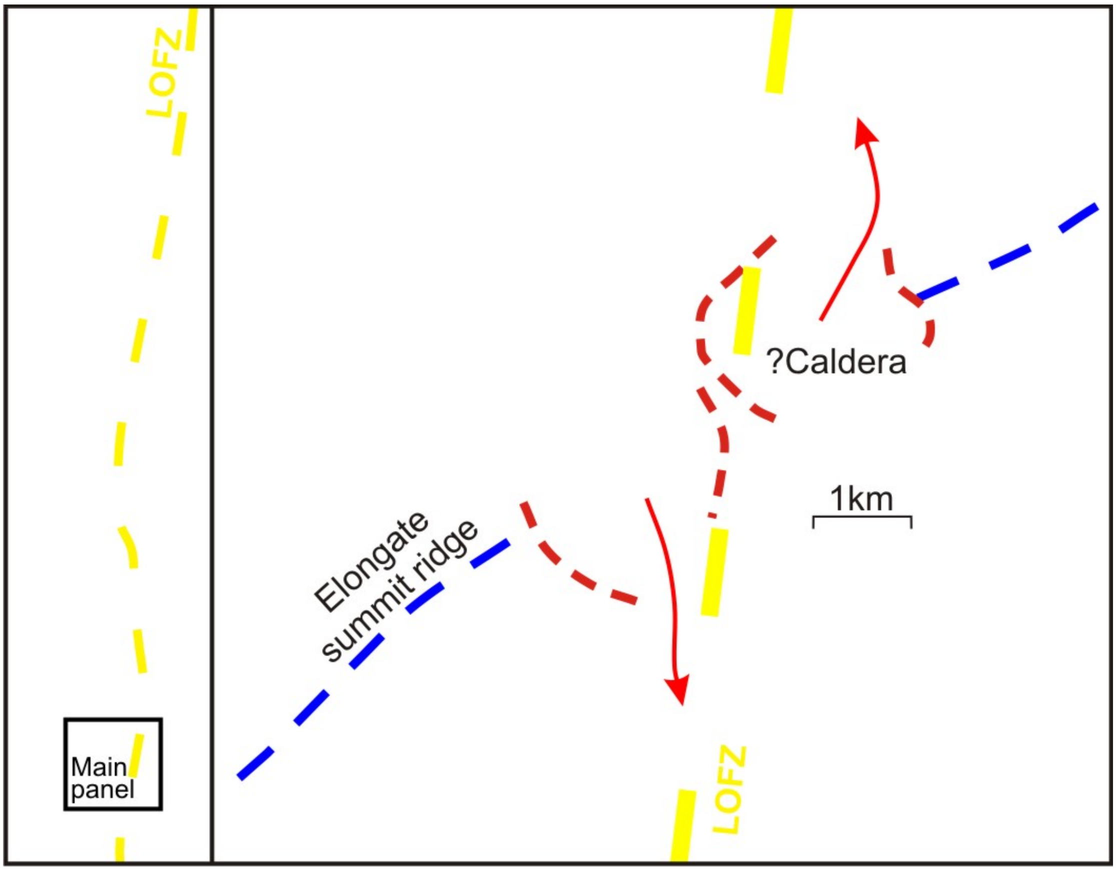

Figure 4.12: Failure directions at Minchinmávida volcano. A breached caldera to the north and a depression to the south open at angles slightly oblique to the LOFZ, consistent with the model of Lagmay et al. [2000]. The overall structure is similar to Yate, with volcanic ridges parallel to σ_1. The image on the left shows the context of these volcanoes on the LOFZ, apparent as a series of fjords and glacial valleys parallel with the volcanic arc, and in many cases directly beneath it. The location of the main image is outlined.

amphitheatre, interpreted as a caldera [Naranjo and Stern, 2004], breaches the cone to the north. A similar depression lies south of the summit area, from which a large debris-filled valley exits, approximately aligned with the LOFZ. The structure of the edifice is similar to Yate, with N-S orientated debris-filled valleys on each side of a deeply eroded summit, centred upon a volcanic ridge approximately aligned with the σ_1 direction. These similarities suggest that collapse orientations are influenced by strike-slip tectonics at other volcanoes along the LOFZ. According to Norini and Lagmay [2005] underlying strike-slip fault systems may also generate internal stresses and deformation at edifices where the morphology does not suggest such influences. Thus volcanoes such as Hornopirén, a symmetrical cone elongated along the strike of the LOFZ, may also pose a landslide hazard through specifically orientated slope failure.

4.5 Previous landslides at Yate

The two major historical landslides SW of Yate added to an already extensive debris fan in the El Derrumbe valley. Several arcuate scars are evident around the summit of Yate, and the volcano's deeply indented morphology indicates that numerous previous collapses of similar style and magnitude to those of 1965 and 2001 have occurred in the past. Construction of the debris fan deposits has probably occurred throughout post-glacial time. Given the present extent of the El Derrumbe fan, only larger debris flows are likely to reach Lago Cabrera and produce tsunamis in the future; most will come to rest on the fan, as in 2001. Prior landslides almost certainly caused tsunamis similar to that of 1965, and the record of these past events should be evident in the sediments of Lago Cabrera. Although the historical records are insufficient to investigate the long-term frequency of landslides, the timing of historical events may provide some insight into the factors controlling failure.

While vegetation was well established in the El Derrumbe valley in 1961, the forest is identifiably less mature on the valley floor, than on higher slopes, indicating that events comparable to that of 1965 had occurred within the preceding few hundred years. The 1965 collapse was then followed by another major landslide within less than 40 years. Northeast of the summit, major landslides occurred in 1870 and 1896 from different source regions, and with no reported events since. Thus, in spite of the close spacing in time of these historical summit collapses, as compared to the inferred longer term failure rates, it remains unclear whether these failures were structurally related. Historical records, although available over only a short period, suggest a frequency of

$\leq 10^2$ yr for landslides of 10^6–10^7 m^3 at the summit of Yate.

Although regional tectonics may explain the direction of failure at Yate, the predisposition of the edifice to failure was enhanced by the retreat of ice throughout the Holocene, exposing slopes that were previously stabilized and buttressed by ice. Additionally, incremental eruptive construction of the edifice during the late Pleistocene and early Holocene, for which there is evidence in the summit region, may have generated steeper slopes that became unstable in post-glacial time. The lithological composition of the edifice, with massive lavas overlying weaker pyroclastic deposits, may further contribute to instability (Figure 4.8) [Siebert, 1984].

The immediate causes of major landslides include a wide range of external processes, such as extreme rainfall [Iverson, 2000], seismicity [Miller, 1960, Davis and Karzulovíc, 1963, Evans et al., 1989], or a special combination of factors [Kerle et al., 2003], though there may also be no trigger other than the exceedance of a stability threshold. None of the four historical events at Yate correspond to known earthquakes. Hauser [1985] considered that glacial melting associated with high temperatures triggered the 1871 landslide, and that extreme rainfall triggered the 1896 event. Unusually heavy rainfall occurred for 15 days prior to the 1965 collapse, possibly with the 0 °C isotherm lying above the summit elevation, and similar weather conditions occurred before the 2001 event. Both events occurred in mid-February, the height of summer, when snow levels are likely to have retreated to their minimum extent, with meltwater increasing pore water pressures. Thus, seasonal temperature effects, coupled with unusually wet weather conditions, may have triggered the past two landslides at Yate. Long periods of intense rainfall, as well as snowmelt, are a well documented cause of deep-seated, rather than surficial, landslides, where the pore water pressure in a body of fractured rock is elevated to failure thresholds [e.g., Schuster and Wieczorek, 2002]. Yate may have approached critical failure conditions over several decades, perhaps linked to retreating summit ice. Although Yate is situated within the rupture zone of the May 1960 (M_W 9.5) subduction zone earthquake, and in spite of the earthquake magnitude, this earthquake did not initiate slope failure at Yate. Elsewhere in the region, widespread landslide generation was observed following this earthquake [e.g., Davis and Karzulovíc, 1963, Dobrovolny et al., 1963]. Subaerially these were predominantly small events, but the earthquake also generated a large turbidite in the Reloncaví fjord, at the Puelo river estuary, immediately north of Yate [Chapron et al., 2006]. The lack of triggering at Yate suggests that, subaerially, large earthquakes are most likely to trigger shallow, small landslides in these settings, given the large distance of the rupture from the volcanic arc (approximately 150 km). Earthquake triggering of larger, deep-seated landslides such as the 1965 failure at Yate may depend on pre-conditioning of the failure region through other processes, such as high rainfall. Increases in pore-water pressure, following snowmelt or intense rainfall, are likely to be of primary importance for such events, but if such a situation is obtained, then large earthquakes may provide an immediate trigger.

In the longer term, hazards of this type may increase on glaciated volcanoes. Glacier retreat between 1961 and 1982 is evident on aerial photographs from those dates (Figure 4.3), and has been observed at many southern Andean volcanoes over the past 50 years [Carrasco et al., 2005, Rivera et al., 2005]. There is not such a clear change in snowline in aerial photographs from 1944 and 1961, suggesting that glacial retreat may have accelerated at Yate in the latter half of the 20th century. In addition to seasonal or shorter-term changes in pore water pressure due to weather conditions, a longer-term increase in meltwater production may destabilize slopes. Furthermore, stress release associated with debuttressing of slopes following ice load removal may condition bedrock for failure [Cossart et al., 2008], while also exposing mechanically weathered rock to further degradation, potentially increasing the likelihood of large landslides. Increased rain rather than snowfall, due to warmer conditions, may further destabilize upper slopes through increased erosion.

Debris flows at Yate appear to have occurred throughout post-glacial time, with evidence for multiple events in recent centuries. The factors resulting in recurring collapses at Yate, without significant magmatic renewal and edifice growth, may be distinct from those that cause significantly larger sector-collapse debris avalanches at many volcanoes. Large Neogene sector-collapses are well documented at several Central Andean volcanoes [e.g., Richards and Villeneuve, 2001], with many occurring near the end of the last ice-age. An example is that at Parinacota (est. 6 km^3 [Clavero et al., 2002, Hora et al., 2007]), which may in part have been induced by rapid deglaciation. At Yate there is no evidence for events significantly larger than that in 1965. The 1965 landslide volume is over an order of magnitude smaller than many volcanic sector collapses, the largest of which may have a repeat time of 1:10 kyr [Ui et al., 2000]. However, many volcanoes produce repeated landslides in combination with larger flank failures. For example, Mount Meager, British Columbia, Canada, has undergone three flank collapses of $> 10^8$ m^3 in the last 7.5 kyr, possibly associated with eruptions [Friele et al., 2005], in addition to numerous smaller landslides. Mombacho, Nicaragua, has displayed similar behaviour [Shea et al., 2008]. However, the apparent frequency of landslides at Yate of $\leq 10^2$ yr for events of 10^6–10^7 m^3 is notably high given the lack of volcanism. Landslides of this scale and frequency, originating at the headwalls of erosive features commonly related to structural instabilities, may be common to many volcanoes, and may constitute a similar, if not greater, cumulative destructive potential for life and property than that posed by larger landslides or sector collapses. To summarise, it appears likely that Yate's sprawling, glacially eroded, composite edifice, its relatively low level of late-Pleistocene and Holocene magmatic activity, and its tectonic situation, resulting in deeply incised orientated valleys, may all be contributing factors to such rapid edifice destruction behaviour in discrete large landslides. However, it is possible that the frequency derived from historical records is atypical, and that current landslide rates are high, and potentially increasing, due to melting of summit glaciers.

4.6 Conclusions

The edifice of Yate, a glacially dissected stratocone, has failed in post-glacial time through a series of mass movements, generating debris flows that reach the coast to the north and approach Lago Cabrera to the south. The largest historical event occurred on 19th February 1965, when a rock face collapsed around a 1.3 km wide amphitheatre and generated a debris flow. The failed material comprised ice and weathered lavas and pyroclastic rocks, with estimated volume of $6.1\text{-}10 \times 10^6$ m^3. Fifteen days of heavy rain prior to the landslide is likely to have provided the immediate cause of failure.

The 1965 debris flow travelled 7500 m to reach the shore of Lago Cabrera, an intermontane lake, descending 1490 m in height. Maximum velocity, before deceleration and deposition, is estimated to have been 40 m s^{-1}. Total deposit volume, including entrainment and bulking, is estimated at $1.5\text{–}2.7 \times 10^7$ m^3, at least 50% of which came to rest subaerially. Part of the flow deposit (an estimated volume of $9 \pm 3 \times 10^6$ m^3) entered the eastern end of Lago Cabrera, producing an impulse wave that caused extensive damage around the lake and killed 27 people living at the southwest shore of the lake. Field evidence and calculations indicate a tsunami wave height of approximately 25 m with a vertical run-up at the southwest shore of approximately 60 m.

The orientation of landsliding at Yate forms an angle of 10° in the Riedel shear direction with the line of the dextral strike-slip Liquiñe-Ofqui fault zone (LOFZ), on which the volcano is constructed. This orientation corresponds closely to modelled failure directions of volcanoes on strike-slip faults [Lagmay et al., 2000], and is consistent with tectonically mediated collapse.

Movement on the LOFZ during the lifetime of the volcano is likely to have imposed an orientated weak tectonic fabric. This pattern may have been subsequently enhanced by glacial erosion, leading to preferentially orientated glacial valleys, and generating a feedback mechanism with collapses followed by further rapid glacial erosion, and accelerating the rate of edifice incision through repeated landslides. Additionally, post-glacial ice retreat and subsequent erosion after debuttressing may have rendered the upper slopes of thick lavas overlying pyroclastic rocks unstable, promoting mass wasting. Shrinkage of summit glaciers in recent decades, increased meltwater, and greater volumes of rainfall, rather than snow, may have augmented the conditions necessary for failure in 1965 and 2001, and may increase the likelihood of similar future events as summit glaciers melt further.

Several southern Chilean volcanoes lie on the LOFZ, and numerous volcanoes globally are situated on strike-slip faults. Many of these volcanoes may be susceptible to edifice collapse in orientations controlled by fault systems. Although volcanic landslide frequency may have increased immediately after late-Pleistocene deglaciation due to processes associated with rapid climatic change [cf. Capra, 2006], the hazard from similar events is still present. While the long-term rates of edifice collapse cannot be esimated in this case, continued melting of summit glaciers and increasing amounts of higher altitude rainfall, rather than snow, as a consequence of a warming climate, may increase the frequency of large landslides in these environments, particularly on volcanoes where the substrate is mechanically weakened, hydrothermally altered, or poorly consolidated, and especially in settings where orientated structural instabilities exist, such as strike-slip fault zones. Recognition of deposits from these events and awareness of the hazard to settlements in vulnerable areas are important in mitigating future disasters, particularly when debris flows may interact with water bodies.

This chapter is an updated version of: Watt, SFL, DM Pyle, TA Mather, RS Martin, NE Matthews, 2009. Fallout and distribution of volcanic ash over Argentina following the May 2008 explosive eruption of Chaitén, Chile. Journal of Geophysical Research 114, B04207, doi:10.1029/2008JB006219, which was published by the American Geophysical Union, and which is available at http://www.agu.org/journals/jb/jb0904/2008JB006219/. The American Geophysical Union have granted permission for this chapter to be made available in ORA.

Chapter 5

Tephra fallout from the May 2008 Chaitén eruption[1]

5.1 Introduction

On May 2nd, 2008 a large explosive eruption began at Chaitén volcano (42.8° S), without recognised warning and preceded by little precursory seismic activity [Lara, 2009]. The event was the largest explosive eruption globally since that of Hudson, Chile, in August 1991, and as such it provided a rare opportunity to track the long-range dispersal and deposition of fine volcanic ash, using both remote [e.g., Carn et al., 2009] and field-based methods. The eruption was particularly notable, since the last identified activity at Chaitén (Cha1; Naranjo and Stern, 2004, Chapter 6) was thought to have occurred at ~9.8 kyr. Furthermore, Chaitén produced the first explosive rhyolitic eruption [e.g., Castro and Dingwell, 2009] since Novarupta, Alaska, in 1912. The eruption had immediate social and economic impacts across southern Chile and Argentina, with more than 5000 people evacuated from settlements up to 75 km from the volcano, and extensive ash deposition leading to regional disruption of agriculture and aviation.

The most energetic phase of eruption occurred during the first week. Following this explosive phase, dome growth initiated, with minor explosions and a continuous vapour-rich plume, and is continuing at the present day (February 2010). Ash clouds produced during the initial phase of eruption were transported eastwards, depositing tephra across Chile and Argentina. Such deposition across a continental area allows detailed mapping of ash distribution, potentially leading

---

[1] Much of the material in this chapter is published in Watt et al. [2009b], *Journal of Geophysical Research*.

to insights regarding ash transport processes, important for the accurate calibration of ash dispersal and forecasting models [e.g., Folch et al., 2008], and environmental impacts [e.g., Martin et al., 2009]. The possibility of mapping ash deposition over such a wide area is unusual, with the few previous instances including eruptions at Mount St. Helens (1980; Carey and Sigurdsson, 1982), Hudson (1991; Scasso et al., 1994) and Ruapehu (1996; Bonadonna and Houghton, 2005). This chapter summarises the results obtained through detailed mapping of the Chaitén ash deposit in Argentina, where the unit was thin and fine-grained. Although volumetrically large, it is this fraction of tephra deposits that is most rarely preserved and which is commonly very poorly constrained in past eruption reconstructions.

5.1.1 Early stages of eruption

Using satellite imagery of the ash-rich eruption plume (MODIS; Moderate Resolution Imaging Spectroradiometer; http://modis.gsfc.nasa.gov) and contemporary reports [Folch et al., 2008] a summary of the direction of ash cloud dispersal during the early phases of the Chaitén eruption has been produced (Figure 5.1).

Activity was most vigorous during the first week of eruption, beginning with an energetic phase on 2nd May, for which contemporary reports estimate a column height of 15 km. The plume from this episode was directed SE across the Andes, with sharp edges, before becoming more dispersed and drifting northward towards the Argentinean city of Bariloche (Figure 5.1). This was followed by a sustained explosive phase, with a lower column height (estimated at 10 km or less), beginning on 3rd May. This phase formed a continuous, linear, sharp-edged plume, moving SE and travelling beyond the Atlantic coast of Argentina (Figure 5.1). The intensity of this phase may have been variable, but by 5th May a similarly continuous, linear plume had an easterly orientation, with dispersed ash clouds reaching across the Atlantic Ocean and others drifting northward along the Atlantic coast of Argentina. On these images ash deposition is visible on the ground, with a dense grey coverage in the region around Esquel (Figure 5.1), arising from the 2nd May phase, but no clear evidence of ground-deposition as far as Bariloche. Similarly, ground deposits of ash are visible south of the 5th May plume, and are presumed to result from the 3rd–4th May plume. The edges of these visible deposits are summarised on the map in Figure 5.1.

On 6th May the eruption entered a more intense but short-lived phase, with column height estimates of up to 30 km, producing a cloud that drifted NE across the Andes, before spreading

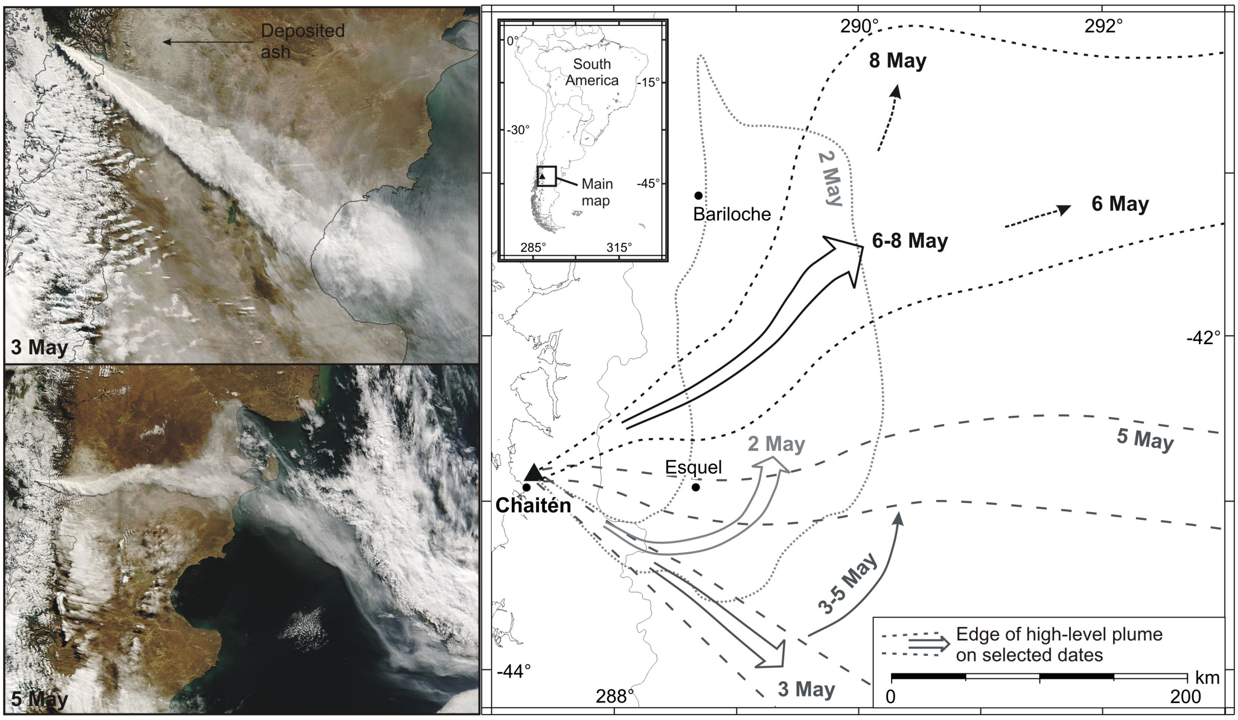

Figure 5.1: Ash cloud dispersal from the Chaitén 2008 eruption. MODIS satellite images are shown from the 3rd and 5th May, 2008, with the cloud reaching across Argentina and far over the Atlantic Ocean after three days of eruption. The grey patches on the ground beneath the cloud on images are deposited ash. The map on the right has been produced using these images to provide a summary of cloud distribution directions during the most vigorous stages of eruption.

eastwards and then ENE across Argentina. A second burst later in the day resulted in similar plume trajectories, and ash fallout the following day occurred as far as 1000 km from source [Folch et al., 2008]. A further explosive phase, of unknown intensity, occurred on 8th May, with transport directions corresponding closely to those of the 6th May. Extensive ash deposits from the 6th–8th May episodes are seen on the 12th May MODIS image to reach the Atlantic coast of Argentina. Explosive activity continued, but with much lower plume heights in the range of 2–5 km, throughout the following months. There is little evidence that this subsequent activity resulted in measurable fallout in Argentina, except for minor ash-fall observed in the border regions on 30th–31st May, and the volume of distal ash fallout in Argentina from this continuing activity is considered negligible in comparison to the 2nd–8th May period.

5.2 Sampling methods

In order to measure and sample the distal ash deposit, fieldwork was conducted across affected regions of Argentina between 30th May – 11th June 2008. Deposition patterns obtained from MODIS images was used to guide sampling. Ash samples and thickness and mass-loading measurements were taken at 227 sites transecting the deposit (Figures 5.2 and 5.3), with full site details provided in Appendix G.

Heavy rainfall in mid-May had disturbed the deposit in places. In such locations, measurements were taken in protected spots or by taking an average thickness across the site. At higher elevations snowfall disturbed the deposit to a lesser extent. The ash formed a continuous surface crust at thicknesses >0.5 mm; below this, wind erosion resulted in patchy preservation. There was clear evidence in most areas of the influence of rain and wind erosion on the deposit, particularly where the deposit was thinnest, and preservation here was restricted to sheltered pockets, such as pits in rock or pieces of refuse. Care was taken at such sites to take measurements and samples from such locations. In some cases a degree of accumulation had occurred in these sheltered spots due to rain-washing, and in these cases an average site measurement was produced by estimating the area of washing-in (in as many places as possible). Thus, while the deposit was no longer pristine in many areas, because the removal or reworking of ash by wind and water action had not been wholesale and by carefully selecting sampling sites it was still possible to take measurements. Some winnowing of fine particles, as well as some deposit compaction, may have occurred, though the degree to which this may have taken place is not clear. Using these methods, the deposit

Figure 5.2: Photographs of the distal ash deposit in May and June 2008 (taken between 30th May and 10th June 2008, by N.E. Matthews). **A** (43.174°S, 71.753°W) Deposit 40 km south of Esquel, showing continuous ground cover. In spite of wetting of the deposit, possibly by snowmelt, ash has not been washed off local topographic highs. **B** (43.173°S, 71.751°W) Continuous cover and accumulation in grass, south of Esquel. **C** (42.949°S, 71.218°W) Sample collection near Esquel. **D** (43.035°S, 70.588°W) Ash fall outlined around removed stone, 60 km east of Esquel. **E** (41.804°S, 70.795°W) Ground crusting of ash fall into two layers (possibly from 2nd and 6th May units) near Ñorquinco. **F** (43.325°S, 70.896°W) Ground crusting of deposit 20 km north of Tecka. **G** (42.321°S, 71.133°W) Ash washed around the base of stones, 30 km south of El Maitén. **H** (40.825°S, 65.375°W) Distal preservation in grooves of tyre, 40 km west of San Antonio Oeste, and 640 km from Chaitén volcano.

was mapped self-consistently to low ash thicknesses, adopting as a minimum criterion [cf. Martin-Del Pozzo et al., 2008] an assigned thickness of <0.1 mm where ash was detectable only as a pale dusting on stiff leaves. Both local people's estimates of fresh ash-fall thickness and that estimated from coupled meteorological and dispersal models [Folch et al., 2008] correspond well with the data obtained here. In some cases a discrepancy exists, with these measurements being slightly lower than fresh thickness estimates. This is likely to be a result of closer particle packing and settling of the deposit upon wetting by rainfall, resulting in a thinner, but denser deposit, when compared to the fresh ash-fall.

5.3 Ash deposit analyses

Ash thicknesses have been plotted on isopach maps, showing lines of constant deposit thickness (Figure 5.3). The mapping reveals a complex distribution pattern, corresponding closely to plume transport directions during different phases of the eruption. The deposit edges inferred from MODIS satellite images (Figure 5.1) lie slightly outside the 0.1 mm isopach, validating the interpretation that thin, fresh ash-fall units are observable remotely. This correspondence of the mapped ash distribution with the edges of fresh ash-fall observed using satellite imagery indicates that wind-driven remobilization and redeposition of ash had not affected the deposit over spatial scales large enough to alter the primary distribution. When mapped, the measured thickness values show a highly self-consistent pattern, decaying with distance. This suggests that, in spite of reworking and removal of ash in many locations, the approach of selecting sheltered localities and taking site averages of thickness was valid. A more erratic pattern would be expected if removal, redeposition and accumulation had affected the measurements to a significant degree.

Individual eruption phases produced discrete ash units, which overlap in a complex fashion in medial regions (<200 km from the vent). In more distal locations (>200 km from the vent), ash fallout from discrete eruptive phases may be distinguished when transported over areas without previous ash-fall (e.g., 3rd and 6th May; Figure 5.1). This complexity is the result of multiple eruption phases occurring over a time period sufficient to encompass changes in wind conditions.

The total area enclosed by the 0.1 mm isopach is $\sim 1.7 \times 10^5$ km^2. In comparison with previously studied explosive eruption deposits, this is much larger than that of the Fuego 1974 deposit ($\sim 3 \times 10^3$ km^2; Rose et al. [2008]), but comparable to the 1980 Mount St. Helens eruption ($\sim 3 \times 10^5$ km^2; Sarna-Wojcicki et al., 1981, Bonadonna and Houghton, 2005). The 1 mm isopach

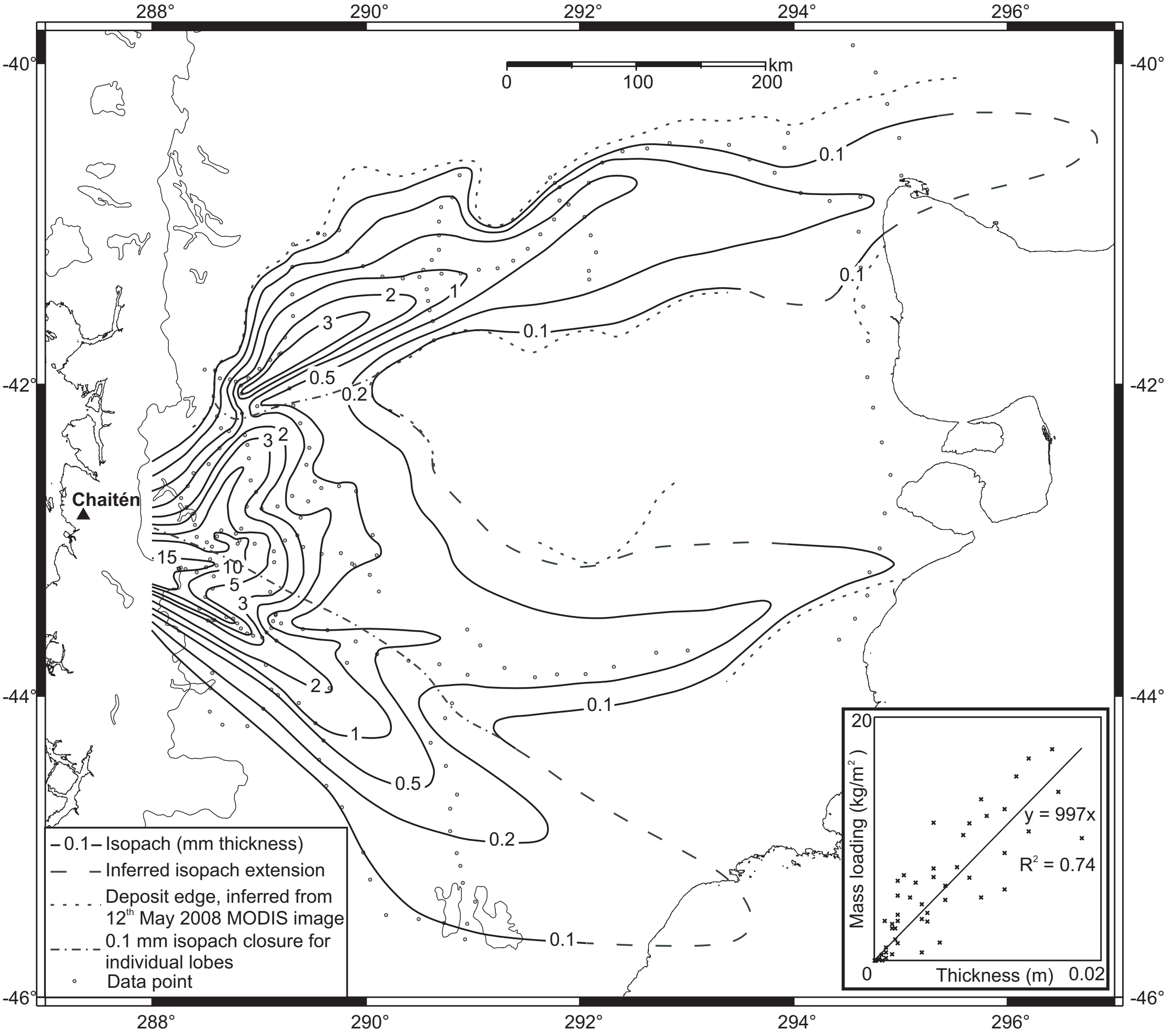

Figure 5.3: Isopach map of the Chaitén distal ash deposit. Isopachs are drawn by hand and extended to the approximate Andean watershed (288° longitude). Individual ash-falls are identifiable distally, for example from the 3rd (southernmost) and 6th May (northernmost), but in the Argentinean border regions units overlap, with an additive thickness effect. Deposit edges, inferred where possible from satellite images, correspond with and fall slightly outside the mapped 0.1 mm isopach. The inset graph plots field measurements of mass-loading against ash thickness. The linear relationship allows an estimation of deposit density, at 997 kg m^{-3}.

area (2.9×10^4 km^2) suggests that the Chaitén eruption was an order of magnitude smaller than that of Hudson, 1991 (1.1×10^5 km^2; Scasso et al., 1994). However, such thickness-based comparisons should be treated with a degree of caution, since the measurements described here potentially reflect a degree of post-depositional compaction, and may not be directly comparable to fresh measurements made for other fall deposits. Such comparisons may therefore slightly underestimate the scale of the Chaitén eruption.

The bulk deposit density at the time of sampling, estimated from sites where weighed samples were collected over measured areas, indicates a mean of 997 kg m^{-3} (Figure 5.3), and is within the range expected for a rhyolitic ash-fall deposit. The fresh deposit (i.e. prior to rainfall) is likely to have had a slightly lower bulk density than the deposit measured in the field. If the only post-depositional change to the deposit is an increase in bulk density, then this does not affect the mass or dense-rock-equivalent volume estimates. Therefore, quoting eruption size in terms of mass and deposition in terms of mass-loading is more meaningful, and more readily transferable for the purpose of inter-event comparisons, than magnitudes based on tephra thickness or volume alone.

5.3.1 Volume calculations

Using plots of the logarithm of ash thickness, T, against the square root of isopach area, A (Figure 5.4) ash-fall volumes have been calculated by integration [Pyle, 1989, Fierstein and Nathenson, 1992, Pyle, 1995]. On such plots, straight-line segments are defined by exponential decay, describing an exponential cone:

$$T = T_0 \exp\left(-kA^{0.5}\right) \tag{5.1}$$

where k is the line slope and T_0 is the maximum deposit thickness. Integrating below the cone to find V gives:

$$V = 2\left(T_0/k^2\right) \tag{5.2}$$

To account for multiple straight-line segments, resulting from increasingly rapidly decaying proximal deposit thicknesses, a correction p is applied to each of N segments, deriving [from Pyle, 1995]:

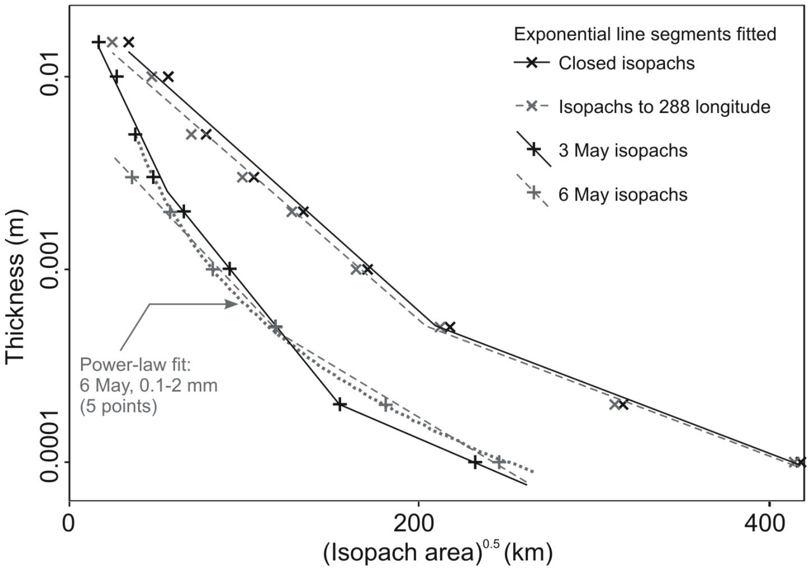

Figure 5.4: Isopach area against thickness plots. Straight line (exponential) segments are fitted, with a power-law fit also shown for the 6th May deposit. Areas for the whole deposit were found by closing mapped isopachs around the volcano location, while extrapolation of distal isopachs distinguished the 3rd and 6th May deposits as separate units, such that the 6th May deposit centres around a secondary maximum and the 3rd May closes around the volcano. More rapid proximal thickening (a steeper line segment) is likely in all cases and is necessary to prevent the 3rd May segment, when extrapolated back, from projecting above the whole-deposit data.

$$p_N = \frac{2}{k_{n+1}^2}\left\{T_{n+1} - T_x\left(1 - \ln\left(\frac{T_x}{T_{n+1}}\right)\right)\right\} - \frac{2}{k_n^2}\left\{T_n - T_x\left(1 - \ln\left(\frac{T_x}{T_n}\right)\right)\right\} \tag{5.3}$$

where n and $n+1$ represent values obtained from the line-segment at distances larger and smaller than the break in slope, respectively, and T_x is the deposit thickness at the break in slope. Thus, using T_0 and k from the most distal straight-line segment, total deposit volume is:

$$V = 2\left(T_0/k^2\right) + p_1 + \ldots + p_N \tag{5.4}$$

From Fierstein and Nathenson [1992] the volume inside a particular isopach of area A is found using:

$$V = \left(2T_0/k^2\right)\{1 - (kA + 1)\exp(-kA)\} \tag{5.5}$$

and a correction p must again be applied where necessary.

All the mapped isopach data can in this case be approximated by two or three exponential segments, as commonly observed for explosive eruption deposits [Pyle, 1989, Bonadonna and

Table 5.1: Estimates of eruption volumes and magnitudes.

	Whole deposit (isopachs closed)[a]	Whole deposit (mapped area[b])	3rd May lobe[c]	6th May lobe[d]
Volume (exponential; km^3)[e]	0.17	0.15	0.05	0.03
Volume (power-law; km^3)[e]	-	-	-	0.04
Magnitude [Pyle, 2000]	4.24	4.19	3.69	3.54
Volume inside 0.1 mm isopach[e]	0.16	0.14	-	0.03
Total grain size mode(s) (μm)	-	-	46	30; 115
Total grain size 98th percentile (μm)	-	-	320	435

[a] These estimates are minimum values. An increased rate of proximal thickening is likely, and, for example, a maximum deposit thickness of 1 m would increase the volume to 0.24 km^3 and the magnitude to 4.37.

[b] Isopachs mapped to 288° longitude.

[c] Isopachs closed around volcano.

[d] Estimates based on deposit centred around the secondary maximum in Argentina, thus not directly comparable to data calculated for isopach closure around the volcano.

[e] Volumes, in km^3, can be converted to mass, in kg, by multiplying these values by 10^{12}.

Houghton, 2005] (Figure 5.4). This leads to an estimate of 1.6×10^{11} kg of ash deposited over Argentina, equivalent to a tephra volume of 0.16 km^3 or a dense rock equivalent volume of 0.07 km^3, assuming a density of 2350 kg m^{-3} for crystal-poor rhyolite. Similarly, a minimum total tephra volume of 0.17 km^3 (Table 5.1; a mass of 1.7×10^{11} kg) is estimated. This estimate projects the thickening rate derived from the mapped regions in Argentina to the volcano location but in reality, based on observations elsewhere [Pyle, 1989, Bonadonna and Houghton, 2005], more rapid proximal thickening is likely. For example, assuming proximal thickening to a maximum of 1 m, based on events of similar magnitude, a total tephra mass of 2.4×10^{11} kg is produced, using the same density for the proximal deposit as for the distal. Although the proximal thickening rate is unconstrained, this estimation demonstrates the potential uncertainty in eruption volumes produced using only distal data. Overall, this suggests that ~70% of ash, by volume, produced by the eruption fell east of 288° longitude, over Argentina and the Atlantic Ocean.

The 6th and 8th May eruptive phase, as described in Section 5.1.1, involved up to three short-lived energetic explosions, with similar plume transport directions. The relative intensity of these episodes is unclear, but the 8th May cloud may have drifted northward in mid-Argentina [Folch et al., 2008], rather than following the easterly direction of the 6th May (Figure 5.1). For simplicity, this northern depositional lobe is referred to as the 6th May deposit. This produced a 0.1 mm isopach extending up to ∼800 km from the volcano, which accounts for 22% by volume of the mapped Argentinean ash-fall, forming closed isopachs around an isolated maximum ∼200 km NE of Chaitén. This unit, mid-grey in colour, was distinctively coarser in mid-Argentina than the paler deposit resulting from earlier eruption phases, and thinned (but did not fine) towards the Andean region. Given these field observations and the mapped isopach dispersion patterns, it is likely that the isolated isopachs represent a secondary thickness maximum, rather than arising simply from overlap with the 2nd May fallout, although this may have added complexity to the distribution. If this is the case, more proximal thickening is likely to occur in the unmapped region towards the volcano. Such a feature may arise from fine-particle aggregation [Carey and Sigurdsson, 1982, Brazier et al., 1983], resulting in a larger effective grain size, due to ash interaction with frozen or liquid hydrometeors [Textor et al., 2006, Durant et al., 2008]. The less explosive 3rd May eruptive phase produced 0.05 km^3 of tephra, dispersed by strong winds (Figure 5.1) and depositing ash in a sharp-edged linear lobe. The complex distribution of the 2nd May deposit, affected by later ash overlap (Figure 5.1), does not permit its volume to be estimated.

From the volume estimations, <8% of the whole deposit volume lies beyond the 0.1 mm isopach, increasing to 14% for the 6th May unit. This may reflect a higher 6th May eruption column, but is potentially an artefact of deposit overlap elsewhere, thickening distal ash-fall through repeated or long-lasting deposition. These estimates are made on the basis of extrapolating the most distal exponential segment. It is not clear whether thickness decay remains exponential at distances beyond a few hundred km, since the grain size distribution may change very little at such distances, with meteorological factors potentially having a significant effect on particle sedimentation.

Athough a multiple-segment exponential decay model fits the data for the whole deposit well (Figure 5.4) and has a sound physical basis, with a maximum thickness decaying to zero, individual units are not described by a single exponential segment. This may reflect depositional complexities, whereby multiple phases occur within an apparent single mappable unit, or changing controls on particle settling and diffusion with changing distance, grain-size and Reynolds number [Ernst et al., 1996, Bonadonna et al., 1998].

For tephra deposits with few distal data points the extrapolation of a proximal exponential segment can produce volume underestimation [Bonadonna and Houghton, 2005], and a power-law relationship may better represent the deposit:

$$T = T_{PL} A^{-m/2} \tag{5.6}$$

Here, T_{PL} is a constant and m is the power-law coefficient. Deposit volume is found using:

$$V = \left(2T_{PL}/\left(2-m\right)\right)\left(C^{2-m} - B^{2-m}\right) \tag{5.7}$$

where B is defined by the maximum thickness predicted from the exponential relationship, such that $B = (T_0/T_{PL}) - 1/m$ and C is the downwind distance limit of volcanic-cloud spreading, assessed from satellite images [Bonadonna and Houghton, 2005].

As expected from its temporal and spatial complexity, a single power-law does not fit the whole Chaitén deposit. However, a power-law curve fits the 6th May unit (Figure 5.4; the inner-point misfit may be attributed to a lack of proximal data). Estimating downwind plume dispersion, C, of 800 km, a volume 19% larger than that found using exponential segments is produced. Again, it is unclear whether a single power-law would be expected to hold at the most distal locations, where factors influencing fallout are likely to change. Problems also arise in this method through the subjective selection of integration limits, particularly C, and the exponential segment method is thus considered the most appropriate in this case, providing a good fit to the data and requiring the fewest assumptions.

In summary, the estimated volumes and bulk ash density of 997 kg m^{-3} indicate a minimum deposit mass of 1.7×10^{11} kg, or an eruption magnitude (defined as magnitude = $\log_{10}$(erupted mass, kg) – 7; Pyle, 2000) of >4.2 (Table 5.1). This confirms that Chaitén was the largest explosive eruption globally since Hudson, 1991.

5.3.2 Deposit grain size

Grain size was measured for 140 samples by laser-diffraction size analysis, using a Malvern Mastersizer 2000 with Hydro-MU attachment, with measurements assuming a refractive index of 1.52 and absorption coefficient of 0.1. Replicate samples from 13 sites showed good reproducibility of distribution shape and mode positions. Analyses of samples contaminated by dirt, recognizable by containing anomalous coarse grain size modes, or with skewed size distributions resulting from post-depositional erosion were rejected. Several samples showed bimodality and very few produced a smooth lognormal shape, with many unimodal curves being skewed or showing a shoulder on one or both limbs, potentially indicating multiple populations within a single grain size distribution.

5.3.2.1 Unit characteristics and total grain size

Modal grain size, a precisely measurable parameter, generally unaffected by coarse particle contamination, was used to construct isopleth maps, showing lines of constant grain size (Figure 5.5), and based here on the modal (rather than maximum) grain size. For multi-modal distributions, the coarsest mode was selected to produce isopleths. The various units distinguished correspond well with mapped isopachs (Figure 5.3). The 6th May modal grain size trend shows exponential decay with a single line segment (analogous to the plots used for isopach area; Figure 5.4). However, without sufficient data from other units, this cannot be confirmed as a general case. West of the 6th May thickness maximum grain size increases as thickness decreases. In some of these medial areas the 6th May modal grain size exceeded thickness, and the deposit was visible as scattered white pumices up to ~1 mm in diameter, lying on earlier ash-fall. The ubiquity of this feature in these localities and the strong bimodality of grain size distributions in this region, with a prominent fine mode, indicates that this does not result from winnowing of fine material. This demonstrates that the overlap of deposits from different eruption phases is one mechanism characteristic of the Chaitén deposits that leads to multiple populations within a single grain size distribution.

The 6th May unit shows grain size bimodality, with modes at a stable ~25 µm and at a coarser value, which decreases steadily with distance from ~300 µm, such that the modes merge in a unimodal distribution ~400 km from the volcano (Figure 5.5).

There are several possible explanations for this complexity in grain size distribution shape. One is that, in addition to the buoyant column, a co-ignimbrite cloud may have been present during individual eruption phases. This could give rise to tephra populations of different granulometries, in clouds at different heights. However, such an explanation is not necessary to explain the complex tephra dispersal pattern, since this is well accounted for by the changing wind conditions during several days of eruption. Furthermore, there is not at present clear evidence from the region around Chaitén for the occurrence of large-scale pyroclastic flows sufficient to generate co-ignimbrite clouds of sufficient size to produce this feature. Therefore, it is likely that the grain size distribution complexities arise both from multiple deposit overlap and from fine-particle aggregation processes. For example, the 6th May deposit overlaps with those from earlier days in the medial region north

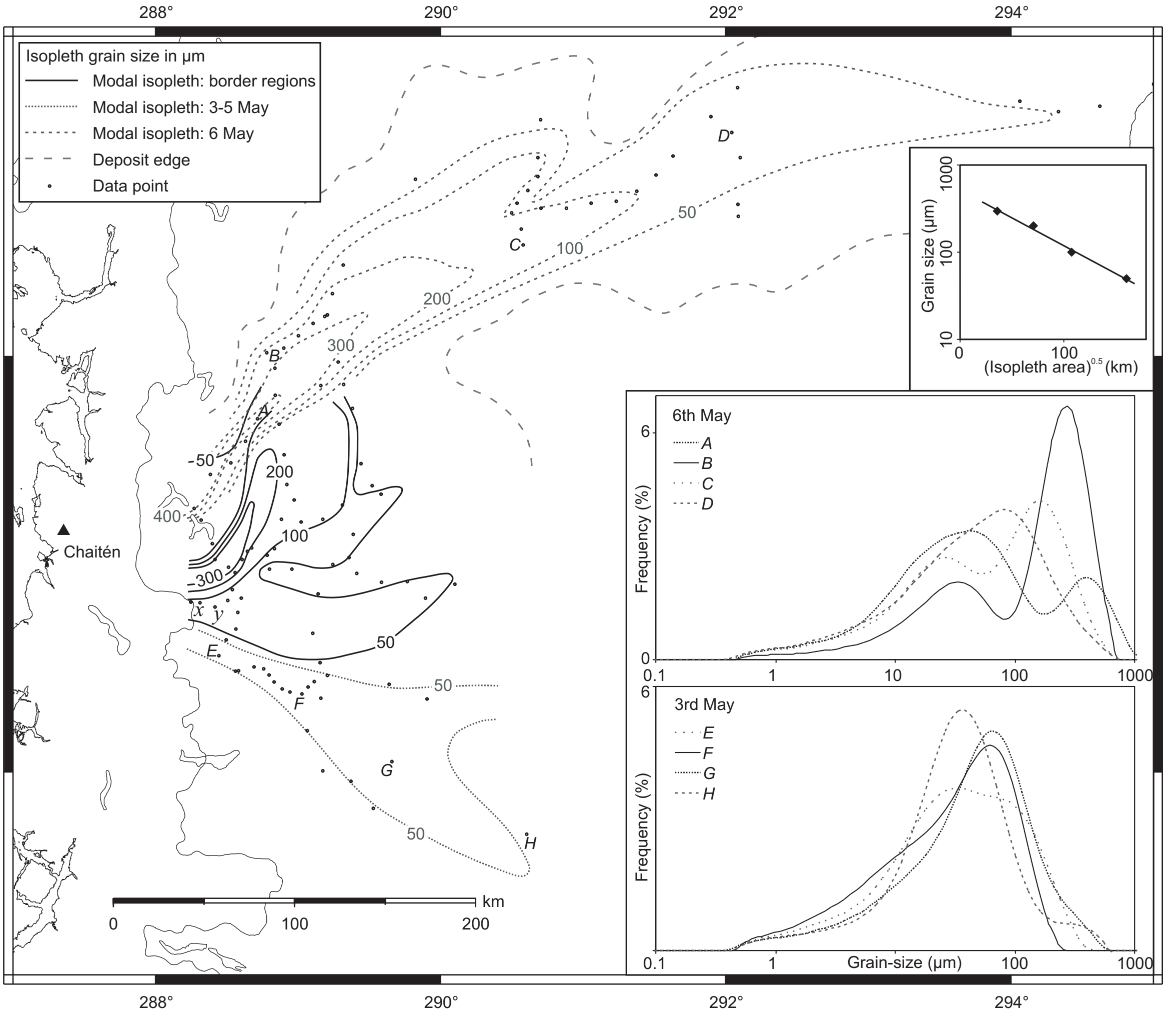

Figure 5.5: Isopleth map and grain size distributions. Isopleths are drawn for modal grain size, with sample sites marked as black dots. For bimodal distributions the coarser mode is used. Isopleths are distinguished for the 3rd–5th and 6th May deposits, and for the remainder of the deposit, resulting from complex deposit overlaps but dominated by the 2nd May fallout which, with the 6th May, is far coarser than intervening ash-falls. The top inset plot shows ln(grain size) against (area)$^{0.5}$ for the 6th May isopleths, showing an exponential decay in coarse mode grain size. The lower plots show grain size distributions for selected sites from the 3rd and 6th May fallouts, at locations marked on the main figure. The bimodality and distance-related decay for the 6th May contrasts with the relatively stable unimodal character of the 3rd May. Curve *E* shows bimodality due to overlap with finer deposits in the border region, while curve *H* may suffer from both coarse contamination and fine-particle removal through wind erosion, a problem encountered in thinner distal deposits. Locations marked *x* and *y* on the main map refer to Figure 5.8.

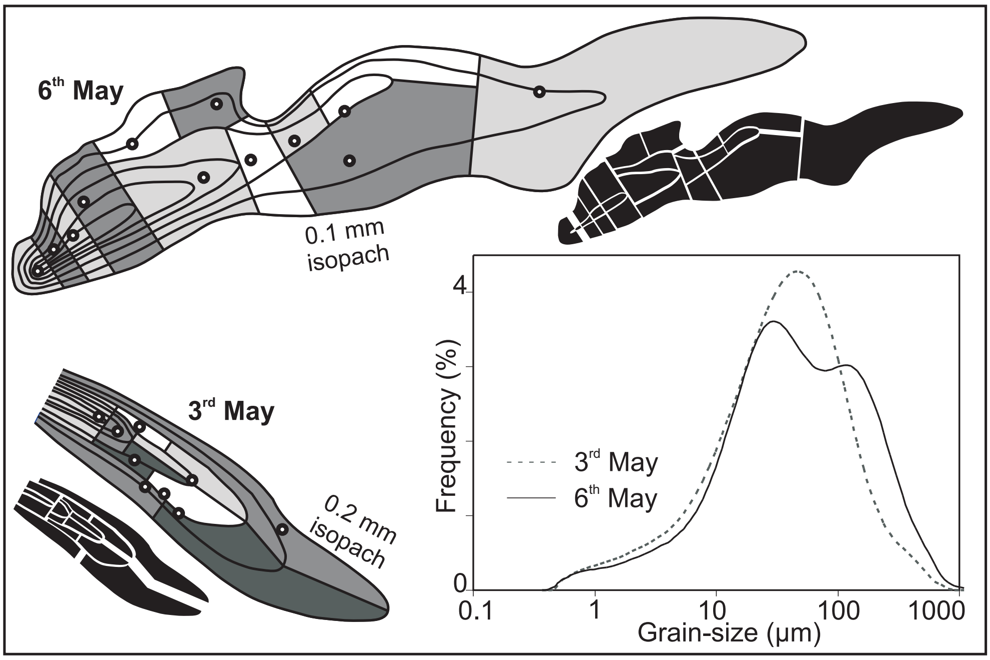

Figure 5.6: Distal deposit total grain size distribution. Separate estimates have been made for the 3rd and 6th May units. Shaded maps, showing isopachs for these units, were divided into sectors as shown, around selected points (black ringed circles), which were then used to estimate total distal deposit grain size. Further sector subdivisions, by isopachs, are shown in the silhouettes. These areas were used to weight each selected grain size distribution using an assigned thickness based on the geometric mean of the enclosing isopachs.

of Esquel (Figure 5.1), and here some of the complexity of shape is due to this overlap. In addition, the unit itself is the product of two or three similar explosive pulses, potentially introducing further overlap-type complexities.

The finest mode seen in the 6th May deposit may reflect a different process, of fine-particle aggregation. Both the stability of this peak with distance, remaining static at ∼25 μm, and its fineness (e.g., when compared to the 3rd May deposit at similar distances) points to the possibility that aggregation led to volumetrically large proportions of fines falling out relatively early. Grain size data identified from the 2nd May deposit show similar features. In contrast, ash-falls from the 3rd–5th May are finer and unimodal, fining only gradually with distance, with a highly consistent distribution shape and a mode, at ∼60 μm, coarser than the fine mode of the bimodal units. This suggests a sustained activity level from 3rd–5th May, with a lower column height than the more intense 2nd and 6th May phases. Cloud height differences may explain the lack of a clear aggregation-type signature in the 3rd–5th May deposits, if higher eruption clouds result in more efficient fine-particle aggregation and scavenging through frozen hydrometeor interactions [e.g., Durant et al., 2008].

Total grain size distributions (Figure 5.6) for the tephra deposited over Argentina have been estimated for the 3rd May (15-2 mm isopach range) and 6th May (down to 0.1 mm thickness) units by dividing the deposit into sectors around selected sites, a modification of the method of Carey and Sigurdsson [1982]. Given the wide coverage but relatively sparse distribution of mapped data-points, particularly in the most distal regions, this method was selected over alternatives [e.g., Bonadonna and Houghton, 2005]. Sectors were separated perpendicular to the deposit axis, where possible at the midpoint of successive sites or at the nearest mapped isopach. Sectors were then split based on isopachs, and each subdivision received a representative thickness using the geometric mean of the enclosing isopachs. The product of subdivision-area and thickness gave a weight to the grain size distribution of a particular sector, the sum of which then provided a total grain size distribution estimate. The data confirm a finer 3rd May deposit, and show bimodality in the 6th May fallout (Table 5.1).

With respect to respiratory hazard [Horwell and Baxter, 2006], both deposits have similar total proportions of thoracic ($<$10 µm) material. For the 6th May this increases from 10% in the border regions to 20% distally, and is generally 20–25% for other units, approaching 30% distally. The respirable ($<$4 µm) proportion varies similarly, ranging from 5% in medial regions of the 6th May unit to 15% in other distal areas, a similar proportion to that in Mount St Helens' 1980 ash at comparable distances [Durant et al., 2009]. However, importantly for health concerns, locally resuspended ash is likely to contain a greater proportion of fine material than that estimated for the whole deposit [Martin et al., 2009].

5.3.2.2 Post-depositional erosion

Winnowing of fine material, by either wind or water erosion, may have affected the grain size distributions of samples, even if such processes did not clearly alter the thickness measurements, since any removal of material is likely to be selective towards the finest particles. One feature of these data, which suggests the collected samples are representative of the original material, lies in the consistency seen in distribution shape over large areas, such as those for all samples of the 3rd May depositional lobe (Figure 5.5). In contrast, degrees of winnowing would be expected to vary locally, depending on the particular environment from which a sample had been collected, leading to differences in distribution shape between sites. In a few cases, predominantly from the most distal locations, where sample collection had been most difficult, such secondary alteration was immediately apparent from anomalous grain size distribution shapes, and these outliers were removed from the analysis. Otherwise, however, winnowing processes do not appear to have altered these samples significantly.

Further evidence in support of this arises from sites in the Esquel region revisited in January 2009, seven months after the original fieldwork (Figure 5.7). Thicknesses had changed relatively little during this time period, and by an approximately constant amount (i.e. similar absolute reductions in thickness). As such, deposits originally measured at 3 mm thickness or more remained largely intact as a continuous cover, with reductions of the order of 2 mm, but still forming a surface crust. Thicker deposits, such as those near the Chilean border, originally measured at 10–15 mm, had thus only decreased by a relatively small proportion (<20%). Originally thinner deposits had mostly disappeared as a surface cover, with evidence remaining in sheltered localities, such as around the base of large stones. For deposits originally measured at 1.5 mm or below, virtually all evidence of the ash-fall had disappeared. In short, the ash-fall remained surprisingly persistent, in spite of its extremely fine-grained nature, wherever the original deposit thickness had exceeded a few mm.

Unexpectedly, deposit preservation may have been aided by rainfall, since the ash was observed to have commonly formed a cohesive surface crust, presumably on drying, offering a degree of resistance to erosion. Hence, the early wetting of the deposit may in fact have helped its short-term preservation. In some areas, low level ground plants had stabilized the deposit and incorporation within the soil sequence had begun to occur. In spite of the semi-arid, frequently windy conditions of the region, ground vegetation and surface crusting helped stabilize the deposit, and at thicknesses above a few mm the ash-fall was not as ephemeral as might initially be thought.

Grain size measurements from the January 2009 samples confirm that winnowing had not occurred to a significant degree in the seven-month period since initial sample collection (Figure 5.8). Samples collected from sheltered localities, showing a lack of internal structure, with a locally-representative thickness and, in some cases, with surface crusting were deemed to be in their original position. These showed no changes in grain size distribution. In contrast, where ash was accumulated by run-off (commonly showing fine-scale laminations) the grain-size distribution was narrowed, with a loss of fines (Figure 5.8). The main process of deposit alteration in the region (which had already occurred to some extent by the time of initial fieldwork) therefore appears to be through water run-off (and subsequent redeposition) accompanied by a loss of fines. Deposits

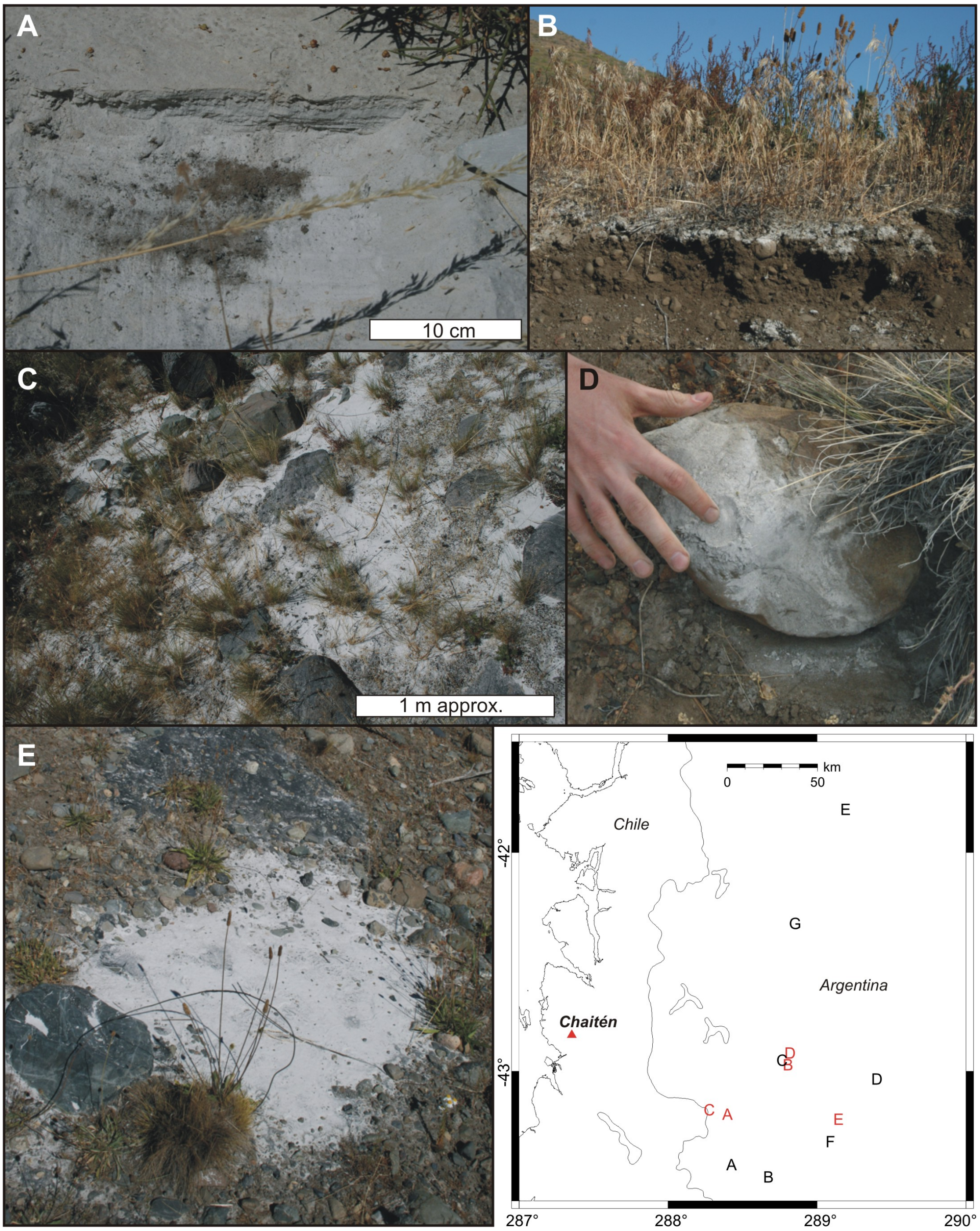

Figure 5.7: Photographs of the distal ash deposit eight months after eruption (taken 10-11th January 2009 by D.M. Pyle). **A** (43.198°S, 71.583°W) Ash accumulated by water run-off at roadside, 40 km south-west of Esquel, showing laminations and anomalous thickening. **B** (42.969°S, 71.178°W) Continuous cover of ash amongst grass and ground vegetation, seen in freshly exposed soil face, 20 km east of Esquel. **C** (43.176°S, 71.708°W) Continuous ground cover, with ash washed off inclined rock faces, 50 km south-west of Esquel, **D** (42.916°S, 71.167°W) Ash accumulated around base of large rounded stone, and a fine ground crust, 15 km east of Esquel. **E** (43.221°S, 70.842°W) Ash accumulation by water run-off down an impermeable patch of asphalt, 20 km north of Tecka. A ground crust remains around this patch. The map at the bottom right shows locations for these photographs (red letters) and also those in Figure 5.2 (black letters). The location of image **H** in Figure 5.2 lies 400 km east of the map edge.

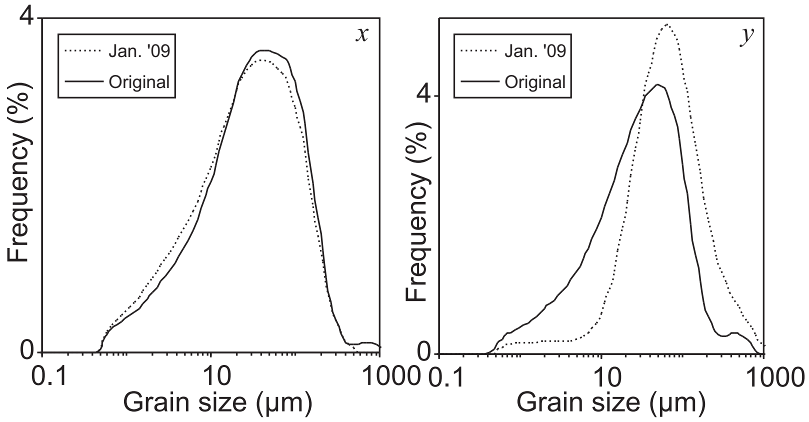

Figure 5.8: Erosional impacts on grain size distributions. Data are shown for two locations near the Chilean border (x and y; Figure 5.5), where thicknesses exceeded 1 cm. At each site sampling was conducted initially on 5th June 2008, and subsequently on 11th January 2009. At site x the 2009 sample was taken 1 km east of the original location, from a deposit that appeared undisturbed. The grain size distribution is unaltered from the 2008 condition. At site y the 2009 sample was taken at the same location, from a water-accumulated, stratified deposit. The 2009 sample shows the effects of grain size distribution alteration: a long, flat, fine tail; a narrowed peak; and possibly, in this instance, coarse particle contamination.

affected by this process were highly localized, commonly occurring around the edges of impermeable surfaces such as paved roads. Such locations were easily recognizable and were avoided during sample collection.

5.4 Ash chemistry and potential impacts

Bulk ash compositional analyses, undertaken on four ash samples by X-ray fluorescence spectroscopy (at the Open University, Milton Keynes; see Chapter 2), and glass analyses on 219 points from 15 ash samples by electron microprobe (Table 5.2), have been combined with compositional data on the recent and previous eruptions of Chaitén [Naranjo and Stern, 2004, Horwell et al., 2008]. Based on calculated CIPW norm compositions [Kelsey, 1965] and examination by electron microprobe, the eruption was found to involve a weakly peraluminous rhyolitic melt, lacking phenocrysts, with minor proportions of plagioclase and rarer biotite microlites, and with a mean glass silica content of 74.5 wt% (Figure 5.9).

The distal ash lacked lithic and crystal particles, comprising variably vesicular pumice and glass shards. Ash composition was relatively uniform, with very subtle chemical differences between eruptive phases suggested by discrete domains within the overall compositional range, occupied by samples from specific depositional lobes (Figure 5.9b). The ash has similar silica content to, but

Table 5.2: Bulk ash and glass compositions.

	Bulk ash[a]				Chaitén glass[b]					
	05-07a	05-12a	05-20a	06-16b	05-18B/14	30-08/11	04-08/8	06-08/3	0707/13	Average (219 points)
Longitude	-43.17	-43.43	-43.59	-42.06	-43.53	-42.68	-43.16	-42.72	-42.51	-
Latitude	-71.75	-71.56	-71.11	-71.16	-71.2	-71.03	-70.11	-71.73	-70.56	-
Source distance (km)	82	111	151	149	140	133	210	76	175	-
Ash thickness (mm)	18	9	6	3	10	3	0.5	1	0.4	-
Modal grain size(s) (μm)[c]	30,95	32,78	67	314,42	67	32	59	61,400	21	-
Major elements (wt%)										
SiO_2	73.78	71.06	72.85	73.86	74.49	75.05	74.44	75.01	74.04	74.5
TiO_2	0.15	0.246	0.195	0.162	0.16	0.14	0.14	0.14	0.13	0.14
Al_2O_3	13.76	14.17	13.83	13.96	13.87	13.53	13.91	14	13.82	13.86
Fe_2O_3	1.51	2.23	1.79	1.59	-	-	-	-	-	-
FeO*[d]	-	-	-	-	1.26	1.16	1.28	1.28	1.23	1.27
MnO	0.057	0.065	0.059	0.059	0	0.08	0.06	0.06	0.06	0.05
MgO	0.26	0.47	0.33	0.32	0.26	0.18	0.26	0.26	0.24	0.26
CaO	1.47	1.71	1.55	1.62	1.36	1.24	1.39	1.39	1.39	1.35
Na_2O	4.08	3.91	4.01	4.14	3.64	3.51	3.73	3.69	3.6	3.61
K_2O	2.93	2.71	2.86	2.94	3.01	3.08	3	3.06	3.09	3.03
P_2O_5	0.062	0.089	0.07	0.068	-	-	-	-	-	-
L.O.I.	0.89	2.38	1.08	1.04	-	-	-	-	-	-
Total	98.95	99.03	98.62	99.75	98.05	97.98	98.21	98.88	97.61	98.07
Trace elements (ppm)										
Rb	113	107	111	111	-	-	-	-	-	-
Sr	145	161	152	153	-	-	-	-	-	-
Y	13.4	16.8	14.4	13.7	-	-	-	-	-	-
Zr	109	117	115	109	-	-	-	-	-	-
Nb	7.8	8.1	8.4	7.7	-	-	-	-	-	-
Ba	604	597	599	599	-	-	-	-	-	-
Pb	19	19	21	20	-	-	-	-	-	-
Th	11	12	13	12	-	-	-	-	-	-
V	13	27	12	11	-	-	-	-	-	-
Cu	4	22	13	5	-	-	-	-	-	-
Zn	35	42	39	36	-	-	-	-	-	-
Ga	13	14	14	14	-	-	-	-	-	-
As	15	15	16	17	-	-	-	-	-	-

[a] Measured by XRF at the Open University, Milton Keynes. Cr, Co, Mo, Ni, S, Sc, U were around or below the detection limit. Results were mostly within 2% of reference values for three standard materials for major elements, and within similar levels for four standards for trace elements, except for Zn and Pb (4%), Cu (6%) and Nb (9%).

[b] Analyses by electron microprobe: beam diameter 10 μm, beam current 15 nA. Glass data given for five selected samples, with an average of all analyses.

[c] Main distribution peak listed first if bimodal.

[d] FeO*: Total Fe as FeO.

is more sodic and less potassic than, the ~10 kyr Cha1 ash [López-Escobar et al., 1993, Naranjo and Stern, 2004].

Rhyolites are rare in this portion of the southern Andean volcanic arc, the only regional tephra of comparable composition being the eastward-dispersed Mic2 unit (Figure 5.9), identified as originating from Minchinmávida, 20 km east of Chaitén [Naranjo and Stern, 2004]. However, this rock composition is not typical of that produced by Minchinmávida, and the identification of the source volcano, based on a lack of the Mic2 tephra cropping out west of Minchinmávida, may not be correct, with Chaitén as the alternative. Field mapping of the Cha1 and Mic2 tephra (Chapter 6 and Watt, unpublished data) suggest that, although compositionally similar, these eruptions were an order of magnitude larger than the current Chaitén eruption. The only other documented regional rhyolite is a sample from Yate [Mella, 2008], although again this is atypical of the volcano. Thus, the rhyolite produced at Chaitén is unusual in a regional context, yet is the only magma type produced in significant volumes during the recognised activity of Chaitén.

The homogeneous compositional character of the current eruptive episode does not provide evidence for the involvement of mafic magma in the eruption, and its highly evolved nature may be a result of long-term magma storage and melting of the granitoid basement, resulting in infrequent eruptions of silicic magma. It remains unclear, however, why this situation is not encountered at other regional centres. The Hudson 1991 ash [Gutiérrez et al., 2005, Kratzmann et al., 2009], the product of the last large explosive eruption in the region, is far less evolved, with a broader compositional range.

Comparison of incompatible trace element concentrations in the Chaitén ash with other southern Andean volcanoes suggests distinct evolutionary paths for the Chaitén magma (Figure 5.9). While the Rb data suggest a trend potentially consistent with fractionation of a melt similar to those erupted at Hudson, Zr shows significant differences, and the compositions are distinct from the fractionation trend defined by volcanoes located between Chaitén and Hudson [Naranjo and Stern, 2004]. These data again show a close similarity between the Mic2 tephra and Chaitén's volcanic products, while other Minchinmávida volcanics do not correspond. The trace element data are consistent with a model whereby significant crustal assimilation occurred in the Chaitén magma, through wholesale melting of Patagonian batholith granitoids. Major element data from these granitoids [Pankhurst et al., 1999] are also consistent with such a process.

Following the method of Blundy and Cashman [2001], compositional norms of glass and bulk

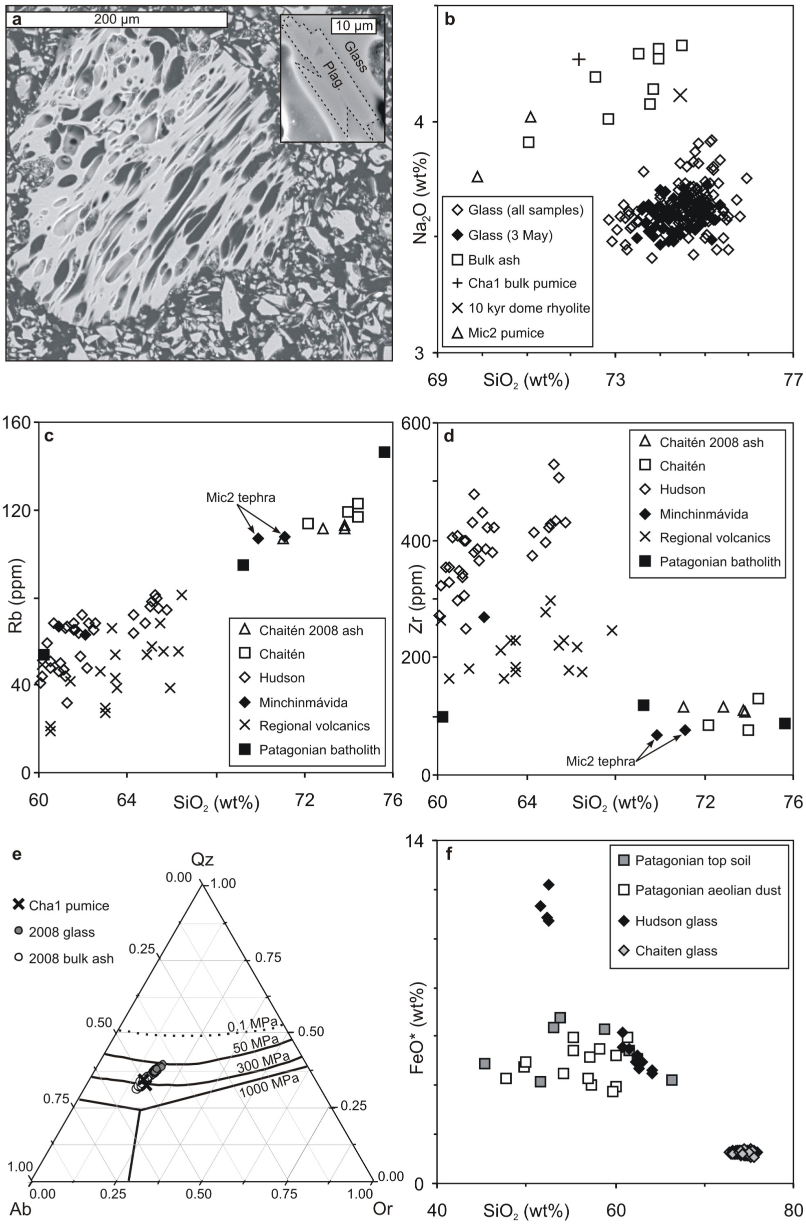

Figure 5.9: Ash compositional and chemical data. **a** scanning electron microscope image of pumice from the 2nd or 6th May, collected 150 km from source. Inset shows plagioclase microlite (An_{29}) in the same sample. **b** Na_2O against silica for glass and bulk ash from the recent Chaitén ash, showing Cha1 and Mic2 (from Minchinmávida volcano) for comparison [Naranjo and Stern, 2004]. The glass forms a single compositional group, but the 3rd May data covers a discrete domain within this, suggesting slight compositional differences between eruption phases. **c**-**d** Rb and Zr against silica comparing the ash with regional volcanics (Cay, Corcovado, Hudson, Maca, Melimoyu, Mentolat and Yanteles) containing >60 wt% SiO_2 and older Chaitén rocks [Notsu et al., 1987, Kilian and López-Escobar, 1991, López-Escobar et al., 1993, D'Orazio et al., 2003, Naranjo and Stern, 2004, Gutiérrez et al., 2005], and local samples of the Patagonian batholith (from Futaleufú and Palena [Pankhurst et al., 1999]). **e** Glass compositions plotted on the granitic ternary diagram (method from Blundy and Cashman [2001]), and compared with the Cha1 composition. The data suggest equilibration at pressures corresponding to magma chamber depths of 3–6 km. **f** FeO* (total Fe as FeO) against silica comparing the Chaitén glass with that from the compositionally-mixed Hudson 1991 eruption [Kratzmann et al., 2009] and compositions of modern Patagonian top soils and aeolian dust [Gaiero et al., 2007].

ash, plotted on the granitic ternary diagram (Figure 5.9), are consistent with magma equilibration under water-saturated conditions at ∼100–200 MPa, or ca. 3–6 km depth, where dissolved water content of up to 6 wt% [Tamic et al., 2001] may explain the high eruption explosivity. Earthquakes recorded beneath Chaitén in 2005 at ∼10 km depth [Lange et al., 2008] may thus correspond to deeper magma chamber replenishment, precursory to the eruption.

From the volumes lying beyond our mapped isopachs, ∼5% of the ash (9×10^9 kg) fell over the Atlantic Ocean, mostly of grain size <50 µm. Eruptions of this magnitude are potentially recorded in Argentine shelf sediments, and are periodic contributors to the Antarctic and Southern Ocean dust budget [McConnell et al., 2007]. Comparison with Patagonian dust (Figure 5.9), for which Andean volcanic ash of the more common andesitic composition forms an important component [Gaiero et al., 2007], shows that rarer rhyolitic ash, such as that from Chaitén, is a minor dust component. The low iron content of Chaitén glass (<1 wt% FeO) suggests this ash would have had a minor impact on nutrient-limited portions of the Southern Ocean [cf. Martin et al., 1990] in comparison to large explosive andesitic eruptions.

5.5 Summary and conclusions

The measurements and analyses described here provide the first field-based estimates of the volume and magnitude of the Chaitén 2008 eruption. The mapped distribution of the ash deposit reflects the dominant features of the wind-field during the most intense, week-long episode of the eruption. The pattern observed can be used to define separate eruptions units, which, although compositionally highly uniform, have distinctive granulometric characteristics. Grain size distributions can be used to elucidate both transport and depositional processes, related to factors such as changing column height, eruption intensity and plume water content. The complexity observed is a direct result of the duration of the eruption (i.e. lasting several days), amplified due to its sporadic nature, in terms of variable explosive intensity defining a multi-phase event.

In summary, $\sim 1.6 \times 10^{11}$ kg of ash (dense rock equivalent volume of ~ 0.07 km^3) was deposited over $\sim 2 \times 10^5$ km^2 of Argentina during the first week of eruption. The minimum eruption magnitude, estimated from the mass of the tephra deposit, is 4.2. The more energetic eruption phases have a bimodal grain size distribution, providing evidence of particle aggregation processes. Ash chemistry was uniform throughout the early stages of eruption, and is consistent with magma storage prior to eruption at depths of 3–6 km. The aphyric rhyolitic magma produced is highly similar to that erupted previously at Chaitén.

Although it has been widely stated that the recent Chaitén activity has been the first since the Cha1 eruption [Folch et al., 2008, Carn et al., 2009, Castro and Dingwell, 2009, Lara, 2009], if the source of the Mic2 tephra [Naranjo and Stern, 2004] has been mis-identified (i.e. it originated from Chaitén), then this would suggest more recent activity (<4 kyr). This is further supported by a field section located a few km west of Chaitén volcano, examined in January 2009 and exposed following a recent landslide. Here, at least four pyroclastic units, containing rhyolitic pumiceous material, were identified. Although this sequence remains undated and uncorrelated elsewhere, it does suggest that Chaitén may have been more active during the Holocene than previously recognised.

The volume and magnitude parameters derived here are significantly smaller than some estimates made based on column height observations and simple assumptions about eruption duration [e.g., Folch et al., 2008], and demonstrate the importance of field sampling in producing accurate estimations of eruption parameters. Since eruptions of this magnitude are relatively rare, particularly in depositing tephra over land, investigations such as this one provide data useful for the understanding of tephra production and transport processes. One application for such data is in constraining and testing tephra fallout models [e.g., Searcy et al., 1998, Connor et al., 2001, Folch and Felpeto, 2005], which seek to predict the impact and distribution of tephra deposition from explosive eruptions. It is important that such models produce accurate results if they are to be used to help mitigate the impacts of explosive eruptions.

The complexity of the ash dispersal pattern arising from the Chaitén 2008 eruption is a result of a changing wind field during a week-long main eruption period. Variability in wind and transport direction over this timescale may be a relatively common process affecting tephra plumes, particularly if column height is variable. However, temporal and spatial variability in wind patterns can be computationally difficult to reproduce in tephra transport models. It is possible to investigate the behaviour of tephra fallout models using an inversion approach, based on field data, to investigate the input parameters that best produce the observed depositional pattern. Testing the accuracy of these input parameters against observations can then be used to understand and improve the modelling process. An example is provided (Figure 5.10), using the distal field data obtained in this study. This has been produced using `Tephra2` [Connor et al., 2001, Bonadonna et al., 2005], which uses an advection-diffusion model to forecast the transport and sedimentation

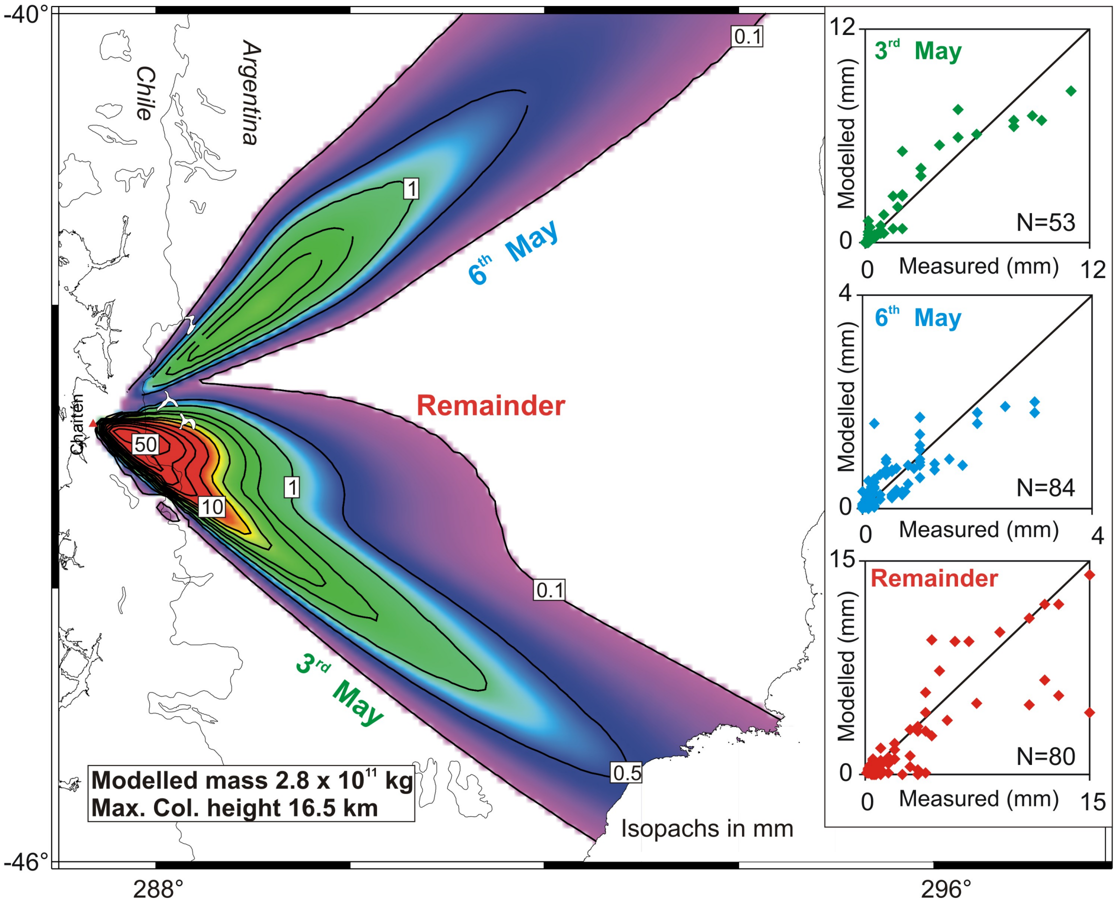

Figure 5.10: Modelled tephra dispersion patterns. The results are based on an inversion of the field data to find the model input parameters that best fit the data. The map shown is the result of a forward model, using these parameters. The `Tephra2` model was used, and the eruption data was divided into three phases (3rd May, 6th May and remainder) to account for the wind-field complexities. The fit of the modelled data to the field data (deposit thickness) is shown in the inset plots (a perfect fit would follow the diagonal).

of volcanic particles. In producing this result, separate phases of the eruption have been modelled individually, during which column height and wind-field varied. The complexity of the Chaitén deposit meant that it could not be modelled as a single eruptive episode, due to the changing wind field. In general, however, the parameters produced (i.e. volume) are of similar order to those estimates derived directly from the field data. More detailed testing may be used to better constrain the particle transport modelling, particularly using data such as the deposit grain size distributions, which can be used to understand the dispersal of a particular size fraction.

The complex nature of the Chaitén tephra deposit further highlights the importance of constraining the distal ash fraction if accurate assessments of eruption parameters are to be made from field-based measurements. Past-event reconstruction often relies only on proximal deposit measurements, fitted with elliptical isopachs (and an implicit assumption of a single eruption phase). Commonly, only proximal measurements are available, since the distal portion of the deposit is rapidly eroded and rarely preserved as a measurable unit. In such cases a simple elliptical fit is the best that can be used (e.g., Chapter 6). However, this work makes clear that extrapolating proximal data to obtain estimates of eruption parameters may be highly imprecise, but that the error involved cannot be constrained without information regarding the dispersal pattern of the unit, which must be inferred from the distal deposit. The distal portion of the Chaitén tephra in Argentina, all at thicknesses below 2 cm and with a medium-ash maximum grain size, is volumetrically large and spatially complex but is likely to be very sparsely preserved. Mapping of the unit based simply on the proximal deposit, which would show a relatively wide angle of dispersion, and then assuming elliptical isopachs would be likely to significantly overestimate the eruption magnitude.

Part III

Volcanic Records on a Range of Timescales

Chapters 6 and 7 of this thesis are currently not available in ORA.

This chapter is an updated version of: Watt, SFL, DM Pyle, TA Mather, 2009. The influence of Great Earthquakes on volcanic eruption rate along the Chilean subduction zone. Earth and Planetary Science Letters 277(3-4), 399-407,doi: 10.1016/j.epsl.2008.11.005, which was published by Elsevier, and which is available at http://dx.doi.org/10.1016/j.epsl.2008.11.005 and http://www.sciencedirect.com/science/journal/0012821X.

Chapter 8

Earthquakes and volcanism in the southern volcanic zone[1]

8.1 Introduction

Earthquakes and volcanic eruptions are among the most dramatic and rapid processes affecting Earth's surface, with the potential to generate devastating human and environmental consequences. Over broad spatial scales a clear relationship exists between these phenomena, explained by plate tectonics. As such, the locations of volcanic arcs are associated with regions characterised by large earthquakes, with both resulting from subduction processes. On small temporal and spatial scales, seismic activity directly associated with the magmatic system represents an integral part of volcanic activity, and earthquakes resulting from magmatic movement, accompanying volcanic unrest, are detectable locally. However, on scales beyond a single volcanic system, it is not clear that invididual occurrences of large earthquakes and volcanic eruptions are linked, in that the occurrence of one may precipitate the other. Here, I investigate potential evidence of such a relationship between large subduction zone earthquakes and volcanic eruptions in Chile, using historical earthquake and eruption records.

The Chilean plate boundary and adjacent Andean southern volcanic zone (SVZ) represent an ideal area to study relationships between volcanism and earthquakes. For around 3200 km of the Chilean coastline the Nazca plate is subducted beneath the western edge of South America along a straight north-south margin. Subduction is oblique and proceeds at approximately 8 cm yr^{-1}

---

[1] Much of the material in this chapter is published in Watt et al. [2009a], *Earth and Planetary Science Letters.*

[DeMets et al., 1994]. The SVZ runs along the southern 1400 km of this margin, from 33.4°–45.9° S, and contains over 60 volcanoes considered to have been active in the Holocene [Siebert and Simkin, 2002-]. The plate boundary between these latitudes is characterised by extremely large thrust earthquakes, and includes the largest event recorded in modern times, the M_W 9.5 earthquake of 22nd May 1960 [Barrientos and Ward, 1990, Cisternas et al., 2005].

8.1.1 Previous work

Anecdotal evidence suggestive of large earthquakes triggering subsequent volcanic eruptions exists from the SVZ. The possibility of a relationship was noted by Darwin [1840] following the 1835 earthquake that devastated the city of Concepción. Darwin experienced the earthquake and observed its effects during the *Beagle* voyage, and summarised several reports of subsequent volcanic eruptions throughout the region [Darwin, 1835]. A further eruption, often cited as a possible earthquake-triggered event [e.g., Barrientos, 1994, Lara et al., 2004b, Manga and Brodsky, 2006], is that of Cordón Caulle volcano, Chile, 38 hours after the 1960 Chilean earthquake. Such instances have stimulated previous investigations of earthquake triggering of volcanic eruptions.

Seismic activity can elicit a variety of dynamic crustal responses, including triggered remote seismicity [Hill et al., 1993], hydrological responses [e.g., Brodsky et al., 2003, Montgomery and Manga, 2003] and magmatic activity [Linde and Sacks, 1998, Hill et al., 2002, Manga and Brodsky, 2006, Harris and Ripepe, 2007, Walter and Amelung, 2007, Walter et al., 2007], in some cases at distances far in excess of the source-fault dimensions. As a trigger of volcanic eruption, seismic activity has been postulated to operate on a range of timescales [e.g., Linde and Sacks, 1998, Nostro et al., 1998, Marzocchi, 2002], but the precise mechanisms of seismic volcanic eruption triggering, particularly at distances far from the rupture zone, remain enigmatic. Furthermore, demonstrating conclusively the occurrence of triggered eruptions on timescales beyond a few days has proven difficult, and a suggested interaction may thus appear speculative. Linde and Sacks [1998] investigated the relationship between large earthquakes and volcanic eruptions, and found that for great earthquakes ($M > 8$) a far larger proportion of eruptions occurred in the 24 hour period immediately following the earthquake than would be expected if no relationship existed. They concluded that rapid triggering could occur on the timescale of one or two days, and for earthquakes of this magnitude, at distances of up to 750 km from the earthquake epicentre. They did not find evidence for triggering on longer timescales, or for the reverse interaction (volcanic triggering of large earthquakes).

In regions close to the fault rupture static stress changes in rock surrounding stored magma, associated with movement along the earthquake fault plane, may explain eruption triggering. Walter and Amelung [2007] use such a process to suggest that triggering may occur on timescales of months to years in the vicinity of a large earthquake rupture zone. The magnitude of static stresses decays rapidly with distance r, as r^{-3}. At greater distances, dynamic stresses, associated with the passage of seismic waves, are often cited as a possible eruption trigger [e.g., Linde and Sacks, 1998]. Dynamic stresses decay more slowly with distance than static stresses, approximately as $r^{-1.66}$ [Manga and Brodsky, 2006]. These explanations focus on seismic wave interactions with crustal fluids, causing fluid movement, disruption or bubble growth through a variety of possible mechanisms leading to magmatic overpressure, but the timescale of such responses is poorly understood. Where studies have identified examples of seismically-triggered phenomena they have focussed on occurrences immediately following an earthquake (e.g., within a few days), where the suggestion of a causal link is straightforward. However, without an agreed causal mechanism or careful analysis of event records this, and similar examples, might be dismissed as coincidences. Linde and Sacks [1998] used a systematic examination of global earthquake and eruption datasets to demonstrate that rapid eruption triggering did occur. This relationship was quantified by Manga and Brodsky [2006], who showed that 0.4% of explosive volcanic eruptions occur within a few days of large distant earthquakes; a much larger proportion than expected (0.01–0.1%) if there were no causal relationship.

Although these prior studies did not find evidence for triggered response times longer than about five days, this does not necessarily mean they do not occur. It might be expected that eruptions triggered after a longer delay will be less frequent than those triggered within days of an earthquake, with potential variability between arc settings. Thus, such events may not be detectable above the natural background variability of eruption rate in global data sets, as studied by Linde and Sacks [1998], and in addition, certain regions of the globe appear to display earthquake triggered eruptions far more than others [Eggert and Walter, 2009]. Hydrological observations of wells have shown persistent pressure responses following distant earthquakes, but in some cases the response is delayed by several weeks, and is of a magnitude that cannot be explained by static stress changes alone [Brodsky et al., 2003, Montgomery and Manga, 2003]. Similarly, interaction with crustal magma bodies may not be manifested as surface activity (eruption) for timescales of months or more. Mechanisms involving near-field static stress changes have been highlighted by Walter and Amelung [2007], who note that following four $M_W \geq 9$ subduction zone earthquakes a number of adjacent arc volcanoes erupted in the following three years, while Marzocchi [2002] suggests that there is a relationship between earthquakes and the largest volcanic eruptions operating on a timescale of up to 35 years. However, while individual instances of delayed triggered eruptions have been proposed, demonstrating whether a general relationship between earthquakes and eruptions exists on timescales longer than a few days has proven difficult. Examination of data from individual seismically-active volcanic regions, rather than a global data set, may help elucidate such relationships by investigating the effects of large earthquakes in a single setting.

8.2 Event records

8.2.1 Earthquake records

The dates of large earthquakes along the Chilean subduction zone are relatively well documented from the 16th century onwards [Lomnitz, 1970, Kelleher, 1972, Comte et al., 1986], although there are some uncertainties regarding magnitude and fault rupture length in the earlier parts of this record due to sparsely distributed damage reports. Table 8.1 shows a record of all earthquakes along the plate boundary with estimated moment magnitudes, M_W, greater than approximately 7.5. There is general agreement in the literature as to which were the largest events ($M_W \geq 8$), hereafter termed 'great earthquakes'. These main ruptures dominate subduction zone convergence and regional crustal deformation [Klotz et al., 2001]. Events of this magnitude present the most likely candidates for producing an eruption response, since their rupture lengths ($>$ 150 km) greatly exceed the typical spacing of local arc volcanoes (approximately 25 km), and several volcanic centres are potentially affected.

The great earthquake record shows a remarkably well-defined cyclicity (Figure 8.1), with main ruptures generally propagating southwards from the epicentre, and stepping southward along the subduction zone in a temporally clustered pattern, as adjacent locked segments are seismically loaded [e.g., Li and Kisslinger, 1984]. This cyclic pattern has been noted numerous times [e.g., Kelleher, 1972, Lomnitz, 1985, Nishenko, 1985]. Although repeat times show a high degree of consistency, the rupture length and magnitude of events is more variable, with some smaller 'great

Table 8.1: Chilean main ruptures between 32° and 46° S

Date	Epicentre	Estimated rupture length (km)	Estimated M_W[a]
8 Feb 1570	36.7°S 73.0°W	280	8–8.5
17 Mar 1575[b]	32.5°S 71.5°W	110	? 7.5
16 Dec 1575	39.8°S 72.8°W	800	>8.5
13 May 1647	32.9°S 71.3°W	380	8.5
15 Mar 1657	36.7°S 73.0°W	390	8
8 Jul 1730	33.1°S 72.0°W	560	>8.75
24 Dec 1737	39.8°S 73.0°W	530	7.5–8
25 May 1751	36.7°S 73.0°W	440	>8.5
19 Nov 1822	33.1°S 71.8°W	220	8.3
20 Feb 1835	36.6°S 73.0°W	440	8–8.3
7 Nov 1837	40.0°S 73.0°W	630	>8
17 Aug 1906	33.0°S 72.0°W	330	8.3
1 Dec 1928	35.0°S 72.0°W	140	8.2
25 Jan 1939	36.3°S 72.3°W	190	8.0
22 May 1960	39.5°S 74.5°W	940	9.5
4 Mar 1985	33.2°S 71.9°W	170	8.0

[a] Magnitude estimated from data in Lomnitz [1970, 1985], Kelleher [1972], Nishenko [1985], Comte et al. [1986], Cisternas et al. [2005], Okal [2005].

[b] Considered a great earthquake by Comte et al., 1986, the event fits well with the seismic cycle, though contemporaneous reports provide very little information on damage.

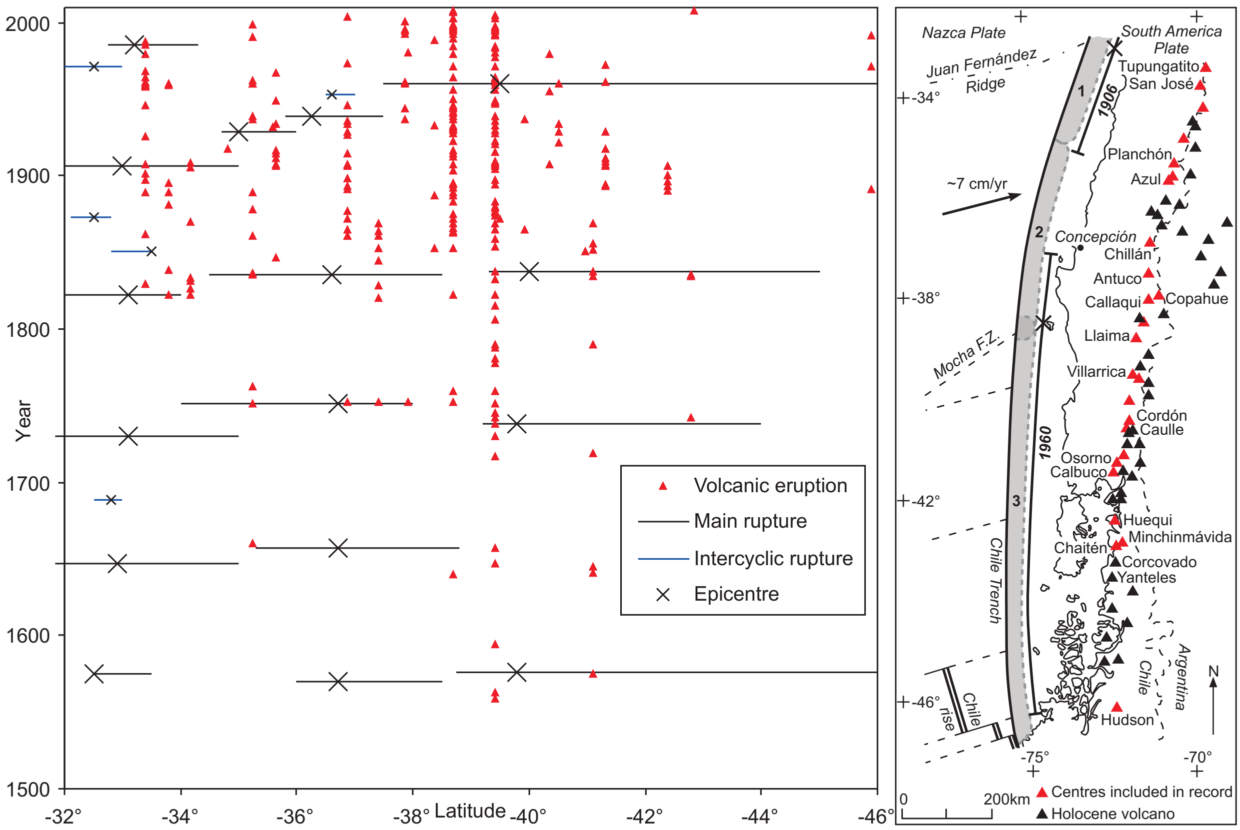

Figure 8.1: Historically recorded large earthquakes ($M_W > 7.5$) and volcanic eruptions in central and southern Chile, shown by latitude, with event occurrence through time. The left panel shows main ruptures ($M_W > 8$) and intercyclic events as horizontal lines, with epicentres and approximate rupture lengths. Earthquake occurrence shows a cyclic temporal clustering and broad southward stepping pattern. Reliably recorded volcanic eruptions are also depicted. Eruptions from a few centres dominate the record, and those in the far south of the region appear to be underrepresented. The map shows approximate limits of plate boundary segments, corresponding to the Central Chile (1), Central Valley (2), and Southern Nazca (3) rupture zones [Lomnitz, 1970, 1985]. The 1906 and 1960 rupture zones, with epicentres, are also shown. Named volcanoes are discussed in the text.

earthquakes' thought to only partially release seismic strain, themselves being intercyclic to much larger events [e.g., Comte et al., 1986, Cisternas et al., 2005, Moernaut et al., 2007]. The cause of plate boundary segmentation, defined by the limits of great earthquakes ruptures, may relate to physical features on the subducting plate and variable coupling at the plate margin. For example, the boundary between the Central Valley and Southern Nazca zones (Figure 8.1) may be related to subduction of the Mocha fracture zone [Herron, 1981, Hackney et al., 2006]. Subduction of the Juan Fernández seamounts may be related to the onset of the volcanic gap north of the SVZ [e.g., Von Huene et al., 1997].

8.2.2 Eruption records

A record of all historical SVZ volcanic eruptions has been compiled from Siebert and Simkin [2002-] (Appendix H), rejecting all events where uncertainty exists over the authenticity of the record or the year of eruption. Of 325 eruptions listed since 1558, 63 are rejected for these reasons, leaving 262 eruptions from 25 volcanoes. The number of historically recorded eruptions is widely variable between volcanoes, with some centres appearing to dominate the record, and many volcanoes characterised by clusters of eruptions on decadal timescales (Figure 8.1).

Previous workers investigating earthquake-triggered eruptions (see Section 8.1.1) have rejected small or non-explosive events (Volcanic Explosivity Index, or VEI, < 2; [Linde and Sacks, 1998, Manga and Brodsky, 2006, Walter and Amelung, 2007]). This approach is not taken here, primarily because the VEI is uncertain for most events beyond the recent past, and to reject all eruptions of uncertain magnitude would make the eruption catalogue too small for any meaningful study. Furthermore, my interest lies not only in explosive events, but in any activity that may contribute to arc-wide fluctuations in rates of volcanism. Filtering of small eruptions would remove records from some volcanoes that have gone through periods of persistent but low-level activity, such as Villarrica. While such volcanoes may appear to dominate the eruption record (Figure 8.1), they are more likely to have magma-filled plumbing systems than dormant volcanoes, and should therefore be ideal candidates for showing responses to external forcing. This is suggested, for example, by the seasonal response to earth-surface deformation observed in small and near-continuous eruptions of Sakura-jima, Japan [Mason et al., 2004a]. Thus, while explosive eruptions at long-quiescent volcanoes may provide the most compelling individual cases of potentially earthquake-triggered eruptions, it would be unwise to reject smaller eruptions, which may hold more potential for providing evidence of arc-scale magmatic disturbance following great earthquakes.

The parameter measured in the volcanic records is eruption occurrence, and not magnitude. While this is an imperfect measurement of the rate of volcanism, it is the only viable parameter given the variable detail on eruption scale in historical records. Eruptions are measured by their onset date, and with an assumption of short duration in comparison to the inter-eruption time period, they form point events in time. Thus, eruption length is also not accounted for, and significant changes in behaviour *during* eruption (potentially a result of remote seismic interaction) are therefore not included in this record; in any case, such data are sparsely available. Of the 262 dated eruptions in the final catalogue, the month of onset is known for 182 (69% of the total), and the day for 146 (56%). Each eruption is recorded by a decimal onset date, and shown by date and latitude in Figure 8.1. For eruptions where the exact onset date is unknown the midpoint of the smallest time interval for which the event can be dated is taken, following Bebbington and Lai [1996]. To avoid clustering artefacts, if two or more events are given the same date by this process (e.g., two events occurring in the same year at unknown dates) the data are then spread evenly across the relevant time period. If eruptions with unknown onset month coincided with the year of a great earthquake then they were removed entirely from the analysis, since it is not clear if they preceded or post-dated the earthquake.

Assuming a long-term constant rate of eruption cccurrence on the arc-scale over time periods of decades to centuries, a cumulative plot offers a simple assessment of the period for which the record is approximately complete (Figure 8.2). The linearity of this cumulative plot suggests that from around 1850 onwards long-term eruption occurrence has been constant, or at least that the rate at which eruptions went unrecorded did not change. Recording of eruptions in recent times is likely to be almost complete, and Figure 8.2 thus suggests that the eruption catalogue is approximately complete after 1850. Prior to this time many eruptions are presumed to have occurred for which records do not exist. However, the dating of events that are recorded improves only slightly over time, with the onset day known for 59% and the month for 73% of the 206 eruptions since 1852. Even in the period since 1970 the onset day is still recorded for $<$90% of eruptions. The long-term rate defined by Figure 8.2 is 1.32 eruptions per year.

8.2.3 Record bias and interpretation

Historical records of earthquakes and eruptions must be examined with caution. By their nature both are notable phenomena, but especially so when endangering human life or property, and thus their recording is often sporadic. In particular, following great earthquakes, there may be a heightened awareness of other geological phenomena, including volcanic eruption [e.g., Simkin, 1993]. Confusion and anecdotal evidence can lead to bias in the record, if not the misreporting of events. When looking for relationships between these processes, it is particularly important that doubtful reports are not included in the analysed records. Furthermore, to focus on any one individual eruption following a great earthquake as evidence of a causal relationship is misleading. Such coincidences would be expected (in limited numbers) for any independent stochastic processes. Thus, by examining event records, as in this method or that of Linde and Sacks [1998],

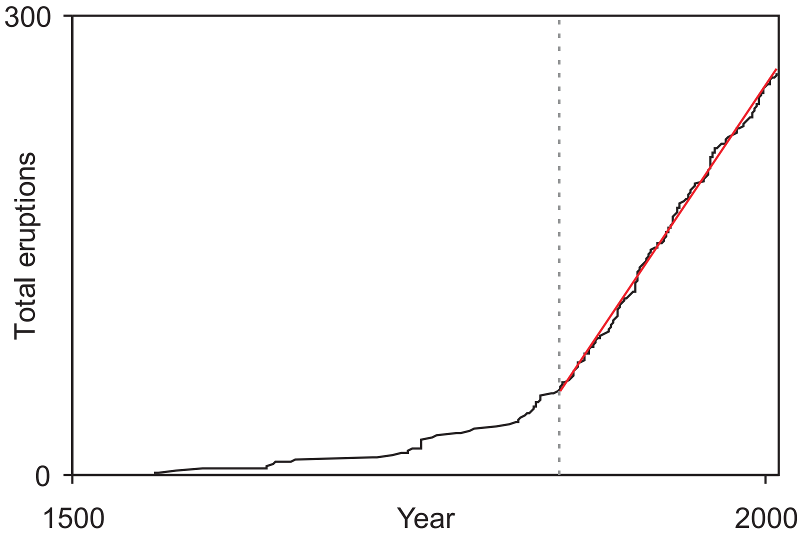

Figure 8.2: Cumulative plot of historically recorded volcanic eruptions in the SVZ. Assuming an constant long-term rate of eruption occurrence, the record is taken to be complete after 1850 (shown by grey dashed line).

any individual eruption cannot be identified statistically as having been triggered by a preceding earthquake. Therefore, the identification of a particular eruption as an example of triggering remains speculative, and for this reason I consider changes in arc-wide eruption rates rather than listing individual eruptions as triggered events [e.g., Walter and Amelung, 2007]. Difficulties of these types are well illustrated by the following examples.

Perhaps the most cited reports suggestive of earthquake-triggered volcanism are those of Darwin [1840] [Linde and Sacks, 1998, Manga and Brodsky, 2006, Walter and Amelung, 2007], following the 20th February 1835 Concepción earthquake:

> A few days after the earthquake, several volcanos within the Cordilleras, to the north of Concepcion, though previously quiescent, were in great activity…During the remainder of the year, the whole of the volcanic chain, from Osorno to Yantales…exhibited, at times, unusual activity.

Much of Darwin's record is based on secondary sources, and some eruptions, such as that of Antuco [Darwin, 1835] he later declares doubtful [Darwin, 1840]. To the north of Concepción, erupting volcanoes are described by Caldcleugh [1836], though his sources are unclear and are not corroborated elsewhere. Reports suggest activity in the Descabezado-Azul system and at Tupungatito. These are unlisted or declared uncertain by Siebert and Simkin [2002-] and so are excluded from the analysed records, while only the year is known for the activity at Planchón. Of the listed volcanoes to the south, eruption reports at Corcovado and Yanteles (based on the disappearance of snow or the appearance of dark patches) and concomitant eruptions at Corcovado and Osorno later in the year, are doubtful or unlisted by Siebert and Simkin [2002-]. Osorno and Minchinmávida were already in a state of eruption before the earthquake, but are stated as exhibiting renewed vigour. Of these, only Minchinmávida is listed as having a reliable eruption record by Siebert and Simkin [2002-] corresponding to the earthquake date. However, since the volcano had started erupting three months before the earthquake, in November 1834, after nearly a century of quiescence, this is not a clear candidate for an earthquake-triggered event; the 1835 record may simply be a result of heightened awareness of geological activity following the earthquake. In spite of this, the example of Yanteles and Minchinmávida are listed as an earthquake-triggered eruption pair by Linde and Sacks [1998]. This is not to say that Darwin's accounts are incorrect, but based on the information given in reports from the time, nearly all of the volcanoes mentioned in his records cannot be included in the final catalogue due to uncertainty over the type of activity or report veracity. Indeed, to quote FitzRoy [1839], following the same earthquake:

> As to the state of neighbouring volcanoes, so various were the accounts of their action, both after and before the earthquake, that I had no means of ascertaining the full truth.

It is of interest to note, however, that the four erupting volcanoes south of Concepción listed by Darwin [1840] as erupting after the earthquake are at latitudes well beyond the rupture limits, Minchinmávida being approximately 500 km outside the rupture zone.

The above discussion illustrates the difficulties in interpreting the historical record, but also demonstrates that individual eruptions can only ever be identified as potential examples of triggered events. For example, Tupungatito, listed by Walter and Amelung [2007] as one of four volcanoes that erupted within a year of the May 22$^{\text{nd}}$ 1960 Chilean earthquake, certainly represents a candidate triggered eruption. However, in spite of the volcano's relatively infrequent activity, any stronger assertion is difficult to argue, given that it entered a new eruptive phase in 1958 after 12 years of quiescence, and erupted twice in 1959 before erupting again two months after the 1960 earthquake.

By removing events from the record for which there is uncertainty over occurrence or timing, and by only examining in detail the record for which the long-term eruption rate is constant

(Figure 8.2), I aim to avoid erroneous reports and record bias. Furthermore, the focus of this analysis is on changes in arc-scale eruption rate, and is not an attempt to explicitly indentify individual triggered eruptions, which would not be justified by the data available.

8.3 Event Analysis

From Figure 8.2 it is assumed that the eruption record is complete since 1850. To compare eruption rate since this time with the timing of great earthquakes requires a measure of short-term eruption rate on the arc scale. This is based on eruption incidence, and does not account for magnitude or duration of eruptions. The hypothesis being investigated is whether great earthquakes lead to an eruption rate increase on a timescale greater than a few days. Thus, in order to verify, or otherwise, whether an increase in eruption rate occurs *after* great earthquakes, the eruption rate measurement in any time increment must be based upon the timing of recent prior eruptions, rather than future events. In this way, any abrupt increase in eruption rate will be shown at its real time position, rather than artificially early. To achieve this, a rectangular window was passed across the full eruption records, with a minimum span of 12 months. Due to the poor quality of some data, in terms of eruption date, a more complex or narrower window was not chosen. This method has the advantage of producing data that are readily interpreted as being equal to the number of eruptions in the window-width period prior to that time point. This measure is not necessarily equal to the number of active volcanoes in that time period, since the figure may include two or more eruptions from a single volcano. Wider windows smooth the record and show longer-frequency variations, but artificially spread these variations along the time axis, though the onsets of rate increases appear at their real time. The filter was run with various widths, and results are presented in Figure 8.3 for three cases: 1850–present with a 12-month window (Figure 8.3a); 1850–present with a 3-year window (Figure 8.3b); and analysis of the incomplete pre-1850 eruption records with a 12-month window (Figure 8.3c).

8.4 Discussion

8.4.1 Eruption rates

Figure 8.3a shows that the eruption rate in the SVZ has fluctuated widely. However, two outlying maxima occur where the eruption rate is significantly increased above the norm. These two

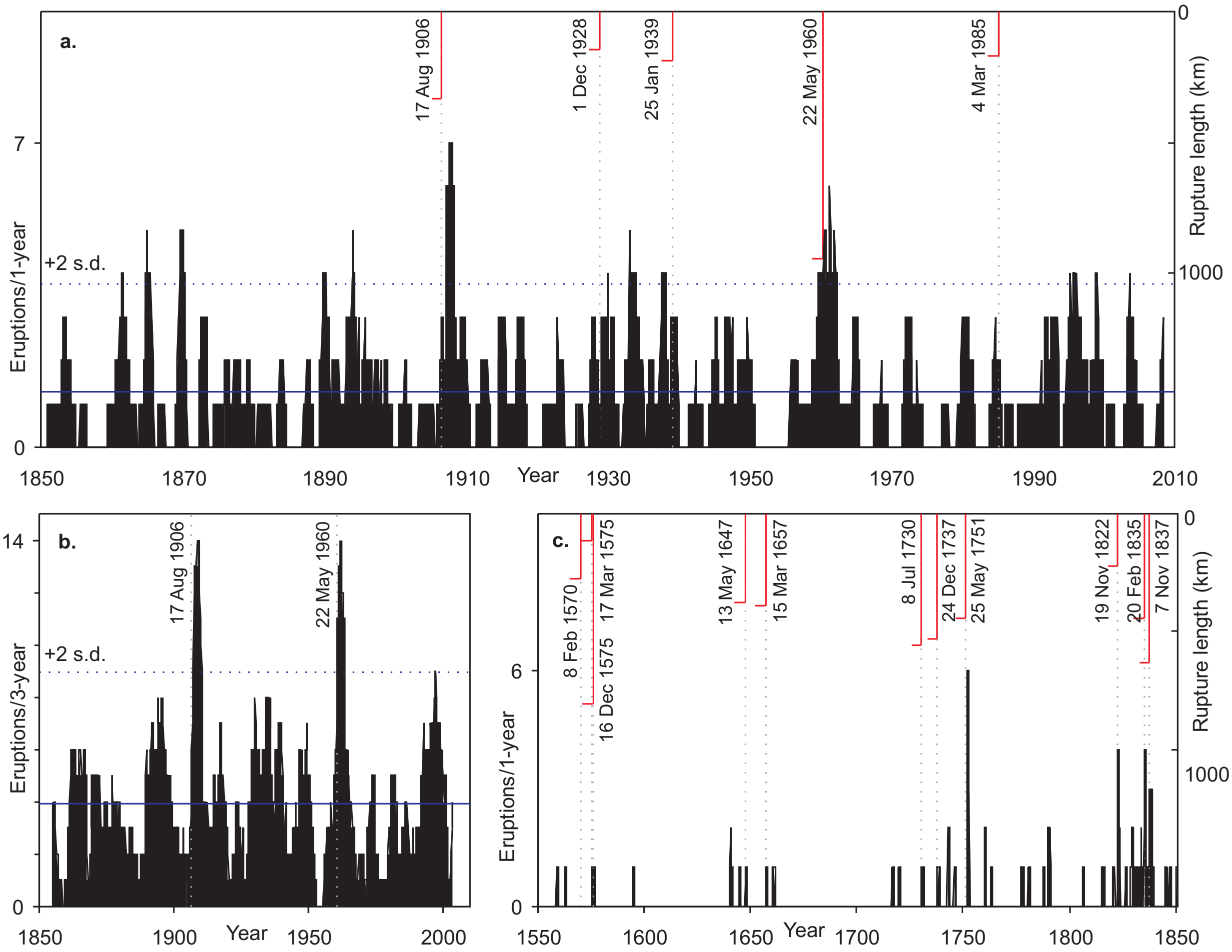

Figure 8.3: Arc-scale volcanic eruption rates. Great earthquake timing and rupture lengths are also shown as vertical lines from top (right hand axes). Sharp eruption rate increases occur immediately following the 1906 and 1960 earthquakes, with rates above the background range lasting for several months. Mean values of the calculated eruption rates are shown as a horizontal line, with a dashed line at +2 standard deviations indicating background rate variability. A: Rate since 1850 using a 12-month rectangular window passed over the eruption record at 0.05 year increments, such that only eruptions prior to the time point contribute to the eruption rate. B: Using the method described for A, with a 3-year window at 0.1 year increments, giving a smoother long-term eruption rate. C: Using the method described for A, with a 12-month window at 0.1 year increments, for the record prior to 1850. While data are highly incomplete, eruptions are almost always recorded in the year following great earthquakes, most notably in 1751.

periods commence in late-1906 and mid-1960, and the rate of activity exceeds the background for approximately 12 months. The filter in Figure 8.3b gives a smoothed longer-term eruption rate pattern which reveals the two peaks in eruption rate very clearly. These two periods correspond to times immediately following the two largest Chilean earthquakes since 1850: in August 1906 in the northern part of the study area, and in May 1960 in the southern half of the study area.

Following the 1906 earthquake and before the end of 1907 at least seven volcanoes erupted in the SVZ, in a possible maximum of ten eruptions (Table 8.2). Similarly, at least six, and possibly seven, volcanoes erupted by the end of 1961 following the 1960 earthquake, in up to nine eruptions. In the rest of the record, the eruption of five volcanoes in any 12-month period occurs three times, in 1863-4, 1869 and 1893, while four erupting volcanoes in a year occurs several times.

8.4.1.1 Poisson processes and probabilities

The distribution of eruption occurrence on an arc-scale may be modelled as a Poisson process [e.g., Bebbington and Lai, 1996]. In such a model the number of future events, occurring at instants in time, is independent of behaviour in the past, and the distribution of the number of events is constant over time (i.e. the process is stationary). For eruption timings on the arc scale it may reasonably be expected that the occurrence of eruption at any one centre is independent of the timing of eruption at another volcano in the arc. This model can be tested by examining the time intervals between eruptions, using the sample mean of 1.32 eruptions per year. If the data do define a Poisson process, then the cumulative density function of the process has density $\lambda \exp(-\lambda t)$ where λ is the sample mean, and t is time. That is, the inter-event times are exponentially distributed, and the expected time for n events to occur is n/λ. The inter-event times do show a good fit to the exponential distributions (Figure 8.4), suggesting that, broadly, the data are consistent with a Poisson process. A Kolmogorov-Smirnov test for a fit to the exponential distribution shows that for the 205 data values, a test-statistic of 0.063 is produced. This is well below the Kolmogorov-Smirnov 0.05 critical value, but since the sample was used to estimate the exponential parameters the power of the test statistic is reduced, and a Lilliefors-type critical value should be used, likely to be close to the measured test statistic at the 0.05 level [e.g., Schafer et al., 1972]. In general however, given that these data are of variable quality (e.g., the occurrence of an artefact showing a large number of inter-event times of 1 year (Figure 8.4), resulting from eruptions only dated by year of occurrence) and that for some part of the data set temporary non-independence and

Table 8.2: Potentially triggered volcanic eruptions after the 1906 and 1960 earthquakes

Earthquakes		Latitude		
	Date	Epicentre	Rupture N limit	Rupture S limit
	17 Aug 1906	33.0	32.0	35.0
	22 May 1960	39.5	37.5	46.0

Volcano[a]			Arc-parallel distance from earthquake:	
	Date	Latitude	epicentre	rupture zone[b]
Tupungatito	15 Feb 1907	33.4	0	-
Carrán-los Ven.	9 Apr 1907	40.4	790	560
Calbuco[c]	22 Apr 1907	41.3	900	680
Villarrica	5 May 1907	39.4	690	460
Azul[c]	28 Jul 1907	35.7	260	30
Nev. de Chillán	1907	36.9	400	170
Llaima	1907	38.7	600	380
Huequi[d]	1906	42.4	1020	790
Cordón Caulle	24 May 1960	40.5	70	-
Planchón-P.	10 Jul 1960	35.2	530	300
Tupungatito[e]	15 Jul 1960	33.4	730	510
Calbuco	1 Feb 1961	41.3	160	-
Copahue[f]	1961	37.9	230	-
Villarrica	1961	39.4	50	-
San José[d]	1960	33.8	690	460

[a] Volcanoes assumed to lie 200 km E of tabulated rupture line, which is taken to be trench-parallel.

[b] For volcanoes that lie outside the tabulated rupture zone limits.

[c] Also erupted in 1906, at unknown date (eruption excluded from analysis).

[d] Erupted at unknown date, so unclear if post-dated earthquake, and excluded from analysis (Fig. 3a).

[e] Also erupted on 5 May 1961

[f] Also erupted in 1960, at unknown date (eruption excluded from analysis).

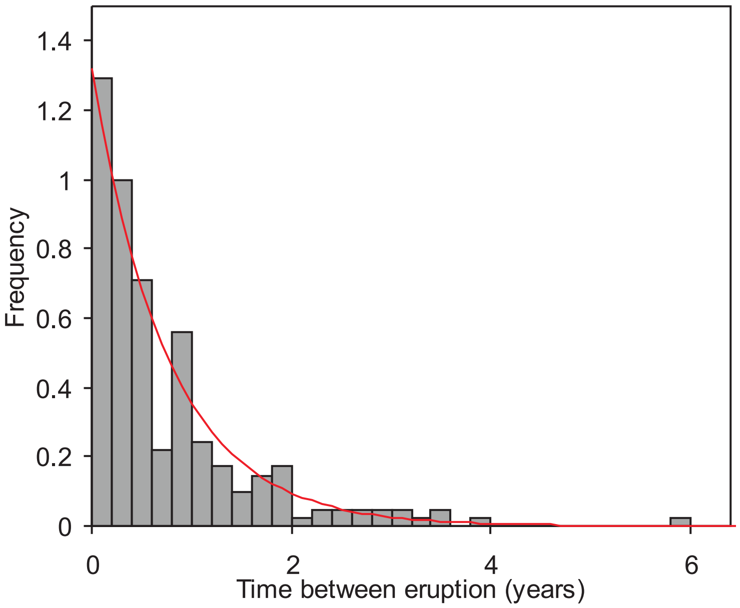

Figure 8.4: Histogram of SVZ eruption inter-event times, with a 0.2 year bin width. The data fit closely the exponential curve shown, as expected if the eruption rate on the arc scale represents a Poisson process. The peak in the histogram in the 0.8–1 year bin is an artefact from occasions in the record where only the year of eruption is recorded for consecutive events in consecutive years.

Poisson-process departure would be expected (if there is a response to external forcings such as large earthquakes), the inter-event data are consistent with an exponential distribution.

Thus, if the arc-scale eruption rate is Poissonian, the probability of six eruptions occurring in a one-year period can be calculated, and is found to be 2.0×10^{-3}. This indicates that such a rate would be expected once every 500 years. In fact, this rate occurs twice during the study period, such that the probability of this rate occurring in any year is 0.013, and hence these 'eruption clusters' do not fit well with a Poissonian model. Over the same period five great earthquakes occur, such that the probability of a great earthquake in any one year is 0.032. Thus, from the product of these, the probability of a cluster and great earthquake coinciding is 4×10^{-4}. Such a situation occurs twice in the record, on both occasions where an eruption cluster is observed, and the dates of these correspond to the two largest earthquakes in the record. Hence, it is likely that the highest eruption rates represent a departure from the typical Poissonian background eruption rate, and during these periods eruptions are not independent events, but are linked to a common cause of a preceding great earthquake. During these periods the eruption record may in fact be better modelled by a negative binomial distribution, suited to contagious events. During other parts of the record eruption occurrence is presumed to be governed by internal and continuous-external factors at any individual system, whereas during the observed clusters at least some eruptions are governed by factors relating to great earthquakes, which have the ability to affect a significant portion of the volcanoes in the arc. Following these great earthquakes, even if the background rates of volcanism were above average at the time, eruptions at 3–4 volcanoes may be plausibly assigned the status of seismically triggered events. Interestingly, the probability of five eruptions in a one-year period is 8.9×10^{-3}, but between 1863 and 1893 five volcanoes erupt in a yearly period on three occasions (in addition five eruptions occur at four volcanoes in 1932-33 and 1959) suggesting that there may be other underlying processes, besides great earthquakes, leading to enhanced eruption rates at certain times. It must be emphasised that there is no statistical basis by which any particular one of the eruptions following the 1906 or 1960 earthquakes may be asserted to be earthquake-triggered, but that there is an extremely small probability that the observed eruption rates occurred by chance.

8.4.1.2 Triggering response

Figure 8.3 begs the question of why the 1906 and 1960 earthquakes show such a clear response in eruption rate, while the other main ruptures during this period do not. There is evidence of an above-average eruption rate after the 1928 M_W 8.2 earthquake, but no such evidence following the 1939 and 1985 (M_W 8.0) earthquakes. Thus, there is a lack of correlation between eruption rate and large earthquake occurrence for the 1939 and 1985 earthquakes. This observation has been made in studies of rapid triggering [Manga and Brodsky, 2006], highlighting cases such as the 2004 Sumatra earthquake, after which no unambiguous triggering response has been observed, although subsequent eruptions in the region have been postulated as triggered events [Walter and Amelung, 2007]. Indeed, the immediate triggering examined by Linde and Sacks [1998] appears to be a relatively unusual event, perhaps requiring special conditions, given that only eight of their catalogue of 120 great earthquakes are identified as having produced rapid eruption triggering. Here, by using the arc-scale approach, it is also clear that not all great earthquakes elicit a similar eruptive response. The greater size of the 1906 and 1960 earthquakes is not an entirely satisfactory explanation; a smaller event would still be expected to show some response, albeit less pronounced. However, the mechanisms and timescale of these responses are not yet well understood.

The 1960 earthquake was much larger in terms of rupture length (940 km) and seismic moment

(M_W 9.5) than the 1906 event (330 km and M_W 8.3), and yet the post-seismic eruption rate increases are of similar magnitude. If the system disturbance is ultimately related to stress changes associated with the earthquake, some relationship with earthquake magnitude might be expected. However, an additional factor is the state of a particular volcano, in terms of how near the magmatic system is to the critical threshold at which dyke propagation may occur, which can be simply described by competing load and strength functions [cf. Jupp et al., 2004]. The greater the stress changes associated with an earthquake, the higher the probability of conditions at any individual volcano exceeding the threshold for eruption. In other words, triggered eruptions occur at volcanoes that were already likely to erupt in the near future, had the earthquake not occurred, but the occurrence of the earthquake results in systems already primed for eruption crossing an eruption threshold, and thus may produce several concomitant eruptions. At any one time, the number of volcanoes in the arc approaching this threshold is likely to vary randomly, and, given the rarity of rapid triggering observed by Linde and Sacks [1998], may also be small. Such variation is likely to be complex, and related both to internal factors at any individual volcanic system, and external factors, such as the time since the previous large earthquake. The 1906 earthquake occurred after a relatively long gap in great earthquakes. This lapse in time may have allowed more volcanic centres to approach a critical state, undisturbed by large seismic events. This analysis, revealing a variable magnitude of response to great earthquakes, suggests that the number of volcanoes primed for eruption may be highly variable. On an arc scale, therefore, the likelihood of an observable response following a large earthquake is a function both of the state of the arc's volcanoes, as well as the scale of the earthquake, and this may explain why some large earthquakes do not register an increased eruption rate.

It has been proposed by other workers that the converse relationship, an eruptive trigger to earthquakes, may exist on a range of timescales [Acharya, 1982, Lemarchand and Grasso, 2007]. There is not a clear relationship between great earthquakes and the immediately preceding arc-scale eruption rate, although prior to the 1960 earthquake the eruption rate was higher than average, with several eruptions in the SVZ and also in the Austral volcanic zone, further to the south. However, this pattern is not repeated before other large earthquakes, and the eruption rate in 1959 does not constitute a statistical outlier from the record, unlike the post-earthquake records. It is interesting, though, that the case of the 1960 earthquake does not concur with the general conclusion of Eggert and Walter [2009], who suggested that earthquakes showing a triggered response are commonly preceded by a period of volcanic silence. The relatively high eruption rate prior to the 1960 earthquake reflects the inherent variability in eruption frequency and the fluctuating background rate of volcanism in the SVZ. Other periods of increased eruption rate (Figure 8.3b) occur in the 1890s, 1930s and 1990s. This may simply be natural variation, but does hint at a periodicity, potentially related to changing crustal stress conditions through the seismic cycle [e.g., Klotz et al., 2001].

Ideally, eruption magnitude would be incorporated into this analysis. However, the major limitation to this approach is record quality and resolution, with accuracy biased towards recent events, and estimates of the past event magnitudes based on sparse data with poorly quantified uncertainties. As a preliminary analysis to investigate whether a magnitude response to great earthquakes exists, I have considered all events with some estimate, however uncertain, of magnitude. The smallest events are under-represented in this record, and only the 170 events of VEI ≥ 2 are included. This record contains five eruptions of VEI ≥ 4 (including that of Chaitén in May 2008), which show no clear correspondence to great earthquake dates. Nor do the patterns of VEI 2 and 3 events suggest any variability in eruption scale that can be related to great earthquake occurrence. This is not to say such a relationship does not exist, but a larger data-set with a better quantified and more precise measure of eruption scale would be necessary to test this hypothesis.

8.4.2 Eruption locations and seismic stresses

The locations of potentially triggered eruptions can provide constraints on the stresses that disturb magmatic systems following great earthquakes. Static stress changes decay more rapidly with distance from the fault zone than dynamic stresses. The magnitude of static stress change after an M8 earthquake is of the order of 10^{-1} MPa at 100 km, decreasing to 10^{-4} MPa at 1000 km, comparing with 3 to 0.06 MPa for dynamic stress changes in the same locations respectively [cf. Manga and Brodsky, 2006]. The two are not directly comparable, due to the transience of dynamic stresses, but the significantly greater magnitude of dynamic stresses at large distances makes them a more plausible far-field trigger. If the mechanisms involved in eruption triggering are solely due to static stress change, candidate triggered eruptions would be located predominantly in the arc section parallel to the rupture zone.

The subduction zone can be split into three segments (Figure 8.1), defined by portions of the plate boundary which fail in each seismic cycle, and spanning the latitudes 31.5–34.8°S, 34.8–38.4°S and 37.8–46°S. Data were analysed for each of these segments individually, but no strong pattern of eruption rate variation following earthquakes within the same segment was found for any of the individual segments. It is only on the arc-scale that the relationship between earthquakes and volcanism is seen, and this response is not limited to the arc-section adjacent to the rupture zone. This is clear from Table 8.2, where, in both 1906 and 1960, several of the candidate triggered eruptions occurred at locations far beyond the rupture zone. In 1906, seven of eight potentially triggered volcanoes lie outside the rupture zone, at distances of up to 790 km. In 1960, three of the potentially triggered volcanoes lie outside the rupture zone, up to a maximum distance of 450 km. This concurs with the conclusion of Linde and Sacks [1998], that seismic triggering mechanisms are capable of acting at distances of several hundred kilometres from a great earthquake rupture zone.

The strain modelling of Walter and Amelung [2007] shows that following the 1960 earthquake, the whole of the crustal region beneath the SVZ experienced volumetric strain expansion, with strain experienced at candidate triggered volcanoes ranging from > 25 µ at Cordón Caulle, Calbuco and Villarica, to 10-15 µ at Copahue, and approaching zero at Planchón, San José and Tupungatito. From the modelling, all of these systems would have experienced magma chamber dilatation, but if static changes were the sole initiator of eruptive processes, a non-zero strain threshold for the observation of such effects would be expected. Static stress changes may therefore be a plausible mechanism for eruptions such as that of Cordón Caulle, but are less so at locations experiencing very low strain, which would have experienced much larger dynamic stresses. This is reiterated by the 1906 triggered eruptions, half of which lie at > 450 km beyond the rupture zone (Table 8.2). This smaller (though poorly constrained) earthquake is unlikely to have generated significant static strains at such distances [cf. Walter and Amelung, 2007]. The prevalence of candidate triggered eruptions at distances where static stresses were minor indicates a likely important role for dynamic stresses in triggering eruptions, and suggests that both dynamic and static stresses can initiate magmatic changes that may not be manifested as eruptions for periods of several months.

The reliable eruption record only covers a period of five main ruptures. Further back in time data become sparse. While reporting bias following large earthquakes is more likely in this period, the pattern seen in Figure 8.3c is still striking. Virtually all of the great earthquakes are followed by eruptions in the following year. For example, six well-dated eruptions occurred in the nine months following the 1751 Concepción earthquake, at Planchón, Villarrica, Llaima, Callaqui, Chillán and

Antuco. Four of these volcanoes lie outside the rupture zone, at distances of up to 160 km, although in this case the rupture zone is poorly defined. In contrast, there is no clear response to the 1835 earthquake seen in Figure 8.3c (two eruptions occur in the three months prior to the earthquake, contributing to the peak). As discussed in Section 8.2.3, the contemporary reports of Caldcleugh [1836] and Darwin [1840] strongly suggest a significant volcanic response, but the record quality is insufficient for the reliable identification of specific eruptions; hence, no response is identifiable from this statistical analysis. What is also notable about the 1835 earthquake, and not cited in recent work, is a possible triggered eruption at Robinson Crusoe [Darwin, 1840, Siebert and Simkin, 2002-], in the Juan Fernández Islands. This is the only well-reported historical eruption at this Pacific Ocean island group, 635 km from Concepción, and occurred on the same day as the earthquake. If genuine, it suggests that perturbations to volcanic systems may occur quite remote from the rupture zone and in a wholly different tectonic setting, presumably due to dynamic stresses.

8.4.3 Triggering mechanisms

Given that the identified candidate triggered eruptions following the 1906 and 1960 earhtquakes lies both within the fault rupture zone latitudes and also at distances of several hundred km, it is likely that both static and dynamic stresses arising from these great earthquakes are acting as eruption triggers. However, mechanisms are required by which these stresses precipitate magmatic processes that ultimately generate eruption, with a possible time lag of several months. Many hypotheses for such processes have been proposed. The data available, which comprises only the event timings and distance separation, are not suitable to differentiate between most of these mechanisms, but it is useful to discuss them to test if they can account for the relationships observed in this analysis. Whether the effects of great earthquakes on volcanic systems persist for longer periods cannot be deduced from these records, since after approximately 12 months eruption rates fall to within the background range. The period of response that has been identified is on the order of 1 year, though this figure is difficult to constrain precisely since it is not possible to identify specific seismically triggered eruptions.

Magmatic overpressure is likely to be a key factor determining the apparent time lag before eruption [e.g., Tait et al., 1989, McLeod and Tait, 1999]. Eruptions within days of a large earthquake will only occur at magma bodies that were already near a critical eruptive overpressure.

Volcanoes displaying a slightly longer response may be slightly further below this tipping point, but stress changes must still be significant enough to produce permanent pressure changes that set the system on the path to eruption. In more general terms, the triggering event must be sufficient to initiate failure by exceeding a threshold, but the failure event (eruption) might then occur after an extended incubation period [cf. Jupp et al., 2004].

Various models have been proposed by which stresses effect physical changes and movement within the magmatic system. Static stress changes have been invoked for rapidly triggered events within the rupture zone, notably for the 1960 eruption of Cordón Caulle [Barrientos, 1994]. This eruption, within 48 hours of the May 22^{nd} earthquake, was considered to be triggered as a result of strain arising from extension beneath the volcano, which was in a mature stage of its eruptive cycle. Walter and Amelung [2007] proposed that volumetric strain expansion of rock surrounding stored magma would trigger eruption by magmatic decompression stimulating gas exsolution and ultimately increasing overpressure. The same strain changes may enhance the unclamping of fracture systems, and allow dyke formation. This model provides a plausible explanation for responses on the timescale observed, while other static changes, such as models associated with viscous relaxation in the crust [Marzocchi, 2002] are likely to act on longer timescales. However, it remains unclear why some volcanoes show a near-immediate response to static stress changes, while others may take several months for triggering effects to result in eruption. Magma composition and rheology, storage depth and state of volatile saturation, as well as system overpressure, may all play a role [e.g., Woods and Pyle, 1997, McLeod and Tait, 1999, Jellinek and DePaolo, 2003]. Particular mechanisms may also operate on different timescales, but the physical differences between each system, in terms of plumbing and crustal structure, may ultimately be the most important control in influencing the timing at which eruption occurs following the initial triggering process, and the time lag may not inform directly on potential mechanisms. Time lags of this order have been postulated before, and have been difficult to account for. For example, coupling relationships between eruptions of Vesuvius and Apennine earthquakes have been suggested to operate over a timescale of several years [Nostro et al., 1998], due to static stress changes, and in two directions, with eruptions both preceding and following earthquakes.

Dynamic stresses, due to their transience, require a mechanism by which they are rapidly converted into permanent pressure changes [Manga and Brodsky, 2006]. While such a response must be rapid, it may not result in eruption for several months. Several mechanisms proposed for triggering through the passage of seismic waves involve bubbles, which, through nucleation and growth, are of primary importance in initiating eruption. One such process involves advective overpressure, by which bubbles are dislodged by seismic waves and, through rising, transmit larger pressures across a decreasing pressure gradient. However, in most real magmas, such processes produce insufficiently large pressure changes to initiate eruption [Pyle and Pyle, 1995]. A second proposed mechanism involves rectified diffusion, whereby bubble oscillation during the passage of seismic waves results in a net addition of mass into the bubble, increasing bubble volume and magmatic pressure. Again, modelling of this process with realistic parameters suggests the resulting pressure increase is insignificant in most cases [Ichihara and Brodsky, 2006]. While both these processes increase pressure, if the change is too minor to initiate pre-eruption processes then the excess pressure is likely to dissipate over a short timescale due to gas loss and no permanent change will have arisen. Hence, in most cases, these are not considered to be important eruption triggering mechanisms. Finally, if the magma is close to volatile saturation, the pressure change associated with dynamic stresses may be sufficient to directly generate rapid bubble nucleation, leading to eruption [Manga and Brodsky, 2006].

Magmatic overturn, whereby a crystal mush at the roof of a magma chamber may be dislodged as inter-crystal yield strength decreases due to dynamic stresses, may also initiate eruption processes, by promoting vesiculation of rising magma and convection. Physical models suggest this process to be plausible [Manga and Brodsky, 2006, Davis et al., 2007], and one that may operate on the timescales of interest.

Sumita and Manga [2008] show that candidate rapidly-triggered eruptions, as well as hydrological and other seismic responses, fall within a general distance-magnitude bound, corresponding closely to the liquefaction limit for hydrological system responses. The correlation suggests a common mechanism influencing both magmatic and hydrological systems, and they suggest that liquefaction may play a role in eruption-triggering. For the 1960 earthquake, all of the candidate triggered eruptions lie inside the bounds shown by Sumita and Manga [2008], and liquefaction may provide a plausible triggering process for these events. However, for the 1906 earthquake the same magnitude-distance bounds suggest that triggered effects should not occur beyond 800 km, while three of the candidate triggered eruptions lie at or beyond this limit. Thus, results based on previously postulated triggered responses suggest that these eruptions are too distal to be earthquake-triggered.

While it is not possible to differentiate between the discussed mechanisms on the basis of these records alone, distinguishing between the postulated models may be attainable through petrological and geochemical analysis of triggered-eruption products [cf. Higgins, 2009]. For example, chemical zonation in phenocrysts may reveal the short timescale ($<$1 month – $<$1 year) pre-eruption changes in the magma system that would occur as a consequence of inter-mixing and re-equilibration of disturbed crystalline mush and melt [e.g., Morgan et al., 2004, Martin et al., 2008].

8.5 Conclusions

Eruption rates are enhanced above background levels for ∼12 months following the 1906 and 1960 earthquakes, with the onset of 3–4 eruptions estimated to have been seismically influenced in each instance. Eruption locations suggest that these effects occur from the near-field to distances of ∼500 km or more beyond the limits of the earthquake rupture zone. This suggests that both dynamic and static stresses associated with large earthquakes are important in eruption-triggering processes and have the potential to initiate volcanic eruption in arc settings over timescales of several months.

Demonstrating the occurrence of triggered eruptions on timescales beyond a few days has proven difficult using global data sets, but volcanoes in the Andean SVZ respond to earthquakes of $M > 8$ in the adjacent subduction zone through an increased rate of eruption over a period of several months. This pattern is observable in the earthquake and eruption records since 1850. The mean eruption rate in the arc is 1.32 eruptions per year. The highest eruption rates in the record show a deviation from the long-term Poissonian background trend, and occur in the 12–18 month periods following the 1906 and 1960 earthquakes, with up to eight volcanoes erupting in 1906–7. The probability of this event coinciding with the date of a great earthquake is 4×10^{-4}, a situation which occurs for the two periods of highest eruption rates. Thus, the arc-scale volcanic eruption rate does not represent an independent process during the periods of most elevated eruption rates, but is governed by the occurrence of great earthquakes in the adjacent subduction zone, which have the ability to trigger multiple eruptions over a period of several months. Based on the average eruption rate during the remainder of the record, it is likely that 3–4 eruptions were seismically triggered following each earthquake. Not all large earthquakes elicit similar responses in eruption rate, and the relationship between the two is not simply based on earthquake magnitude, but an interplay between magnitude and the number of arc volcanoes in a critical pre-eruptive state at any one time, itself highly variable and subject to multiple internal and external factors. The locations of candidate triggered eruptions suggest that triggering occurs both in the near-field, where static stress changes are likely to be important, and also at distances up to $\geq$ 500 km beyond the rupture zone. Here, dynamic stresses associated with the passage of seismic waves are likely to be the primary cause of magma body disturbance. While individual triggered eruptions cannot be identified, it is clear that seismic eruption triggering following large earthquakes, with delays of up to several months, is a significant process in volcanic arcs.

Chapter 9

Summary and Conclusions

By producing and investigating detailed observations of volcanism in southern Chile, the aim of this thesis has been to obtain a better understanding of physical volcanic processes and parameters controlling volcanic behaviour, both in the study region and in a more general sense. The results therefore provide extensive new information regarding the history of volcanic eruptions in the study areas, particularly in Hualaihue, but also provide insights regarding the influence of external systems on volcanic processes, from magma ascent through to edifice destruction, and a clearer understanding of the limits and constraints placed on the investigation of such processes based on records of past activity.

9.1 Volcanic records in Hualaihue and the SSVZ

A large amount of data relating to volcanism in the Chilean SSVZ (actually spanning the region from Calbuco to Puyuhuapi) has been collected and described in this thesis. Much of this work has focussed on the Hualaihue region, previously very little known. Holocene explosive activity in this area was relatively limited. Yate, a large stratovolcano and the main focus of Pleistocene volcanism on Hualaihue, has undergone effusive Holocene eruptions but only one minor explosive eruption of evolved magma, in contrast with extensive pumiceous units derived from stratovolcanoes both to the north (e.g., Calbuco) and south [Naranjo and Stern, 2004]. Volumetrically, tephra records preserved in the vicinity of Hualaihue are dominated by fall deposits from Calbuco, while the early Holocene eruption of Chaitén, to the south, also deposited tephra in the region.

Aside from effusive activity at Yate, Holocene explosive eruptions on Hualaihue occurred at Hornopirén and Apagado volcanoes. Both were similar in style, erupting mafic compositions in pulsatory explosions, although that of Apagado is unusual in several respects. The magma produced during the early eruption phases was picritic, in part due to olivine accumulation, and water-rich compared to the basalt erupted at Hornopirén, which was more similar to the eruptions of mafic cones along the Liquiñe-Ofqui fault zone (LOFZ). The Apagado magma also equilibrated at higher temperatures and contains more forsteritic olivines than the latter. Being at a similar trench distance to many of the arc frontal volcanoes further south (closer than centres lying on the LOFZ) highly magnesian magmas of the Apagado type may be widespread, feeding stored crustal magma systems throughout the region. This eruption forms an isolated event, and the exposure of these highly magnesian magmas at the surface is unusual, providing a window into primitive magmas away from the locus of the LOFZ, where primitive compositions are more commonly erupted.

Although trace element contents do not suggest any direct genetic relationship between the Apagado and Hornopirén magmas, further evidence of high-Mg magmas is provided by olivine phenocrysts erupted widely on the south flank of Yate, out of equilibrium in the erupted rock. In general, magma compositions and petrological characteristics suggest a variety of independently evolving stored magmas beneath the Hualaihue volcanoes, commonly mixing prior to eruption, with distinct late-Pleistocene and Holocene compositions erupted in different parts of the peninsula.

Topographically, Yate forms the major volcanic centre on Hualaihue, yet extensive eroded volcanics surround the Apagado region. However, no volcanic rocks more evolved than basaltic andesites occur away from Yate. The Holocene Apagado scoria cone is nested within an eroded ring structure, interpreted as a caldera, and the lack of more evolved compositions is surprising. It is clear, however, that the exposed rock sequence at Apagado preserves the eroded record of an older volcanic centre, and it is conduits associated with this structure that the Apagado scoria, rising from mid-crustal depths, exploited.

Volcanic structures at Hornopirén and Yate indicate tectonic controls on upper crustal magma ascent. Volcanic ridges at Yate, as elsewhere in the region, reflect dyke formation parallel to the maximum principal stress orientation of the transpressional regime along the LOFZ, while Hornopirén has a long axis associated with fracturing along a pull-apart structure on the same fault system. The main axis of Yate, however, deviates from this direction, and may reflect an older crustal structure, leading to construction of the volcano at its intersection with the LOFZ.

The three Hualaihue volcanic centres, although all active in the Holocene, may be considered a single volcanic group, and although the chemistry shows a complex magmatic system the rocks also have shared characteristics. The occurrence of multiple polygenetic eruption sites occurs further north in the region, such as at the Puyehue-Cordón Caulle system [Lara et al., 2006b], although further south each volcanic system is generally characterised by a single stratovolcanic centre. Yate-Hornopirén is likely to remain the main focus of activity on Hualaihue, since the Apagado scoria cone, although the most recent activity in the area, appears anomalous in the longer term.

The overall level of Holocene activity in Hualaihue is of a similar order to that characterising volcanoes further south, although the flux of volcanic material through all these systems remains very poorly constrained, with recognised activity at volcanoes to the south generally restricted to records of the largest explosive eruptions. Immediately to the north of Hualaihue, the record from Calbuco suggests a far greater level of activity in post-glacial time, although the reasons for this are unclear.

The location of Yate, on the LOFZ, has not only influenced the constructive evolution of the volcano, controlling dyke orientation, but has also imposed a structural grain on the volcano, modulating the pattern of its destruction through repetitive landsliding. Numerous large landslides have incised the edifice at angles slightly oblique to the strike of the LOFZ, in the Riedel shear direction. The hazard arising from edifice collapse processes at this volcano thus varies with orientation, relating to weaknesses imposed during volcano construction, relating to strain associated with the LOFZ, and perpetuated by glacial erosion. A particularly devastating landslide, triggered by heavy summer rainfall in 1965, led to a mass flow that interacted with Lago Cabrera, generating a tsunami with a run-up in excess of 50 m.

In general, activity and levels of motion along the LOFZ remain relatively poorly resolved [Lavenu and Cembrano, 1999, Rosenau et al., 2006, Adriasola and Stöckhert, 2008]. Monogenetic cones throughout the region indicate that, at least under certain conditions, fractures associated with the fault system provide a route for rapid magmatic ascent. Magmas erupting along several hundred kilometres of the LOFZ show broadly comparable compositions, with arc compositional signatures but relatively low volatile contents. At Puyuhuapi, conditions have led to the eruption of alkaline compositions, unique in a regional context, likely to reflect decompression melting of a fluid-enriched source. Although the reason for eruption of such magmas in this precise location remains unclear, the ages of both this activity and that at Palena, a little further north, appear to be restricted to the early post-glacial period, and may relate to isostatic recovery and enhanced and atypical upper crustal strain rates following removal of the regional ice sheet.

9.2 Volcanism and external processes

This thesis set out with the intention of using a range of volcanic data to assess evidence for the control or modulation of volcanism by external geological processes. In this context, external processes are those not immediately related to the volcano-magmatic system, operating within the crust or upon the Earth's surface. In any single tectonic setting, in spite of similar plate tectonic scale parameters, a wide range in eruption style, composition, magnitude, rate and explosivity occurs. Much of this variation reflects differences in crustal parameters and subduction inputs, influencing both magma generation and evolution. However, differences may also result from near-surface processes, variable on geologically small spatial and temporal scales, relating to crustal stress regimes and local tectonic structures, seismic activity or to climatic changes. The investigation of the importance, or otherwise, of such controls relies on the premise that their influence varies over time or space, and would therefore be manifested through changes in the style or rate of volcanism.

Records of volcanic activity may be examined over a range scales in order to deduce if patterns exist, potentially reflecting controlling variables operating at similar scales. Changes in eruption rate have been widely examined in the past, on a range of timescales, and several hypotheses have been developed to explain observations, with causal factors including global tectonic changes [McBirney et al., 1974, Kennett et al., 1977, Sigurdsson, 2000] and the effect of glacial cycles [e.g., Jull and McKenzie, 1996, McGuire et al., 1997] through to Earth tides and sea level changes [Dzurisin, 1980, McNutt and Beavan, 1981, McNutt, 1999, Neuberg, 2000]. The precise nature of such interactions remains, in many cases, poorly understood, but it is increasingly evident that processes external to the magmatic system may exert some control on volcanism.

The tephra record in southern Chile, documenting large explosive eruptions (magnitude >4) and compiled from this work as well as other sources, does not show definitive temporal variability in either eruption rate or volumetric flux. The length of the preserved post-glacial record decreases southwards, mapping the persistence of ice with latitude during the deglaciation period, with retreat occurring most rapidly in the north of the region. The onset of the post-glacial record, thus defined, is marked by extremely large eruptions at the most active of the region's volcanic systems: Villarrica, Llaima and Hudson. Although the lack of a prior record and a general paucity of data prevents statistically rigorous conclusions from being made, the observations are consistent with crustally stored magma accumulating to relatively greater volumes during the glacial period, with an enhanced period of magmatic release upon ice retreat. Data from the Osorno to Hudson region provide further evidence for such effects, with an increase in eruption frequency suggested for the few thousand years following deglaciation. A time lag between the recorded large explosive eruptions and the well-dated retreat of the ice sheet may reflect the timescale of the crustal response to ice retreat, if it is the changing strain rates that are important in mediating dyke formation and the ascent of magma, or may arise due to local effects relating to the, potentially delayed, retreat of summit ice caps at individual volcanoes. As mentioned above, activity on the LOFZ at Palena and Puyuhuapi represents a special case, with early eruptions potentially reflecting both enhanced ascent processes and melt generation (in the case of Puyuhuapi).

The suggestion of a relationship between deglaciation an volcanism is not new [Rampino et al., 1979, Hall, 1982, Nakada and Yokose, 1992, Jull and McKenzie, 1996, Glazner et al., 1999, Nowell et al., 2006]. Indeed, the data obtained here show a weaker pattern than might have been expected from extrapolation of results from other regional studies. The dramatic increases observed in Iceland following the last deglaciation [Maclennan et al., 2002], and other increases in settings such as continental Europe [Nowell et al., 2006] are not observed in Chile. The primary difference relates to tectonic setting, and melt generation processes in the Chile's typical continental arc do not appear to have been significantly affected by isostatic recovery following ice sheet removal. However, there is limited evidence that magma release was suppressed during deglaciation, and the controlling mechanism thus operates at upper crustal rather than mantle depths, relating to stress conditions becoming more conducive to vertical magma ascent upon ice removal [e.g., Glazner et al., 1999]. This result, the first to assess records in detail from an arc setting, suggests that global increases in volcanism upon deglaciation are likely to largely reflect contributions from non-arc volcanism, and may thus be smaller than has in some cases been postulated [e.g., Huybers and Langmuir, 2009].

Evidence of rapid timescale controls on volcanic eruption is provided by historical eruption records in the Andean SVZ, spanning over four hundred years and approaching completion for the past 150 years. These records indicate that statistical outliers in eruption rate have occurred at times corresponding to the occurrence of large earthquakes (M_W>8) in the adjacent subduction zone. Particularly large impacts on the arc-scale eruption rate occurred in 1906 and 1960, and are also suggested by limited evidence further back in the record, such as in 1751. The magnitude of the impact in part relates to random variation in the number of volcanoes in a critical pre-eruptive state, and since even in the recognised responses the number of triggered events is small (<5), the impacts of some great earthquakes are likely not to be observable above background variability (i.e. if the earthquake occurs at a time when few volcanoes are in a critical pre-eruptive state). The distance of potential triggered volcanic eruptions from the earthquake rupture zone shows that in many cases the dynamic stresses experienced by the magmatic system were far larger than the static stress changes arising from fault movement. This implies that the passage of seismic waves may set in place processes leading to eruption, even if the manifestation of this is not observed at the surface for up to several months. Triggering effects postulated in the past [e.g., Linde and Sacks, 1998, Marzocchi, 2002, Manga and Brodsky, 2006], generally for rapid eruption (e.g., within a few days) may also apply on the longer, several month, timescale demonstrated here, although the nature of magma chamber processes determining the time period between earthquake and eruption occurrence remains unclear.

More generally, as discussed above, tectonic structures and stress regimes in the continental crust control magma ascent in the southern Chilean arc, with an influence on eruption style, volcano morphology and volcano stability and collapse. In this respect, the transpressional regime and structures associated with the LOFZ have played a particularly important role in influencing the history of volcanism on the SSVZ, acting throughout the lifetime of a volcano such as Yate, from construction through to destruction processes.

The range of interactions outlined above demonstrates that the null hypothesis, of complete independence of volcanic processes from other earth systems, can be rejected. There is evidence from the southern Chilean volcanic arc that climate change on the timescale of glaciations, by exerting a control on crustal deformation, has the capacity to influence the release of magma, and hence the timing and magnitude of eruption. On short timescales seismic activity and climate systems can act as triggers to volcanic events, from eruption through to collapse processes. All of these interactions are secondary, in that they are not controlling melt formation in the arc system, but are able to mediate processes relating to melt storage, evolution and ascent. In this sense, it is useful to understand a crustal system linked by complex feedbacks, and patterns observed within a range of volcanic data can be used to provide information regarding specific processes and mechanisms leading from magma generation to volcanic eruption.

9.3 Uncertainties in volcanic records

The level of quantitative interpretation that can be made using geological records is often constrained by imprecision on incompleteness in the available data. Uncertainties in volcanic records of the types outlined in the above section limit the observation of potentially subtle controls on eruption processes, and must also be carefully accounted for when analysing such records.

The detailed mapping of the Chaitén ash fall deposit demonstrated that great complexity may arise during a relatively short eruptive episode (<1 week) if there are changes in eruption intensity and in the wind field. The mapped portion of the deposit, with sub-mm grain-size and sub-cm thicknesses is unlikely to be widely preserved beyond an annual to decadal time period, and future mapping of the unit, given the exposure and preservation typical of the region, would be limited to the proximal deposit. This restriction is clear from the regional tephrostratigraphy constructed in Chapter 6; recognition of deposits is limited to those preserved on several cm-scales, aided by coarse-ash to lapilli grain sizes, and even if finer, distal units are recognised their correlation presents difficulties. In many cases, units are constrained only by a segment of a single isopach. The outcome of this is that eruption parameters are reconstructed by assuming a simple model of a single explosive phase, fitted by elliptical isopachs, and using only proximal records. As is clear from the Chaitén 2008 deposit, the lack of constraints on the rate of distal deposit thinning can generally produce significant volume underestimates, although further complications, such as the existence of distinct depositional lobes, as from Chaitén, may also lead to overestimation if elliptical proximal isopachs are extrapolated into the distal domain. It is thus only valid to use the (proximal) data available, but this imposes limits on precise quantification of erupted volumes.

Both the relative precision of reconstruction and the recognition of past explosive eruptions is strongly influenced by eruption magnitude. The post-glacial eruption record contains far more eruptions of magnitude 3 [cf. Pyle, 2000] during the past 2 millennia than earlier in the record. The limited evidence of these moderately sized eruptions further back in the post-glacial period is restricted to volcanoes where particularly detailed studies have been undertaken. Such temporal and spatial sampling bias obscures any relatively subtle patterns or structure in the data. The changing rate of recording of smaller events can most accurately be accounted for by neglecting eruption records below a certain magnitude, but this results in a small sample size, again reducing the likelihood of observing changes within the data. Spatial sampling bias cannot easily be corrected for, and relies on the assumption that the available records are representative of the wider region. In general, even with detailed studies of the types described in this thesis, a very large part of the record of past activity remains unconstrained, not least regarding the timing and volume of effusive activity, with very few data of this type from anywhere in southern Chile. Assessments of arc-scale magmatic fluxes or long-term levels of activity at individual volcanoes thus remain difficult to quantify.

The limits imposed by the uncertainties described above are best demonstrated by considering post-glacial explosive eruptive records, examined in Chapter 7. Below magnitude 4 the record of any activity in the early post-glacial period is absent for many volcanoes, as are dated effusive eruptions. Even though magnitude estimates can be made for the recognised events (with their own uncertainties), the lack of a prior record, from the late glacial period, means that it is not possible to definitively reject the hypothesis that eruption style changed (e.g., from effusive or small-scale explosive activity to larger explosive eruptions) even if an increase in the rate of large explosive eruptions can be demonstrated for the early post-glacial period. Nonetheless, if a difference is observable between the early and later post-glacial periods then this might still suggest a departure in the early post-glacial from the longer-term steady state eruption rate. Given the general lack of data, however, the available record, adjusted to span a comparable time period across the arc, is simply too small to draw firm conclusions regarding temporal changes in activity. Furthermore, the sporadic distribution of detailed field studies (coupled with the widely variable rates of activity between volcanoes, itself not well understood) potentially introduces a spatial sampling bias even on this regional scale, since the timing of deglaciation varied with latitude, and volcanoes in the south, due to generally poorer accessibility and exposure, are less well studied. On a global scale, although data-sets are larger, such problems are compounded and unless variability in the spatial, as well as temporal, rate of sampling can be properly corrected for then changes in eruptive patterns cannot accurately be quantified.

In summary, deailed studies of contemporary events, such as the Chaitén eruption, and examination of the, albeit relatively short, historical eruption record highlight the degree to which records based on the reconstruction of past events are hindered by a lack of preservation, erosion, poor exposure and temporally and spatially variable sampling rates. It is essential that such limitations are considered when interpreting past volcanic records. At present, without more comprehensive data-sets arising from further detailed field studies, our ability to quantify and understand a range of controls and mechanisms in volcanic processes is restricted.

9.4 Future directions

The investigations of southern Chilean volcanism described in this thesis raise several questions, as well as highlighting shortcomings in the approaches used and in the records produced. Detailed analysis of past volcanic activity has the capacity to provide a wealth of information regarding volcano-magmatic mechanisms, but requires an approach combining petrological, geochemical, geophysical and modelling data, reliant upon a base of precise and comprehensive field observations.

The main limitation in interpreting rates of volcanism over thousand year timescales at present is a shortage of data, with available records heavily skewed towards the largest events and also affected by sporadic coverage, making quantitative conclusions difficult to achieve. In terms of the tephra record of southern South America, this is unlikely to be greatly improved through the study of soil sequences, but detailed investigations of lake sediment and peat core records would produce both a wider coverage of smaller events and more accurate parameterisation, reduce spatial sampling bias, and may also provide samples spanning a longer period, unaffected by late-glacial erosion, if distal samples can be taken in Argentina. Such data could then be used to test in more detail some of the hypotheses relating to changing rates of volcanism put forward in this thesis. Dated records of effusive flux at individual volcanoes would render such investigations more complete, but require significant logistical and analytical effort, posing a less tractable problem in the short term.

With regard to rapid eruption triggering, by processes such as earthquakes, there is the potential to use petrological observations [e.g., Higgins, 2009] in an effort to better understand immediately pre-eruptive process, in combination with more detailed analysis of magmatic responses to seismic stresses. Similarly, longer term variation in the petrology of eruption products may be used to assess the evidence for storage effects associated with glaciation.

Short-term impacts on the rate of volcanic hazard generation in southern Chile are likely to arise not through eruption processes, but due to increased edifice instability following ice retreat. Summit ice-cap shrinkage in response to a warming climate, debuttressing upper slopes and exposing large volumes of weathered rock, coupled with potentially raised pore-fluid pressures through meltwater generation and high altitude rainfall, may lead to increased rates of edifice destruction through landslide generation. The scale of this effect and the edifice stress changes resulting from load redistribution are poorly understood, and require further investigation, but the potential frequency, poor predictability and widespread coverage of such hazards makes them significant.

Bibliography

H. Acharya. Volcanic activity and large earthquakes. *Journal of Volcanology and Geothermal Research*, 13(3-4):373–378, 1982.

R.P. Ackert Jr., R.A. Becker, B.S. Singer, M.D. Kurz, M.W. Caffee, and D.M. Mickelson. Patagonian glacier response during the late glacial-holocene transition. *Science*, 321:392–395, 2008.

A.C. Adriasola and B. Stöckhert. Cooling histories and deformation of plutonic rocks along the Liquiñe-Ofqui Fault Zone, Southern Chile (41-42° 15'S). *Revista Geológica de Chile*, 35(1):39–61, 2008.

A.C. Adriasola, S.N. Thomson, M.R. Brix, F. Hervé, and B. Stöckhert. Postmagmatic cooling and late Cenozoic denudation of the North Patagonian Batholith in the Los Lagos region of Chile, 41°- 42° 15' S. *International Journal of Earth Sciences*, 95(3):504–528, 2006.

A. Aiuppa, P. Allard, W. D'Alessandro, A. Michel, F. Parello, M. Treuil, and M. Valenza. Mobility and fluxes of major, minor and trace metals during basalt weathering and groundwater transport at Mt. Etna volcano (Sicily). *Geochimica et Cosmochimica Acta*, 64(11):1827–1841, 2000.

B. Andersen, G.H. Denton, and T.V. Lowell. Glacial geomorphologic maps of Llanquihue drift in the area of the southern Lake District, Chile. *Geografiska Annaler: Series A*, 81(2):155–166, 1999.

D. Andronico, S. Scollo, S. Caruso, and A. Cristaldi. The 2002–03 Etna explosive activity: Tephra dispersal and features of the deposits. *Journal of Geophysical Research*, 113(B4):B04209, 2008.

R.C. Antweiler and J.I. Drever. The weathering of a late Tertiary volcanic ash: importance of organic solutes. *Geochimica et Cosmochimica Acta*, 47(3):623–629, 1983.

G. Arancibia, J. Cembrano, and A. Lavenu. Transpresión dextral y partición de la deformación en la Zona de Falla Liquiñe-Ofqui, Aisén, Chile (44-45° S). *Revista Geológica de Chile*, 26:3–22, 1999.

D. Ariztegui, M.M. Bianchi, J. Masaferro, E. Lafargue, and F. Niessen. Interhemispheric synchrony of Late-glacial climatic instability as recorded in proglacial Lake Mascardi, Argentina. *Journal of Quaternary Science*, 12(4):333–338, 1997.

N. Atmaoui, N. Kukowski, B. Stöckhert, and D. König. Initiation and development of pull-apart basins with Riedel shear mechanism: insights from scaled clay experiments. *International Journal of Earth Sciences*, 95(2):225–238, 2006.

C.R. Bacon and M.A. Lanphere. Eruptive history and geochronology of Mount Mazama and the Crater Lake region, Oregon. *Geological Society of America Bulletin*, 118:1331–1359, 2006.

C.R. Bacon, P.E. Bruggman, R.L. Christiansen, M.A. Clynne, J.M. Donnelly-Nolan, and W. Hildreth. Primitive magmas at five Cascade volcanic fields; melts from hot, heterogeneous sub-arc mantle. *Canadian Mineralogist*, 35(2):397–423, 1997.

I. Baker and S.E. Haggerty. The alteration of olivine in basaltic and associated lavas. *Contributions to Mineralogy and Petrology*, 16(3):258–273, 1967.

N.L. Bangs and S.C. Cande. Episodic development of a convergent margin inferred from structures and processes along the southern Chile margin. *Tectonics*, 16(3):489–503, 1997.

M. Barazangi and B.L. Isacks. Spatial distribution of earthquakes and subduction of the Nazca plate beneath South America. *Geology*, 4(11):686–692, 1976.

S. Barrientos and P. Acevedo. Seismological aspects of the 1988-1989 Lonquimay (Chile) volcanic eruption. *Journal of Volcanology and Geothermal Research*, 53(1-4):73–87, 1992.

S.E. Barrientos. Large thrust earthquakes and volcanic eruptions. *Pure and Applied Geophysics*, 142(1):225–237, 1994.

S.E. Barrientos and S.N. Ward. The 1960 Chile earthquake: inversion for slip distribution from surface deformation. *Geophysical Journal International*, 103(3):589–598, 1990.

F.C. Bassinot, L.D. Labeyrie, E. Vincent, X. Quidelleur, N.J. Shackleton, and Y. Lancelot. The astronomical theory of climate and the age of the Brunhes-Matuyama magnetic reversal. *Earth and Planetary Science Letters*, 126:91–108, 1994.

R.C. Bay, N. Bramall, and P.B. Price. Bipolar correlation of volcanism with millennial climate change. *Proceedings of the National Academy of Sciences*, 101(17):6341–6345, 2004.

M.S. Bebbington and C.D. Lai. On nonhomogeneous models for volcanic eruptions. *Mathematical Geology*, 28(5):585–600, 1996.

C. Beck, F. Manalt, E. Chapron, P.V. Rensbergen, and M.D. Batist. Enhanced seismicity in the early post-glacial period: evidence from the post-Würm sediments of Lake Annecy, northwestern Alps. *Journal of Geodynamics*, 22(1-2):155–171, 1996.

K.D. Bennett, S.G. Haberle, and S.H. Lumley. The last glacial-Holocene transition in southern Chile. *Science*, 290:325–328, 2000.

S. Bertrand, J. Castiaux, and E. Juvigne. Tephrostratigraphy of the late glacial and Holocene sediments of Puyehue Lake (Southern Volcanic Zone, Chile, 40 S). *Quaternary Research*, 70(3): 343–357, 2008a.

S. Bertrand, F. Charlet, B. Charlier, V. Renson, and N. Fagel. Climate variability of southern Chile since the Last Glacial Maximum: a continuous sedimentological record from Lago Puyehue (40 S). *Journal of Paleolimnology*, 39(2):179–195, 2008b.

M. Bevis and B.L. Isacks. Hypocentral trend surface analysis: Probing the geometry of Benioff zones. *Journal of Geophysical Research*, 89(B7):6153–6170, 1984.

S.P.E. Blockley, J.J. Lowe, M.J.C. Walker, A. Asioli, F. Trincardi, G.R. Coope, and R.E. Donahue. Bayesian analysis of radiocarbon chronologies: examples from the European Late-glacial. *Journal of Quaternary Science*, 19(2):159–175, 2004.

J. Blundy and K. Cashman. Ascent-driven crystallisation of dacite magmas at Mount St Helens, 1980-1986. *Contributions to Mineralogy and Petrology*, 140(6):631–650, 2001.

C. Bonadonna and B.F. Houghton. Total grain-size distribution and volume of tephra-fall deposits. *Bulletin of Volcanology*, 67(5):441–456, 2005.

C. Bonadonna, G.G.J. Ernst, and R.S.J. Sparks. Thickness variations and volume estimates of tephra fall deposits: the importance of particle Reynolds number. *Journal of Volcanology and Geothermal Research*, 81(3-4):173–187, 1998.

C. Bonadonna, C.B. Connor, B.F. Houghton, L. Connor, M. Byrne, A. Laing, and T.K. Hincks. Probabilistic modeling of tephra dispersal: Hazard assessment of a multiphase rhyolitic eruption at Tarawera, New Zealand. *Journal of Geophysical Research*, 110(B3):B03203, 2005.

N. Boultbee, D. Stead, J. Schwab, and M. Geertsema. The Zymoetz River rock avalanche, June 2002, British Columbia, Canada. *Engineering Geology*, 83(1-3):76–93, 2006.

M.J. Branney and J.S. Gilbert. Ice-melt collapse pits and associated features in the 1991 lahar deposits of Volcán Hudson, Chile: criteria to distinguish eruption-induced glacier melt. *Bulletin of Volcanology*, 57(5):293–302, 1995.

J.R. Bray. Pleistocene volcanism and glacial initiation. *Science*, 197:251–254, 1977.

S. Brazier, R.S.J. Sparks, S.N. Carey, H. Sigurdsson, and J.A. Westgate. Bimodal grain size distribution and secondary thickening in air-fall ash layers. *Nature*, 301:115–119, 1983.

E.E. Brodsky, E. Roeloffs, D. Woodcock, I. Gall, and M. Manga. A mechanism for sustained groundwater pressure changes induced by distant earthquakes. *Journal of Geophysical Research*, 108(B8):2390, 2003.

C. Bronk Ramsey. Deposition models for chronological records. *Quaternary Science Reviews*, 27 (1-2):42–60, 2008.

C. Bronk Ramsey. Bayesian analysis of radiocarbon dates. *Radiocarbon*, 51(1):337–360, 2009.

C.E. Buck, J.B. Kenworthy, C.D. Litton, and A.F.M. Smith. Combining archaeological and radiocarbon information: a Bayesian approach to calibration. *Antiquity*, 65:808–821, 1991.

A.F. Buddington and D.H. Lindsley. Iron-titanium oxide minerals and synthetic equivalents. *Journal of Petrology*, 5(2):310, 1964.

T. Cahill and B.L. Isacks. Seismicity and shape of the subducted Nazca plate. *Journal of Geophysical Research*, 97(B12):17503–17529, 1992.

A. Caldcleugh. An account of the great earthquake experienced in Chile on the 20th of February, 1835; with a map. *Philosophical Transactions of the Royal Society of London*, 126:21–26, 1836.

L. Capra. Abrupt climatic changes as triggering mechanisms of massive volcanic collapses. *Journal of Volcanology and Geothermal Research*, 155(3-4):329–333, 2006.

S. Carey and R.S.J. Sparks. Quantitative models of the fallout and dispersal of tephra from volcanic eruption columns. *Bulletin of Volcanology*, 48(2):109–125, 1986.

S.N. Carey and H. Sigurdsson. Influence of particle aggregation on deposition of distal tephra from the May 18, 1980, eruption of Mount St. Helens volcano. *Journal of Geophysical Research*, 87 (B8):7061–7072, 1982.

S.A. Carn. The Lamongan volcanic field, East Java, Indonesia: physical volcanology, historic activity and hazards. *Journal of Volcanology and Geothermal Research*, 95(1-4):81–108, 2000.

S.A. Carn, J.S. Pallister, L. Lara, J.W. Ewert, S. Watt, A.J. Prata, R.J. Thomas, and G. Villarosa. The unexpected awakening of Chaitén volcano, Chile. *EOS Transactions AGU*, 90:205–206, 2009.

J.F. Carrasco, G. Casassa, and J. Quintana. Changes of the 0 °C isotherm and the equilibrium line altitude in central Chile during the last quarter of the 20 th century. *Hydrological Sciences Journal*, 50(6):933–948, 2005.

M.A. Carrigy. Experiments on the angles of repose of granular materials. *Sedimentology*, 14(3-4): 147–158, 1970.

J.M. Castro and D.B. Dingwell. Rapid ascent of rhyolitic magma at Chaitén volcano, Chile. *Nature*, 461:780–783, 2009.

J. Cembrano and F. Hervé. The Liquiñe Ofqui fault zone: a major Cenozoic strike-slip duplex in the southern Andes. In *Second International Symposium on Andean Geodynamics, Extended Abstracts*, volume 26, pages 175–178, 1993.

J. Cembrano, M.E. Beck, R.F. Burmester, C. Rojas, A. García, and F. Hervé. Paleomagnetism of Lower Cretaceous rocks from east of the Liquine-Ofqui fault zone, southern Chile: evidence of small in-sity clockwise rotations. *Earth and planetary science letters*, 113(4):539–551, 1992.

J. Cembrano, F. Hervé, and A. Lavenu. The Liquine Ofqui fault zone: a long-lived intra-arc fault system in southern Chile. *Tectonophysics*, 259(1-3):55–66, 1996.

J. Cembrano, E. Schermer, A. Lavenu, and A. Sanhueza. Contrasting nature of deformation along an intra-arc shear zone, the Liquine–Ofqui fault zone, Southern Chilean Andes. *Tectonophysics*, 319(2):129–149, 2000.

J. Cembrano, A. Lavenu, P. Reynolds, G. Arancibia, G. López, and A. Sanhueza. Late Cenozoic transpressional ductile deformation north of the Nazca–South America–Antarctica triple junction. *Tectonophysics*, 354(3-4):289–314, 2002.

J. Cembrano, A. Lavenu, G. Yañez, R. Riquelme, M. García, G. González, and G. Hérail. Neotectonics. In T. Moreno and W. Gibbons, editors, *The Geology of Chile*, pages 231–262. The Geological Society, London, 2007.

P. Cervantes and P.J. Wallace. Role of H2O in subduction-zone magmatism: New insights from melt inclusions in high-Mg basalts from central Mexico. *Geology*, 31(3):235–238, 2003.

E. Chapron, D. Ariztegui, S. Mulsow, G. Villarosa, M. Pino, V. Outes, E. Juvignié, and E. Crivelli. Impact of the 1960 major subduction earthquake in Northern Patagonia(Chile, Argentina). *Quaternary International*, 158:58–71, 2006.

R. Charrier, L. Pinto, and M.P. Rodríguez. Tectonostratigraphic evolution of the Andean Orogen in Chile. In T. Moreno and W. Gibbons, editors, *The Geology of Chile*, pages 21–114. The Geological Society, London, 2007.

D.S. Chinn and B.L. Isacks. Accurate source depths and focal mechanisms of shallow earthquakes in western South America and in the New Hebrides island arc. *Tectonics*, 2(6):529–563, 1983.

M. Cisternas, B.F. Atwater, F. Torrejon, Y. Sawai, G. Machuca, M. Lagos, A. Eipert, C. Youlton, I. Salgado, T. Kamataki, et al. Predecessors of the giant 1960 Chile earthquake. *Nature*, 437: 404–7, 2005.

J. Clavero and H. Moreno. Evolution of Villarrica Volcano. *Boletín de Servicio Nacional de Geología y Minería, Gobierno de Chile*, 61:17–27, 2004.

J. Clavero, R. Sparks, H. Huppert, and W. Dade. Geological constraints on the emplacement mechanism of the Parinacota debris avalanche, northern Chile. *Bulletin of Volcanology*, 64(1): 40–54, 2002.

S.C. Cohen. Does rapid change in ice loading modulate strain accumulation and release in glaciated, tectonically active regions. *Geophysical Research Letters*, 20(19):2123–2126, 1993.

M. Coltelli, P. Del Carlo, and L. Vezzoli. Discovery of a Plinian basaltic eruption of Roman age at Etna volcano, Italy. *Geology*, 26(12):1095–1098, 1998.

D. Comte, A. Eisenberg, E. Lorca, M. Pardo, L. Ponce, R. Saragoni, SK Singh, and G. Suarez. The 1985 Central Chile Earthquake: A Repeat of Previous Great Earthquakes in the Region? *Science*, 233:449–453, 1986.

CONAF. Parque Nacional Hornopirén, Chapter 2: Recursos y características naturales y culturales. *CONAF (Corporación Nacional Forestal, Chile) Internal document*, 2007.

C.B. Connor, J.A. Stamatakos, D.A. Ferrill, B.E. Hill, G.I. Ofoegbu, B. Sagar, FM Conway, and J. Trapp. Geologic factors controlling patterns of small-volume basaltic volcanism- Application to a volcanic hazards assessment at Yucca Mountain, Nevada. *Journal of Geophysical Research*, 105:417–432, 2000.

C.B. Connor, B.E. Hill, B. Winfrey, N.M. Franklin, and P.C. La Femina. Estimation of volcanic hazards from tephra fallout. *Natural Hazards Review*, 2(1):33–42, 2001.

F.M. Conway, D.A. Ferrill, C.M. Hall, A.P. Morris, J.A. Stamatakos, C.B. Connor, A.N. Halliday, and C. Condit. Timing of basaltic volcanism along the Mesa Butte Fault in the San Francisco Volcanic Field, Arizona, from 40Ar/39Ar dates: Implications for longevity of cinder cone alignments. *Journal of Geophysical Research*, 102:815–824, 1997.

J.A. Cortés, M. Wilson, E. Condliffe, and L. Francalanci. The occurrence of forsterite and highly oxidizing conditions in basaltic lavas from Stromboli volcano, Italy. *Journal of Petrology*, 47(7): 1345–1373, 2006.

E. Cossart, R. Braucher, M. Fort, DL Bourlès, and J. Carcaillet. Slope instability in relation to glacial debuttressing in alpine areas (Upper Durance catchment, southeastern France): Evidence from field data and 10Be cosmic ray exposure ages. *Geomorphology*, 95(1-2):3–26, 2008.

L. Costantini, C. Bonadonna, B.F. Houghton, and H. Wehrmann. New physical characterization of the Fontana Lapilli basaltic Plinian eruption, Nicaragua. *Bulletin of Volcanology*, 71(3):337–355, 2009.

L. Costantini, B.F. Houghton, and C. Bonadonna. Constraints on eruption dynamics of basaltic explosive activity derived from chemical and microtextural study: The example of the Fontana Lapilli Plinian eruption, Nicaragua. *Journal of Volcanology and Geothermal Research*, 189(3-4): 207–224, 2010.

D.R. Cox and V. Isham. *Point processes.* Chapman and Hall, 1980.

R. Daga, S. Ribeiro Guevara, M.L. Sánchez, and M. Arribére. Source identification of volcanic ashes by geochemical analysis of well preserved lacustrine tephras in Nahuel Huapi National Park. *Applied Radiation and Isotopes*, 66(10):1325–1336, 2008.

L.V. Danyushevsky, F.N. Della-Pasqua, and S. Sokolov. Re-equilibration of melt inclusions trapped by magnesian olivine phenocrysts from subduction-related magmas: petrological implications. *Contributions to Mineralogy and Petrology*, 138(1):68–83, 2000.

L.V. Danyushevsky, S. Sokolov, and T.J. Falloon. Melt inclusions in olivine phenocrysts: using diffusive re-equilibration to determine the cooling history of a crystal, with implications for the origin of olivine-phyric volcanic rocks. *Journal of Petrology*, 43(9):1651–1671, 2002.

C. Darwin. Darwin's Beagle Diary (1831-1836). *http://darwin-online.org.uk/*, 1835.

C. Darwin. On the connexion of certain volcanic phenomena in South America; and on the formation of mountain chains and volcanos, as the effect of the same power by which continents are elevated: Geological Society [London] Transactions, v. 2. *Transactions of the Geological Society of London, 2d ser., pt*, 3(5):601–631, 1840.

M. Davis, M.A. Koenders, and N. Petford. Vibro-agitation of chambered magma. *Journal of Volcanology and Geothermal Research*, 167(1-4):24–36, 2007.

S.N. Davis and J.K. Karzulovíc. Landslides at Lago Riñihue, Chile. *Bulletin of the Seismological Society of America*, 53(6):1403–1414, 1963.

C.S. de Fontaine, D.S. Kaufman, R. Scott Anderson, A. Werner, C.F. Waythomas, and T.A. Brown. Late Quaternary distal tephra-fall deposits in lacustrine sediments, Kenai Peninsula, Alaska. *Quaternary Research*, 68(1):64–78, 2007.

M. De Saint Blanquat, B. Tikoff, C. Teyssier, and J.L. Vigneresse. Transpressional kinematics and magmatic arcs. *Geological Society London Special Publication*, 135(1):327–340, 1998.

W.A. Deer, R.A. Howie, and J. Zussman. *Rock-forming minerals. Volume 2A, single-chain silicates.* Longman, 1978.

P.T. Delaney, D.D. Pollard, J.I. Ziony, and E.H. McKee. Field relations between dikes and joints: emplacement processes and paleostress analysis. *Journal of Geophysical Research*, 91:4920–4938, 1986.

C. DeMets, R.G. Gordon, D.F. Argus, and S. Stein. Effect of recent revisions to the geomagnetic reversal time scale on estimates of current plate motions. *Geophysical Research Letters*, 21(20): 2191–2194, 1994.

G.H. Denton, C.J. Heusser, T.V. Lowell, P.I. Moreno, B.G. Andersen, L.E. Heusser, C. Schluchter, and D.R. Marchant. Interhemispheric linkage of paleoclimate during the last glaciation. *Geografiska Annaler: Series A*, 81(2):107–153, 1999a.

G.H. Denton, T.V. Lowell, C.J. Heusser, C. Schluchter, B.G. Andersen, L.E. Heusser, P.I. Moreno, and D.R. Marchant. Geomorphology, Stratigraphy, and Radiocarbon Chronology of Llanquihue Drift in the Area of the Southern Lake District, Seno Reloncavi, and Isla Grande de Chiloe, Chile. *Geografiska Annaler: Series A*, 81(2):167–229, 1999b.

J.F. Dewey and S.H. Lamb. Active tectonics of the Andes. *Tectonophysics*, 205(1-3):79–95, 1992.

R.S. D'lemos, M. Brown, and R.A. Strachan. Granite magma generation, ascent and emplacement within a transpressional orogen. *Journal of the Geological Society*, 149(4):487–490, 1992.

E. Dobrovolny, R. Lemke, W. Bowes, H. Thomas, N. Bravo S, and P. Saint-Amand. Relation between geology and the damage in Puerto Montt, Chile, caused by the earthquake of 22 May 1960. *Bulletin of the Seismological Society of America*, 53(6):1299–1314, 1963.

M. D'Orazio, F. Innocenti, P. Manetti, M. Tamponi, S. Tonarini, O. González-Ferrán, A. Lahsen, and R. Omarini. The Quaternary calc-alkaline volcanism of the Patagonian Andes close to the Chile triple junction: geochemistry and petrogenesis of volcanic rocks from the Cay and Maca volcanoes (45° S, Chile). *Journal of South American Earth Sciences*, 16(4):219–242, 2003.

G.T.R. Droop. A general equation for estimating Fe3+ concentrations in ferromagnesian silicates and oxides from microprobe analyses, using stoichiometric criteria. *Mineralogical Magazine*, 51 (361):431–435, 1987.

A.J. Dugmore, A.J. Newton, D.E. Sugden, and G. Larsen. Geochemical stability of fine-grained silicic Holocene tephra in Iceland and Scotland. *Journal of Quaternary Science*, 7(2), 1992.

M.A. Dungan, A. Wulff, and R. Thompson. Eruptive Stratigraphy of the Tatara-San Pedro Complex, 36°S, Southern Volcanic Zone, Chilean Andes: Reconstruction Method and Implications for Magma Evolution at Long-lived Arc Volcanic Centers. *Journal of Petrology*, 42(3):555–626, 2001.

A.J. Durant, R.A. Shaw, W.I. Rose, Y. Mi, and G.G.J. Ernst. Ice nucleation and overseeding of ice in volcanic clouds. *Journal of Geophysical Research*, 113(D9):D09206, 2008.

A.J. Durant, W.I. Rose, A.M. Sarna-Wojcicki, S. Carey, and A.C.M. Volentik. Hydrometeor-enhanced tephra sedimentation: Constraints from the 18 May 1980 eruption of Mount St. Helens. *Journal of Geophysical Research*, 114(B3):B03204, 2009.

D. Dzurisin. Influence of fortnightly earth tides at Kilauea Volcano, Hawaii. *Geophysical Research Letters*, 7(11):925–928, 1980.

J. Echegaray, H. Moreno, and L. López-Escobar. El depósito de pómez pliniana del Centro Volcánico Mocho-Choshuenco, Andes del Sur (40°S), Chile. *Actas 7th Chilean Geological Congress, Concepción*, 1:269–272, 1994.

S. Eggert and T.R. Walter. Volcanic activity before and after large tectonic earthquakes: Observations and statistical significance. *Tectonophysics*, 471(1-2):14–26, 2009.

G.G.J. Ernst, R.S.J. Sparks, S.N. Carey, and M.I. Bursik. Sedimentation from turbulent jets and plumes. *Journal of Geophysical Research*, 101(B3):5575–5589, 1996.

S.G. Evans. The 1946 Mount Colonel Foster rock avalanche and associated displacement wave, Vancouver Island, British Columbia. *Canadian Geotechnical Journal*, 26(3):447–452, 1989.

S.G. Evans, J.J. Clague, G.J. Woodsworth, and O. Hungr. The Pandemonium Creek rock avalanche, British Columbia. *Canadian Geotechnical Journal*, 26(3):427–446, 1989.

S.G. Evans, O. Hungr, and J.J. Clague. Dynamics of the 1984 rock avalanche and associated distal debris flow on Mount Cayley, British Columbia, Canada; implications for landslide hazard assessment on dissected volcanoes. *Engineering Geology*, 61(1):29–51, 2001.

S.G. Evans, R.H. Guthrie, N.J. Roberts, and N.F. Bishop. The disastrous 17 February 2006 rockslide-debris avalanche on Leyte Island, Philippines: a catastrophic landslide in tropical mountain terrain. *Natural Hazards and Earth System Science*, 7(1):89–101, 2007.

J. Fierstein and M. Nathenson. Another look at the calculation of fallout tephra volumes. *Bulletin of Volcanology*, 54(2):156–167, 1992.

T.J. Fitch. Plate convergence, transcurrent faults, and internal deformation adjacent to southeast Asia and the western Pacific. *Journal of Geophysical Research*, 77(23):4432–4460, 1972.

R. FitzRoy. *Narrative of the Surveying Voyages of His Majesty's Ships Adventure and Beagle between the years 1826 and 1836, vol. 2.* Henry Colburn, London, 1839.

Flash. El lago Cabrera ahogo a un pueblo. *Flash, Santiago, Chile, 26th February 1965, no. 84, Año 11, aero norte*, 1965.

A. Folch and A. Felpeto. A coupled model for dispersal of tephra during sustained explosive eruptions. *Journal of Volcanology and Geothermal Research*, 145(3-4):337–349, 2005.

A. Folch, O. Jorba, and J. Viramonte. Volcanic ash forecast application to the May 2008 Chaitén eruption. *Natural Hazards and Earth System Sciences*, 8:927–940, 2008.

A. Folguera, V. Ramos, R.L. Hermanns, and J. Naranjo. Neotectonics in the foothills of the Southernmost Central Andes (37°-38° S). Evidence of the strike-slip displacement along the Antiñir-Copahue fault zone. *Tectonics*, 62(3):TC5008, 2004.

R. Forsythe and E. Nelson. Geological manifestations of ridge collision: evidence from the Golfo de Penas-Taitao Basin, Southern Chile. *Tectonics*, 4(5):477–495, 1985.

R.D. Forsythe and J.A. Diemer. Late Cenozoic movement associated with the arc-parallel Liquiñe-Ofqui fault zone and the Chile triple junction documented by acoustic profiling of shallow marine and lacustrine deposits of southern Chile. In *GSA Speciality Meeting (Backbone of the Americas) Abstracts with Programs*, volume 2, page 48, 2006.

A. Freundt, W. Strauch, S. Kutterolf, and H.U. Schmincke. Volcanogenic tsunamis in lakes: examples from Nicaragua and general implications. *Pure and Applied Geophysics*, 164(2):527–545, 2007.

P.A. Friele, J.J. Clague, K. Simpson, and M. Stasiuk. Impact of a quaternary volcano on holocene sedimentation in Lillooet River valley, British Columbia. *Sedimentary Geology*, 176:305–322, 2005.

G.A. Gaetani and E.B. Watson. Modeling the major-element evolution of olivine-hosted melt inclusions. *Chemical Geology*, 183(1-4):25–41, 2002.

E.S. Gaffney, B. Damjanac, and G.A. Valentine. Localization of volcanic activity: 2. Effects of pre-existing structure. *Earth and Planetary Science Letters*, 263(3-4):323–338, 2007.

D.M. Gaiero, F. Brunet, J.L. Probst, and P.J. Depetris. A uniform isotopic and chemical signature of dust exported from Patagonia: Rock sources and occurrence in southern environments. *Chemical geology*, 238(1-2):107–120, 2007.

A. Garcia, M.E. Beck, R.F. Burmester, F. Munizaga, and F. Hervé. Palaeomagnetic reconnaissance of the region of Los Lagossouthern Chile, and its tectonic implications. *Revista Geológica de Chile*, 15:13–30, 1988.

M.A.M. Gee, R.N. Taylor, M.F. Thirlwall, and B.J. Murton. Glacioisostacy controls chemical and isotopic characteristics of tholeiites from the Reykjanes Peninsula, SW Iceland. *Earth and Planetary Science Letters*, 164(1-2):1–5, 1998.

S.R. Gislason and S. Arnórsson. Dissolution of primary basaltic minerals in natural waters: saturation state and kinetics. *Chemical geology*, 105(1-3):117–135, 1993.

S.R. Gislason, S. Arnorsson, and H. Armannsson. Chemical weathering of basalt in Southwest Iceland; effects of runoff, age of rocks and vegetative/glacial cover. *American Journal of Science*, 296(8):837, 1996.

N.F. Glasser, S. Harrison, V. Winchester, and M. Aniya. Late Pleistocene and Holocene palaeoclimate and glacier fluctuations in Patagonia. *Global and Planetary Change*, 43(1-2):79–101, 2004.

N.F. Glasser, K.N. Jansson, S. Harrison, and J. Kleman. The glacial geomorphology and Pleistocene history of South America between 38°S and 56°S. *Quaternary Science Reviews*, 27: 365–390, 2008.

A.F. Glazner, C.R. Manley, J.S. Marron, and S. Rojstaczer. Fire or ice: Anticorrelation of volcanism and glaciation in California over the past 800,000 years. *Geophysical Research Letters*, 26 (12):1759–1762, 1999.

The Global CMT Project. Global Centroid Moment Tensor database. *http://www.globalcmt.org/*, 2010-.

C.S.G. Gogorza, A.M. Sinito, I.D. Tommaso, J.F. Vilas, K.M. Creer, and H. Nunez. Geomagnetic secular variations 0–12kyr as recorded by sediments from Lake Moreno (southern Argentina). *Journal of South American Earth Sciences*, 13(7):627–645, 2000.

O. González-Ferrán. *Volcanes de Chile*. Instituto Geográfico Militar, Santiago, Chile, 1995.

O. González Ferrán, F. Innocenti, A. Lahsen, P. Manetti, R. Mazzuoli, R. Omarini, and M. Tamponi. Alkali basalt volcanism along a subduction related magmatic arc: the case of Puyuhuapi quaternary volcanic line, southern Andes, 44°20'S. *XIII Congreso Geológico Argentino y III Congreso de Exploración de Hidrocarburos, Actas*, 3:549–565, 1996.

D.H. Green. Experimental melting studies on a model upper mantle composition at high pressure under water-saturated and water-undersaturated conditions. *Earth and Planetary Science Letters*, 19:37–53, 1973.

T.L. Grove and T.C. Juster. Experimental investigations of low-Ca pyroxene stability and olivine-pyroxene-liquid equilibria at 1-atm in natural basaltic and andesitic liquids. *Contributions to Mineralogy and Petrology*, 103(3):287–305, 1989.

F. Gutiérrez, A. Gioncada, O. González Ferran, A. Lahsen, and R. Mazzuoli. The Hudson Volcano and surrounding monogenetic centres (Chilean Patagonia): An example of volcanism associated with ridge–trench collision environment. *Journal of Volcanology and Geothermal Research*, 145 (3-4):207–233, 2005.

Y. Guyodo and J.P. Valet. Global changes in intensity of the Earth's magnetic field during the past 800 kyr. *Nature*, 399:249–252, 1999.

S.G. Haberle and S.H. Lumley. Age and origin of tephras recorded in postglacial lake sediments to the west of the southern Andes, 44 S to 47 S. *Journal of Volcanology and Geothermal Research*, 84(3-4):239–256, 1998.

R. Hackney, H. Echtler, G. Franz, H.J. Götze, F. Lucassen, D. Marchenko, D. Melnick, U. Meyer, S. Schmidt, Z. Tašárová, et al. The segmented overriding plate and coupling at the south-central Chilean margin (36–42° S). *The Andes–active subduction orogeny. Frontiers in Earth Science Series*, 1:355–374, 2006.

S.E. Haggerty and I. Baker. The alteration of olivine in basaltic and associated lavas. *Contributions to Mineralogy and Petrology*, 16(3):233–257, 1967.

I. Hajdas, G. Bonani, P.I. Moreno, and D. Ariztegui. Precise radiocarbon dating of Late-Glacial cooling in mid-latitude South America. *Quaternary Research*, 59(1):70–78, 2003.

K. Hall. Rapid deglaciation as an initiator of volcanic activity: An hypothesis. *Earth Surface Processes and Landforms*, 7(1):45–51, 1982.

A. Hampel and R. Hetzel. Response of normal faults to glacial-interglacial fluctuations of ice and water masses on Earth's surface. *Journal of Geophysical Research*, 111(B6):B06406, 2006.

R.S. Harmon, B.A. Barreiro, S. Moorbath, J. Hoefs, P.W. Francis, R.S. Thorpe, B. Deruelle, J. McHugh, and J.A. Viglino. Regional O-, Sr-, and Pb-isotope relationships in late Cenozoic calc-alkaline lavas of the Andean Cordillera. *Journal of the Geological Society*, 141(5):803, 1984.

A.J.L. Harris and M. Ripepe. Regional earthquake as a trigger for enhanced volcanic activity: Evidence from MODIS thermal data. *Geophysical Research Letters*, 34(2):2304, 2007.

A. Hauser. Flujos aluvionales de 1870 y 1896 ocurridos en la ladera norte del volcan Yates, X región: su implicancia en la evaluación de riesgos naturales. *Revista Geológica de Chile*, 25–26: 125–133, 1985.

N.A. Heckert and J.J. Filliben. *NIST Handbook 148: DATAPLOT Reference Manual.* National Institute of Standards and Technology Handbook Series, 2003.

E.M. Herron. Chile Margin near lat 38° S: Evidence for a genetic relationship between continental and marine geologic features or a case of curious coincidences? *Geological Society of America, Memoir*, 31(2), 1981.

F. Hervé and Y. Ota. Fast Holocene uplift rates at the Andes of Chiloé, southern Chile. *Revista Geológica de Chile*, 20(1):15–23, 1993.

F. Hervé, R.J. Pankhurst, R. Drake, and M.E. Beck. Pillow metabasalts in a mid-tertiary extensional basin adjacent to the Liquiñe-Ofqui fault zone: the Isla Magdalena area, Aysén, Chile. *Journal of South American Earth Sciences*, 8(1):33–46, 1995.

F. Hervé, S.F.M. Calderón, H.-J. Massonne, and A.P. Willner. Metamorphic and plutonic basement complexes. In T. Moreno and W. Gibbons, editors, *The Geology of Chile*, pages 5–19. The Geological Society, London, 2007.

F. Hervé. The Southern Andes between 39° and 44° S latitude: the geological signature of a transpressive tectonic regime related to a magmatic arc. In K.-J. Reutter, E. Scheuber, and P. Wigger, editors, *Tectonics of the Southern Central Andes*, pages 243–248. Springer, Berlin, 1994.

F. Hervé, R.J. Pankhurst, R. Drake, M.E. Beck, and C. Mpodozis. Granite generation and rapid unroofing related to strike-slip faulting, Aysén, Chile. *Earth and planetary science letters*, 120 (3-4):375–386, 1993.

C.J. Heusser. Vegetation and climate of the southern Chilean Lake District during and since the last interglaciation. *Quaternary Research*, 4(3):290–315, 1974.

C.J. Heusser. On glaciation of the southern Andes with special reference to the Península de Taitao and adjacent Andean cordillera (46° 30' S). *Journal of South American Earth Sciences*, 15(5): 577–589, 2002.

C.J. Heusser and L.E. Heusser. Submillennial palynology and palaeoecology of the last glaciation at Taiquemó (50,000 cal yr, MIS 2–4) in southern Chile. *Quaternary Science Reviews*, 25(5-6): 446–454, 2006.

C.J. Heusser, L.E. Heusser, and A. Hauser. Paleoecology of late Quaternary deposits in Chiloé continental, Chile. *Revista Chilena de Historia Natural*, 65:235–245, 1992.

C.J. Heusser, L.E. Heusser, and T.V. Lowell. Paleoecology of the southern Chilean Lake District-Isla Grande de Chiloe during middle-late Llanquihue glaciation and deglaciation. *Geografiska Annaler: Series A*, 81(2):231–284, 1999.

C.J. Heusser, T.V. Lowell, L.E. Heusser, A. Moreira, and S. Moreira. Pollen sequence from the Chilean Lake District during the Llanquihue glaciation in marine Oxygen Isotope Stages 4-2. *Journal of Quaternary Science*, 15(2):115–125, 2000.

L. Heusser, C. Heusser, and N. Pisias. Vegetation and climate dynamics of southern Chile during the past 50,000 years: results of ODP Site 1233 pollen analysis. *Quaternary Science Reviews*, 25(5-6):474–485, 2006.

R.L. Hickey, F.A. Frey, D.C. Gerlach, and L. Lopez-Escobar. Multiple sources for basaltic arc rocks from the southern volcanic zone of the Andes (34°–41° S): trace element and isotopic evidence for contributions from subducted oceanic crust, mantle, and continental crust. *Journal of Geophysical Research*, 91(B6):5963–5983, 1986.

R. Hickey-Vargas and M. Sun. Decompression and flux melting in the Chilean Southern Volcanic Zone: Implications for Slab-Wedge and Wedge-Crust mass transfer. *SOTA 2004, Mt Hood, Oregon, Abstracts*, 2004.

R. Hickey-Vargas, M. Sun, L. López-Escobar, H. Moreno-Roa, M.K. Reagan, J.D. Morris, and J.G. Ryan. Multiple subduction components in the mantle wedge: evidence from eruptive centers in the Central Southern volcanic zone, Chile. *Geology*, 30(3):199–202, 2002.

M.D. Higgins. The Cascadia megathrust earthquake of 1700 may have rejuvenated an isolated basalt volcano in western Canada: Age and petrographic evidence. *Journal of Volcanology and Geothermal Research*, 179(1-2):149–156, 2009.

W. Hildreth and S. Moorbath. Crustal contributions to arc magmatism in the Andes of Central Chile. *Contributions to Mineralogy and Petrology*, 98:455–489, 1988.

W. Hildreth and S. Moorbath. Reply to Comment on "Crustal contributions to arc magmatism in the Andes of Central Chile" by W. Hildreth and S. Moorbath. *Contributions to Mineralogy and Petrology*, 108(1):247–252, 1991.

D.P. Hill, P.A. Reasenberg, A. Michael, W.J. Arabaz, G. Beroza, D. Brumbaugh, J.N. Brune, R. Castro, S. Davis, D. dePolo, et al. Seismicity Remotely Triggered by the Magnitude 7.3 Landers, California, Earthquake. *Science*, 260:1617–1623, 1993.

D.P. Hill, F. Pollitz, and C. Newhall. Earthquake-volcano interactions. *Physics Today*, 55(11): 41–47, 2002.

R.W. Hinton. Ion microprobe trace-element analysis of silicates: Measurement of multi-element glasses. *Chemical Geology*, 83(1-2):11–25, 1990.

J.M. Hora, B.S. Singer, and G. Wörner. Volcano evolution and eruptive flux on the thick crust of the Andean Central Volcanic Zone: 40Ar/39Ar constraints from Volcán Parinacota, Chile. *Geological Society of America Bulletin*, 119(3):343–362, 2007.

C.J. Horwell and P.J. Baxter. The respiratory health hazards of volcanic ash: a review for volcanic risk mitigation. *Bulletin of Volcanology*, 69(1):1–24, 2006.

C.J. Horwell, S. Michnowicz, and J. Le Blond. Report on the mineralogical and geochemical characterisation of Chaitén ash for the assessment of respiratory health hazard. *Univ. Durham/IVHHN report*, 2008.

B.F. Houghton and H.M. Gonnermann. Basaltic explosive volcanism: Constraints from deposits and models. *Chemie der Erde-Geochemistry*, 68(2):117–140, 2008.

C. Huggel, J. Caplan-Auerbach, C.F. Waythomas, and R.L. Wessels. Monitoring and modeling ice-rock avalanches from ice-capped volcanoes: A case study of frequent large avalanches on Iliamna Volcano, Alaska. *Journal of Volcanology and Geothermal Research*, 168(1-4):114–136, 2007.

N.R.J. Hulton, R.S. Purves, R.D. McCulloch, D.E. Sugden, and M.J. Bentley. The last glacial maximum and deglaciation in southern South America. *Quaternary Science Reviews*, 21(1-3): 233–241, 2002.

O. Hungr and S.G. Evans. Entrainment of debris in rock avalanches: An analysis of a long run-out mechanism. *Bulletin of the Geological Society of America*, 116(9-10):1240–1252, 2004.

P. Huybers and C. Langmuir. Feedback between deglaciation, volcanism, and atmospheric CO_2. *Earth and Planetary Science Letters*, 286:479–491, 2009.

G. Iaffaldano and H.P. Bunge. Strong plate coupling along the Nazca-South America convergent margin. *Geology*, 36(6):443–446, 2008.

M. Ichihara and E.E. Brodsky. A limit on the effect of rectified diffusion in volcanic systems. *Geophysical Research Letters*, 33(2), 2006.

IGM. *Mapa Geologico de Chile, 1:1,000,000.* Instituto Geográfico Militar, Santiago, Chile, 1968.

D.L. Inman. Measures for describing the size distribution of sediments. *Journal of Sedimentary Petrology*, 22(3):125–145, 1952.

T.N. Irvine and W.R.A. Baragar. A guide to the chemical classification of the common volcanic rocks. *Canadian Journal of Earth Sciences*, 8(5):523–548, 1971.

R.M. Iverson. Landslide triggering by rain infiltration. *Water Resources Research*, 36(7):1897–1910, 2000.

E.R. Ivins and T.S. James. Simple models for late Holocene and present-day Patagonian glacier fluctuations and predictions of a geodetically detectable isostatic response. *Geophysical Journal International*, 138(3):601–624, 1999.

E.R. Ivins and T.S. James. Bedrock response to Llanquihue Holocene and present-day glaciation in southernmost South America. *Geophysical Research Letters*, 31(24):L24613, 2004.

M. Jakob. A size classification for debris flows. *Engineering geology*, 79(3-4):151–161, 2005.

T.S. James and A.L. Bent. A comparison of eastern North American seismic strain-rates to glacial rebound strain-rates. *Geophysical Research Letters*, 21(19):2127–2130, 1994.

T.S. James, J.J. Clague, K. Wang, and I. Hutchinson. Postglacial rebound at the northern Cascadia subduction zone. *Quaternary Science Reviews*, 19(14):1527–1542, 2000.

A.M. Jellinek and D.J. DePaolo. A model for the origin of large silicic magma chambers: precursors of caldera-forming eruptions. *Bulletin of Volcanology*, 65(5):363–381, 2003.

A.M. Jellinek, M. Manga, and M.O. Saar. Did melting glaciers cause volcanic eruptions in eastern California? Probing the mechanics of dike formation. *Journal of Geophysical Research*, 109: B09206, 2004.

A.C. Johnston. The effect of large ice sheets on earthquake genesis. In S. Gregerson and P.W. Basham, editors, *Earthquakes at North-Atlantic Passive Margins: Neotectonics and Postglacial Rebound*, pages 581–599. Kluwer Academic Pub, 1989.

A.D. Johnston and J.H. Stout. Development of orthopyroxene-Fe/Mg ferrite symplectites by continuous olivine oxidation. *Contributions to Mineralogy and Petrology*, 88(1):196–202, 1984.

P. Johnston, P. Wu, and K. Lambeck. Dependence of horizontal stress magnitude on load dimension in glacial rebound models. *Geophysical Journal International*, 132(1):41–60, 1998.

T.E. Jordan, W.M. Burns, R. Veiga, F. Pángaro, P. Copeland, S. Kelley, and C. Mpodozis. Extension and basin formation in the southern Andes caused by increased convergence rate: a mid-Cenozoic trigger for the Andes. *Tectonics*, 20(3):308–324, 2001.

P.C. Jowsey. An improved peat sampler. *New Phytologist*, 65(2):245–248, 1966.

M. Jull and D. McKenzie. The effect of deglaciation on mantle melting beneath Iceland. *Journal of Geophysical Research*, 101(B10):21815–21828, 1996.

T.E. Jupp, D.M. Pyle, B.G. Mason, and W.B. Dade. A statistical model for the timing of earthquakes and volcanic eruptions influenced by periodic processes. *Journal of Geophysical Research*, 109:B02206, 2004.

S. Kay and C. Mpodozis. Magmatism as a probe to the Neogene shallowing of the Nazca plate beneath the modern Chilean flat-slab. *Journal of South American Earth Sciences*, 15(1):39–57, 2002.

S.M. Kay and R.W. Kay. Aleutian tholeiitic and calc-alkaline magma series I: The mafic phenocrysts. *Contributions to Mineralogy and Petrology*, 90(2):276–290, 1985.

S.M. Kay, E. Godoy, and A. Kurtz. Episodic arc migration, crustal thickening, subduction erosion, and magmatism in the south-central Andes. *Bulletin of the Geological Society of America*, 117 (1-2):67–88, 2005.

J.A. Kelleher. Rupture zones of large South American earthquakes and some predictions. *Journal of Geophysical Research*, 77(11):2087–2103, 1972.

C.H. Kelsey. Calculation of the CIPW norm. *Mineralogical Magazine*, 34(268):276–282, 1965.

E. Kendrick, M. Bevis, R. Smalley, B. Brooks, R.B. Vargas, E. Laurıá, and L.P.S. Fortes. The Nazca–South America Euler vector and its rate of change. *Journal of South American Earth Sciences*, 16(2):125–131, 2003.

J.P. Kennett, A.R. McBirney, and R.C. Thunell. Episodes of Cenozoic volcanism in the circum-Pacific region. *Journal of Volcanology and Geothermal Research*, 2:145–163, 1977.

A.J.R. Kent. Melt inclusions in basaltic and related volcanic rocks. *Reviews in Mineralogy and Geochemistry*, 69(1):273–331, 2008.

A.J.R. Kent and T.R. Elliott. Melt inclusions from Marianas arc lavas: implications for the composition and formation of island arc magmas. *Chemical Geology*, 183(1-4):263–286, 2002.

N. Kerle. Volume estimation of the 1998 flank collapse at Casita volcano, Nicaragua: a comparison of photogrammetric and conventional techniques. *Earth Surface Processes and Landforms*, 27 (7):759–772, 2002.

N. Kerle, B. van Wyk de Vries, and C. Oppenheimer. New insights into the factors leading to the 1998 flank collapse and lahar disaster at Casita volcano, Nicaragua. *Bulletin of Volcanology*, 65 (5):331–345, 2003.

G. Khazaradze and J. Klotz. Short-and long-term effects of GPS measured crustal deformation rates along the south central Andes. *Journal of Geophysical Research*, 108(B6):2289, 2003.

R. Kilian and L. López-Escobar. Petrology of the Southern Southandean Volcanic Zone (41-46°S) with emphasis on the Michinmáhuida-Chaitén complex. *Zeitblatt Geologie und Paläontologie, Teil 1*, 6:1693–1708, 1991.

J.L. Kirschvink. The least-squares line and plane and the analysis of paleomagnetic data. *Geophysical Journal of the Royal Astronomical Society*, 62(3):699–718, 1980.

J. Klotz, G. Khazaradze, D. Angermann, C. Reigber, R. Perdomo, and O. Cifuentes. Earthquake cycle dominates contemporary crustal deformation in Central and Southern Andes. *Earth and Planetary Science Letters*, 193(3-4):437–446, 2001.

E.J. Kohut, R.J. Stern, A.J.R. Kent, R.L. Nielsen, S.H. Bloomer, and M. Leybourne. Evidence for adiabatic decompression melting in the Southern Mariana Arc from high-Mg lavas and melt inclusions. *Contributions to Mineralogy and Petrology*, 152(2):201–221, 2006.

I. Koukouvelas, G. Pe-Piper, and D.J.W. Piper. The role of dextral transpressional faulting in the evolution of an early Carboniferous mafic–felsic plutonic and volcanic complex: Cobequid Highlands, Nova Scotia, Canada. *Tectonophysics*, 348(4):219–246, 2002.

D.J. Kratzmann, S. Carey, R. Scasso, and J.A. Naranjo. Compositional variations and magma mixing in the 1991 eruptions of Hudson volcano, Chile. *Bulletin of Volcanology*, 71(4):419–439, 2009.

V.C. Kress and M.S. Ghiorso. Thermodynamic modeling of post-entrapment crystallization in igneous phases. *Journal of Volcanology and Geothermal Research*, 137(4):247–260, 2004.

A.C. Kurtz, L.A. Derry, O.A. Chadwick, and M.J. Alfano. Refractory element mobility in volcanic soils. *Geology*, 28(8):683–686, 2000.

A.M.F. Lagmay and W. Valdivia. Regional stress influence on the opening direction of crater amphitheaters in Southeast Asian volcanoes. *Journal of Volcanology and Geothermal Research*, 158(1-2):139–150, 2006.

A.M.F. Lagmay, B. van Wyk de Vries, N. Kerle, and D.M. Pyle. Volcano instability induced by strike-slip faulting. *Bulletin of Volcanology*, 62(4):331–346, 2000.

K. Lambeck, P. Johnston, and M. Nakada. Holocene glacial rebound and sea-level change in NW Europe. *Geophysical Journal International*, 103(2):451–468, 1990.

F. Lamy, D. Hebbeln, U. Röhl, and G. Wefer. Holocene rainfall variability in southern Chile: a marine record of latitudinal shifts of the Southern Westerlies. *Earth and Planetary Science Letters*, 185(3-4):369–382, 2001.

F. Lamy, J. Kaiser, U. Ninnemann, D. Hebbeln, H.W. Arz, and J. Stoner. Antarctic timing of surface water changes off Chile and Patagonian ice sheet response. *Science*, 304:1959–1962, 2004.

D. Lange, A. Rietbrock, C. Haberland, K. Bataille, T. Dahm, F. Tilmann, and E.R. Flüh. Seismicity and geometry of the south Chilean subduction zone (41.5° S–43.5° S): Implications for controlling parameters. *Geophysical Research Letters*, 34(6):L06311, 2007.

D. Lange, J. Cembrano, A. Rietbrock, C. Haberland, T. Dahm, and K. Bataille. First seismic record for intra-arc strike-slip tectonics along the Liquiñe-Ofqui fault zone at the obliquely convergent plate margin of the southern Andes. *Tectonophysics*, 455(1-4):14–24, 2008.

M. Lanphere, D. Champion, L. Melluso, V. Morra, A. Perrotta, C. Scarpati, D. Tedesco, and A. Calvert. 40 Ar/39 Ar ages of the AD 79 eruption of Vesuvius, Italy. *Bulletin of Volcanology*, 69(3):259–263, 2007.

L. Lara, C. Rodríguez, H. Moreno, and C. Pérez de Arce. Geocronología K-Ar y geoquímica del volcanismo plioceno superior-pleistoceno de los Andes del sur (39°–42° S). *Revista Geológica de Chile*, 28:67–90, 2001.

L.E. Lara. The 2008 eruption of the Chaitén Volcano, Chile: a preliminary report. *Revista Geológica de Chile*, 36(1):95–99, 2009.

L.E. Lara and A. Folguera. The Pliocene to Quaternary narrowing ofthe Southern Andean volcanic arc between 37° and 41° S latitude. In S.M. Kay and V.A. Ramos, editors, *Evolution of an Andean Margin: A Tectonic and Magmatic View from the Andes to the Neuquén Basin (35°–39° S lat), GSA Special Paper 407*, pages 299–315. Geological Society of America, 2006.

L.E. Lara, J.A. Naranjo, and H. Moreno. Lanín volcano (39.5° S), Southern Andes: geology and morphostructural evolution. *Revista geológica de Chile*, 31:241–257, 2004a.

L.E. Lara, J.A. Naranjo, and H. Moreno. Rhyodacitic fissure eruption in Southern Andes (Cordón Caulle; 40.5° S) after the 1960 (Mw: 9.5) Chilean earthquake: a structural interpretation. *Journal of Volcanology and Geothermal Research*, 138(1-2):127–138, 2004b.

L.E. Lara, A. Lavenu, J. Cembrano, and C. Rodríguez. Structural controls of volcanism in transversal chains: resheared faults and neotectonics in the Cordón Caulle–Puyehue area (40.5° S), Southern Andes. *Journal of Volcanology and Geothermal Research*, 158(1-2):70–86, 2006a.

L.E. Lara, H. Moreno, J.A. Naranjo, S. Matthews, and C. Pérez de Arce. Magmatic evolution of the Puyehue–Cordón Caulle volcanic complex (40° S), Southern Andean Volcanic Zone: from shield to unusual rhyolitic fissure volcanism. *Journal of Volcanology and Geothermal Research*, 157(4):343–366, 2006b.

L.M. Larsen and A.K. Pedersen. Processes in high-Mg, high-T magmas: evidence from olivine, chromite and glass in Palaeogene picrites from West Greenland. *Journal of Petrology*, 41(7): 1071–1098, 2000.

A. Lavenu and J. Cembrano. Compressional-and transpressional-stress pattern for Pliocene and Quaternary brittle deformation in fore arc and intra-arc zones (Andes of Central and southern Chile). *Journal of Structural Geology*, 21(12):1669–1691, 1999.

M.J. Le Bas. IUGS reclassification of the high-Mg and picritic volcanic rocks. *Journal of Petrology*, 41(10):1467–1470, 2000.

M.J. Le Bas, R.W. Le Maitre, and A.R. Woolley. The construction of the total alkali-silica chemical classification of volcanic rocks. *Mineralogy and Petrology*, 46(1):1–22, 1992.

R.W. Le Maitre. *Igneous rocks: a classification and glossary of terms: recommendations of the International Union of Geological Sciences, Subcommission on the Systematics of Igneous Rocks*. Cambridge University Press, 2002.

J. Lee and R.J. Stern. Glass inclusions in Mariana arc phenocrysts: A new perspective on magmatic evolution in a typical intra-oceanic arc. *The Journal of Geology*, 106(1):19–34, 1998.

W.P. Leeman, J.F. Lewis, R.C. Evarts, R.M. Conrey, and M.J. Streck. Petrologic constraints on the thermal structure of the Cascades arc. *Journal of Volcanology and Geothermal Research*, 140(1-3):67–105, 2005.

N. Lemarchand and J.R. Grasso. Interactions between earthquakes and volcano activity. *Geophysical Research Letters*, 34(24):L24303, 2007.

R. Leonhardt, C. Heunemann, and D. Krása. Analyzing absolute paleointensity determinations: acceptance criteria and the software ThellierTool4.0. *Geochemistry Geophysics Geosystems*, 5 (12):Q12016, 2004.

D.T. Lescinsky and J.H. Fink. Lava and ice interaction at stratovolcanoes: Use of characteristic features to determine past glacial extents and future volcanic hazards. *Journal of Geophysical Research*, 105(B10):23711–23726, 2000.

V.C. Li and C. Kisslinger. Stress transfer and nonlinear stress accumulation at subduction-type plate boundaries - Application to the Aleutians. *Pure and Applied Geophysics*, 122(6):812–830, 1984.

Y. Li and F. Raichlen. Non-breaking and breaking solitary wave run-up. *Journal of Fluid Mechanics*, 456:295–318, 2002.

A.T. Linde and I.S. Sacks. Triggering of volcanic eruptions. *Nature*, 395:888–890, 1998.

S. Lohmar, C. Robin, M.A. Parada, A. Gourgaud, L. López-Escobar, H. Moreno, and J. Naranjo. The two major postglacial (13-14,000 BP) pyroclastic eruptions of Llaima and Villarrica volcanoes (Southern Andes): A comparison. *6th International Symposium on Andean Geodynamics (ISAG 2005, Barcelona), Extended Abstracts*, pages 442–445, 2005.

C. Lomnitz. Major earthquakes and tsunamis in Chile during the period 1535 to 1955. *International Journal of Earth Sciences*, 59(3):938–960, 1970.

C. Lomnitz. Tectonic feedback and the earthquake cycle. *Pure and Applied Geophysics*, 123(5): 667–682, 1985.

L. López-Escobar, M.A. Parada, H. Moreno, F.A. Frey, and R.L. Hickey-Vargas. A contribution to the petrogenesis of Osorno and Calbuco volcanoes, Southern Andes (41° 00'-41° 30'S): comparative study. *Revista Geológica de Chile*, 19(2):211–226, 1992.

L. López-Escobar, R. Kilian, P.D. Kempton, and M. Tagiri. Petrography and geochemistry of Quaternary rocks from the Southern Volcanic Zone of the Andes between 41° 30'and 46° 00'S, Chile. *Revista Geológica de Chile*, 20(1):33–55, 1993.

L. López-Escobar, J. Cembrano, and H. Moreno. Geochemistry and tectonics of the Chilean Southern Andes basaltic Quaternary volcanism (37°–46° S). *Revista Geológica de Chile*, 22: 219–234, 1995a.

L. López-Escobar, M.A. Parada, R. Hickey-Vargas, F.A. Frey, P.D. Kempton, and H. Moreno. Calbuco Volcano and minor eruptive centers distributed along the Liquiñe-Ofqui Fault Zone, Chile (41°–42° S): contrasting origin of andesitic and basaltic magma in the Southern Volcanic Zone of the Andes. *Contributions to Mineralogy and Petrology*, 119(4):345–361, 1995b.

T.V. Lowell, C.J. Heusser, B.G. Andersen, P.I. Moreno, A. Hauser, L.E. Heusser, C. Schluchter, D.R. Marchant, and G.H. Denton. Interhemispheric correlation of Late Pleistocene glacial events. *Science*, 269:1541–1549, 1995.

G.R. Lumpkin. Physical and chemical characteristics of baddeleyite (monoclinic zirconia) in natural environments: an overview and case study. *Journal of Nuclear Materials*, 274(1-2):206–217, 1999.

J. Maclennan, M. Jull, D. McKenzie, L. Slater, and K. Grönvold. The link between volcanism and deglaciation in Iceland. *Geochemistry, Geophysics, Geosystems*, 3(11):1062–1087, 2002.

M. Manga and E. Brodsky. Seismic Triggering of Eruptions in the Far Field: Volcanoes and Geysers. *Annual Reviews in Earth and Planetary Sciences*, 34:263–291, 2006.

J.H. Martin, S.E. Fitzwater, and R.M. Gordon. Iron deficiency limits phytoplankton growth in Antarctic waters. *Global Biogeochemical Cycles*, 4(1):5–12, 1990.

R.S. Martin, S.F.L. Watt, D.M. Pyle, T.A. Mather, N.E. Matthews, R.B. Georg, J.A. Day, T. Fairhead, M.L.I. Witt, and B.M. Quayle. Environmental effects of ashfall in Argentina from the 2008 Chaiten volcanic eruption. *Journal of Volcanology and Geothermal Research*, 184(3-4):462–472, 2009.

U. Martin and K. Németh. How Strombolian is a "Strombolian" scoria cone? Some irregularities in scoria cone architecture from the Transmexican Volcanic Belt, near Volcán Ceboruco,(Mexico) and Al Haruj (Libya). *Journal of Volcanology and Geothermal Research*, 155(1-2):104–118, 2006.

V.M. Martin, D.J. Morgan, D.A. Jerram, M.J. Caddick, D.J. Prior, and J.P. Davidson. Bang! Month-Scale Eruption Triggering at Santorini Volcano. *Science*, 321:1178, 2008.

A.L. Martin-Del Pozzo, T. González-Morán, R. Espinasa-Pereña, M.A. Butron, and M. Reyes. Characterization of the recent ash emissions at Popocatepetl Volcano, Mexico. *Journal of Volcanology and Geothermal Research*, 170(1-2):61–75, 2008.

W. Marzocchi. Remote seismic influence on large explosive eruptions. *Journal of Geophysical Research*, 107:2018, 2002.

B.G. Mason, D.M. Pyle, W.B. Dade, and T. Jupp. Seasonality of volcanic eruptions. *Journal of Geophysical Research*, 109:B04206, 2004a.

B.G. Mason, D.M. Pyle, and C. Oppenheimer. The size and frequency of the largest explosive eruptions on Earth. *Bulletin of Volcanology*, 66(8):735–748, 2004b.

G.I. Massaferro, M.J. Haller, M. D'Orazio, and V.I. Alric. Sub-recent volcanism in Northern Patagonia: A tectonomagmatic approach. *Journal of Volcanology and Geothermal Research*, 155(3-4):227–243, 2006.

C. Maurel and P. Maurel. Etude expérimentale de l'équilibre Fe2+ Fe3+ dans les spinelles chromifiere et les liquides silicatés basiques coexistants, a 1 atm. *Comptes Rendus de l'Academie des Sciences*, 295:209–212, 1982.

A.R. McBirney, J.F. Sutter, H.R. Naslund, K.G. Sutton, and C.M. White. Episodic volcanism in the central Oregon Cascade Range. *Geology*, 2(12):585–589, 1974.

J.R. McConnell, A.J. Aristarain, J.R. Banta, P.R. Edwards, and J.C. Simões. 20th-Century doubling in dust archived in an Antarctic Peninsula ice core parallels climate change and desertification in South America. *Proceedings of the National Academy of Sciences*, 104(14):5743–5748, 2007.

F.G. McCormac, A.G. Hogg, P.G. Blackwell, C.E. Buck, T.F.G. Higham, and P.J. Reimer. SHCal04 Southern Hemisphere calibration, 0-11 cal. kyr BP. *Radiocarbon*, 46:1087–1092, 2004.

R.D. McCulloch, M.J. Bentley, R.S. Purves, N.R.J. Hulton, D.E. Sugden, and C.M. Clapperton. Climatic inferences from glacial and palaeoecological evidence at the last glacial termination, southern South America. *Journal of Quaternary Science*, 15(4):409–417, 2000.

I. McDougall and T.M. Harrison. *Geochronology and Thermochronology by the 40Ar/39Ar Method.* Oxford University Press, USA, 1999.

W.J. McGuire, R.J. Howarth, C.R. Firth, A.R. Solow, A.D. Pullen, S.J. Saunders, I.S. Stewart, and C. Vita-Finzi. Correlation between rate of sea-level change and frequency of explosive volcanism in the Mediterranean. *Nature*, 389:473–476, 1997.

P. McLeod and S. Tait. The growth of dykes from magma chambers. *Journal of Volcanology and Geothermal Research*, 92(3-4):231–245, 1999.

S.R. McNutt. Eruptions of Pavlof Volcano, Alaska, and their possible modulation by ocean load and tectonic stresses: re-evaluation of the hypothesis based on new data from 1984–1998. *Pure and Applied Geophysics*, 155(2):701–712, 1999.

S.R. McNutt and R.J. Beavan. Volcanic earthquakes at Pavlof Volcano correlated with the solid earth tide. *Nature*, 294:615–618, 1981.

K. Mee, J.S. Gilbert, D.W. McGarvie, J.A. Naranjo, and M.S. Pringle. Palaeoenvironment reconstruction, volcanic evolution and geochronology of the Cerro Blanco subcomplex, Nevados de Chillán volcanic complex, central Chile. *Bulletin of Volcanology*, 71:933–952, 2009.

M. Mella. *Petrogenesis of the Yate volcanic complex (42°30'S), southern Andes, Chile.* PhD Thesis, Institute of Geosciences, University of Sao Paolo, Brazil, 2008.

D. Melnick and H.P. Echtler. Inversion of forearc basins in south-central Chile caused by rapid glacial age trench fill. *Geology*, 34(9):709–712, 2006.

J.H. Mercer. Glacial history of southernmost South America. *Quaternary Research*, 6(2):125–166, 1976.

El Mercurio. Aluvión en Cochamó. *El Mercurio, Santiago, Chile, 15th February 2001*, 2001.

N. Metrich and P.J. Wallace. Volatile abundances in basaltic magmas and their degassing paths tracked by melt inclusions. *Reviews in Mineralogy and Geochemistry*, 69(1):363–402, 2008.

D.J. Miller. Giant waves in Lituya Bay Alaska. *US Geological Survey Professional Paper*, 354-C:1: 1–86, 1960.

J. Moernaut, M. De Batist, F. Charlet, K. Heirman, E. Chapron, M. Pino, R. Brümmer, and R. Urrutia. Giant earthquakes in South-Central Chile revealed by Holocene mass-wasting events in Lake Puyehue. *Sedimentary Geology*, 195(3-4):239–256, 2007.

D.R. Montgomery and M. Manga. Streamflow and Water Well Responses to Earthquakes. *Science*, 300:2047–2049, 2003.

G. Moore. Interpreting H2O and CO2 contents in melt inclusions: constraints from solubility experiments and modeling. *Reviews in mineralogy and geochemistry*, 69(1):333–361, 2008.

H. Moreno. Osorno-Calbuco). *IAVCEI General Assembly 2004, Pucon, Chile Field Trip Guide C4*, 2004.

P.I. Moreno, G.L. Jacobson, B.G. Andersen, T.V. Lowell, and G.H. Denton. Vegetation and climate changes during the last glacial maximum and the last termination in the Chilean lakes region: a case study from Canal de la Puntilla (41°S). *Geografiska Annaler*, 81:285–311, 1999.

P.I. Moreno, G.L. Jacobson, T.V. Lowell, and G.H. Denton. Interhemispheric climate links revealed by a late-glacial cooling episode in southern Chile. *Nature*, 409:804–808, 2001.

D.J. Morgan, S. Blake, N.W. Rogers, B. DeVivo, G. Rolandi, R. Macdonald, and C.J. Hawkesworth. Time scales of crystal residence and magma chamber volume from modelling of diffusion profiles in phenocrysts: Vesuvius 1944. *Earth and Planetary Science Letters*, 222(3-4):933–946, 2004.

I. Moriya. Bandaian eruption and landforms associated with it. In *Collection of articles in memory of retirement of Prof. K. Nishimura*, pages 214–219. Tohoku University, Tokyo, 1980.

N.A. Mörner. Faulting, fracturing, and seismicity as functions of glacio-isostasy in Fennoscandia. *Geology*, 6(1):41–45, 1978.

F. Munizaga, F. Hervé, R. Drake, R.J. Pankhurst, M. Brook, and N. Snelling. Geochronology of the Lake Region of south-central Chile(39°-42° S): preliminary results. *Journal of South American Earth Sciences*, 1(3):309–316, 1988.

M. Nakada and H. Yokose. Ice age as a trigger of active Quaternary volcanism and tectonism. *Tectonophysics*, 212(3-4):321–329, 1992.

K. Nakamura. Volcanoes as possible indicators of tectonic stress orientation–principle and proposal. *Journal of Volcanology and Geothermal Research*, 2(1):1–16, 1977.

J.A. Naranjo and H. Moreno. Actividad explosiva postglacial en el Volcán Llaima, Andes del Sur (38° 45'S). *Revista Geológica de Chile*, 18(1):69–80, 1991.

J.A. Naranjo and C.R. Stern. Holocene explosive activity of Hudson Volcano, southern Andes. *Bulletin of Volcanology*, 59(4):291–306, 1998.

J.A. Naranjo and C.R. Stern. Holocene tephrochronology of the southernmost part (42° 30'-45° S) of the Andean Southern Volcanic Zone. *Revista Geológica de Chile*, 31:224–240, 2004.

J.A. Naranjo, H. Moreno, C. Emparan, and M. Murphy. Volcanismo explosive reciente en la caldera del volcán Sollipulli, Andes del sur (39° S). *Revista Geológica de Chile*, 20(2):167–192, 1993.

J.A. Naranjo, M. Arenas, J. Clavero, and O. Muñoz. Mass movement-induced tsunamis: main effects during the Patagonian Fjordland seismic crisis in Aisén (45°25'S), Chile. *Andean Geology*, 36(1):137–145, 2009.

E. Nelson, R. Forsythe, and I. Arit. Ridge collision tectonics in terrane development. *Journal of South American Earth Sciences*, 7(3):271–278, 1994.

J. Neuberg. External modulation of volcanic activity. *Geophysical Journal International*, 142(1): 232–240, 2000.

C.G. Newhall and S. Self. The volcanic explosivity index (VEI): An estimate of explosive magnitude for historical volcanism. *Journal of Geophysical Research*, 87(C2):1231–1238, 1982.

S. Newman and J.B. Lowenstern. VolatileCalc: a silicate melt–H2O–CO2 solution model written in Visual Basic for excel. *Computers and Geosciences*, 28(5):597–604, 2002.

S.P. Nishenko. Seismic potential for large and great interplate earthquakes along the Chilean and southern Peruvian margins of South America: A quantitative reappraisal. *Journal of Geophysical Research*, 90(B5):3589–3616, 1985.

E.O. Norabuena, T.H. Dixon, S. Stein, and C.G.A. Harrison. Decelerating Nazca-South America and Nazca-Pacific plate motions. *Geophysical Research Letters*, 26(22):3405–3408, 1999.

G. Norini and A.M.F. Lagmay. Deformed symmetrical volcanoes. *Geology*, 33(7):605–608, 2005.

C. Nostro, R.S. Stein, M. Cocco, M.E. Belardinelli, and W. Marzocchi. Two-way coupling between Vesuvius eruptions and southern Apennine earthquakes, Italy, by elastic stress transfer. *Journal of Geophysical Research*, 103(B10):24487–24504, 1998.

K. Notsu, L. López-Escobar, and N. Onuma. Along arc variation of Sr-isotope composition in volcanic rocks from the southern Andes (33°-55° S). *Geochemical Journal*, 21:307–313, 1987.

D.A. Nowell, M.C. Jones, and D.M. Pyle. Episodic Quaternary volcanism in France and Germany. *Journal of Quaternary Science*, 21(6):645–675, 2006.

E.A. Okal. A re-evaluation of the great Aleutian and Chilean earthquakes of 1906 August 17. *Geophysical Journal International*, 161(2):268–282, 2005.

C. Pagli and F. Sigmundsson. Will present day glacier retreat increase volcanic activity? Stress induced by recent glacier retreat and its effect on magmatism at the Vatnajökull ice cap, Iceland. *Geophysical Research Letters*, 35(9):L09304, 2008.

A. Panizzo, P. De Girolamo, M. Di Risio, A. Maistri, and A. Petaccia. Great landslide events in Italian artificial reservoirs. *Natural Hazards and Earth System Sciences*, 5(5):733–740, 2005.

R.J. Pankhurst, F. Hervé, L. Rojas, and J. Cembrano. Magmatism and tectonics in continental Chiloé, Chile(42°-42° 30'S). *Tectonophysics*, 205(1-3):283–294, 1992.

R.J. Pankhurst, P.T. Leat, P. Sruoga, C.W. Rapela, M. Márquez, B.C. Storey, and T.R. Riley. The Chon Aike province of Patagonia and related rocks in west Antarctica: A silicic large igneous province. *Journal of Volcanology and Geothermal Research*, 81(1-2):113–136, 1998.

R.J. Pankhurst, SD Weaver, F. Hervé, and P. Larrondo. Mesozoic-Cenozoic evolution of the North Patagonian batholith in Aysén, southern Chile. *Journal of the Geological Society*, 156(4): 673–694, 1999.

R.J. Pankhurst, T.R. Riley, C.M. Fanning, and S.P. Kelley. Episodic silicic volcanism in Patagonia and the Antarctic Peninsula: chronology of magmatism associated with the break-up of Gondwana. *Journal of Petrology*, 41(5):605–625, 2000.

R.J. Pankhurst, C.W. Rapela, W.P. Loske, M. Márquez, and C.M. Fanning. Chronological study of the pre-Permian basement rocks of southern Patagonia. *Journal of South American Earth Sciences*, 16:27–44, 2003.

M.A. Parada, A. Lahsen, and C. Palacios. The Miocene plutonic event of the Patagonian Batholith at 44° 30' S: thermocronological and geobarometric evidence for melting of a rapidly exhumated lower crust. *Transactions of the Royal Society of Edinburgh: Earth Sciences*, 91:169–179, 2000.

M.A. Parada, L. López-Escobar, V. Oliveros, F. Fuentes, D. Morata, et al. Andean magmatism. In T. Moreno and W. Gibbons, editors, *The Geology of Chile*, pages 115–146. The Geological Society, London, 2007.

F. Pardo-Casas and P. Molnar. Relative motion of the Nazca (Farallon) and South American plates since Late Cretaceous time. *Tectonics*, 6(3):233–248, 1987.

E.A. Parfitt and L. Wilson. A Plinian treatment of fallout from Hawaiian lava fountains. *Journal of Volcanology and Geothermal Research*, 88(1-2):67–75, 1999.

A. Pavez. Geología e historia evolutiva del complejo volcánico Quetrupillán, Andes del Sur, 39.5°L.S. *Actas 8th Chilean Geological Congress*, 2:1443–1447, 1997.

J.A. Pearce and D.W. Peate. Tectonic implications of the composition of volcanic arc magmas. *Annual Review of Earth and Planetary Sciences*, 23(1):251–285, 1995.

M. Pérez-Gussinyé, A.R. Lowry, J.P. Morgan, and A. Tassara. Effective elastic thickness variations along the Andean margin and their relationship to subduction geometry. *Geochemistry Geophysics Geosystems*, 9(2):Q02003, 2008.

T.C. Pierson. Initiation and flow behavior of the 1980 Pine Creek and Muddy river lahars, Mount St. Helens, Washington. *Bulletin of the Geological Society of America*, 96(8):1056–1069, 1985.

R.H. Pilger. Cenozoic plate kinematics, subduction and magmatism; South American Andes. *Journal of the Geological Society*, 141(5):793–802, 1984.

V. Pinel, F. Sigmundsson, E. Sturkell, H. Geirsson, P. Einarsson, M.T. Gudmundsson, and T. Hognadottir. Discriminating volcano deformation due to magma movements and variable surface loads: application to Katla subglacial volcano, Iceland. *Geophysical Journal International*, 169 (1):325–338, 2007.

L. Pioli, E. Erlund, E. Johnson, K. Cashman, P. Wallace, M. Rosi, and H. Delgado Granados. Explosive dynamics of violent Strombolian eruptions: The eruption of Parícutin Volcano 1943–1952 (Mexico). *Earth and Planetary Science Letters*, 271(1-4):359–368, 2008.

T. Plank and C.H. Langmuir. An evaluation of the global variations in the major element chemistry of arc basalts. *Earth and Planetary Science Letters*, 90(4):349–370, 1988.

T. Plank, L.B. Cooper, and C.E. Manning. Emerging geothermometers for estimating slab surface temperatures. *Nature Geoscience*, 2:611–615, 2009.

S.C. Porter. Pleistocene glaciation in the southern Lake District of Chile. *Quaternary Research*, 16(3):263–292, 1981.

M. Portnyagin, K. Hoernle, P. Plechov, N. Mironov, and S. Khubunaya. Constraints on mantle melting and composition and nature of slab components in volcanic arcs from volatiles (H2O, S, Cl, F) and trace elements in melt inclusions from the Kamchatka Arc. *Earth and Planetary Science Letters*, 255(1-2):53–69, 2007.

K.D. Putirka. Thermometers and barometers for volcanic systems. *Reviews in Mineralogy and Geochemistry*, 69(1):61–120, 2008.

K.D. Putirka, M. Perfit, F.J. Ryerson, and M.G. Jackson. Ambient and excess mantle temperatures, olivine thermometry, and active vs. passive upwelling. *Chemical geology*, 241(3-4):177–206, 2007.

D.M. Pyle. The thickness, volume and grainsize of tephra fall deposits. *Bulletin of Volcanology*, 51(1):1–15, 1989.

D.M. Pyle. Assessment of the minimum volume of tephra fall deposits. *Journal of Volcanology and Geothermal Research*, 69(3-4):379–382, 1995.

D.M. Pyle. Widely dispersed Quaternary tephra in Africa. *Global and Planetary Change*, 21(1-3): 95–112, 1999.

D.M. Pyle. Sizes of volcanic eruptions. In H. Sigurdsson, editor, *Encyclopedia of volcanoes*, pages 463–475. Academic Press, San Diego, 2000.

D.M. Pyle and D.L. Pyle. Bubble migration and the initiation of volcanic eruptions. *Journal of Volcanology and Geothermal Research*, 67(4):227–232, 1995.

J. Rabassa. Late Cenozoic glaciations in Patagonia and Tierra del Fuego. In J. Rabassa, editor, *The Late Cenozoic of Patagonia and Tierra del Fuego*, pages 151–204. Elsevier, 2008.

J. Rabassa and C.M. Clapperton. Quaternary glaciations of the southern Andes. *Quaternary Science Reviews*, 9(15):153–174, 1990.

J. Rabassa, A.M. Coronato, and M. Salemme. Chronology of the Late Cenozoic Patagonian glaciations and their correlation with biostratigraphic units of the Pampean region (Argentina). *Journal of South American Earth Sciences*, 20(1-2):81–103, 2005.

V. Ramos. Plate tectonic setting of the Andean Cordillera. *Episodes*, 22(3):183–190, 1999.

V.A. Ramos. Terranes of southern Gondwanaland and their control in the Andean structure (30°–33° S latitude). In K.-J. Reutter, E. Scheuber, and P. Wigger, editors, *Tectonics of the Southern Central Andes*, pages 249–261. Springer, 1994.

M.R. Rampino, S. Self, and R.W. Fairbridge. Can rapid climatic change cause volcanic eruptions? *Science*, 206:826–829, 1979.

M.H. Ramsey, P.J. Potts, P.C. Webb, P. Watkins, J.S. Watson, and B.J. Coles. An objective assessment of analytical method precision: comparison of ICP-AES and XRF for the analysis of silicate rocks. *Chemical Geology*, 124(1-2):1–19, 1995.

C.W. Rapela, R.J. Pankhurst, C. Casquet, E. Baldo, J. Saavedra, and C. Galindo. Early evolution of the Proto-Andean margin of South America. *Geology*, 26(8):707–710, 1998.

P.J. Reimer, M.G.L. Baillie, E. Bard, A. Bayliss, J.W. Beck, C.J.H. Bertrand, P.G. Blackwell, C.E. Buck, G.S. Burr, K.B. Cutler, et al. IntCal04 terrestrial radiocarbon age calibration, 0–26 cal kyr BP. *Radiocarbon*, 46(3):1029–1058, 2004.

J.M. Rhodes, M.A. Dungan, D.P. Blanchard, and P.E. Long. Magma mixing at mid-ocean ridges: Evidence from basalts drilled near 22°N on the mid-Atlantic ridge. *Tectonophysics*, 55:35–61, 1979.

J.P. Richards and M. Villeneuve. The Llullaillaco volcano, northwest Argentina: construction by Pleistocene volcanism and destruction by sector collapse. *Journal of Volcanology and Geothermal Research*, 105(1-2):77–105, 2001.

A. Rivera, F. Bown, G. Casassa, C. Acuña, and J. Clavero. Glacier shrinkage and negative mass balance in the Chilean Lake District (40° S). *Hydrological Sciences Journal*, 50(6):963–974, 2005.

A. Robock. Volcanic eruptions and climate. *Reviews of Geophysics*, 38(2):191–219, 2000.

P.L. Roeder and R.F. Emslie. Olivine-liquid equilibrium. *Contributions to Mineralogy and Petrology*, 29(4):275–289, 1970.

A. Rohrbach, S. Schuth, C. Ballhaus, C. Münker, S. Matveev, and C. Qopoto. Petrological constraints on the origin of arc picrites, New Georgia Group, Solomon Islands. *Contributions to Mineralogy and Petrology*, 149(6):685–698, 2005.

C. Rojas, M.E. Beck Jr., R.F. Burmester, J. Cembrano, and F. Hervé. Paleomagnetism of the Mid-Tertiary Ayacara Formation, southern Chile: Counterclockwise rotation in a dextral shear zone. *Journal of South American Earth Sciences*, 7(1):45–56, 1994.

W.I. Rose, S. Self, P.J. Murrow, C. Bonadonna, A.J. Durant, and G.G.J. Ernst. Nature and significance of small volume fall deposits at composite volcanoes: Insights from the October 14, 1974 Fuego eruption, Guatemala. *Bulletin of Volcanology*, 70(9):1043–1067, 2008.

M. Rosenau, D. Melnick, and H. Echtler. Kinematic constraints on intra-arc shear and strain partitioning in the Southern Andes between 38° S and 42° S latitude. *Tectonics*, 25(4):TC4013, 2006.

M.R. Rosenau. Tectonics of the southern Andean intra-arc zone (38°-42°S). *Ph.D. Thesis, Free Univ., Berlin*, 2004.

A.M. Rubin. Propagation of magma-filled cracks. *Annual Review of Earth and Planetary Sciences*, 23(1):287–336, 1995.

J.E. Sable, B.F. Houghton, C.J.N. Wilson, and R.J. Carey. Complex proximal sedimentation from Plinian plumes: the example of Tarawera 1886. *Bulletin of Volcanology*, 69(1):89–103, 2006.

A.M. Sarna-Wojcicki, S. Shipley, R.B. Waitt, D. Dzurisin, and S.H. Wood. Areal distribution, thickness, mass, volume, and grain size of air-fall ash from the six major eruptions of 1980. The 1980 eruptions of Mount St. Helens. *US Geological Survey Professional Paper*, 1250:577–600, 1981.

J. Sauber, G. Plafker, B.F. Molnia, and M.A. Bryant. Crustal deformation associated with glacial fluctuations in the eastern Chugach Mountains, Alaska. *Journal of Geophysical Research*, 105 (B4):8055–8077, 2000.

S.B. Savage and K. Hutter. The motion of a finite mass of granular material down a rough incline. *Journal of Fluid Mechanics*, 199:177–215, 1989.

R.A. Scasso, H. Corbella, and P. Tiberi. Sedimentological analysis of the tephra from the 12–15 August 1991 eruption of Hudson volcano. *Bulletin of Volcanology*, 56(2):121–132, 1994.

R.E. Schafer, J.M. Finkelstein, and J. Collins. On a goodness-of-fit test for the exponential distribution with mean unknown. *Biometrika*, 59(1):222–224, 1972.

M.W. Schmidt and S. Poli. Experimentally based water budgets for dehydrating slabs and consequences for arc magma generation. *Earth and Planetary Science Letters*, 163(1-4):361–379, 1998.

R.L. Schuster and G.F. Wieczorek. Landslide triggers and types. In *Landslides: Proceedings of the First European Conference on Landslides, Prague, Czech Republic, June 24-26, 2002*, pages 59–78. Taylor & Francis Group, 2002.

W.J. Schweller, L.D. Kulm, and R.A. Prince. Tectonics, structure, and sedimentary framework of the Peru-Chile trench. *Geological Society of America Memoir*, 154:323–349, 1981.

K.M. Scott, J.W. Vallance, N. Kerle, J. Luis Macias, W. Strauch, and G. Devoli. Catastrophic precipitation-triggered lahar at Casita volcano, Nicaragua: occurrence, bulking and transformation. *Earth Surface Processes and Landforms*, 30(1):59–79, 2005.

C. Searcy, K. Dean, and W. Stringer. PUFF: A high-resolution volcanic ash tracking model. *Journal of Volcanology and Geothermal Research*, 80(1-2):1–16, 1998.

S. Self and R.S.J. Sparks. *Tephra studies.* Reidel, Dordrecht, 1981.

S.A. Sepúlveda, S. Rebolledo, and G. Vargas. Recent catastrophic debris flows in Chile: Geological hazard, climatic relationships and human response. *Quaternary international*, 158:83–95, 2006.

T. Shea, B. van Wyk de Vries, and M. Pilato. Emplacement mechanisms of contrasting debris avalanches at Volcan Mombacho (Nicaragua), provided by structural and facies analysis. *Bulletin of Volcanology*, 70(8):899–921, 2008.

L. Siebert. Large volcanic debris avalanches: characteristics of source areas, deposits, and associated eruptions. *Journal of Volcanology and Geothermal Research*, 22(3-4):163–197, 1984.

L. Siebert and T. Simkin. Volcanoes of the World: an Illustrated Catalog of Holocene Volcanoes and their Eruptions. *Smithsonian Institution, Global Volcanism Program Digital Information Series, GVP-3,(http://www. volcano. si. edu/world/)*, 2002-.

H. Sigurdsson. Volcanic episodes and rates of volcanism. In H. Sigurdsson, editor, *Encyclopedia of volcanoes*, pages 271–279. Academic Press, San Diego, 2000.

G.E. Sigvaldason. Volcanic and tectonic processes coinciding with glaciation and crustal rebound: an early Holocene rhyolitic eruption in the Dyngjufjöll volcanic centre and the formation of the Askja caldera, north Iceland. *Bulletin of Volcanology*, 64(3):192–205, 2002.

G.E. Sigvaldason, K. Annertz, and M. Nilsson. Effect of glacier loading/deloading on volcanism: postglacial volcanic production rate of the Dyngjufjöll area, central Iceland. *Bulletin of Volcanology*, 54(5):385–392, 1992.

T. Simkin. Terrestrial Volcanism in Space and Time. *Annual Reviews in Earth and Planetary Sciences*, 21(1):427–452, 1993.

T. Simkin and L. Siebert. Earth's volcanoes and eruptions: an overview. In H. Sigurdsson, editor, *Encyclopedia of volcanoes*, pages 249–261. Academic Press, San Diego, 2000.

B.S. Singer, R.A. Thompson, M.A. Dungan, T.C. Feeley, S.T. Nelson, J.C. Pickens, L.L. Brown, A.W. Wulff, J.P. Davidson, and J. Metzger. Volcanism and erosion during the past 930 ky at the Tatara-San Pedro complex, Chilean Andes. *Geological Society of America Bulletin*, 109(2): 127–142, 1997.

B.S. Singer, B.R. Jicha, M.A. Harper, J.A. Naranjo, L.E. Lara, and H. Moreno-Roa. Eruptive history, geochronology, and magmatic evolution of the Puyehue-Cordón Caulle volcanic complex, Chile. *Bulletin of the Geological Society of America*, 120(5-6):599–618, 2008.

J. Sinton, K. Grönvold, and K. Sæmundsson. Postglacial eruptive history of the Western volcanic zone, Iceland. *Geochemistry, Geophysics, Geosystems*, 6(12):Q12009, 2005.

T.W. Sisson and T.L. Grove. Temperatures and H 2 O contents of low-MgO high-alumina basalts. *Contributions to Mineralogy and Petrology*, 113(2):167–184, 1993.

T.W. Sisson and G.D. Layne. H2O in basalt and basaltic andesite glass inclusions from four subduction-related volcanoes. *Earth and Planetary Science Letters*, 117(3-4):619–635, 1993.

L. Slater, M. Jull, D. McKenzie, and K. Gronvöld. Deglaciation effects on mantle melting under Iceland: results from the northern volcanic zone. *Earth and Planetary Science Letters*, 164(1-2): 151–164, 1998.

J.L. Smellie and I.P. Skilling. Products of subglacial volcanic eruptions under different ice thicknesses: two examples from Antarctica. *Sedimentary geology*, 91(1-4):115–129, 1994.

D.R. Smith and W.P. Leeman. Chromian spinel–olivine phase chemistry and the origin of primitive basalts of the southern Washington Cascades. *Journal of Volcanology and Geothermal Research*, 140(1-3):49–66, 2005.

A.V. Sobolev and M. Chaussidon. H2O concentrations in primary melts from supra-subduction zones and mid-ocean ridges: Implications for H2O storage and recycling in the mantle. *Earth and Planetary Science Letters*, 137(1-4):45–55, 1996.

R. Somoza. Updated Nazca (Farallon) - South America relative motions during the last 40 My: implications for mountain building in the central Andean region. *Journal of South American Earth Sciences*, 11(3):211–215, 1998.

R.S.J. Sparks, M.I. Bursik, G.J. Ablay, R.M.E. Thomas, and S.N. Carey. Sedimentation of tephra by volcanic plumes. Part 2: controls on thickness and grain-size variations of tephra fall deposits. *Bulletin of Volcanology*, 54(8):685–695, 1992.

N. Spilliaert, P. Allard, N. Métrich, and A.V. Sobolev. Melt inclusion record of the conditions of ascent, degassing, and extrusion of volatile-rich alkali basalt during the powerful 2002 flank eruption of Mount Etna (Italy). *Journal of Geophysical Research*, 111(B4):B04203, 2006.

S. Stein, S. Cloetingh, N.H. Sleep, and R. Wortel. Passive margin earthquakes, stresses and rheology. In S. Gregerson and P.W. Basham, editors, *Earthquakes at North-Atlantic Passive Margins: Neotectonics and Postglacial Rebound*, pages 231–259. Kluwer Academic Pub, 1989.

P. Stelling, J. Beget, C. Nye, J. Gardner, J. Devine, and R. George. Geology and petrology of ejecta from the 1999 eruption of Shishaldin Volcano, Alaska. *Bulletin of Volcanology*, 64(8): 548–561, 2002.

M.A. Stephens. EDF statistics for goodness of fit and some comparisons. *Journal of the American Statistical Association*, 69:730–737, 1974.

M. Sterken, E. Verleyen, K. Sabbe, G. Terryn, F. Charlet, S. Bertrand, X. Boës, N. Fagel, M. De Batist, and W. Vyverman. Late Quaternary climatic changes in southern Chile, as recorded in a diatom sequence of Lago Puyehue (40° 40' S). *Journal of Paleolimnology*, 39(2): 219–235, 2008.

C.R. Stern. Comment on "Crustal contributions to arc magmatism in the Andes of Central Chile" by W. Hildreth and S. Moorbath. *Contributions to Mineralogy and Petrology*, 108(1):241–246, 1991.

C.R. Stern. Active Andean volcanism: its geologic and tectonic setting. *Revista Geológica de Chile*, 31:161–206, 2004.

C.R. Stern. Holocene tephrochronology record of large explosive eruptions in the southernmost Patagonian Andes. *Bulletin of Volcanology*, 70(4):435–454, 2008.

C.R. Stern and M.A. Skewes. Miocene to present magmatic evolution at the northern end of the Andean Southern Volcanic zone, Central Chile. *Revista Geológica de Chile*, 22:261–272, 1995.

C.R. Stern, H. Moreno, L. López-Escobar, J.E. Clavero, L.E. Lara, J.A. Naranjo, M.A. Parada, and M.A. Skewes. Chilean volcanoes. In T. Moreno and W. Gibbons, editors, *The Geology of Chile*, pages 147–178. The Geological Society, London, 2007.

I.S. Stewart, J. Sauber, and J. Rose. Glacio-seismotectonics: ice sheets, crustal deformation and seismicity. *Quaternary Science Reviews*, 19(14-15):1367–1389, 2000.

M. Suárez and C.M. Bell. Triassic rift-related sedimentary basins in northern Chile (24°–29° S). *Journal of South American Earth Sciences*, 6:109–121, 1992.

D.E. Sugden, M.J. Bentley, C.J. Fogwill, N.R.J. Hulton, R.D. McCulloch, and R.S. Purves. Late-glacial glacier events in southernmost South America: a blend of 'northern' and 'southern' hemispheric climatic signals? *Geografiska Annaler: Series A*, 87(2):273–288, 2005.

I. Sumita and M. Manga. Suspension rheology under oscillatory shear and its geophysical implications. *Earth and Planetary Science Letters*, 269(3-4):467–476, 2008.

S.-s. Sun and W.F. McDonough. Chemical and isotopic systematics of oceanic basalts: implications for mantle composition and processes. *Geological Society London Special Publication*, 42(1):313–345, 1989.

C.E. Synolakis. The runup of solitary waves. *Journal of Fluid Mechanics*, 185:523–545, 1987.

S. Tait, C. Jaupart, and S. Vergniolle. Pressure, gas content and eruption periodicity of a shallow, crystallising magma chamber. *Earth and Planetary Science Letters*, 92(1):107–123, 1989.

A. Takada. The influence of regional stress and magmatic input on styles of monogenetic and polygenetic volcanism. *Journal of Geophysical Research*, 99(B7):13–563, 1994.

N. Tamic, H. Behrens, and F. Holtz. The solubility of H2O and CO2 in rhyolitic melts in equilibrium with a mixed CO2–H2O fluid phase. *Chemical Geology*, 174(1-3):333–347, 2001.

Z.A. Tašárová. Towards understanding the lithospheric structure of the southern Chilean subduction zone (36°S-42°S) and its role in the gravity field. *Geophysical Journal International*, 170(3): 995–1014, 2007.

A. Tassara and G. Yáñez. Relación entre el espesor elástico de la litosfera y la segmentación tectónica del margen andino (15-47° S). *Revista Geológica de Chile*, 30:159–186, 2003.

C. Textor, H.F. Graf, M. Herzog, J.M. Oberhuber, W.I. Rose, and G.G.J. Ernst. Volcanic particle aggregation in explosive eruption columns. Part I: Parameterization of the microphysics of hydrometeors and ash. *Journal of Volcanology and Geothermal Research*, 150(4):359–377, 2006.

S.N. Thomson, F. Hervé, and B. Stöckhert. Mesozoic-Cenozoic denudation history of the Patagonian Andes (southern Chile) and its correlation to different subduction processes. *Tectonics*, 20 (5):693–711, 2001.

T.M. Thornburg and L.D. Kulm. Sedimentation in the Chile Trench: Depositional morphologies, lithofacies, and stratigraphy. *Geological Society of America Bulletin*, 98(1):33–52, 1987.

R.S. Thorpe. The tectonic setting of active Andean volcanism. In R.S. Harmon and B.A. Barreiro, editors, *Andean Magmatism: Chemical and Isotopic Constraints*, pages 4–8. Shiva, Nantwich, U.K., 1984.

R.S. Thorpe and P.W. Francis. Variations in Andean andesite compositions and their petrogenetic significance. *Tectonophysics*, 57(1):53–70, 1979.

A. Tibaldi. Morphology of pyroclastic cones and tectonics. *Journal of Geophysical Research*, 100 (B12):24521–24535, 1995.

A. Tibaldi. Volcanism in compressional tectonic settings: Is it possible? *Geophysical Research Letters*, 32(6):L06309, 2005.

A. Tibaldi and A.M.F. Lagmay. Interaction between volcanoes and their basement. *Journal of Volcanology and Geothermal Research*, 158(1-2):1–5, 2006.

D.R. Tormey, R. Hickey-Vargas, F.A. Frey, and L. López-Escobar. Recent lavas from the Andean volcanic front (33 to 42° S); interpretations of along-arc compositional variations. In R.S. Harmon and C.W. Rapela, editors, *Andean magmatism and its tectonic setting: Geological Society of America Special Paper 265*, pages 57–77. 1991a.

D.R. Tormey, P. Schuller, L. López-Escobar, and F. Frey. Uranium-Thorium activities and disequilibrium in volcanic rocks from the Andes (33°–46° S): petrogenetic constraints and environmental consequences. *Revista Geológica de Chile*, 31(2):165–175, 1991b.

T.H. Torsvik. *Interactive Analysis of Palaeomagnetic Data, IAPD User Guide.* University of Bergen, Norway, 1986.

H. Turpeinen, A. Hampel, T. Karow, and G. Maniatis. Effect of ice sheet growth and melting on the slip evolution of thrust faults. *Earth and Planetary Science Letters*, 269(1-2):230–241, 2008.

F.C. Ugolini, R. Dahlgren, J. LaManna, W. Nuhn, and J. Zachara. Mineralogy and weathering processes in recent and Holocene tephra deposits of the Pacific Northwest, USA. *Geoderma(Amsterdam)*, 51(1-4):277–299, 1991.

T. Ui, S. Takarada, and M. Yoshimoto. Debris avalanches. In H. Sigurdsson, editor, *Encyclopedia of volcanoes*, pages 617–626. Academic Press, San Diego, 2000.

J. van der Plicht and A. Hogg. A note on reporting radiocarbon. *Quaternary Geochronology*, 1(4): 237–240, 2006.

G. Villarosa, V. Outes, A. Hajduk, E.C. Montero, D. Sellés, M. Fernández, and E. Crivelli. Explosive volcanism during the Holocene in the Upper Limay River Basin: The effects of ashfalls on human societies, Northern Patagonia, Argentina. *Quaternary International*, 158(1):44–57, 2006.

R. Von Huene, J. Corvalan, E.R. Flueh, K. Hinz, J. Korstgard, C.R. Ranero, W. Weinrebe, and C. Scientists. Tectonic control of the subducting Juan Fernandez Ridge on the Andean margin near Valparaiso, Chile. *Tectonics*, 16:474–488, 1997.

S. Wacaster, R. Hickey-Vargas, and M. Sun. Olivine hosted melt inclusions from mafic small eruptive centers, Central Southern Volcanic Zone, Chile - an approach for characterizing primitive arc magma compositions. *MAG 2007, Taipei, International Conference on Evolution, Transfer and Release of Magmas and Volcanic Gases, Program, Abstracts and Fieldguide*, page 42, 2007.

J.S. Walder, P. Watts, O.E. Sorensen, and K. Janssen. Tsunamis generated by subaerial mass flows. *Journal of Geophysical Research*, 108:2236, 2003.

P.C. Wallman, G.A. Mahood, and D.D. Pollard. Mechanical models for correlation of ring-fracture eruptions at Pantelleria, Strait of Sicily, with glacial sea-level drawdown. *Bulletin of Volcanology*, 50:327–339, 1988.

T.R. Walter and F. Amelung. Volcanic eruptions following M>= 9 megathrust earthquakes: Implications for the Sumatra-Andaman volcanoes. *Geology*, 35(6):539–542, 2007.

T.R. Walter, R. Wang, M. Zimmer, H. Grosser, B. Luhr, and A. Ratdomopurbo. Volcanic activity influenced by tectonic earthquakes: Static and dynamic stress triggering at Mt. Merapi. *Geophysical Research Letters*, 34(5):5304, 2007.

S.F.L. Watt, D.M. Pyle, and T.A. Mather. The influence of great earthquakes on volcanic eruption rate along the Chilean subduction zone. *Earth and Planetary Science Letters*, 277(3-4):399–407, 2009a.

S.F.L. Watt, D.M. Pyle, T.A. Mather, R.S. Martin, and N.E. Matthews. Fallout and distribution of volcanic ash over Argentina following the May 2008 explosive eruption of Chaitén, Chile. *Journal of Geophysical Research*, 114(B4):B04207, 2009b.

S.F.L. Watt, D.M. Pyle, J.A. Naranjo, and T.A. Mather. Landslide and tsunami hazard at Yate volcano, Chile as an example of edifice destruction on strike-slip fault zones. *Bulletin of Volcanology*, 71:559–574, 2009c.

S.N. Williams. Plinian airfall deposits of basaltic composition. *Geology*, 11(4):211–214, 1983.

L. Wilson and G.P.L. Walker. Explosive volcanic eruptions-VI. Ejecta dispersal in plinian eruptions: the control of eruption conditions and atmospheric properties. *Geophysical Journal International*, 89:657–679, 1987.

A. Wolodarsky-Franke, P.I. Moreno, A. Lara, M. Pino, and G. Villarrosa. Tree-ring, stratigraphic, and palynological evidence for volcanic and climatic controls on Fitzroya cupressoides forests in southern Chile over the last 5700 years. In *Holocene environmental catastrophes in South America: From the lowlands to the Andes, March 11-17, 2005, Laguna Mar Chiquita, Miramar, Córdoba Province, Argentina*, 2005.

C.A. Wood. Morphometric analysis of cinder cone degradation. *Journal of Volcanology and Geothermal Research*, 8(2-4):137–160, 1980.

A.W. Woods and D.M. Pyle. The control of chamber geometry on triggering volcanic eruptions. *Earth and Planetary Science Letters*, 151(3-4):155–166, 1997.

L. Wooller, J. Murray, H. Rymer, and B. van Wyk de Vries. Volcano instability and collapse from basement faulting. In *EGS-AGU-EUG Joint Assembly, Abstracts from the meeting held in Nice, France, 6-11 April 2003, abstract 304*, 2003.

G. Yáñez, J. Cembrano, M. Pardo, C. Ranero, and D. Selles. The Challenger–Juan Fernández–Maipo major tectonic transition of the Nazca–Andean subduction system at 33–34 S: geodynamic evidence and implications. *Journal of South American Earth Sciences*, 15(1):23–38, 2002.

G.A. Yáñez, C.R. Ranero, R. von Huene, and J. Díaz. Magnetic anomaly interpretation across the southern central Andes (32°–34° S): The role of the Juan Fernández Ridge in the late Tertiary evolution of the margin. *Journal of Geophysical Research*, 106(B4):6325–6345, 2001.

X. Yuan, G. Asch, K. Bataille, G. Bock, M. Bohm, H. Echtler, R. Kind, O. Oncken, and I. Wölbern. Deep seismic images of the Southern Andes. In *Evolution of an Andean Margin: A Tectonic and Magmatic View from the Andes to the Neuquén Basin (35°–39° S lat, GSA Special Paper 407*, pages 61–72. Geological Society of America, 2006.

A.M. Ziegler, S.F. Barrett, C.R. Scotese, and B.W. Sellwood. Palaeoclimate, Sedimentation and Continental Accretion [and Discussion]. *Philosophical Transactions of the Royal Society of London, Series A*, 301(1461):253–264, 1981.

G.A. Zielinski, P.A. Mayewski, L.D. Meeker, S. Whitlow, M.S. Twickler, and K. Taylor. Potential atmospheric impact of the Toba mega-eruption approximately 71,000 years ago. *Geophysical Research Letters*, 23(8):837–840, 1996.

A. Ziv, A.M. Rubin, and A. Agnon. Stability of dike intrusion along preexisting fractures. *Journal of Geophysical Research*, 105(B3):5947–5961, 2000.

Appendix A

Sample details

Lavas, proximal ejecta, bedded scoria and basement rocks

All samples listed, except ash samples from the Chaitén 2008 eruption (Chapter 5) and radiocarbon samples (Chapter 6).

Samples numbered as follows: Two digits immediately before hyphen give the specific day of the month of collection, after hyphen is site number for that day, and then sample letter (starting from A) for that site. Samples preceded by 8 were collected from late February to early March 2008. Samples preceded by C were collected during the fieldwork investigating the Chaitén 2008 ash, and follow the Chaitén sample format. Otherwise, all samples collected from mid-January to early February 2007.

For location Ho= Hornopirén, Y=Yate, A=Apagado, Pa = Palena, Pu=Puyuhuapi, LaVig=La Viguería, Mi= Cone south of Minchinmávida, Hua=Hualaihue region, Aya=Ayacara region. Section refers tothin section preparation: p=polished, c=covered. Analyses as marked, by XRF, ICP-MS and palaeomagnetic measurements. Column refers to the stratigraphic columns in the tephrochronology of Chapter 6. For position, S=in situ, L=Loose block, B=bedded, C=In cone. For types, Lav=Lava, Sco=Scoria, Pum=Pumice, Bas=Basement rock, X=xenolith, O=other. For xrf etc. x marks sample analysed, t for trace elements only. p=polished thin section, c=covered, r=resin mounted stub.

	Sample	Location	Section	XRF	ICP-MS	Palaeomag.	Column	Long.	Lat.	Type	Position	Notes
Lavas	15-4B	Ho		x				-72.466	-41.871	Lav	S	Same flow as 30-2A
	15-5A	Ho	p	x	x	x		-72.470	-41.891	Lav	S	Coarsely vesicular
	15-7A	Ho	p	x				-72.476	-41.929	Lav	S	Highly vesicular
	19-1A	Ho	p	x				-72.434	-41.860	Lav	S	Vesicular, common clots, breccia
	19-1B	Ho	p					-72.434	-41.860	Lav	S	Contains concentric clots
	19-2A	Ho	c					-72.436	-41.860	Lav	L	Dense porphyry
	19-2B	Ho	c					-72.436	-41.860	Lav	L	Dense porphyry
	19-2C	Ho	c					-72.436	-41.860	Lav	L	Vent agglomerate
	19-2D	Ho	c					-72.436	-41.860	Lav	L	Dense porphyry
	19-4A	Ho	p	t	x			-72.439	-41.860	Lav	S	Dense
	19-5A	Ho						-72.456	-41.867	Lav	S	Fresh, dense
	21-14A	Ho	p	x			F	-72.405	-41.904	Lav	S	Dense block below breccia
	21-15B	Ho	p	t		x	F	-72.408	-41.909	Lav	S	Dense
	24-3A	Ho	p	t		x		-72.394	-41.871	Lav	S	Dense
	24-7A	Ho	p	x				-72.398	-41.884	Lav	S	Dense block below breccia
	30-2A	Ho	p	x		x		-72.464	-41.871	Lav	S	Fresh, dense
	30-9A	Ho	p	t		x		-72.473	-41.936	Lav	S	Massive, pale, vesicular
	05-3A	Ho	p	x				-72.429	-41.878	Lav	L	Vesicular
	23-4X	Y						-72.339	-41.659	Lav	L	Assorted blocks in debris flow

	Sample	Location	Section	XRF	ICP-MS	Palaeomag.	Column	Long.	Lat.	Type	Position	Notes
Lavas	26-3A	Y	p	x		x		-72.348	-41.819	Lav	S	Flow banded, above 26-2A
	23-8A	Y				x	M	-72.436	-41.713	Lav	S	Coarsely porphyritic, massive
	23-8B	Y	p	x	x		M	-72.436	-41.713	Lav	S	Same as 23-8A
	23-10A	Y	p	x	x	x		-72.443	-41.717	Lav	S	Dense, columnar jointed
	23-12A	Y				x	K	-72.465	-41.726	Lav	S	Coarsely porphyritic
	23-12B	Y	p	x			K	-72.465	-41.726	Lav	S	Same as 23-12A
	26-2A	Y	p	x	x	x		-72.347	-41.823	Lav	S	Black, glassy, columnar jointed
	26-4A	Y	p	x	x	x		-72.349	-41.823	Lav	S	Dense
	26-4B	Y						-72.349	-41.823	Lav	L	Contains inclusions
	26-4C	Y						-72.349	-41.823	Lav	L	Contain coarse inclusions
	26-4F	Y						-72.349	-41.823	Lav	L	Scaly surface texture
	26-6A	Y	p	x	x	x		-72.362	-41.866	Lav	S	Red-grey, dense
	26-7A	Y	p	x				-72.370	-41.880	Lav	S	Jointed, dense
	02-3A	Y	p	x		x		-72.403	-41.704	Lav	S	Fresh, massive
	20-3A	A		x				-72.588	-41.883	Lav	L	Dense, young
	20-3B	A	p	x				-72.588	-41.883	Lav	L	Similar to 20-3A
	20-4A	A	p	x	x	x		-72.594	-41.879	Lav	S	Dense, blocky jointing
	20-5A	A	p	x		x		-72.607	-41.880	Lav	S	Jointed, dense, subglacial?
	21-2A	A	p	x	x			-72.595	-41.880	Lav	S	Close jointing, subglacial?, dense
	21-3A	A	p	x				-72.594	-41.879	Lav	S	Hyaloclastite rind, finely vesicular
	21-4A	A	p	x	x			-72.594	-41.879	Lav	S	Dense, similar to 21-2A
	21-6A	A				x		-72.616	-41.872	Lav	S	Jointed, porphyritic
	21-6B	A	p	x	x			-72.616	-41.872	Lav	S	Same as 21-6A, less weathered
	21-9B	A	p	x				-72.641	-41.850	Lav	S	Porphyry
	21-9C	A	p	x		x		-72.641	-41.850	Lav	S	Dense, blocky jointing
	827-1B	Pu	p	x				-72.525	-44.290	Lav	S	Vesicular
	828-1A	Pu	p					-72.574	-44.326	Lav	S	Dense, blocky
	828-2A	Pu	p	x				-72.596	-44.365	Lav	S	Dense, blocky
	828-3A	Pu	p					-72.585	-44.357	Lav	S	Dense, columnar jointed
	828-4A	Pu	p					-72.575	-44.343	Lav	S	Vesicular
	828-5A	Pu						-72.574	-44.333	Lav	S	Vesicular
	828-7A	Pu	p	x				-72.561	-44.320	Lav	S	Dense
	828-8B	Pu						-72.532	-44.290	Lav	S	Ropy texture, from roof of lava tube
Proximal ejecta	05-3B	Ho		x	x			-72.429	-41.878	Sco	C	Black scoria from summit
	05-3C	Ho	r	x				-72.429	-41.878	Sco	C	Red scoria from summit
	19-2E	Ho						-72.436	-41.860	Sco	C	Vesicular, in bedded debris deposit
	19-2F	Ho						-72.436	-41.860	Sco	C	Vesicular, in bedded debris deposit
	19-2G	Ho						-72.436	-41.860	Sco	C	Vesicular, in bedded debris deposit
	24-1A	Y						-72.396	-41.866	Pum	B	Rounded, washed in bed
	24-2A	Y		x	x			-72.397	-41.862	Pum	B	As 24-1A (yellow, white analysed)
	26-4D	Y						-72.349	-41.823	Pum	L	Broken pumice
	26-4E	Y						-72.349	-41.823	Pum	L	Crystal rich pumice
	26-5AG	Y	p	x	x			-72.345	-41.851	Pum	L	Grey pumice
	26-5AY	Y	p	x				-72.345	-41.851	Pum	L	White, yellow pumices
	03-1A	Y						-72.346	-41.842	Pum	B	Broken fragments in bog section
	03-1B	Y						-72.346	-41.842	Pum	B	Broken fragments in bog section
	03-1D	Y						-72.346	-41.842	Pum	B	Broken fragments in bog section
	20-3C	A		x				-72.588	-41.883	Sco	C	Brown scoria from cone
	20-3D	A		x				-72.588	-41.883	Sco	C	Black scoria from cone

	Sample	Location	Section	XRF	ICP-MS	Palaeomag.	Column	Long.	Lat.	Type	Position	Notes
Basement	04-1A	Hua	c					-72.478	-41.931	Bas	S	Metamorphics in LOFZ wall
	04-1B	Hua	c					-72.478	-41.931	Bas	S	Metamorphics in LOFZ wall
	04-1C	Hua	c					-72.478	-41.931	Bas	S	Metamorphics in LOFZ wall
	15-4A	Hua	c					-72.466	-41.870	Bas	L	Gabbro
	25-1B	Hua	c	x			O	-72.295	-41.647	Bas	S	White, coarse granite
	25-10A	Hua	c	x				-72.539	-41.739	Bas	S	Finer, more intermediate granitoid
	04-4A	Hua	c	x				-72.379	-41.888	Bas	S	Medium grained, greener granitoid
Other sample type	20-3E	A	p2					-72.588	-41.883	X	C	Granitic contact with lava
	20-3F	A						-72.588	-41.883	X	C	Lava coating exotic
	20-3G	A						-72.588	-41.883	X	C	Altered granitic
	20-3H	A	p					-72.588	-41.883	X	C	Altered granitic
	20-3I	A						-72.588	-41.883	X	C	Altered granitic
	20-3J	A						-72.588	-41.883	X	C	Altered granitic
	20-3K	A						-72.588	-41.883	X	C	Lava erratic
	20-3L	A	p					-72.588	-41.883	X	C	Granitic xenoliths
	20-3M	A	p					-72.588	-41.883	Sco	C	Lava with melt glass
	20-3N	A						-72.588	-41.883	X	C	Altered granitic
	21-1A	A						-72.595	-41.880	O	S	Old hyaloclastite scoria
	21-2B	A						-72.595	-41.880	O	S	Fine grey tuff in old sequence
	21-9A	A						-72.641	-41.850	O	S	Pyroclastic flow
	21-11A	A	c					-72.657	-41.851	O	S	Welded tuff
	21-12A	A	c					-72.667	-41.851	O	S	Welded tuff
Bedded scoria (proximal)	20-6A	A						-72.613	-41.876	Sco	B	Top, from bog section
	20-6D	A						-72.613	-41.876	Sco	B	From bog section
	20-6E	A						-72.613	-41.876	Sco	B	Top, from bog section
	21-5A	A	r		x		I	-72.610	-41.879	Sco	B	Basal scoria
	21-5BB	A	r	x			I	-72.610	-41.879	Sco	B	Black component (analyse Φ -1,-2)
	21-5BY	A		t			I	-72.610	-41.879	Sco	B	Yellow component (analyse Φ -1,-2)
	21-5C	A		x	x		I	-72.610	-41.879	Sco	B	Analyse Φ -2
	21-5D	A					I	-72.610	-41.879	Sco	B	Basal, yellow component
	15-6A	A		x				-72.475	-41.913	Sco	B	Black (analyse Φ 1)
	15-6B	A	r	x				-72.475	-41.913	Sco	B	Black (analyse Φ 1)
	24-6A	H			x		F	-72.397	-41.881	Sco	B	Coarse, grey
	24-6B	H					F	-72.397	-41.881	Sco	B	Coarse, grey
	24-6D	A			x		F	-72.397	-41.881	Sco	B	Coarse, black
	26-8A	H	r	x	x		E	-72.374	-41.887	Sco	B	Black (analyse Φ -1,-2)
	30-3A	A			x			-72.467	-41.877	Sco	B	Coarse, black
	30-3B	A			x			-72.467	-41.877	Sco	B	Coarse, black
	30-3C	A						-72.467	-41.877	Sco	B	Coarse, black
	30-3D	A						-72.467	-41.877	Sco	B	Coarse, black
	30-3E	A						-72.467	-41.877	Sco	B	Coarse, black
	30-3F	A			x			-72.467	-41.877	Sco	B	Coarse, black
	30-7A	A						-72.474	-41.911	Sco	B	Coarse, black
	30-8A	A						-72.474	-41.929	Sco	B	Fine, top part
	01-6A	H					G	-72.458	-41.954	Sco	B	Dark grey, fine, top
	01-6B	H					G	-72.458	-41.954	Sco	B	Coarse, grey, near base
	04-2A	A			x		E	-72.374	-41.887	Sco	B	Coarse
	819-2B	A					F	-72.396	-41.879	Sco	B	Coarse, dark
	801-1A	A					E	-72.373	-41.886	Sco	B	Coarsest bed, centre
	801-1B	H			x		E	-72.373	-41.886	Sco	B	Coarse

	Sample	Location	Section	XRF	ICP-MS	Palaeomag.	Column	Long.	Lat.	Type	Position	Notes
Bedded scoria (proximal)	801-1C	H					E	-72.373	-41.886	Sco	B	Coarse
	801-1D	H					E	-72.373	-41.886	Sco	B	Coarse
	801-1G	H					E	-72.373	-41.886	Sco	B	Coarsest bed, centre
	826-3A	Pa	x		x			-72.334	-43.668	Sco	B	Coarse, base
	826-3B	Pa	x		x			-72.334	-43.668	Sco	B	Coarse, centre
	826-3C	Pa	x		x			-72.334	-43.668	Sco	B	Coarse, top
	826-4A	Pa			x			-72.335	-43.687	Sco	B	Coarsest bed
	827-1A	Pu						-72.525	-44.290	Sco	B	Stratified ash block
	828-6A	Pu	x		x			-72.569	-44.354	Sco	B	Coarse, lower unit
	828-6B	Pu			x			-72.569	-44.354	Sco	B	Coarse, upper unit
	828-8A	Pu						-72.532	-44.290	Sco	B	Bedded ash, on top of lava flow
	803-5C	LaVig	x		x		Y	-72.283	-41.409	Sco	B	Bedded black ash
	803-6A	LaVig						-72.273	-41.385	Sco	B	Coarse ash
	C16-G7B	Mi			x			-72.468	-42.950	Sco	C	Bedded, on slopes of cone
	C16-G7C	Mi						-72.468	-42.950	Sco	C	Large cinders in bedded scoria

Tephra samples

Source refers to eruption labels detailed in Chapter 6.

Sample	Area	Column	ICP-MS	Long.	Lat.	Type	Source	Notes
13-1C	Hornopirén	A		-72.457	-42.076	Pumice	Cha1	White pumice in clay
13-1E	Hornopirén	A	x	-72.457	-42.076	Scoria	Ap1	Very fine, dark grey
13-1F	Hornopirén	A		-72.457	-42.076	Scoria	Ap1	Oxidised top to 13-1E
13-3A	Hornopirén	B	x	-72.436	-42.004	Scoria	Ap1	Very fine, grey
13-3B	Hornopirén	B		-72.436	-42.004	Scoria	Ap1	Fine, dark grey
13-3C	Hornopirén	B	x	-72.436	-42.004	Scoria	Ap1	Fine, dark grey to black
20-1A	Hornopirén	C		-72.424	-41.965	Pumice	Cha1	Pumice soil mix
20-1B	Hornopirén	C		-72.424	-41.965	Pumice	Cha1	Sandy pumice
20-2A	Hornopirén	B		-72.434	-41.997	Scoria	Ap1	Stratified, grey
20-2C	Hornopirén	B	x	-72.434	-41.997	Pumice	Cha1	White pumice in clay
20-2D	Hornopirén	B	x	-72.434	-41.997	Yellow ash	Cha1	Pumice flecks
24-6C	Hornopirén	F	x	-72.397	-41.881	Scoria	Ho1	Grey, white 'rootlets'
24-8A	Hornopirén	H	x	-72.494	-41.948	Pumice	Cha1	Millet seed texture in clay
26-8B	Hornopirén	E	x	-72.374	-41.887	Pumice	Cha1	Millet seed texture in clay
17-1A	W Hualaihue			-72.712	-41.827	Weathered ash?	Ca?	Orange unit, unclear if tephra
17-1B	W Hualaihue			-72.712	-41.827	Pumice	Ca?	In glacial sands, oldest
17-1C	W Hualaihue			-72.712	-41.827	Pumice	Ca?	In glacial sands
17-1D	W Hualaihue			-72.712	-41.827	Pumice	Ca?	In glacial sands, youngest
23-9A	Yate	M	x	-72.438	-41.715	Scoria	YaSc	Lead grey, coarse, on lava
14-1A	N of Yate	J	x	-72.507	-41.725	Grey ash	Ap1	Mid-grey
14-4A	N of Yate			-72.062	-41.730	Yellow ash	Ca?	Pumiceous
14-5A	N of Yate	Q	x	-72.026	-41.750	Yellow ash	Tagua	Pumiceous
14-5B	N of Yate	Q	x	-72.026	-41.750	Grey ash	Ap1	Fine ash
14-5D	N of Yate	Q	x	-72.026	-41.750	Yellow ash	Ca11?	Orange, Sandy, pumiceous
14-7A	N of Yate	Q	x	-72.028	-41.749	Yellow ash	Ca11?	Orange, weathered, sandy
23-1A	N of Yate			-72.265	-41.656	Pumice	Ca?	Washed into river sands
23-1C	N of Yate			-72.265	-41.656	Pumice	Ca?	Washed into river sands
23-2A	N of Yate	P	x	-72.225	-41.636	Pumice	Ca13	Pumice in clay
23-5A	N of Yate	N	x	-72.392	-41.702	Pumice	Cha1	Orange-white, sandy
23-11A	N of Yate	L		-72.459	-41.723	Weathered ash?	Ca1	Orange unit, unclear if tephra
23-11E	N of Yate	L	x	-72.459	-41.723	Grey ash	Ap1	Fine ash
25-1A	N of Yate	O	x	-72.295	-41.647	Pumice	Cha1	White, sandy
25-4A	N of Yate	S		-72.320	-41.586	Pumice	Ca1	Orange pumice
25-5C	N of Yate	S	x	-72.319	-41.582	Pumice	Ca1	Deep orange pumice
25-5D	N of Yate	S		-72.319	-41.582	Pumice	Ca2	Deep orange pumice
25-5G	N of Yate	S	x	-72.319	-41.582	Yellow ash	Ca11	Very fine ash
25-5H	N of Yate	S	x	-72.319	-41.582	Pumice	Ca12	Coarse pumice, poorly sorted
25-5I	N of Yate	S		-72.319	-41.582	Yellow ash	Ca12/13	Fine ash
25-5L	N of Yate	S		-72.319	-41.582	Pumice	Ca13	Coarse pumices (resin mounted)
25-5M	N of Yate	S	x	-72.319	-41.582	Pumice	Cha1	White, sandy
25-5N	N of Yate	S	x	-72.319	-41.582	Pumice	Ca7	Orange, rounded pumices
25-6A	N of Yate	U		-72.297	-41.533	Pumice	Ca1	Orange, very soft pumices
25-7A	N of Yate	T		-72.311	-41.561	Pumice	Ca12	Coarse pumices (resin mounted)
802-2A	N of Yate	O	x	-72.289	-41.647	Yellow ash	Ca11?	Fine, pumiceous
802-5A	N of Yate	T		-72.311	-41.560	Pumice	Ca13	Yellow-brown pumices
802-5B	N of Yate	T		-72.311	-41.560	Pumice	Ca12	Yellow-brown pumices
803-1A	N of Yate	V	x	-72.285	-41.519	Yellow ash	Ca3	Orange, fine pumice
803-1B	N of Yate	V	x	-72.285	-41.519	Pumice	Ca4	Orange, coarse pumice

Sample	Area	Column	ICP-MS	Long.	Lat.	Type	Source	Notes
803-1C	N of Yate	V	x	-72.285	-41.519	Yellow ash	Ca5	Fine, pumiceous
803-1D	N of Yate	V	x	-72.285	-41.519	Yellow ash	Ca8	Fine, pumiceous
803-1E	N of Yate	V	x	-72.285	-41.519	Yellow ash	Ca10	Very fine
803-1F	N of Yate	V	x	-72.285	-41.519	Yellow ash	Ca11	Yellow-orange, very fine
803-2B	N of Yate			-72.308	-41.467	Pumice	Ca?	Yellow, coarse pumice
803-2C	N of Yate			-72.308	-41.467	Pumice	Ca?	Yellow, coarse pumice
803-5A	N of Yate	Y	x	-72.283	-41.409	Pumice	Ca12	Yellow-brown pumices
803-5B	N of Yate	Y	x	-72.283	-41.409	Pumice	Ca13	Yellow-brown pumices
820-1A	Ayacara			-72.784	-42.314	Ash and pumice	Cha1	Weathered, poorly sorted
825-1A	N of Chaitén			-72.581	-42.611	Pumice	Cha1	Yellow, coarse pumice
825-1B	N of Chaitén			-72.581	-42.611	Pumice	Cha1	Top, pumice in clay
825-2A	N of Chaitén		x	-72.577	-42.706	Pumice	Cha1	Coarse pumice (thin sectioned)
826-1A	N of Palena			-72.345	-43.580	Yellow ash	Yan1	Fine ash
829-1A	La Junta			-72.387	-44.151	Pumice	Mel1	Yellow, coarse pumice
829-1B	La Junta			-72.387	-44.151	Pumice	Mel2	Yellow pumice
C06-6C	Los Alerces			-71.618	-42.822	Pumice	Mic2	White pumice
C12-C2	Futaleufú			-72.073	-43.367	Pumice	Cor?	Orange, fine pumice
C15-F2C	Chaitén			-72.676	-42.810	Pumice	Cha?	Thin basal pumice
C15-F2D	Chaitén			-72.676	-42.810	Pumice	Cha?	Above F2C
C15-F2E	Chaitén			-72.676	-42.810	Pumice	Cha?	Top pumice, coarse
C15-F2G	Chaitén			-72.676	-42.810	Pumice	Cha?	Parallel bedded, coarse base
C15-F2H	Chaitén			-72.676	-42.810	Yellow ash	Cha?	Fine, laminated, above F2G
C15-F2I	Chaitén			-72.676	-42.810	Pumice	Cha?	Coarse lens, above F2H
C15-F2J	Chaitén			-72.676	-42.810	Pumice	Cha?	Coarse unit, cross stratified
C15-F2K	Chaitén			-72.676	-42.810	Pumice	Cha?	Lithic rich with obsidians, top
C15-F2L	Chaitén			-72.676	-42.810	Obsidians	Cha?	Basal debris flow
C15-F2M	Chaitén			-72.676	-42.810	Pumice	Cha?	Bulk indurated basal unit
C16-G7A	Minchinmávida			-72.468	-42.950	Pumice	Mic?	Millet seed texture in clay
C17-H10A	Minchinmávida			-71.899	-43.193	Pumice	Mic?	Yellow reworked pumice

Appendix B

ICP-MS data

	Apagado																	LaVig
	Lava				Ap1													
ppm	20-4A	21-2a	21-4a	21-6B	21-5A	24-6D	04-2A	13-3C	21-5C	14-5B	23-11E	13-3A	13-1E	30-3A	30-3B	30-3F	14-1A	803-5C
Sc	29	33	33	33	32	35	34	37	34	34	33	28	29	33	34	33	37	32
V	236	254	244	247	222	236	245	265	247	244	234	198	199	236	242	229	259	267
Cr	150	-	-	-	813	679	833	457	870	724	648	812	860	567	452	660	246	202
Co	34	35	37	23	46	51	48	39	50	44	49	53	53	47	45	48	34	38
Ni	78	-	-	-	258	226	235	102	246	194	220	364	361	235	183	259	88	91
Cu	60	66	57	85	58	65	64	88	59	56	56	52	45	69	80	70	61	75
Zn	-	89	99	101	91	78	72	79	78	78	74	-	-	-	-	-	-	79
Ga	-	19	18	20	15	15	17	17	16	17	16	-	-	-	-	-	-	19
Rb	8	8	4	30	4	5	5	5	4	7	6	9	8	4	4	4	5	9
Sr	443	441	477	331	437	409	408	475	438	434	355	350	327	445	467	440	414	539
Y	22	19	19	30	16	15	15	17	17	16	17	17	16	17	18	17	19	17
Zr	82	75	78	138	66	60	61	60	63	62	66	60	58	61	63	62	77	77
Nb	2.9	2.6	2.9	5.5	2.2	1.6	1.9	1.7	2.1	2.1	2.2	2.2	2.2	1.7	1.6	1.7	2.2	2.4
Mo	0.7	0.4	0.3	1.3	-	-	-	-	-	-	-	0.2	0.1	1.1	0.3	0.4	0.5	-
Sn	-	0.6	0.7	1.4	16.3	3.3	3.1	12.7	2.3	2.7	4.0	-	-	-	-	-	-	1.6
Cs	0.3	-	-	-	-	-	-	-	-	-	-	0.6	0.5	0.2	0.2	0.1	0.3	-
Ba	192	188	221	238	90	82	91	104	93	113	87	133	132	95	98	92	142	159
La	9	9	11	12	7	6	6	7	7	6	7	7	5	6	6	6	7	9
Ce	22	20	25	29	15	14	15	16	15	15	16	17	14	14	15	15	18	22
Pr	3.0	2.9	3.5	4.2	2.3	2.1	2.2	2.4	2.3	2.3	2.5	2.3	2.0	2.2	2.3	2.2	2.6	3.1
Nd	14	13	16	20	10	9	10	11	11	11	11	10	9	10	11	10	12	14
Sm	3.4	3.3	3.7	5.1	2.6	2.5	2.7	2.9	2.8	2.7	2.8	2.7	2.5	2.6	2.8	2.7	3.0	3.5
Eu	1.0	-	-	-	0.9	0.8	0.9	1.0	0.9	0.9	0.9	0.8	0.8	0.8	0.9	0.8	0.9	1.1
Gd	3.5	3.6	4.0	5.7	3.0	2.8	2.9	3.1	3.0	3.0	3.1	2.7	2.5	2.7	2.8	2.7	3.1	3.5
Tb	0.6	0.6	0.6	1.0	0.5	0.4	0.5	0.5	0.5	0.5	0.5	0.4	0.4	0.4	0.5	0.4	0.5	0.5
Dy	3.4	3.5	3.7	5.7	3.0	2.8	2.9	3.2	3.1	3.0	3.2	2.7	2.6	2.7	2.8	2.8	3.0	3.3
Ho	0.7	0.7	0.7	1.2	0.6	0.6	0.6	0.7	0.6	0.6	0.6	0.6	0.6	0.6	0.6	0.6	0.6	0.7
Er	2.1	2.1	2.2	3.5	1.6	1.5	1.7	1.8	1.8	1.7	1.7	1.7	1.6	1.7	1.8	1.7	1.9	1.8
Tm	0.3	0.3	0.3	0.5	0.2	0.2	0.2	0.3	0.3	0.3	0.3	0.3	0.2	0.2	0.2	0.2	0.3	0.3
Yb	1.9	1.9	2.0	3.2	1.6	1.5	1.6	1.7	1.7	1.6	1.6	1.5	1.5	1.5	1.6	1.6	1.7	1.7
Lu	0.3	0.3	0.3	0.5	0.2	0.2	0.2	0.3	0.3	0.3	0.2	0.2	0.2	0.2	0.2	0.2	0.3	0.3
Hf	2.1	-	-	-	1.7	1.5	1.8	1.8	1.8	1.8	1.7	1.6	1.6	1.6	1.7	1.7	2.0	2.2
Ta	0.2	0.2	0.2	0.4	0.1	0.1	0.1	0.1	0.1	0.1	0.1	0.2	0.2	0.1	0.1	0.1	0.1	0.1
Pb	4.2	4.4	5.8	7.9	3.2	2.9	4.5	4.7	3.9	4.3	4.0	3.8	3.7	3.7	3.6	3.5	4.6	7.2
Th	-	-	-	-	1.1	1.1	1.1	1.2	1.0	1.5	1.5	-	-	-	-	-	-	1.6
U	0.3	0.3	0.4	0.8	0.2	0.3	0.3	0.3	0.3	0.4	0.3	0.6	0.4	0.3	0.3	0.3	0.4	0.5
Ti	6548	5780	5876	7230	4738	4609	4805	5036	5178	5006	4898	4815	4865	5188	5174	5087	5871	5661

	Hornopirén							Yate						Palena				Puyuhuapi		S. Minch	Tagua	Calbuco			Cha1
	Lava		Summ.	Ho1				Lava					YaSc									Ca1	Ca7	Ca13	
ppm	15-5A	19-4A	05-3B	26-8A	24-6A	801-1B	24-6C	23-8b	23-10a	26-2a	26-4a	26-6a	23-9A	826-3A	826-3B	826-3C	826-4A	828-6A	828-6B	C16-G7b	14-5a	25-5c	25-5n	23-2A	26-8b
Sc	28	29	29	30	30	29	31	35	33	23	28	26	31	32	31	30	31	28	30	29	25	32	29	20	3
V	239	241	248	230	225	237	207	317	245	167	257	212	229	232	226	243	220	241	237	226	161	375	224	192	13
Cr	98	95	79	207	105	171	101	-	-	-	-	-	82	164	202	176	182	283	294	221	-	-	-	-	-
Co	32	31	30	33	33	32	22	21	36	14	28	26	31	40	41	42	53	45	50	41	15	30	17	22	2
Ni	50	63	34	79	47	75	-	-	-	-	-	-	41	86	116	127	251	211	186	150	-	-	-	-	-
Cu	63	62	63	65	65	65	46	55	67	26	70	41	35	51	54	33	57	43	42	48	31	27	26	33	8
Zn	91	99	88	72	81	81	76	100	90	96	86	70	-	-	-	-	-	-	-	-	112	103	78	93	50
Ga	19	19	20	19	19	19	19	22	20	21	17	17	-	-	-	-	-	-	-	-	23	29	23	21	14
Rb	21	21	14	14	17	17	16	17	10	79	84	47	11	9	9	3	7	13	14	15	40	1	23	16	103
Sr	460	453	420	401	409	431	339	427	431	336	631	476	402	421	393	275	384	678	657	416	342	138	130	330	140
Y	26	25	26	25	25	25	24	24	20	34	31	21	20	22	23	17	23	26	26	25	39	9	17	19	12
Zr	135	129	140	117	128	120	150	85	101	219	190	108	62	81	85	95	94	168	157	122	368	115	81	97	76
Nb	5.4	5.0	5.4	4.2	5.0	4.3	5.5	3.1	3.4	6.2	4.7	3.0	2.1	2.6	3.1	3.2	3.1	24.0	21.1	5.1	15.1	3.3	3.7	2.9	8.0
Mo	-	-	-	-	-	-	-	0.5	0.4	2.2	1.8	1.4	0.4	0.4	0.4	0.4	0.4	1.1	1.1	0.6	1.6	0.4	0.7	0.7	1.6
Sn	1.3	1.4	2.8	10.4	11.9	1.9	1.3	0.7	0.8	2.7	2.1	1.1	-	-	-	-	-	-	-	-	12.7	26.7	6.6	33.2	14.5
Cs	-	-	-	-	-	-	-	-	-	-	-	-	0.6	0.4	0.4	0.2	0.2	0.2	0.3	0.5	-	-	-	-	-
Ba	330	323	294	227	269	288	232	219	276	578	428	399	162	156	149	94	129	387	393	212	556	36	177	174	571
La	20	19	19	16	19	16	17	10	13	24	24	17	6	9	10	6	10	38	34	12	39	3	10	7	24
Ce	43	41	42	34	41	35	39	22	29	54	58	36	15	20	21	18	23	81	72	30	96	7	21	18	47
Pr	5.7	5.4	5.5	4.7	5.6	4.8	5.3	3.2	3.9	7.1	8.1	4.7	2.1	2.7	2.9	2.3	3.1	10.4	8.8	4.0	11.4	1.1	2.7	2.5	4.9
Nd	24	23	24	21	24	21	22	15	17	30	36	19	10	12	12	11	13	41	34	17	46	5	12	12	17
Sm	5.2	5.0	5.2	4.7	5.2	4.8	4.8	4.0	3.8	6.7	8.7	4.3	2.6	3.0	3.1	2.9	3.2	7.6	6.6	4.0	9.3	1.5	2.7	3.1	2.9
Eu	1.5	1.4	1.5	1.4	1.5	1.4	1.4	-	-	-	-	-	0.8	1.0	1.0	0.9	1.0	2.1	1.9	1.2	-	-	-	-	-
Gd	5.4	5.1	5.4	5.0	5.3	5.0	5.2	4.5	4.2	7.1	8.4	4.4	2.8	3.2	3.4	2.9	3.5	7.1	6.4	4.2	9.5	1.7	3.1	3.4	2.9
Tb	0.8	0.8	0.8	0.7	0.8	0.7	0.7	0.8	0.7	1.1	1.2	0.7	0.5	0.5	0.5	0.5	0.6	0.9	0.9	0.7	1.4	0.3	0.5	0.6	0.4
Dy	4.8	4.7	4.9	4.6	4.8	4.7	4.7	4.6	3.9	6.4	6.3	4.0	3.0	3.3	3.4	3.0	3.6	5.0	4.6	4.0	7.9	1.9	3.0	3.5	2.2
Ho	1.0	0.9	1.0	0.9	1.0	0.9	0.9	1.0	0.8	1.3	1.2	0.8	0.7	0.7	0.7	0.6	0.8	0.9	0.9	0.9	1.5	0.4	0.6	0.7	0.4
Er	2.7	2.6	2.7	2.5	2.6	2.6	2.4	2.9	2.3	3.9	3.2	2.3	1.9	2.0	2.1	1.8	2.2	2.4	2.3	2.4	4.6	1.3	1.9	2.2	1.3
Tm	0.4	0.4	0.4	0.4	0.4	0.4	0.3	0.4	0.3	0.6	0.4	0.3	0.3	0.3	0.3	0.3	0.3	0.3	0.3	0.3	0.7	0.2	0.3	0.3	0.2
Yb	2.5	2.4	2.5	2.3	2.5	2.4	2.3	2.7	2.1	3.7	2.9	2.3	1.7	1.9	1.9	1.8	2.0	2.0	1.9	2.2	4.5	1.3	1.9	2.1	1.4
Lu	0.4	0.4	0.4	0.3	0.4	0.4	0.3	0.4	0.3	0.6	0.4	0.3	0.3	0.3	0.3	0.3	0.3	0.3	0.3	0.3	0.7	0.2	0.3	0.3	0.2
Hf	3.5	3.4	3.7	3.0	3.4	3.2	3.3	-	-	-	-	-	1.6	2.1	2.1	2.4	2.2	3.9	3.6	2.8	-	-	-	-	-
Ta	0.3	0.3	0.3	0.2	0.3	0.2	0.3	0.2	0.2	0.5	0.5	0.3	0.1	0.2	0.2	0.2	0.2	1.5	1.3	0.3	0.9	0.3	0.3	0.2	0.9
Pb	8.6	13.7	9.0	8.8	8.7	7.6	6.6	5.1	6.5	14.9	9.8	10.7	4.4	4.8	4.6	4.4	6.8	8.2	6.4	5.3	16.5	11.8	9.3	8.8	20.8
Th	2.4	2.4	2.5	2.1	2.5	2.3	2.6	-	-	-	-	-	-	-	-	-	-	-	-	-	-	-	-	-	-
U	0.5	0.5	0.5	0.4	0.5	0.5	0.5	0.5	0.5	2.2	1.5	1.9	0.3	0.5	0.4	0.4	0.4	1.9	1.4	0.5	1.6	0.8	1.2	0.4	3.5
Ti	6410	6292	6697	6951	6139	6681	6395	7217	5559	5908	6716	4726	5628	6782	6645	7478	7090	11430	11494	7521	7979	9957	5089	5666	943

Samples used only for tephra correlation, with overall poor analyses except for elements shown

	Ya1		Cha1							Ca3	Ca4
ppm	26-5AG	24-2A	24-8A	20-2C	23-5A	25-1A	20-2D	25-5M	825-2A	803-1A	803-1B
V	92	96	49	12	27	23	85	21	2	248	269
Cr	15	15	7	4	6	6	10	6	0	21	16
Co	8	8	3	1	8	3	10	3	1	30	29
Zr	205	199	92	77	80	83	83	62	77	105	87
Nb	5.6	5.7	9.1	8.0	8.4	7.9	7.4	7.1	6.1	3.7	3.0
Ba	594	594	541	483	460	458	408	408	484	72	45
Hf	5.0	4.9	2.5	2.2	2.3	2.4	2.5	1.9	2.4	2.8	2.3
Ta	0.4	0.4	0.8	0.8	0.8	0.8	0.8	0.5	0.2	0.2	0.2
Ti	3835	4010	1981	846	1143	1235	2653	1309	725	8136	7887
K	25259	25685	25834	24216	23541	23005	16009	19913	20017	1225	883

	Ca5	Ca8	Ca10	Ca11					Ca12		Ca13
ppm	803-1C	803-1D	803-1E	25-5G	802-2A	14-5D	803-1F	14-7A	803-5A	25-5H	803-5B
V	299	275	209	230	231	259	210	201	142	191	171
Cr	20	22	13	14	9	12	9	9	5	7	4
Co	20	23	23	24	20	24	20	22	17	20	20
Zr	98	79	82	75	119	108	89	96	109	85	92
Nb	2.8	2.4	2.6	2.5	3.8	3.4	3.1	3.1	3.2	2.8	2.9
Ba	37	73	72	53	54	79	99	90	178	158	145
Hf	2.7	2.0	2.0	1.8	2.9	2.6	2.6	2.5	2.5	2.5	2.2
Ta	0.2	0.2	0.2	0.1	0.2	0.2	0.2	0.2	0.2	0.2	0.2
Ti	7661	6035	5718	6154	6538	6897	5712	6345	4733	5563	5403
K	823	2134	2067	1508	1710	2627	2659	2254	7118	4873	5810

Appendix C

Palaeomagnetic directional data

Volcano	Demagnetisation	Sample	Declination (deg.)	Inclination (deg.)
Hornopirén	Alternating field	15-5A	33.1	-51.6
Hornopirén	Alternating field	30-2A	13.3	-69.3
Hornopirén	Alternating field	30-9A	23	-53.6
Hornopirén	Alternating field	21-15B	1.7	-57.4
Hornopirén	Alternating field	24-3A	12.1	-59.2
Yate	Alternating field	23-12A	-5.5	-64.5
Yate	Alternating field	23-10A	-4.3	-51.8
Yate	Alternating field	02-3A	47.8	-74.6
Yate	Alternating field	23-8A	15.1	-60.6
Yate	Alternating field	26-3A	-67.7	-68.6
Yate	Alternating field	26-2A	-30.3	-59.5
Yate	Alternating field	26-4A	9.4	-49.6
Yate	Alternating field	26-6A	11.8	13.2
Apagado	Alternating field	20-4A	-14.3	-57.4
Apagado	Alternating field	21-9C	176.9	55.3
Hornopirén	Thermal	15-5A	21.8	-38.3
Hornopirén	Thermal	30-2A	21.4	-70.8
Hornopirén	Thermal	30-9A	-3.1	-54.4
Hornopirén	Thermal	21-15B	7.1	-55.6
Hornopirén	Thermal	24-3A	8.4	-55.8
Yate	Thermal	23-12A	-12.7	-60.2
Yate	Thermal	23-10A	-19.1	-50.0
Yate	Thermal	02-3A	77	-72.9
Yate	Thermal	23-8A	11.7	-63.1
Yate	Thermal	26-3A	-74.9	-68.2
Yate	Thermal	26-2A	-10.4	-59.7
Yate	Thermal	26-4A	27.8	-58.9
Yate	Thermal	26-6A	-0.2	5.6
Apagado	Thermal	20-5A	-42.1	-86.1
Apagado	Thermal	20-4A	-9.4	-57.3
Apagado	Thermal	21-6A	-17.2	-50.5
Apagado	Thermal	21-9C	179	42.3

Appendix D

Thin section descriptions

Hornopirén	
15-5A	Finely holocrystalline, groundmass dominated by tabular plagioclase set in a cryptocrystalline matrix approaching a trachytic texture. Scattered irregular vesicles. Blocky phenocryst plagioclase, commonly sieve-textured and normally zoned, often glomeroporphyritic with olivine. Olivine rounded, usually small, often clustered, with narrow fayalitic rims and reaction corona of orthopyroxene, sometimes with outer rim of augite. Orthopyroxene as less common phenocryst, small and tabular. Coarse Cr-spinel often as euhedral inclusions in olivines, but also in groundmass. Groundmass dominated by plagioclase laths, with euhedral augite, orthopyroxene and less common pigeonite, and ubiquitous fine grained Ti-magnetite.
15-7A	Highly and irregularly vesicular, holocrystalline with cryptocrystalline matrix. Plagioclase and olivine phenocrysts appear as in 15-5A, with olivines very commonly showing an alteration corona of finely crystalline orthopyroxene or pigeonite. Rare subhedral augite (xeno?)phenocryst, sector zoned. Groundmass predominantly plagioclase with euhedral orthopyroxene, pigeonite and augite. Coarse Cr-spinel common, usually associated with olivine. Groundmass Ti-magnetite extremely fine grained.
19-1A	Holocrystalline, with cryptocrystalline black matrix and regular small rounded vesicles. Euhedral blocky plagioclase phenocrysts dominate, some with sieve-textured interiors and/or normal zoning, as above. Glomerocrysts of olivine, sometimes with plagioclase, rarely with micrographic intergrowths, also common, with thin fayalitic rim and reaction corona of orthopyroxene or pigeonite, itself often with narrow rim of clinopyroxene. Groundmass and oxides as in 15-5A.
19-1B	Holocrystalline, cryptocrystalline matrix dominated by plagioclase laths, scattered small vesicles and groundmass euhedral orthopyroxene, pigeonite and augite and Ti-magnetite. Euhedral phenocrysts of plagioclase and rounded olivines, as above. Less commonly euhedral tabular orthopyroxene as phenocrysts. Groundmass and oxides as in 15-5A. Some groundmass pyroxene is highly aluminous (>7.5%) and TiO rich (>1%). Slide contains coarse-grained gabbroic clot of olivine and plagioclase, same composition as phenocrysts, with glassy interstitial matrix.
19-4A	Finely holocrystalline, with some cryptocrystalline black matrix. Olivine phenocrysts small and rounded, occasionally as glomerocrysts, with or without plagioclase, and Cr-spinel often associated. Olivine coronae sometimes thick, of orthopyroxene or less commonly clinopyroxene + Ti-magnetite, in some cases only remaining as embayed relic core to orthopyroxene phenocryst (these are subhedra, uncommon and have clinopyroxene rim). Larger plagioclase phenocrysts common, some with sieve textured cores; also microphenocrystal plagioclase with included mantles. Groundmass of plagioclase laths, three pyroxenes and euhedral Ti-magnetite in a range of feathery or dendritic forms. Contains coarse olivine and plagioclase clot.
21-14A	Sparsely vesicular, holocrystalline, fine groundmass set in cryptocrystalline matrix. Laths and rhombs of phenocryst plagioclase, often with sieve texture interiors and normally zoned. Olivines abundant, usually small, often euhedral to subhedral, occasionally rounded, often as glomerocrysts with plagioclase. More Mg-rich olivines have thin fayalitic rim, but none have reaction coronae; Cr-spinel associated. Groundmass dominated by plagioclase laths, with orthopyroxene and pigeonite showing thin augitic rims. Ti-magnetite extremely fine.
21-15B	Dense, sparsely vesicular, holocrystalline. Olivine phenocrysts common, euhedral to subhedral, occasionally glomerocrysts, with fayalitic rims, and in cases alteration jackets of orthopyroxene; commonly associated with Cr-spinel. Plagioclase phenocrysts tabular or lath shaped, some with sieve textured cores or associated with olivines. Groundmass plagioclase laths, orthopyroxene and augite, with rarer olivine, and Ti-magnetite in feathery and dendritic forms.

24-3A	Holocrystalline, with microcrystalline matrix. Groundmass texture distinctive, with oxides as euhedral evenly distributed phase. Coarse grained groundmass oxides Ti-rich (ülvospinel), while finer groundmass oxides are low Ti as in above samples. Occasional pure magnetite also. Cr-spinel usually associated with olivine. Phenocryst olivine, subhedral with fayalitic rims and orthopyroxene reaction coronae. Rarer olivines show highly forsteritic skeletal patches with fayalitic replacement texture. Plagioclase phenocrysts tabular, some sieve textured, some in glomerocrysts with olivine. Orthopyroxene a less common phenocryst phase, with clinopyroxene rims. Groundmass dominated by plagioclase laths, with oxides and three pyroxenes, as above.
24-7A	Holocrystalline, moderately vesicular, with patchy cryptocrystalline matrix. Phenocrysts of olivine and plagioclase. Olivine euhedral to subhedral, with fayalitic rims and orthopyroxene coronae, occasionally as thick jackets around olivine core, and Cr-spinel associated. Plagioclase tabular, occasionally sieve textured and commonly in glomerocrysts with olivine. Groundmass of plagioclase laths and three pyroxenes, with euhedral Ti-magnetite. Some groundmass clinopyroxene alumina rich. Contains coarse grained clot of phenocryst olivine and plagioclase.
30-2A	Holocrystalline, with cryptocrystalline matrix. Olivine common as phenocryst, euhedral to rounded, or anhedral in glomerocrysts with plagioclase. Fayalitic rims, and commonly with alteration jacket of orthopyroxene, sometimes with oxides. Plagioclase common phenocryst, tabular, normally zoned, often with sieve textures. Coarse euhedral Cr-spinel associated with olivine or plagioclase, or occasionally in groundmass with Cr-poor rims. Orthopyroxene rimming olivine or in groundmass, commonly rimmed with augite. Groundmass dominated by laths of plagioclase, with tabular orthopyroxene and euhedral augite, and feathery and dendritic Ti-magnetite.
30-9A	Holocrystalline, with a wholly microcrystalline groundmass, more so than any other Hornopirén lava samples. Subhedral to anhedral olivine phenocrysts, with more fayalitic rim, and thin reaction rim of orthopyroxene or pigeonite, also often associated with Cr-spinel. Rarer groundmass olivines, more fayalitic, with jackets of orthopyroxene. Phenocryst plagioclases, many with sieve textured cores and normal zoning, often as glomerocrysts with or without olivine. Groundmass a mix of fine grained plagioclase laths and euhedral stubby augite, pigeonite and orthopyroxene, often in fine grained clusters and with calcic rims to low-Ca cores. Ti-magnetite euhedral, often in clusters.
05-3A	Holocrystalline, with microcrystalline groundmass and some cryptocrystalline matrix. Plagioclase phenocrysts tabular and abundant, commonly with normal zoning, some with sieve textured cores. Olivine phenocrysts with fayalitic rims and coronae of orthopyroxene or clinopyroxene, sometimes with plagioclase. Cr-spinel associated with phenocrysts. Rare groundmass olivines, more fayalitic. Uncommon euhedral augite phenocrysts. Groundmass of plagioclase laths, orthopyroxene, augite and euhedral Ti-magnetite.
05-3C	Highly vesicular red scoria, finely crystalline, glassy matrix. Rare phenocrysts of euhedral plagioclase and euhedral to rounded olivine. Plagioclase pitted, appears unstable. Olivine variably altered along grain boundaries and crystal planes, with patchy development to aggregate of hematite and an amorphous, more fayalitic, component. Occasional plagioclase and olivine glomerocrysts, with Cr-spinel associated. Finely crystalline clinopyroxene, pigeonite and plagioclase in matrix. Subcalcic augite to pigeonite coating plagioclase phenocrysts.
Yate	
23-8B	Holocrystalline, moderately vesicular, highly porphyritic. Plagioclase phenocrysts dominate, abundant small and tabular grains, but commonly large, euhedral, often square, with included cores or mantles, and normal zoning, and often in glomerocrysts with syneussis intergrowths. Olivine less common, rounded, small, often zoned, with fayalitic rims, usually with corona of pigeonite or clinopyroxene, sometimes with plagioclase or Ti-magnetite. Augite phenocrysts also, small and subhedral to rounded, some with inclusions of Ti-magnetite, perhaps replacment of olivine, zoned with Fe-rich Ca-poor rims. Microcrystalline groundmass dominated by plagioclase laths, with euhedral pigeonite, augite and Ti-magnetite, both coarse-grained and a ubiquitous fine-grained Ti-richer type. Occasional fayalitic groundmass olivine.
23-10A	Holocrystalline, phenocryst phase dominated by plagioclase, commonly lath shaped and not as coarse or blocky as in 23-8B and 12B. Plagioclase phenocrysts often with included core or mantle, occasionally with a secondary included rim, and showing normal zoning. Olivines a common phenocryst phase, larger subhedral grains with a more fayalitic rim, smaller rounded grains unzoned. In all cases with reaction coronae of orthopyroxene, sometimes thick, often also plagioclase. Coarse euhedral Cr-spinel associated with olivine, or glomerocryst plagioclase and olivine. Phenocryst orthopyroxene common, green coloured, euhedral, often with patchy embayed olivine inclusions, where replaced, and with Fe-rich or augitic rim. Groundmass of plagioclase, pigeonite, augite and less commonly orthopyroxene, with coarse euhedral Ti-magnetite with significant Cr, and fine scale high-Ti Ti-magnetite with low-Cr.
23-12B	Holocrystalline, very similar to 23-8B. Plagioclase phenocrysts dominate, often as glomerocrysts, blocky, with included cores or mantles, often normally zoned, with some inverse zoning outside included mantles. Smaller tabular plagioclase also common. Euhedral to anhedral olivines a secondary phenocryst phase, commonly in glomerocrysts with plagioclase, with fayalitic rims and coronae of pigeonite and plagioclase. Microcrystalline groundmass of plagioclase with euhedral pigeonite and augite, and less commonly olivine, but without reaction coronae. Coarse scale oxides of Ti-magnetite, relatively Ti-poor, some as inclusions in olivine, also fine scale Ti-richer grains.

26-2A	Porphyritic, with finely microcrystalline groundmass set in glass, giving very clear distinction between phenocrysts and groundmass. Tabular or lath shaped plagioclase dominant phenocrysts, commonly with glassy inclusions in the core, and with normal zoning. Large glomerocrysts common. Secondary phenocryst phases of orthopyroxene and augite, both common. Clinopyroxene green and mildly pleochroic. Some orthopyroxene with symplectite cores of magnetite, often centered around embayed patchy olivine as a replacement texture. Pyroxenes unzoned. Occasional euhedral clinoppyroxene rims to rounded, with clinopyroxene lamellar twinned. Groundmass of fine scale plagioclase laths, euhedral orthopyroxene and pigeonite, and apatite, commonly associated with pyroxene phenocrysts, all in glass. The only olivine is as embayed patchy cores to euhedral orthopyroxene phenocrysts, rarely with Cr-spinel associated. Coarse Ti-magnetite common; that in olivine-magnetite symplectites is Ti-poor, while fine groundmass Ti-magnetite is Ti-rich. Occasional pyrite and ilmenite, rare magnetite, all in groundmass.
26-3A	Crystalline, very similar to 26-2A, but with slightly coarser microcrystalline and cryptocrystalline groundmass. Plagioclase phenocrysts dominate, commonly tabular with included cores and normal zoning, or smaller and lath like, often in glomerocrysts with pyroxene. Brown-green pleochroic augite phenocrysts common, some with reverse zoning in Fe (Fe-poorer rims). Orthopyroxene a common phenocryst, often rounded, commonly with thick jacket of augite, and often as a replacement of olivine, with symplectite of oxides and patchy olivine core. Olivine rare, as patchy cores to orthopyroxene. Coarse Ti-magnetite phenocrysts. Groundmass of plagioclase, orthopyroxene, pigeonite and apatite but, like 26-2A, not augite. Ti-magnetite as symplectite or in groundmass, where Ti-richer. Groundmass ilmenite relatively common, pyrite and magnetite occasional.
26-4A	Holocrystalline, microcrystalline to cryptocrystalline matrix. Tabular to lath shaped plagioclase pehnocrysts dominant, some cores included, also pyroxene inclusions, but mainly clean, euhedral, normal zoning. Olivine phenocrysts, thin fayalitic rims, euhedral Cr-spinel inclusions, some with thin orthopyroxene and Ti-magnetite coronae, rarely as core altered to orthopyroxene phenocrysts as symplectite texture, and in such cases a more fayalitic olivine, thus presumed to be xenocrystal grains. Augite phenocrysts common, occasionally twinned, brown green pleochroic, also often as lamellar twinned thick jackets to orthopyroxene, some only as skeletal form, some with minor Cr content. Orthopyroxene phenocrysts euhedral, green/yellow, often as glomerocrysts, sometimes with plagioclase. Groundmass dominated by plagioclase, olivine relatively common, without coronae. Rare alkali feldspar. Augite common, and apatite. Coarse Ti-magnetite, occasional Cr-spinel with Cr-poor Ti-rich rims. Fine groundmass Ti-magnetite less common than in above samples. Occasional pyrite and chalcopyrite.
26-5AG	Glassy grey pumice, abundant phenocrysts, dominated by plagioclase, mostly euhedral, some with sieve textured cores or normal zoning. Euhedral orthopyroxene also common, greenish clinopyroxene slightly less common. Apatite as inclusions in pyroxenes. Coarse oxides abundant, particularly Ti-magnetite, ilmenite also frequent.
26-5AW	White pumice, highly similar to 26-5AG, but with greater vesicularity, accounting for the colour difference, and thus a more distinct phenocryst phase.
26-6A	Tabular to lath-shaped plagioclase phenocrysts dominant, mostly clean, sometimes strong normal zoning, occasionally part reversed outside mantle, some included cores, occasionally highly altered to pseudomoprh aggregates with augite. Olivine common, euhedral to subhedral, more fayalitic rim, commonly narrow reaction coronae of orthopyroxene, Cr-spinel associated. Occasional in groundmass as embayed cores with thick orthopyroxene jackets. Phenocryst orthopyroxene more common than augite, often reverse zoned (Fe-poorer) rims, or twinned augite rims. Phenocryst augite, minor Cr in lower Fe grains, normally zoned (Fe-richer) rims. Microcrystalline groundmass, plagioclase laths, orthopyroxene, augite, common apatite, often with pyroxene or plagioclase phenocrysts. Fine grained clot of plagioclase, augite and orthopyroxene. Glass as stringy patches or interstitial to glomerocrysts. Coarse Ti-magnetites, less than in 26-2A, 3A, 4A, some approaching magnetite. Ilmenite, often intergrown with Ti-Mag. Fine groundmass Ti-richer magnetite, some ilmenite, minor chalcopyrite.
26-7A	Crystalline, occasional large phenocrysts of olivine and plagioclase, common smaller phenocrysts of plagioclase, olivine, augite, orthopyroxene and oxides. Olivines euhedral to subhedral, with fayalitic rims and alteration coronae of pyroxene and plagioclase. Small phenocryst to groundmass scale olivines often as embayed cores with thicker orthopyroxene jacket, some with oxide symplectite, though others subhedral and without reaction rim. Plagioclase occasionally large and blocky, mostly tabular and euhedral to subhedral, strongly normally zoned. Orthopyroxene common phenocryst, subhedral, usually with Fe-poorer Mg-richer rim, some with jacket of clinopyroxene. Clinopyroxene commonly twinned, some with Fe-richer rims with minor Ti, others with minor Cr. Microcrystalline groundmass of plagioclase, orthopyroxene, pigeonite, augite and apatite, with some glass, and Ti-magnetite. Coarser oxide phase of Ti-magnetite, and Cr-spinel associated with olivines, usually as inclusions. Minor ilmenite, pyrite, chalcopyrite, rare zircon, presumed xenocrystal.
02-3A	Holocrystalline, densely porphyritic, phenocryst phase dominated by plagioclase, strongly normally zoned and blocky to tabular, often with cracked or heavily included cores and mantles. Olivine a secondary phenocryst phase, subhedral to rounded and embayed with ubiquitous reaction coronae of orthopyroxene, with occasional oxide symplectite developed. Mostly relatively fayalitic and unzoned, but occasionally with more forsteritic core and fayalitic rim. Phenocryst augite and orthopyroxene also common, euhedral to subhedral, and commonly with augite jackets to orthopyroxene. Groundmass plagioclase dominant. Uncommon alkali feldspar and quartz also present, particularly in interstitial space among glomerocrystal clots. Groundmass orthopyroxene, pigeonite and augite common, with small amounts of ferrohypersthene as well as hypersthene/bronzite. Apatite rare, as inclusions in plagioclase. Ti-magnetite predominant oxide, ilmenite relatively common, minor chalcopyrite. Baddeleyite (ZnO_2) and zircon rare as very fine (<5 micron) euhedral grains.

Apagado	
20-3B	Finely vesicular, holocrystalline, small phenocrysts dominated by olivine, euhedral to subhedral, some with reaction coronae of augite and plag, occasionally as embayed xenocrystal larger fragments with fayalitic rim or reverse zoning to composition of small phenocrysts. Plagioclase absent as phenocrysts. Augite phenocrysts secondary, small and euhedral, without normal zoning, commonly sector zoned with hexagonal habit. Cr-spinel commonly associated with olivine. Microcrystalline matrix of acicular plagioclase, and augite, olivine and pigeonite, and Ti-magnetite common with feathery or dendritic habit; magnetite also present.
20-3E	Two scoria samples, comprising two distinct halves, the first derived from a granitoid protolith, with an extremely crumbly altered texture, with altered quartz to a dirty glass and granitic textured plagioclase, pitted and with irregular twin planes, and dark patches replacing former mafic minerals now replaced by aggregates of Ti-magnetite, clinopyroxene and feldspar or orthopyroxene or olivine and plagioclase. This grades into contact zone with fine grained lava, with some interpenetration of coarse quartz or plagiocalse and lava. Lava fine grained and essentially identical to 20-3B, with a cryptocrystalline matrix. Olivine is the main phenocryst phase, with minor clinopyroxene, both subhedral, occasionally in glomerocrysts. Groundmass of plagioclase, olivine and (some highly aluminous) clinopyroxene, with Cr-spinel associated with olivine. Groundmass oxides extremely fine-grained.
20-3H	Altered granitoid, as Ap1 ejecta, crumbly, texturally plutonic, but altered to fine grained patches, including dark regions which may reflect inflitration by host basaltic melt. Granitoid mafics replaced by fine-grained aggregates of clinopyroxene, glass and magnetite or ol, plag and magnetite. Quartz and feldspar survive, though alteration seen in twin planes and as cloudiness, with some sieve textures. Sphene and apatite, as well as variably titaniferous magnetite. Ilmenite with excess Ti as alteration rim to sphene and included in plagioclase.
20-3L	Plutonic, showing no signs of magmatic alteration, found as ejecta in Ap1 scoria, presumed to be protolith for altered samples above. Granodioritic-tonalitic assemblage. Plagioclase predominant, quartz abundant, small amounts of interstitial alkali feldspar. Biotite (with significant Cl) and hornblende (green pleochroic), in approximately equal proportions, with biotite commonly altered to chlorite. Plagioclase commonly with strong oscillatory zoning. Occasional aplitic patches of biotite, quartz and hornblende. Coarse magnetite very common, euhedral and often clustered with mafics. Fine grained zircon, common apatite, sphene, rare and very fine uranothorite.
20-3M	Ap1 scoria piece with thin glass coating on one surface. Lava is fine grained, cryptocrystalline, with olivine phenocrysts, subhedral and occasionally in glomerocrysts, highly vesicular in parts but with vesicle poor clots, but otherwise as 20-3B.
20-4A	Holocrystalline, relatively coarse, olivine dominant as subhedral to rounded phenocrysts, slightly zoned, often with discontinuous orthopyroxene rim, sometimes thick around a relic olivine core. Plagioclase common as phenocryst, tabular euhedral to anhedral, with normal zoning. Coarse Ti-magnetite common, euhedral, often with well-developed ilmenite lamellae in three growth orientations. Groundmass of acicular plagioclases overgrowing much coarser clinopyroxenes as ophitic intergrowth. Orthopyroxene, pigeonite and augite also in groundmass, with green coloured augite dominant. Quartz a rare groundmass phase. Alkali feldspar widely distributed but uncommon, fine-grained. Occasional alumina-rich glassy clots, associated with quartz, alkali feldspar and minor oxide phases (e.g., rare baddeleyite). Ilmenite and Ti-magnetite in groundmass, Cr-spinel common in association with olivine.
20-5A	Holocrystalline, relatively fine, with very well developed trachytic groundmass, defined by subparallel plagioclase laths. Phenocrysts euhedral, commonly in glomerocrysts, dominated by olivine, with forsterite-rich cores associated with Cr-spinel and more fayalitic rims, without reaction coronae. Plagioclase as secondary phenocryst phase, euhedral to subhedral, often with included cores, sometimes altered to aggregate of olivine, augite and oxides. Trachytic alignment around phenocrysts, flow related. Olivine common in groundmass, in equilibrium. Augite also abundant in groundmass, euhedral, often finer grained and in dendritic forms, and extremely fine Ti-magnetite.
21-2A	Fine grained, holocrystalline, phenocryst phase dominated by olivine, subhedral to rounded, with narrow more fayalitic rim, but without reaction coronae. Plagioclase a secondary phenocryst phase, without inclusions, with normal zoning. Groundmass dominated by plagioclase laths, with pigeonite and augite common, and a subophitic texture. Groundmass olivine common, small and rounded, occasionally rimmed by augite and plagioclase. Quartz widespread but uncommon, cracked but euhedral grains appear to be late stage. Ti-magnetite euhedral, relatively coarse, almost ubiquitously with ilmenite lamellae, though both also occur as individual grains. Cr-spinel common in olivine as inclusions, less common in groundmass, where zoned to Ti-richer composition.
21-3A	Holocrystalline, coarsely vesicular. Phenocrysts dominated by olivine, commonly as glomerocrysts, euhedral to subhedral, with inclusions of Cr-spinel, and a more fayalitic outer rim. Plagioclase also common, euhedral to subhedral, not included, with normal zoning. Groundmass microcrystalline, with cryptocrystalline patches, dominated by plagioclase, augite and olivine also abundant. Olivines small and subhedral, often with fayalitic outer rim, and also present as extremely fine grained laths. Groundmass augite occasionally of scale of olivine and plagioclase, but usually much finer laths or equant grains, often in dendritic forms, the fine grains being highly aluminous (up to 7.8 wt% alumina), while the coarse grains are of more normal composition. Ti-magnetite uncommon and very fine grained, Cr-spinel the only coarse groundmass oxide.

21-4A	Holocrystalline, similar to 21-2A, but sub-trachytic texture. Olivine dominant phenocryst, euhedral, often glomerocrysts, common edge alteration to iddingsite, narrow more fayalitic rims, discontinuous orthopyroxene coronae common, Cr-spinel often included. Plagioclase very common phenocryst, often included cores, some heavily altered, normal zoning; clean phenocrysts often more calcic. Groundmass dominated by plagioclase, augite and pigeonite abundant, often intergrown, pigeonite core, augitic rim; orthopyroxene also. Alkali feldspar widespread, fine. Groundmass oxides often approaching magnetite, ilmenite lamellae commonly associated. Ti-magnetite common, but not dominant, occasionally rutile lamellae associated. Groundmass olivines as two forms, often relics with orthopyroxene jacket as Ti-magnetite symplectite (cf. Yate), but also as rounded forsterite with fayaltitic rim penetrating grain interior as feathery lamellar growths, uneven and slightly curved, but apparently some crystallographic control, the forsteritic component in some cases >96 wt% MgO, the fayalitic correspondingly more Fe-rich than seen elsewhere in these volcanics, origin unclear.
21-6B	Porphyritic, texturally distinct from all above Apagado samples, with coarse blocky phenocrysts, plagioclase dominant, often large, euhedral grains amalgamated from several laths, commonly heavily included mantles and lightly included cores, the whole normally zoned, others cleaner but just as calcic, if not more so. Augite common phenocryst, green, some lamellar twinned, subhedral, tabular or lath like, also rimming orthopyroxene and twinned (as in some Yate samples). Orthopyroxene and pigeonite also as phenocrysts, and olivine relatively common, euhedral to subhedral, often altered with entire pseudomorph or sector replacement to fine grained green-brown aggregate of clays and carbonates, that remaining with thin fayalitic rim and narrow orthopyroxene coronae. Groundmass fine to cryptocrystalline, dominated by plagioclase and pigeonite, augite uncommon, no orthopyroxene. Cr-spinel in association with olivine, Ti-magnetite abundant, often coarse, euhedral. Ilmenite as individual grains. Minor phases include chalcopyrite, and rare nickeline (NiAs), apparently as primary groundmass grains with a honeycomb form.
21-9B	Holocrystalline, coarsely porphyritic, phenocryst phase dominated by blocky plagioclase, commonly as complex glomerocrysts, often cracked or included in core, with normal zoning. Olivine a secondary phenocryst phase, euhedral to subhedral, relatively forsteritic, with slightly more fayalitic outer rim, but no reaction coronae, although a thin weathering rim of hydrated Fe-rich clay minerals is common. Plagioclase dominates groundmass, augite and pigeonite common, olivine also present. Ti-magnetite the dominant oxide, ilmenite occasional, Cr-spinel rare and in association with olivine, relatively Ti-rich and Cr-poor.
21-9C	Holocrystalline, coarsely porphyritic, phenocryst phase dominated by plagioclase, euhedral to subhedral, in glomerocrysts, also laths or tabular grains, ubiquitously included or cracked, often with very heavily sieve textured core, and showing normal zoning. Olivine common as phenocrysts, euhedral to rounded, with thin coronae of pigeonite, not highly forsteritic, only slightly zoned towards margins. Augite also common phenocrysts, euhedral, often in glomerocrysts with olivine, slightly reverse zoned with Fe-poorer rim. Matrix dominated by plagioclase, pigeonite and augite. Groundmass relics of olivine with replacement rims developed as symplectite of calcic orthopyroxene and magnetite; orthopyroxene otherwise absent. Ti-magnetite abundant in groundmass, ilmenite laths also common, with both commonly intergrown.
Other samples (all covered thin sections; those above are all polished)	
15-4A	Coarse plutonic from west of Hornopirén volcano, gabbroic composition, predominantly plagioclase with heavily weathered mafic phases, dominated by a grey green clinopyroxene, commonly heavily included and pitted, much heavily weathered to fine-grained aggregate, possible relic olivine. Also coarse grained oxides.
19-2A	Hornopirén lava block, not in situ, felty texture, holocrystalline, groundmass of plagioclase laths, pyroxenes and oxides, with olivine and plagioclase phenocrysts, some as glomerocrysts. Plagioclase occasionally with heavily included cores, mostly clean and tabular. Olivines rounded, often clustered. Orthopyroxene occasional as subhedral tabular grains.
19-2B	Hornopirén lava block, not in situ, holocrystalline, with microcrystalline matrix composed of plagioclase laths in felty texture, also rich in oxides and clinopyroxene. Plagioclase a common phenocryst, often in glomerocrysts associated with olivine, a second abundant phenocryst, rounded, sometimes with reaction coronae.
19-2C	Hornopirén lava block, not in situ, as vent agglomerate composed of a variety of welded brecciated blocks. Surrounding matrix patchy and cryptocrystalline with microlitic plagioclase laths. A range of crystal and xenolithic phases contained within matrix, including large and heavily included plagioclase, rounded blocks of felty lava with olivine phenocrysts, and aggregates of clean and included plagioclase with clinopyroxene with occasional glassy patches. These aggregates have a matrix similar to the overall welding matrix, and are not clearly non-juvenile. The clinopyroxene here is abundant, green, and commonly twinned, but without any olivine associated. Notably this assemblage was not seen in any other Hornopirén sample, but is similar to the pyroxenes seen at Yate and in one case at Apagado.
19-2D	Hornopirén lava block, not in situ, very fine microcrystalline matrix of plagioclase, oxides and pyroxene, phenocryst phases of plagioclase, clinopyroxene and olivine. Rock similar to parts of that seen in 19-2C, and unlike any previously described Hornopirén lavas, but very like some Yate lavas (e.g., 26-3A). Plagioclases either tabular, euhedral and heavily zoned, or large and highly included. Clinopyroxenes green, commonly lamellar twinned. Olivine also present, and occasional coarse oxides.
21-11A	Fine grained welded tuff, crudely banded, with devifrified brown patches, often curved, possible relics of pumices, with fine-grained alteration minerals. Also patchy fine grained patches with quartz, feldspar, devitrified glass, and individual crystals within tuff, mainly quartz, plagioclase also common.

21-12A	Similar to 21-11A, banding slightly better developed, crystal patches clearer as lithic fragments, probably lavas of relatively evolved composition. Glass fresher, isotropic, commonly containing quartz crystal fragments.
25-1B	Granodioritic basement rock, from near Puelo, quartz rich, texturally equilibrated. Plagioclase coarse but commonly heavily weathered, biotite with deep pleochroic browns, foliated internal texture altering to green brown pleochroic composition. Amphibole subhedral with good cleavage and clean extinction, commonly twinned, with euhedral breakdown cavities. Occasional concentrations of oxides.
25-10A	Granitoid from north side of Hualaihue, predominantly feldspar, some quartz, all heavily pitted and included, with biotite, green brown with fibrous habit, again heavily weathered, and greenish amphibole, also often weathered and with poor crystal shape, and common oxides.
04-1A	Metamorphic basement rock from walls of LOFZ west of Hornopirén, foliated, with fine grained quartzitic and mafic bands, the quartz texturally in equilibrium and regrown, the mafic layers of green amphibole and brown biotite, with each locally concentrated. Sparse oxides.
04-1B	From walls of LOFZ west of Hornopirén, microgranitic texture, with large plagioclases and breakdowns of mafic minerals (pyroxenes), finer feldspars, oxides and biotite, possibly porphyritic protolith.
04-1C	From walls of LOFZ west of Hornopirén, microgranitic, contains plagioclase and clinopyroxene. Pyroxene with dark green brown pleochroism. Plagioclase heavily included or regrown, shows a relic porphyritic texture. Fairly rich in oxides.
04-4A	Granitoid, collected at base of southern flanks of Yate. Quartz feldspar microgranitic texture, extensively weathered. Relic crystals clear but altered to amalgam of finer grains, with pale green amphibole and high relief colourless grains broken down to fine grained assemblage.

Appendix E

Apagado scoria deposit logs

Stratigraphic logs of the Ap1 scoria deposit. Refer to Figure 3.2 for site locations, and to Chapter 3 for unit distribution maps. Coloured bars, showing equivalent positions, refer to the summary stratigraphy in Figure 3.3. The depth in each column is given in centimetres, while the horizontal axis gives approximated mean grain-size, as ash grades (very fine to medium) and in millimetres.

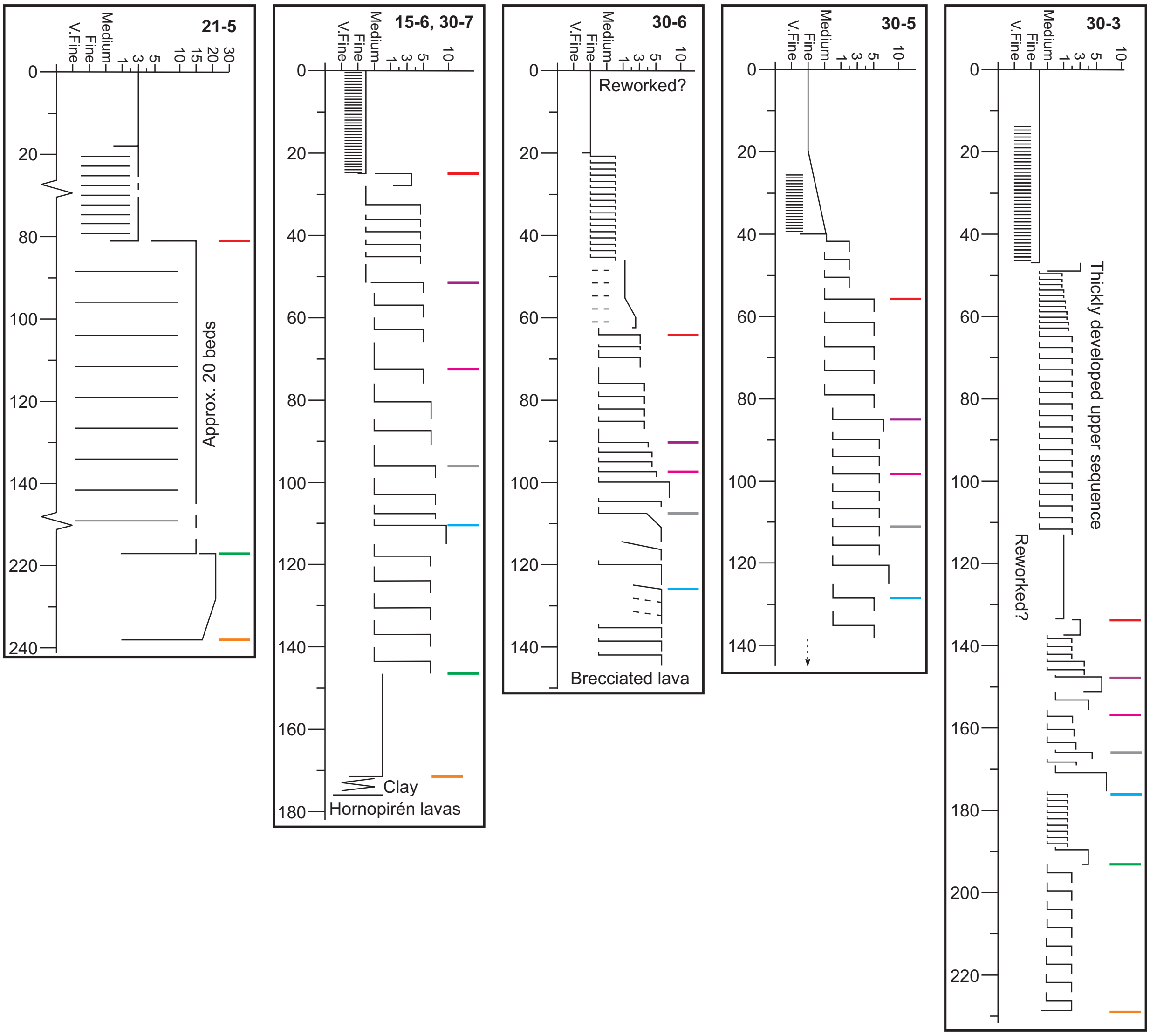

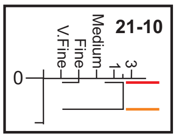
21-10
V.Fine
Fine
Medium
1
3
0

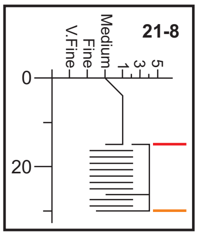
21-8
V.Fine
Fine
Medium
1
3
5
0
20

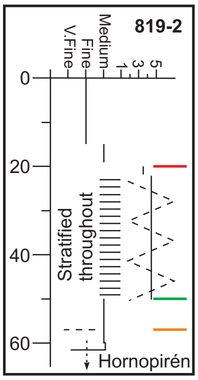
819-2
V.Fine
Fine
Medium
1
3
5
0
20
40
60
Stratified throughout
Hornopirén

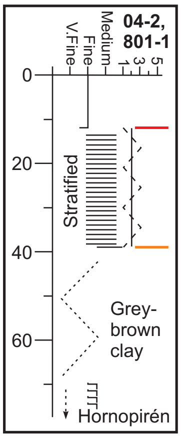
04-2, 801-1
V.Fine
Fine
Medium
1
3
5
0
20
40
60
Stratified
Grey-brown clay
Hornopirén

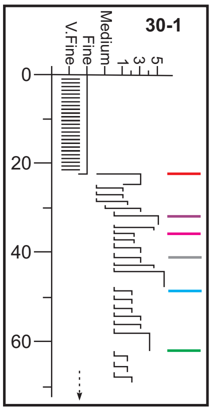
30-1
V.Fine
Fine
Medium
1
3
5
0
20
40
60

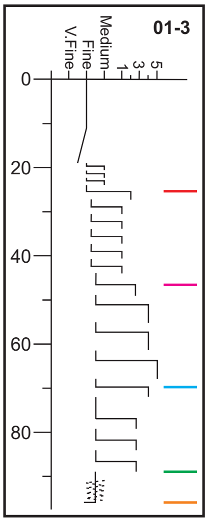
01-3
V.Fine
Fine
Medium
1
3
5
0
20
40
60
80

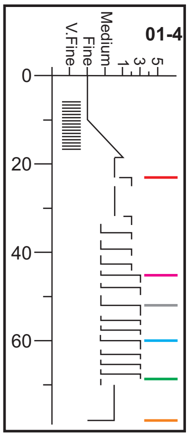
01-4
V.Fine
Fine
Medium
1
3
5
0
20
40
60

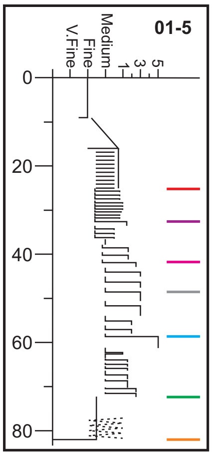
01-5
V.Fine
Fine
Medium
1
3
5
0
20
40
60
80

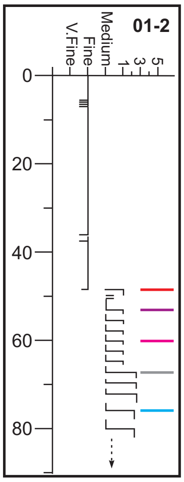
01-2
V.Fine
Fine
Medium
1
3
5
0
20
40
60
80

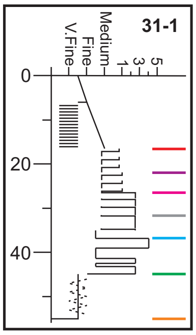
31-1
V.Fine
Fine
Medium
1
3
5
0
20
40

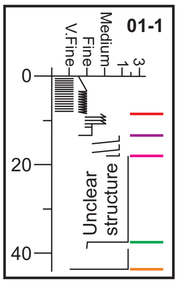
01-1
V.Fine
Fine
Medium
1
3
0
20
40
Unclear structure

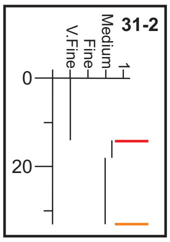
31-2
V.Fine
Fine
Medium
1
0
20

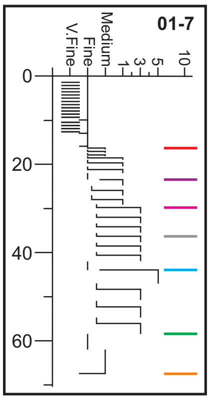
01-7
V.Fine
Fine
Medium
1
3
5
10
0
20
40
60

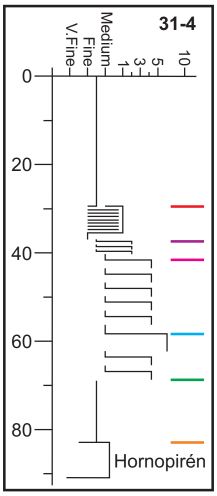
31-4
V.Fine
Fine
Medium
1
3
5
10
0
20
40
60
80
Hornopirén

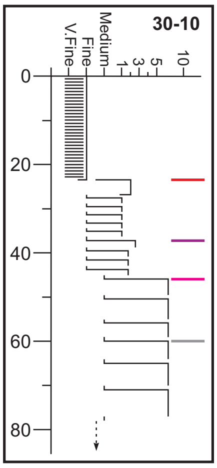
30-10
V.Fine
Fine
Medium
1
3
5
10
0
20
40
60
80

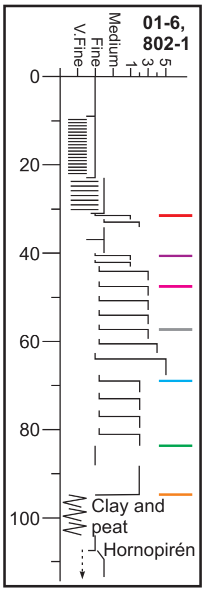
01-6, 802-1
V.Fine
Fine
Medium
1
3
5
0
20
40
60
80
100
Clay and peat
Hornopirén

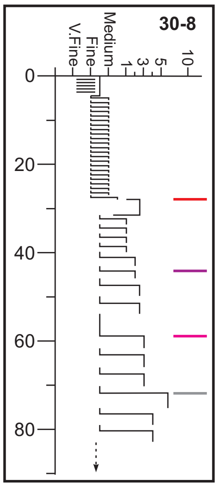
30-8
V.Fine
Fine
Medium
1
3
5
10
0
20
40
60
80

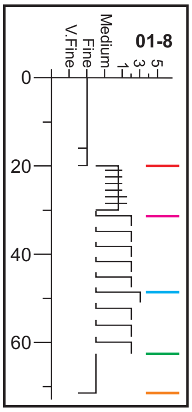
01-8
V.Fine
Fine
Medium
1
3
5
0
20
40
60

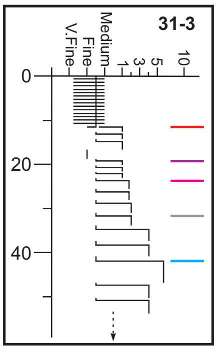
31-3
V.Fine
Fine
Medium
1
3
5
10
0
20
40

Appendix F

Melt inclusion analytical data

Unit	Sample	ppm	wt%	Trace elements (ion probe, ppm)							
		CO_2	H_2O	Ti	Sr	Y	Zr	Nb	Ba	La	Ce
Ap1	15-6B	108	0.31	6330	389	21.7	110	3.8	133	10.8	24.7
Ap1	21-5B	89	0.49	5748	382	20.6	102	4.0	125	10.1	22.9
Ap1	21-5B	551	1.52	4218	430	15.6	74	3.1	98	7.2	17.0
Ap1	21-5B	204	0.44	5775	369	20.6	103	3.7	126	10.4	22.5
Ap1	21-5B	135	0.35	5223	394	18.4	89	3.9	131	8.9	21.1
Ap1	21-5B	248	0.61	4597	418	16.2	79	2.8	106	8.0	19.1
Ap1	21-5B	255	0.57	4531	444	16.3	79	3.3	100	7.3	18.3
Ap1	15-6B	993	3.50	3772	420	14.2	70	2.3	85	6.6	16.0
Ap1	15-6B	76	0.73	5842	414	20.1	100	3.3	127	9.5	23.6
Ap1	15-6B	698	2.99	4004	440	14.2	71	2.3	93	6.7	17.0
Ap1	15-6B	80	0.28	6205	398	20.8	106	3.2	134	9.8	24.3
Ap1	15-6B	43	0.25	4259	335	15.6	67	2.1	81	6.1	15.2
Ap1	15-6B	106	0.33	6054	394	19.9	104	3.1	133	9.0	22.8
Ap1	15-6B	0	0.44	5199	404	17.8	82	3.2	126	9.2	20.8
Ap1	21-5B	45	0.48	4493	425	15.3	79	2.9	99	7.5	18.0
Ap1	15-6A	108	0.49	5225	437	17.6	77	2.5	138	8.9	21.5
Ap1	15-6B	69	0.28	5887	405	19.9	94	2.9	133	9.3	22.5
Ap1	15-6B	63	0.23	6095	384	20.9	105	3.2	130	9.1	23.7
Ap1	15-6B	60	0.29	5673	405	19.7	94	3.4	130	9.1	22.4
Ap1	15-6B	72	0.05	6231	385	20.1	105	3.7	132	8.8	22.7
Ap1	15-6B	545	2.84	4171	433	15.6	79	2.8	96	7.1	18.0
Ap1	15-6A	172	2.26	4156	456	13.4	66	2.0	91	6.7	16.6
Ap1	15-6B	98	0.31	6350	386	21.2	105	3.9	135	9.6	24.3
Ap1	15-6B	888	2.54	3951	439	14.7	73	1.9	94	6.4	16.2
Ho1	801-1C	1490	1.61	5071	358	18.4	121	4.6	271	14.6	32.8
Ho1	801-1C	398	1.71	5060	359	18.6	121	5.0	257	14.2	32.3
Ho1	801-1B	53	0.29	6136	333	23.9	150	5.6	322	18.5	41.8
Ho1	801-1B	59	0.51	5803	351	22.6	147	5.2	317	17.4	40.8
Ho1	801-1B	80	0.35	5565	363	20.7	133	4.9	266	14.9	34.9
Ho1	801-1B	502	2.03	4704	333	17.7	118	4.2	228	13.0	30.3
Ho1	801-1B	123	1.64	5111	357	19.2	127	5.2	274	15.4	35.1
Ho1	801-1B	106	0.43	6638	300	25.1	169	6.0	309	18.6	43.6
Ho1	801-1B	526	1.79	4748	344	18.3	124	4.1	238	14.0	32.5
Ho1	801-1B	705	0.07	5426	393	19.8	135	5.0	263	15.6	36.8
Ho1	801-1B	626	1.50	5006	358	18.9	122	4.4	232	13.3	33.1
Ho1	801-1B	72	0.62	6099	331	22.6	148	6.1	297	17.4	39.8
Ho1	801-1B	96	0.96	5598	341	20.5	139	5.9	270	15.3	35.9
Ho1	801-1B	331	1.55	4947	355	18.1	123	4.5	248	14.4	30.7
Ho1	801-1B	691	1.41	4668	353	18.1	121	4.5	233	13.6	30.8
Ho1	801-1B	103	0.71	5237	347	19.9	129	5.0	254	14.6	33.2

Unit	Sample	ppm	wt%	Trace elements (ion probe, ppm)							
		CO_2	H_2O	Ti	Sr	Y	Zr	Nb	Ba	La	Ce
Ho1	801-1B	1288	1.63	5021	374	18.6	123	5.5	257	14.6	34.3
Ho1	801-1B	91	0.35	5812	352	22.0	143	5.4	261	16.5	37.5
Ho1	801-1D	1296	1.42	6229	413	21.1	109	3.3	273	13.8	30.3
Ho1	801-1D	345	0.49	6106	397	22.2	106	3.5	249	13.8	32.8
Ho1	801-1D	956	1.66	6203	425	21.5	107	3.7	274	14.8	33.2
Ho1	801-1C	658	1.76	5231	369	19.4	124	5.2	263	15.2	34.0
Ho1	801-1C	71	0.55	7206	332	27.1	168	7.1	354	19.7	45.1
Ho1	801-1C	47	0.32	7596	315	27.3	180	7.4	368	20.3	47.7
Ho1	801-1C	237	1.37	5260	381	20.3	130	5.1	273	16.3	35.1
Palena	826-4A	1632	1.77	5001	374	15.7	85	3.4	139	9.7	20.9
Palena	826-4A	87	0.42	8368	318	25.8	147	5.8	240	15.6	36.2
Palena	826-4A	398	1.75	5014	386	15.4	85	4.2	147	9.8	21.6
Palena	826-4A	128	0.18	7824	364	25.0	138	5.6	216	14.9	35.0
Palena	826-4A	79	0.11	13460	247	37.3	309	11.3	354	25.6	55.8
Palena	826-3B	604	0.97	5511	414	17.1	96	4.1	172	10.9	23.4
Palena	826-3B	1959	1.90	4724	350	14.8	82	3.4	142	9.0	20.0
Palena	826-3B	84	0.01	5012	373	16.9	89	3.3	155	9.8	22.2
Palena	826-3B	76	0.17	5964	330	18.5	99	4.4	178	10.2	24.6
Palena	826-3B	70	0.26	7883	284	26.5	139	5.5	240	15.4	35.3
Palena	826-4A	1575	1.48	5299	397	17.1	97	3.4	171	10.5	24.2
Palena	826-4A	216	1.18	5096	398	16.3	87	3.9	155	10.0	23.4
Puyuhuapi	828-6B	136	0.19	10182	821	24.0	194	27.9	592	47.6	95.3
Puyuhuapi	828-6B	151	0.17	12720	485	29.2	256	36.0	695	63.6	123.1
Puyuhuapi	828-6B	350	0.22	9889	648	22.7	185	26.8	610	46.9	92.3
S Minch	C16-G7B	95	0.22	10166	280	32.7	226	12.0	285	22.2	51.4
S Minch	C16-G7B	94	0.29	8674	281	29.1	197	9.4	261	18.5	45.3
S Minch	C16-G7B	164	0.34	6242	322	22.1	132	6.7	232	14.8	35.4
S Minch	C16-G7B	72	0.30	9056	278	31.2	206	8.9	267	20.5	48.0
S Minch	C16-G7B	93	0.26	8936	280	30.8	205	9.6	279	20.2	48.4
S Minch	C16-G7B	1304	1.61	5663	364	18.4	126	5.8	188	13.0	30.5
S Minch	C16-G7B	2211	1.72	5679	369	18.8	129	6.2	189	13.4	31.2

Unit	Sample	Major elements (electron probe, wt%)									Olivine %Fo
		SiO_2	TiO_2	Al_2O_3	FeO	Mn	MgO	CaO	Na_2O	K_2O	
Ap1	15-6B	53.9	1.3	14.8	9.1	0.2	5.3	9.9	3.1	0.9	89.1
Ap1	21-5B	52.9	1.3	13.5	10.2	0.1	5.7	10.8	2.8	0.7	88.6
Ap1	21-5B	49.6	0.8	15.7	8.5	0.1	6.2	11.6	2.9	0.5	88.6
Ap1	21-5B	53.5	1.2	14.1	9.0	0.2	5.3	10.6	3.2	0.8	88.6
Ap1	21-5B	52.6	1.2	15.2	9.2	0.2	4.1	11.2	2.6	0.8	88.6
Ap1	21-5B	51.7	1.1	15.9	8.9	0.3	5.5	11.2	2.8	0.7	89.3
Ap1	21-5B	50.4	1.0	17.0	9.1	0.2	5.5	11.9	2.8	0.7	89.0
Ap1	15-6B	47.9	0.8	15.2	7.6	0.2	7.6	10.5	2.5	0.5	89.5
Ap1	15-6B	53.1	1.2	14.7	8.4	0.2	5.2	10.9	3.0	0.8	88.4
Ap1	15-6B	48.3	0.8	16.1	7.3	0.1	7.0	10.9	2.5	0.5	89.3
Ap1	15-6B	53.7	1.3	14.5	9.2	0.1	5.7	10.0	3.1	0.9	89.7
Ap1	15-6B	51.6	0.9	16.9	7.0	0.2	6.1	11.2	3.0	0.6	89.7
Ap1	15-6B	53.5	1.1	14.3	9.0	0.2	5.6	10.1	3.1	0.9	89.0
Ap1	15-6B	52.0	1.0	15.7	9.2	0.1	5.0	11.1	2.7	0.8	89.1
Ap1	21-5B	53.8	0.9	16.6	7.0	0.0	5.3	10.7	3.2	0.8	88.6
Ap1	15-6A	50.4	1.0	16.3	8.0	0.2	6.0	11.0	3.1	0.8	88.1
Ap1	15-6B	52.2	1.1	13.9	10.3	0.2	5.8	10.4	2.8	0.8	89.7
Ap1	15-6B	51.7	1.1	14.5	9.4	0.2	5.6	10.9	2.9	0.8	88.0
Ap1	15-6B	52.1	1.1	13.9	10.2	0.2	5.8	10.5	2.9	0.8	87.5
Ap1	15-6B	53.4	1.1	15.4	8.7	0.2	4.9	10.0	3.3	0.8	87.5
Ap1	15-6B	48.9	0.8	15.8	6.0	0.1	6.2	10.8	2.8	0.6	88.8
Ap1	15-6A	47.9	0.9	17.1	7.3	0.2	3.8	11.5	3.2	0.6	89.3
Ap1	15-6B	53.7	1.2	13.8	9.3	0.2	5.7	9.9	3.0	0.9	88.9
Ap1	15-6B	47.2	0.7	15.2	7.4	0.1	8.2	10.2	2.7	0.7	89.7

Unit	Sample	Major elements (electron probe, wt%)									Olivine %Fo
		SiO_2	TiO_2	Al_2O_3	FeO	Mn	MgO	CaO	Na_2O	K_2O	
Ho1	801-1C	51.7	1.0	16.2	8.3	0.1	5.9	8.4	3.0	1.0	81.7
Ho1	801-1C	51.0	1.0	15.9	8.5	0.1	6.1	8.6	2.9	0.8	81.8
Ho1	801-1B	53.8	1.3	14.8	9.1	0.1	4.4	8.4	3.4	1.2	82.2
Ho1	801-1B	53.6	1.1	16.8	9.3	0.1	4.3	9.1	3.1	1.0	81.3
Ho1	801-1B	54.3	1.1	16.6	8.0	0.1	4.4	8.5	3.5	1.1	82.0
Ho1	801-1B	51.5	1.0	16.0	7.9	0.2	5.9	8.5	3.1	0.8	82.1
Ho1	801-1B	53.1	1.0	17.0	7.1	0.1	3.6	8.2	3.4	1.0	83.0
Ho1	801-1B	54.3	1.3	14.2	9.8	0.2	4.5	8.3	3.5	1.1	82.3
Ho1	801-1B	51.4	0.9	15.5	8.3	0.1	7.2	8.3	2.9	0.8	82.3
Ho1	801-1B	51.9	1.1	18.0	7.9	0.1	4.7	9.7	3.6	1.0	82.2
Ho1	801-1B	51.7	1.1	17.0	8.0	0.1	5.5	9.0	3.0	0.9	82.0
Ho1	801-1B	54.1	1.1	16.1	8.5	0.1	4.3	9.3	3.4	0.9	82.6
Ho1	801-1B	52.9	1.2	15.4	8.9	0.1	5.0	8.6	3.4	1.0	81.5
Ho1	801-1B	51.4	1.0	16.1	8.0	0.2	5.6	8.8	3.1	0.8	81.7
Ho1	801-1B	51.9	0.9	16.6	7.6	0.2	5.7	8.8	3.3	0.9	83.2
Ho1	801-1B	52.8	1.0	17.2	8.1	0.2	4.5	9.5	3.4	0.9	82.0
Ho1	801-1B	52.0	1.1	16.3	8.1	0.2	5.0	9.1	3.1	0.8	82.3
Ho1	801-1B	53.2	1.2	16.6	8.7	0.1	4.7	9.2	3.4	1.0	82.3
Ho1	801-1D	49.8	1.2	18.0	6.7	0.0	4.0	11.4	3.0	0.8	87.2
Ho1	801-1D	50.4	1.1	16.8	9.1	0.1	7.4	10.3	2.8	0.9	85.2
Ho1	801-1D	49.8	1.2	17.0	8.5	0.2	4.1	10.7	3.0	0.8	83.7
Ho1	801-1C	51.3	1.0	16.0	8.6	0.1	6.0	8.7	2.8	0.8	82.3
Ho1	801-1C	55.7	1.5	15.3	8.8	0.2	4.7	7.9	3.4	1.2	82.4
Ho1	801-1C	54.5	1.2	16.9	7.6	0.2	3.9	9.2	3.3	1.0	82.6
Ho1	801-1C	50.4	1.1	16.0	8.8	0.2	6.1	8.6	3.1	0.9	82.3
Palena	826-4A	48.3	1.0	16.2	8.4	0.1	7.0	9.8	3.1	0.6	84.5
Palena	826-4A	52.5	1.7	13.3	9.9	0.2	4.7	9.4	3.4	1.0	84.7
Palena	826-4A	48.7	1.0	16.0	9.2	0.2	6.8	9.8	3.1	0.5	84.0
Palena	826-4A	51.0	1.5	14.3	9.7	0.2	5.3	9.9	3.5	0.9	84.7
Palena	826-4A	57.0	2.6	13.0	8.5	0.1	4.1	6.2	4.2	1.8	83.2
Palena	826-3B	49.0	1.1	18.2	7.3	0.1	2.9	11.9	3.4	0.6	85.1
Palena	826-3B	48.7	1.0	15.8	7.7	0.1	6.7	10.0	3.1	0.6	84.8
Palena	826-3B	53.0	1.0	17.6	6.4	0.2	4.1	10.9	3.8	0.7	85.8
Palena	826-3B	53.2	1.1	14.2	9.0	0.2	7.1	9.0	3.4	0.9	84.9
Palena	826-3B	52.5	1.6	13.4	10.3	0.2	4.8	9.4	3.2	1.1	85.5
Palena	826-4A	48.9	1.0	16.9	8.6	0.2	6.0	10.0	3.3	0.6	84.6
Palena	826-4A	48.4	1.0	16.5	8.8	0.1	5.9	10.1	3.5	0.7	84.7
Puyuhuapi	828-6B	47.8	1.8	16.7	9.7	0.2	4.5	11.6	3.6	1.7	84.5
Puyuhuapi	828-6B	49.6	2.5	13.7	10.6	0.2	4.3	9.2	3.5	3.2	84.1
Puyuhuapi	828-6B	47.7	1.7	13.8	10.1	0.1	10.2	8.9	3.7	1.9	84.9
S Minch	C16-G7B	52.6	2.0	12.9	9.9	0.2	6.3	8.3	3.2	1.2	83.6
S Minch	C16-G7B	52.4	1.5	15.4	8.5	0.1	4.1	8.9	3.3	0.9	84.3
S Minch	C16-G7B	50.0	1.3	17.0	10.0	0.3	5.1	9.4	3.4	0.9	84.8
S Minch	C16-G7B	52.4	1.8	13.8	10.2	0.3	5.2	9.0	3.3	1.0	84.4
S Minch	C16-G7B	51.7	1.7	14.3	10.8	0.2	5.2	9.3	3.3	1.2	83.5
S Minch	C16-G7B	49.4	1.1	17.2	8.2	0.2	6.4	9.6	3.3	0.7	85.1
S Minch	C16-G7B	49.9	1.2	17.5	8.2	0.1	5.8	8.7	3.6	0.7	84.9

Appendix G

Chaitén 2008 ash sampling sites

Locality	Latitude	Longitude	Thickness (mm)	Locality	Latitude	Longitude	Thickness (mm)
30-03	-42.2953	-71.2839	0.2	01-13	-43.8558	-67.9471	0.2
30-04	-42.3212	-71.1334	2.5	01-14	-43.8095	-67.6821	0.2
30-06	-42.4673	-71.0972	4	01-15	-43.7170	-67.2860	0.2
30-07	-42.6090	-71.0798	3.5	01-16	-43.7028	-66.9912	0.2
30-08	-42.6825	-71.0279	3	02-01	-44.0489	-69.1957	0.15
30-09	-42.7757	-71.1180	3	02-02	-44.1457	-69.2625	0.15
30-10	-42.9161	-71.1668	3.5	02-03	-44.3053	-69.3972	0.2
30-11	-42.9486	-71.2179	4	02-04	-44.4589	-69.2548	0.2
30-12	-42.9292	-71.3549	7.5	02-05	-44.6463	-69.1477	0.25
30-13	-43.0321	-71.4416	4.5	02-06	-44.7400	-69.2137	0.2
31-04	-43.0151	-71.0433	5.5	02-07	-44.8882	-69.2135	0.2
31-05	-43.1338	-70.8601	4	02-08	-45.0346	-69.1533	0.15
31-06	-43.3246	-70.8964	3.5	02-10	-45.2333	-69.0955	0.15
31-07	-43.5285	-70.7948	2	02-11	-45.3585	-68.9815	0.15
31-08	-43.6401	-70.8401	2	02-12	-45.5066	-69.0551	0.1
31-09	-43.7968	-70.9359	1.75	02-14	-45.5000	-69.2700	0.1
31-10	-43.9593	-70.8874	0.5	02-15	-45.4741	-69.5090	0.1
31-11	-43.9944	-70.8270	0.5	02-16	-45.4485	-69.8147	0.1
31-12	-44.0457	-70.6297	1.5	03-01	-44.0829	-70.9609	0.2
31-13	-44.1773	-70.4731	1	03-02	-44.1975	-71.1106	0.1
31-14	-44.2925	-70.4005	0.5	03-05	-43.9499	-71.4557	0.1
31-15	-44.4191	-70.4405	0.2	03-07	-43.5641	-70.5904	0.5
31-16	-44.5889	-70.3706	0.1	03-08	-43.5726	-70.3605	0.5
01-01	-43.9477	-70.3422	2	03-09	-43.4670	-70.8449	1
01-02	-43.7834	-70.1796	0.75	03-10	-42.9927	-71.1834	11
01-03	-43.6439	-70.0969	0.75	03-11	-43.0144	-71.2018	13
01-04	-43.7267	-69.8984	0.5	04-02	-43.0628	-70.8628	4.5
01-05	-43.7706	-69.6022	0.2	04-03	-42.9936	-70.7573	2
01-06	-43.7942	-69.3165	0.2	04-04	-43.0347	-70.5880	1.5
01-07	-43.8620	-69.0502	0.3	04-05	-43.0791	-70.4155	0.9
01-08	-43.6717	-68.9321	0.2	04-06	-43.0749	-70.2350	0.6
01-09	-43.5682	-69.0551	0.2	04-08	-43.1549	-70.1071	0.5
01-10	-43.8172	-68.7052	0.2	04-09	-43.2137	-69.9652	0.4
01-11	-43.8771	-68.4208	0.2	04-10	-43.3223	-69.8793	0.3
01-12	-43.8594	-68.2157	0.15	04-11	-43.0886	-69.9018	0.6

Locality	Latitude	Longitude	Thickness (mm)
04-12	-42.9582	-69.9374	0.4
04-13	-42.9601	-70.6420	2
04-14	-42.8473	-70.6118	1
04-15	-42.7425	-70.5401	0.8
04-16	-42.6562	-70.4192	0.8
04-17	-42.6468	-70.2535	0.5
04-18	-42.6776	-70.0935	0.45
05-01	-43.1135	-71.4603	13
05-02	-43.1663	-71.4949	15.5
05-03	-43.1986	-71.5829	12
05-04	-43.1773	-71.6880	15
05-06	-43.1738	-71.7525	17.5
05-07	-43.1732	-71.7509	17.5
05-08	-43.1548	-71.3980	11
05-09	-43.2239	-71.4235	9
05-10	-43.3040	-71.4356	5
05-11	-43.3564	-71.5046	5
05-12	-43.4324	-71.5569	9
05-13	-43.5100	-71.4807	3
05-14	-43.5083	-71.4396	2
05-15	-43.5067	-71.4184	5
05-16	-43.4884	-71.3084	11
05-17	-43.4968	-71.2426	8
05-18	-43.5276	-71.2041	9.5
05-19	-43.5611	-71.1698	8
05-20	-43.5944	-71.1124	6
05-21	-43.6086	-71.0563	4
05-22	-43.6186	-70.9723	3
05-23	-43.5855	-70.9306	1.5
05-24	-43.5587	-70.8863	1
05-25	-43.5130	-70.8712	0.8
05-26	-43.4737	-70.8463	0.8
06-01	-42.9685	-71.3943	12
06-03	-43.0051	-71.4879	6
06-04	-42.9696	-71.5835	7
06-05	-42.8926	-71.6017	4
06-06	-42.8216	-71.6177	3
06-07	-42.7800	-71.6800	2
06-08	-42.7230	-71.7294	1
06-09	-42.6464	-71.6699	1
06-10	-42.5621	-71.6159	1
06-11	-42.5056	-71.4728	1.5
06-12	-42.4024	-71.3703	1
06-13	-42.2775	-71.3582	0.4
06-14	-42.2005	-71.3954	0.2
06-15	-42.1829	-71.1612	1
06-16	-42.0563	-71.1630	3
06-17	-42.0055	-71.1718	2
06-18	-41.9815	-71.2194	1
06-19	-41.9680	-71.2730	0.4
06-20	-41.9597	-71.3663	0.15
06-21	-41.9098	-71.4118	0.1
06-22	-41.9059	-71.5115	0.05
07-03	-42.7895	-70.9798	2
07-04	-42.7752	-70.8282	1.5
07-05	-42.7074	-70.6888	0.5
07-06	-42.6147	-70.4791	0.7
07-07	-42.5094	-70.5587	0.4
07-08	-42.4006	-70.5316	0.7
07-09	-42.2456	-70.6175	0.5
07-10	-42.1318	-70.6803	0.4
07-11	-42.0256	-70.7178	0.5
07-12	-42.1371	-70.8401	0.6
07-13	-42.1378	-71.0177	0.4
07-14	-41.9598	-71.0997	1
07-15	-41.9010	-70.9969	1
07-16	-41.8437	-70.8961	2
07-17	-41.8106	-70.8124	2.5
07-18	-41.8037	-70.7954	3
07-19	-41.7034	-70.7590	2
07-20	-41.5680	-70.6845	1.5
07-21	-41.4332	-70.6918	0.75
07-22	-41.2596	-70.6904	0.2
08-02	-41.0311	-70.2522	0.1
08-03	-41.1658	-70.1770	0.2
08-04	-41.2555	-70.0304	0.4
08-05	-41.3210	-69.8484	1
08-06	-41.3317	-69.6577	1
08-07	-41.3234	-69.5026	1
08-08	-41.4734	-69.4218	1.75
08-09	-41.5999	-69.3771	0.4
08-11	-41.5316	-69.4059	0.9
08-12	-41.4001	-69.4342	1.25
08-13	-41.2776	-69.4632	1
08-14	-41.2180	-69.3877	0.8
08-16	-41.1538	-69.3190	0.6
08-17	-41.0646	-69.3190	0.5
08-19	-40.8886	-69.2980	0.2
08-20	-40.8273	-69.1950	0.2
08-21	-40.6908	-69.1253	0.15
09-01	-41.3022	-69.2963	1.25
09-02	-41.3015	-69.1164	1
09-03	-41.2781	-68.9448	0.8
09-04	-41.2693	-68.7685	0.6
09-05	-41.2225	-68.6251	0.7
09-06	-41.1465	-68.4892	0.6
09-07	-41.0578	-68.3697	0.7
09-08	-40.9651	-68.2417	0.5
09-09	-40.8733	-68.1054	0.5
09-10	-40.8477	-68.1915	0.3
09-11	-40.7648	-68.1919	0.2
09-13	-40.7369	-68.2349	0.1
09-14	-40.9480	-67.9569	0.5
09-15	-41.0647	-67.8994	0.3
09-16	-41.1700	-67.8500	0.2
09-17	-41.2841	-67.9154	0.2

Locality	Latitude	Longitude	Thickness (mm)
09-18	-41.3402	-67.9119	0.2
09-19	-40.7380	-67.9162	0.5
09-20	-40.6111	-67.7929	0.15
09-22	-40.5247	-67.3724	0.1
09-23	-40.4906	-67.1615	0.05
09-24	-40.4811	-66.8636	0.05
09-25	-40.5027	-66.6069	0.05
10-01	-40.5915	-66.4125	0.1
10-03	-40.5207	-66.0873	0.05
10-05	-40.8010	-65.9366	0.2
10-06	-40.8506	-65.6650	0.2
10-07	-40.8246	-65.3749	0.2
10-08	-41.0405	-65.3951	0.1
10-09	-41.2640	-65.3749	0.1
10-11	-41.7245	-65.3039	0.05
10-16	-42.8200	-65.1500	0.05
10-18	-43.1983	-65.2909	0.1
10-19	-43.3485	-65.3134	0.05
10-20	-43.4970	-65.4286	0.05
11-02	-40.4600	-65.0156	0.1

Appendix H

SVZ volcanic eruption records

			Start date			End date			Location							
Volcano	Lat. (S)	Long. (W)	Year	Month	Day	Year	Month	Day	Central	Flank	Radial fissure	Regional fissure	Explosive	Lava	Fatalities	Est. VEI
Tupungatito	33.40	69.80	1987	11	28	1987	11	30	x				x			2
			1986	1	20	1986	1	20	x				x			1
			1980	1	10	1980	1	11	x				x			2
			1968						x				x			2
			1964	8	3	1964	9	19	x				x			2
			1961	5	5	1961	8		x				x			2
			1960	7	15				x					x		2
			1959	10	16				x				x			2
			1959	3	26				x				x			2
			1958	1					x							2
			1946			1947			x				x			2
			1925						x				x			2
			1907	2	15				x				x			2
			1901	4					x				x			2
			1897	1		1897	4	12	x				x			2
			1889			1890			x				x			2
			1861						x							2
			1829						x				x			2
San José	33.78	69.90	1960						x				x			2
			1959						x				x			2
			1895			1897			x				x			2
			1889			1890			x				x			2
			1881						x				x			2
			1838						x				x			1
			1822	11	19	1838			x				x			2
Maipo	34.16	69.83	1908										x			2
			1905	10	28	1905	10	30					x			2
			1869	8	24								x			2
			1833										x			2
			1831	2	16								x			2
			1826	3	1					x			x	x		2
			1822													
Tinguiririca	34.81	70.35	1917													1?
Planchón-Peteroa	35.24	70.57	1998	11	18	1998	11	21	x				x			1
			1991	2	9	1991	3	2	x				x			2
			1962	1					x				x			1

Volcano	Lat. (S)	Long. (W)	Start date			End date			Location				Explosive	Lava	Fatalities	Est. VEI
			Year	Month	Day	Year	Month	Day	Central	Flank	Radial fissure	Regional fissure				
Planchón-Peteroa (continued)			1960	7	10				x				x			1
			1959	11	6				x				x			1
			1938	9		1938	10		x							2
			1937	4		1937	5	5	x				x			2
			1889	9		1894?			x				x			2
			1878						x							2
			1860						x				x			2
			1837	2					x				x	x		2
			1835						x							2
			1762	12	3				x				x			4
			1751	11		1751	12		x				x			2
			1660													3+
Descabezado Grande	35.58	70.75	1932	6	5	1933				x			x			3
Cerro Azul (Quizapu)	35.65	70.76	1967	8	9					x			x			2?
			1949	4	15					x			x			2?
			1933			1938	7	25		x			x			2
			1916			1932	4	21		x			x			5+
			1914	9	8					x			x			3
			1912	2						x			x			2
			1907	7	28					x			x			2
			1906							x			x			2
			1846	11	26	1853?					x		x	x		2
Nevados de Chillán	36.86	71.38	2003	8	29	2003	9	15	x		x		x			1
			1973	7		1986				x			x	x		2
			1946			1947				x			x			2?
			1935	7	2					x				x		2?
			1934	1	17								x			2?
			1928	11	30	1929				x			x			2?
			1927	4	10								x			2?
			1914										x			2
			1907							x			x			1
			1906	8	6	1906	12			x			x	x		2
			1898										x			2
			1893	3	4								x			2
			1891	2									x			2
			1877	2	12								x			2
			1872	7	22								x			2
			1864	11	30	1865	2	3		x			x	x		3
			1861	6		1863				x			x	x		2
			1860	7	25					x						2?
			1752	1	30											2?
			1749?			1751			x				x			3+
			1650 (+/- 50)										x			3?
Antuco	37.41	71.35	1869						x				x			2
			1863	12					x				x			2
			1861	2		1861	8		x					x		0
			1852	11		1853	1		x	x	x		x	x		3
			1845	2	26	1845	3	1	x				x	x		2
			1828	12	18				x				x	x		2
			1820			1821			x				x			1
			1806?	5					x				x			2
			1752	1	31	1752	2	1	x				x	x		3?
			1750 (+/- 10)										x			2

Volcano	Lat. (S)	Long. (W)	Start date			End date			Location				Explosive	Lava	Fatalities	Est. VEI
			Year	Month	Day	Year	Month	Day	Central	Flank	Radial fissure	Regional fissure				
Copahue	37.85	71.17	2000	7	1	2000	10	18	x				x			2
			1995	9					x				x			2
			1994	12					x				x			2
			1992	7	22	1993			x				x			2
			1961										x			2
			1960													
			1944													
			1937													2?
			1867?													2?
			1750?										x			2
Callaqui	37.92	71.45	1980	10		1980	10		x				x			1
			1751	12	31								x			2
Lonquimay	38.38	71.58	1988	12	25	1990	1	24		x	x		x	x	x	3
			1933	1	4								x	x		2
			1887	6	2	1890	1				x		x	x		3
			1853	2					x				x	x		3
Llaima	38.69	71.73	2008	1	1	2009			x				x	x		3
			2007	5	26	2007	8	8?	x				x			2
			2003	4	9	2003	4	16	x				x			2
			2002	10	13				x				x			1
			1998	11	10				x				x			2
			1998	4	3	1998	4	23	x				x			2?
			1997	3		1997	10		x							1
			1995	10	13	1995	10	22	x				x			2?
			1994	5	17	1994	8	30	x		x		x	x		2
			1992	8	23	1992	9	2	x				x			1
			1990	2	25	1990	11	25	x				x			1
			1984	4	20	1984	11	26	x				x			2
			1979	10	15	1979	11	28	x				x	x		2
			1971	12	1	1972	3	12					x			2
			1964										x	x		2
			1955	10	22	1957	11		x	x			x	x		3
			1949	9					x				x	x		2
			1946	7	23								x	x		2
			1945	3	31	1945	4	3					x	x		3
			1944										x			2
			1942	6	9	1942	11						x			2
			1941	6	23				x				x			2
			1938	12					x				x			1
			1937	2	9	1937	11	2	x				x	x	x	2
			1932	12	31	1933	1	5	x				x	x		3
			1932	3	2	1932	3	2	x				x			2?
			1930	7	6	1930	8	20	x				x	x		2
			1929	12					x				x	x		2
			1927	10	5	1927	12	5	x	x	x		x	x		2
			1922	10	24								x			2
			1917	2	4								x			2
			1914	7	3								x	x		2
			1912						x				x	x		2
			1907			1908	3						x	x		2
			1903	5	12	1903	5	14	x	x			x	x		2
			1895			1896			x				x	x		2
			1893	12		1894	12						x			2
			1892										x			2

Volcano	Lat. (S)	Long. (W)	Start date			End date			Location				Explosive	Lava	Fatalities	Est. VEI
			Year	Month	Day	Year	Month	Day	Central	Flank	Radial fissure	Regional fissure				
Llaima (continued)			1889	4	20	1889	7						x			2
			1883						x				x			2
			1877	1	16	1877	6	24					x	x		2
			1875			1876			x				x	x		2
			1872	6	6				x				x	x		2
			1869	4												2?
			1866						x				x			2
			1864						x				x			3
			1862						x				x			3
			1852			1853			x				x			2
			1822										x			2
			1759	12									x			2
			1751	12	18	1752			x				x	x		2
			1640	2									x			4
Villarrica	39.42	71.93	2008	10	26				x				x			1
			2004	8	5	2006			x				x			1
			2003	5	23	2004	3	25	x				x			1
			1998	2	24	2002	6		x				x			1
			1996	9	14	1997	8		x				x			1
			1996	1					x				x			1
			1995	4	15	1995	6	2	x				x			1
			1994	9	26	1994	12	30	x				x			1
			1992	9	11	1992	12		x				x			1
			1991	8	30	1991	9	17	x				x			2
			1984	8	11	1985	11	18	x				x	x		2
			1983	10	14	1983	10	16	x				x			1
			1980	6	20	1980	9	24	x				x			2
			1977	1	26	1977	1	30	x				x			1
			1971	10	29	1972	2	21	x		x		x	x	x	2
			1964	3	2	1964	4	21	x				x	x	x	2
			1963	2	25	1963	9	21	x		x		x	x	x	3?
			1961						x				x			1
			1958	11	6	1959	12	21	x				x			1
			1956	10	3	1956	11	16	x				x			1
			1948	10	9	1949	2	3	x				x	x	x	3
			1948	4	10				x				x			2?
			1947						x				x			1
			1938	12	1	1939	2	1	x				x			2
			1935	12	1	1936	6	27	x				x			1?
			1933	1	5	1933	1	18	x				x			2
			1929	12	27				x				x			1
			1927			1928			x				x			2
			1922	10	24	1922	11	27	x				x			2
			1920	12	10	1920	12	13	x				x	x		2
			1915			1918			x				x			1
			1909	8	19	1910			x				x	x		2
			1908	10	31	1908	12	12	x				x	x		2
			1907	5	5	1907	5	26	x				x			2
			1906	4	22	1906	12		x				x			2
			1904						x				x			2
			1897	12	1	1898	2	1	x				x			2
			1893	12	1	1894	2	1	x				x			2
			1883						x				x			2
			1880						x				x			2

			Start date			End date			Location							
Volcano	Lat. (S)	Long. (W)	Year	Month	Day	Year	Month	Day	Central	Flank	Radial fissure	Regional fissure	Explosive	Lava	Fatalities	Est. VEI
Villarrica (continued)			1879	2	2	1879	3		x				x			2
			1877	3	12	1877	5		x				x			2
			1875	11	17	1876			x				x			2?
			1874	4	16				x				x			2
			1869	2	4	1869	2	24	x				x			2
			1864	10					x				x			2
			1859	5	19	1860	4	12	x				x			2
			1853	11					x				x			2?
			1837	11	7	1837	11	21	x				x			2
			1832	12	24				x				x			2
			1822	11	19	1822	11	25	x				x			2
			1815			1818			x				x			1
			1806	4		1806	5		x				x			2
			1790	1		1801			x				x			1
			1787						x				x	x		2
			1780						x				x			1
			1777			1779			x				x			1
			1759	12		1759	12		x				x			1
			1751	12	14				x				x			1?
			1745						x				x			1?
			1742						x				x			2?
			1737	12	24				x				x			2?
			1730	7	8				x				x			2?
			1716						x				x			1
			1688?						x				x			1
			1657	3	15				x				x			1?
			1647	5	13				x				x			1?
			1594						x				x			2
			1562						x				x			2
			1558						x				x			2
Quetrupillan	39.50	71.70	1872	6	6											2?
Mocho-Choshuenco	39.93	72.03	1937	6	16											
			1864	11	1	1864	11	3		x			x			2
Carrán-los Venados	40.35	72.07	1979	4	14	1979	5	20	x				x	x		2
			1955	7	27	1955	11	12	x				x		x	4
			1907	4	9	1908	2		x				x	x		3
Cordón Caulle	40.52	72.20	1960	5	24	1960	7	22			x		x	x		3
			1934	3	6							x	x			2?
			1929	1	7							x	x			2?
			1921	12	13	1922	2					x	x	x		3?
Puntiagudo-C. Cenizos	40.97	72.26	1893?									x				
			1850							x			x			
Osorno	41.10	72.49	1869						x				x			2
			1855						x				x			2?
			1851										x			2?
			1837	11	7				x				x			2
			1834	11	29	1835	2	24	x	x			x	x		3?
			1790	3	9	1791	12	26		x			x	x		2
			1765 (+/- 14)						x				x			1
			1719						x							2
			1644													2
			1640													2
			1575													2

Volcano	Lat. (S)	Long. (W)	Start date			End date			Location				Explosive	Lava	Fatalities	Est. VEI
			Year	Month	Day	Year	Month	Day	Central	Flank	Radial fissure	Regional fissure				
Calbuco	41.33	72.61	1972	8	26	1972	8	26	x				x			2
			1961	2	1	1961	3	26	x				x	x		3
			1929	1	6	1929	1	6	x				x	x		3?
			1917	4		1917	5		x				x	x		3?
			1911			1912							x			2
			1909	3									x			2
			1907	4	22								x			2?
			1906										x			2
			1894	11	16	1895?			x				x			2?
			1893	1	7	1894	1	16	x				x			4
			1792?						x				x			
Huequi	42.38	72.58	1920?										x			2
			1906			1907							x			2
			1900										x			2
			1896										x			2
			1893						x				x	x		2
			1890						x				x			3?
Minchinmávida	42.79	72.44	1835	2	20	1835	3	15		x				x		0?
			1834	11	25								x			2
			1742													2
Chaitén	42.83	72.65	2008	5	2	ongoing			x				x	x		4
Mentolat	44.70	73.08	1710 (+/- 5)						x					x		
Cerro Hudson	45.90	72.97	1991	8	8	1991	10	27	x		x		x	x		5+
			1971	8	12	1971	9	18	x				x		x	3
			1891													

Volcanoes without historically recorded eruptions

The following centres are considered to have been active in the Holocene [Siebert and Simkin, 2002-], but do not have historical eruption records.

Volcano	Lat. (S)	Long. (W)	Volcano	Lat. (S)	Long. (W)
Palomo	34.61	70.30	Huanquihue group	39.87	71.55
Caldera del Atuel	34.65	70.05	Mencheca	40.53	72.04
Risco Plateado	34.93	70.00	Puyehue	40.59	72.12
Calabozos	35.56	70.50	Cerro Pantoja	40.77	71.95
San Pedro-Pellado	35.99	70.85	Antillanca group	40.77	72.15
Laguna del Maule	36.02	70.58	Tronador	41.16	72.89
Nevado de Longaví	36.19	71.16	Cayutué-la Viguería	41.25	72.27
Lomas Blancas	36.29	71.01	Cuernos del Diablo	41.40	72.00
Payún Matro	36.42	69.20	Yate	41.76	72.40
Resago	36.45	70.92	Hornopirén	41.87	72.43
Domuyo	36.58	70.42	Apagado	41.88	72.58
Cochiquito cones	36.77	69.82	Corcovado	43.18	72.80
Tromen	37.14	70.03	Cerro Yanteles	43.50	72.80
Puesto Cortaderas	37.55	69.62	Palena cones	43.78	72.47
Trocon	37.75	69.88	Melimoyu	44.08	72.88
Laguna Mariñaqui	38.27	71.10	Puyuhuapi	44.30	72.53
Tolguaca	38.31	71.65	Cay	45.06	72.98
Sollipulli	38.97	71.52	Maca	45.10	73.17
Caburgua-Huelemolle	39.25	71.70	Río Murta	46.17	72.67
Lanín	39.63	71.50			

Large post-glacial eruptions (Magnitude ≥3)

Magnitude estimates follow definition of Pyle (2000)

Years BP defined as years before A.D. 1950

Method refers to eruption dating: Hist=historically recorded, C14=Radiocarbon dating, Tephchr.=Tephrochronology

References: 1=Naranjo and Moreno (1991), 2=Heusser et al. (1992), 3=Naranjo et al. (1993), 4=Echegaray et al. (1994), 5=Pavez (1997), 6=Haberle and Lumley (1998), 7=Naranjo and Stern (1998), 8=Clavero and Moreno (2004), 9=Lara (2004), 10=Lara et al. (2004a), 11=Moreno (2004), 12=Naranjo and Stern (2004), 13=Lohmar et al. (2005), 14=Lara et al. (2006), 15=Villarosa et al. (2006), 16=Stern et al. (2007), 17=Singer et al. (2008), 18=Stern (2008), 19=Watt et al. (2009), 20=Siebert and Simkin (2010-), 21=data in this thesis.

Volcano	Unit name	Magnitude	Years BP	Method	References
Llaima	Lla2009	3	-59	Hist	20
	Lla1955	3	-5	Hist	20
	Lla1945	3	5	Hist	20
	Lla1932	3	18	Hist	20
	Lla1864	3	86	Hist	20
	Lla1862	3	88	Hist	20
	Lla1640	4	310	Hist	20
	Ll-surge2	4	8220	C14	1,13
	Ll-surge1	4	9007	C14	1,13
	Ll-plinian	5.5	9852	C14	1,13
	Ll-subplinian3	4	10582	C14	13
	Ll-subplinian2	4	11958	C14	13
	Ll-subplinian1	4	12839	C14	1,13
	Curacautín 2	5.9	14868	C14	13
	Curacautín 1	6.1	16023	C14	1,13
Sollipulli	So-A	5.8	2960	C14	3
Villarrica	Vil1948	3	2	Hist	9
	Vi-A	3	519	C14	16
	Cónquil	4	1463	C14	8
	Ski	4	1927	Tephchr.	8
	Los Nevados	4	2220	Tephchr.	8
	Pedregoso	4.5	2629	C14	8
	Pucón	5.4	3963	C14	8
	Afunalhue	4.5	4605	C14	8
	Candelaria	4.5	6408	C14	8
	Chépica	4	7990	Tephchr.	8
	Voipir	4	9519	C14	8
	Turbio	4	12601	C14	8
	Pucura	4.5	14504	Tephchr.	8
	Licán	5.9	16418	C14	8,13
Quetrupillan	Qu-A	4	1114	C14	5
Lanín	La-G	4	1346	C14	10
	La-F	4	1516	C14	10
	La-E	4	1988	C14	10
	La-D	4.5	2525	C14	10
	La-C	4	8232	C14	10
	La-B	4	11253	C14	10
	La-A	4	12451	C14	10
Mocho-Choshuenco	Mo-A	4	5162	C14	4
	Neltume	5.3	11050	C14	4
	Pirehueico	5	>11kyr	est.	16

Volcano	Unit name	Magnitude	Years BP	Method	References
Carrán-los Venados	Car1955	4.6	-5	Hist	20
	Car1907	3	43	Hist	20
Puyehue-C. Caulle	CoC1960	3.7	-10	Hist	14,17
	CoC1921	4.4	29	Hist	14,17
	Pu-D	4.5	568	C14	14,17
	Pu-C	4.5	738	C14	14,17
	Pu05	4.9	1064	C14	14,17,20
	Pu-B	4.5	1886	C14	14,17
	Pu-A	4.5	2175	C14	14,17
	Pr2	5	6641	C14	14,17
	Mascardi	4.5	8481	C14	15
	Pr1	4.5	10419	C14	14,15,17
	Trebol	4	12486	C14	15
Antillanca	An-A	4	1731	Tephchr.	17
	NHT	5.4	2200	C14	17,20
Osorno	Oso1834	3	116	Hist	20
	Os-G	3	621	C14	11
	Os-F	3	951	C14	11
	Os-E	4	1185	Tephchr.	11
	Os-D	3	1493	C14	11
	Os-C	3	2165	C14	11
	Os-B	3	3973	C14	11
	Os-A	4	4941	Tephchr.	11
Calbuco	Cal1961	3	-11	Hist	20
	Cal1929	3	21	Hist	20
	Cal1917	3	33	Hist	20
	Cal1893	3.5	57	Hist	20
	Ca13	4.6	1307	C14	21
	Ca12	4.8	2045	C14	21
	Ca11	4.9	7072	C14	21
	Ca10	4.5	7829	Tephchr.	21
	Ca9	3.5	8300	Tephchr.	21
	Ca8	5	8737	Tephchr.	21
	Ca7	4.6	9530	C14	21
	Ca6	3.5	9889	Tephchr.	21
	Ca5	3.5	10009	Tephchr.	21
	Ca4	3.5	10120	Tephchr.	21
	Ca3	3.5	10231	Tephchr.	21
	Ca2	3.5	10356	Tephchr.	21
	Ca1	5	10481	C14	21
La Vigueria	LaVig	4.4	4534	Tephchr.	21
Yate	Ya1	3.5	app. 2500	Tephchr.	21
Hornopirén	Ho1	4.5	5744	C14	21
Apagado	Ap1	5	2622	C14	21
Huequi	Hue1890	3	60	Hist	20
Minchinmávida	MIC2	5.6	4208	C14	12
	MIC1	5.1	7294	C14	12
Chaitén	Cha2008	4.3	-58	Hist	19
	CHA1	5.5	9777	C14	12,21
Corcovado	COR3	4.9	7755	C14	12
	COR2	4.7	8817	C14	12
	COR1	4.6	9293	Tephchr.	12
Yanteles	CM4	4	4470	C14	2
	CM3	4	7478	C14	2
	YAN1	5.3	9696	C14	12

Volcano	Unit name	Magnitude	Years BP	Method	References
Palena	PalRF	5	11426	C14	2,21
Melimoyu	MEL2	4.6	1638	C14	12
	MEL1	5.1	2831	C14	12
Mentolat	MEN1	5.1	7518	C14	12
Maca	MAC1	5.2	1407	C14	12
Hudson	H1991	5.5	-41	Hist	7
	T9/H1971	3.5	-21	Hist	7
	T8	4	252	C14	7
	T7	4	1072	C14	7
	HW7	3.5	1548	C14	6
	T6	4.5	2054	C14	7
	HW6	3.5	2558	C14	6
	H2/T5	6	3851	C14	7
	T4	5	4717	C14	7
	T3	4	7221	C14	7
	H1/T2	6.2	7561	C14	18
	T1	5	7765	C14	7
	HW3	3.5	11428	C14	6
	HW2	3.5	13798	C14	6
	HW1	3.5	14533	C14	6